Soft Chemistry of Layered Chalcogenides

Penny Annabelle Hyde

A thesis submitted in part fulfilment of the requirements for the degree

of

Doctor of Philosophy

Hertford College

University of Oxford

Trinity 2023

To Dad

Soft Chemistry of Layered Chalcogenides

Penny Annabelle Hyde

Abstract

This thesis reports the synthesis and characterisation of several new layered chalcogenides. Low temperature intercalation methods have been used to synthesise new metastable materials which retain the general structure of their precursors, but modify their properties.

Chapters 3 and 4 focus on the intercalation chemistry of excitonic insulator candidate Ta_2NiSe_5 and structurally related compound Ta_2NiSe_7. Several species can be intercalated into Ta_2NiSe_5, all cause significant, but similar, rearrangement of the Ta-Ni-Se layers. Conversely, Li intercalation into Ta_2NiSe_7 is found to be topotactic in nature and highly reversible. High resolution synchrotron XRD data reveals two distinct phases are formed depending on Li content, and neutron diffraction is used to characterise each phase. Electrochemical studies show continuous filling of the Li sites, and are presented as a comparison to the chemical synthesis.

Chapters 5 and 6 of this work explores the manipulation of layered near room temperature ferromagnetic compounds Fe_3GeTe_2 and Fe_5GeTe_2, by insertion of $Li(NH_2)$ or K into the interlayer spacing. Intercalation into Fe_3GeTe_2 results in rearrangement of the Fe-Ge-Te layers and an increase in the Curie temperature by approximately 25 K. In contrast, intercalation into Fe_5GeTe_2 results in no layer rearrangement and very little change to the ferromagnetic behaviour of Fe_5GeTe_2. The magnetic properties are characterised through SQUID magnetometry, neutron diffraction and Mössbauer spectroscopy on polycrystalline samples.

Declaration

The work described in this thesis was carried out in the Inorganic Chemistry Laboratory, South Parks Road, Oxford from October 2020 to July 2023 under the supervision of Prof. Simon J. Clarke. All work described is my own unless stated otherwise, and has not been submitted for any degree at this or any other university.

Penny Annabelle Hyde

Trinity 2023

Acknowledgements

When Mahmoud, Bradley and I joined the Clarke group in 2018 as three dejected undergraduates, thoroughly disillusioned with chemistry, I couldn't have imagined the incredible 5 years which lay ahead. As much as I would like to say this was down to the chemistry, in truth, this was due to the people with which I shared them.

I owe a lot to Prof. Simon Clarke for his guidance, advice and support. I am extremely thankful for the opportunity to be part of the group, without which I would never have met these wonderful people. I also thank him for the fresh garden vegetables.

I would like to thank Mags for being the original japester, and for the crocodile eyes whenever entering the office, Brad for being the dukebox of the group and for the late night office heart to hearts, and Rob (@therealroob) and for introducing me to the makina mix and teaching me the importance of the aaaaangle.

I would also like to thank Souvik for his ringtones and being a true BuLi boy, Lexy for the impromptu whiskey nights and port meadow visits, Mila for the trashy chat and being an inspiration to mothers in STEM (and Ata for the cuddles), Katie for catching them all and teaching me what a Pokémon 'gym' is, and Lemuel for being a calming influence in the office, and being the coolest person I've ever met.

I thank Dr Simon Cassidy for teaching me the ways of the group and the fabled 'rigid body' refinement, Dr Machteld Kamminga for instigating the project that constitutes Chapters 5 and 6, and for her unique style of rain-wear, Dr Shunsuke Sasaki for being a true Dennis Menace and his creative scientific explanations, Dr Viktoria Falkowski for the office date nights and her no-nonsense attitude, and Dr Nicola Kelly for the morning chats and being the true dark horse of the group.

Thank you to all those who have collaborated on numerous projects; Jiayi Cen, Prof. Maxim Avdeev, Dr Sunita Dey, Dr Stanislav Savvin, Dr Alex Scrimshire, Philip Holdship, Dr Nick Rees, and Dr Ron Smith for your hard work, patience and advice.

Finally I would like to thank the other members of the group; Dr Xiaoyu Xu, Dr Bertold Rasche, and 'the filth': Ben, Billy, Emily, Fergus, Adam, Jamie, Quirky and Lurky, not only for the ups and downs but the round and rounds and inside outs.

It's been a hell of a ride.

Contents

♫ Been around the world don't speak the language, but your science don't need explaining... uh, yeah, talk science with me ♫

- Bradley Sheath

1

Introduction

Contents

1.1 Solid State Chemistry

Solid State Chemistry is a broad area which focuses on the synthesis, properties and applications of compounds in the solid state. Solid materials that exhibit long-range atomic ordering are categorised as crystalline, which is the focus of this thesis. Solids can also exist in the amorphous phase (no long-range ordering), or somewhere in between. Advancements in this area have been fuelled by the technological uses of solids with novel properties such as superconductivity, semiconductivity, ferromagnetism and anisotropic magnetism, in addition to thermoelectric, magnetocaloric and optical properties.[1–4]

Probably the most well-known breakthrough in the field is the rechargeable lithium ion-battery, which is now the primary energy storage source in consumer electronics. This technology relies on the reversible intercalation of Li across many charge/discharge cycles where the overall structure of the host material remains unchanged. The first commercial Li-ion battery used $LiCoO_2$[5] as the cathode material and was released by Sony in 1990. However, this technology has certain issues including the growth of Li dendrites[6] which can cause short circuiting, and the ethical issues surrounding the extraction of Co which is almost exclusively sourced from the Democratic Republic of the Congo.[7] The full capacity of this system also cannot be accessed as O_2 is evolved from fully oxidised CoO_2. Modern research is geared towards improving charge density, charge/discharge rates, service life, cost and safety of energy storage materials has generated new cathode materials such as Li_2MnO_2F[8] and $LiFePO_4$,[9] which is the current front runner in the field.

Superconducting materials behave like perfect diamagnets and exhibit zero resistivity in the superconducting state which occurs below a critical temperature, electrical current and magnetic field. Since superconductors often have low critical temperatures, the major breakthrough in this field was the synthesis of YBCO materials ($YBa_2Cu_3O_{7-\delta}$),[2] with critical temperatures of up to 90 K. This is significant as the boiling point of nitrogen in approximately 77 K, so the superconducting state of these materials can be accessed using liquid N_2. YBCO phases are currently used as the central magnet component in state-of-the-art high field NMR systems (1 GHz ^{1}H NMR) because their high critical temperature means that they can carry a high current. Superconductors also have an essential application in the magnets needed to contain plasma in fusion reactors.

Solid state compounds have also been used for data storage using ferromagnetic materials. Giant magnetoresistance can be achieved by layering ferromagnetic and non-ferromagnetic metals, which exhibit large changes in resistivity in the presence of a magnetic field. This is the chemical basis of hard drive data storage. An emerging, related field is that of spintronics (or spin electronics). Whereas conventional electronics only use the charge of the electron for information processing (using binary bits 0 and 1), spintronic systems utilise the fundamental spin of the electron as an additional degree of freedom. This would dramatically increase the data storage density of devices. Some promising examples include Cr_2Te_3[10] thin films and $NiFe_2O_4$.[11]

Semiconductors play an important role in solar cells, which combines a p-type and n-type semiconductor to create and separate electron-hole pairs when irradiated by photons to generate a current. A band gap, comparable to the energy of incident photons, is critical. Although silicon-based cells are the most common due to the cost efficiency and abundance of raw materials, higher energy conversion can be achieved if multiple materials are used to span a greater range of photon wavelengths. The indium gallium pnictides are commonly used in these systems.[3]

Other notable applications of solid state compounds include GaN-based[12] phosphor converted[1] light-emitting diodes (LEDs) for enhanced lower energy lighting, zeolites[13] and metal-organic frameworks (MOFs)[14] as heterogeneous catalysts and Si-based semiconductors used in microchips and computing.[4] The development of solid state compounds has revolutionised the modern world over the past few decades, and fuels the synthesis of new functional materials.

1.2 Layered Materials

Layered materials are formed by stacks of layers a few atoms in thickness connected by weak van der Waals forces. The discovery of graphene (a single sheet of graphite) and its unusual physical properties,[15] fuelled a recent flurry of research into 2D materials.[16] Broadly speaking there are four categories of layered materials; inorganic 2D materials, organic 2D materials, hybrid 2D materials and multidimensional heterostructures.

Inorganic 2D materials include several families of compounds, such as transition metal dichalcogenides (TMDs), including SnS, $MoTe_2$ and $TaSe_2$, oxides such as MoO_3 and V_2O_5, black phosphorus and derivatives, and hexagonal boron nitride. The most heavily studied are the TMDs, such as which have promising applications in nanoelectronics,[17] photodetetors,[18] quantum devices[19,20] and catalysis.[21] Other promising compounds include the group IV chalcogenides SnS and GeS, which have anisotropic crystal structures and are predicted to have high carrier mobility and room-temperature ferroelectricity, which have applications in energy conversion.[22] Another example is h-BN, a wide band-gap and transparent material which has been used as an electrically insulating medium in a variety of laboratory devices.[23,24]

The most famous organic 2D material is graphene, which can be used to increase lubricity when used as a surface coating,[25] or as highly responsive photodetectors when used in conjunction with oxide-semiconductors.[26] 2D organic crystals, such as hexagonal microdisks (MHDs) based on p-distyrylbenzene (DSB) or 1,4-bis(4-methylstyryl)benzene (p-MSB), also have numerous applications as organic LEDs and lasers.[27]

Hybrid layered compounds have both organic and inorganic components, such as metal-organic chalcogenide assemblies (MOCHAs)[28] and hybrid perovskites,[29] which have promising applications in energy harvesting and optoelectronics.

Increased functionality can be achieved by combining different dimensionalities of materials or connecting different phases of the same stoichiometry. Combining 2D MnTe and TiO_2 nanotubes to form a heterostructure can broaden the absorption spectrum into the visible region, and can be applied to photo-electrochemical water splitting.[30] Other heterostructures such as 2D-MoS_2/1D-ZnO are promising candidates for photoanodes and solar fuel generation.[31]

1.2.1 Ternary Chalcogenides

Over 60 binary metal chalcogenides are known, over two thirds form layered compounds as a consequence of the high polarisability of the chalcogenide ions.[32] A surge in the synthesis and characterisation of ternary chalcogenides in the 1980s[33–40] resulted from the development of air-sensitive synthesis techniques and improved characterisation methods. Since then, transition metal chalcogenides have been studied extensively due to their unique physical properties and diverse structural chemistry.

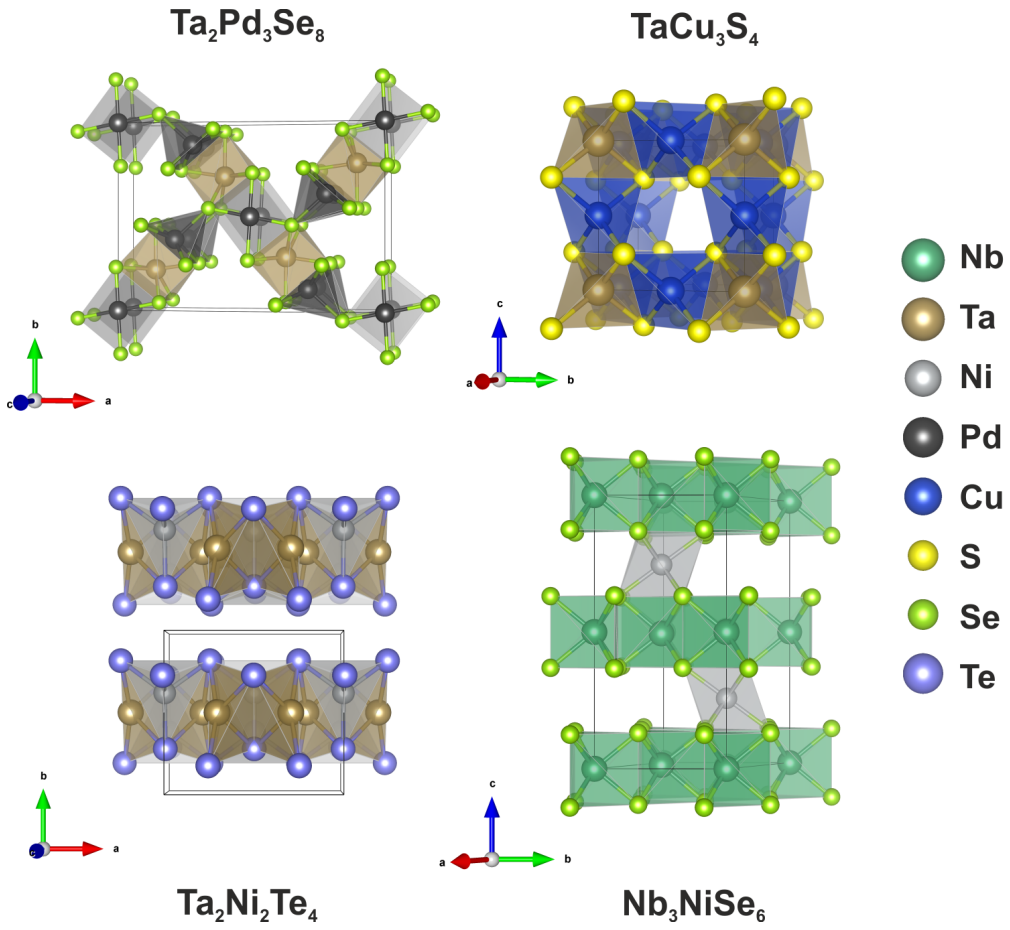

Figure 1.1: Crystal structures of various ternary chalcogenides. **Clockwise from top left**; $Ta_2Pd_3Se_8$, $TaCu_3S_4$, Nb_3NiSe_6, and $Ta_2Ni_2Te_4$.

Some examples of novel structures are shown in Figure 1.1. These include highly 2D systems ($Ta_2Ni_2Te_4$),[41] structures with interlayer linkages (Nb_3NiSe_6),[42] unusual zig-zag planes ($Ta_2Pd_3Se_8$)[34] and woven perpendicular 1D chains which produce large cavities ($TaCu_3S_4$).[43] Many interesting properties arise from the structural anisotropy in these systems.

Because of the addition of a third element, many more stoichiometric variants are available than the binary chalcogenides, and introduce an additional degree of freedom. For example, the introduction of nickel to TaS_2, which crystallises in high symmetry space group $P6_3/mmc$, forms Ta_2NiS_5[38] which features corrugated wave-like layers comprised of distorted TaS_6 octahedra linked by chains of NiS_4 tetrahedra. This distorted chain structure leads to increased electrical anisotropic behaviour.[44]

Many ternary chalcogenide families have been synthesised, including transition metal chalcogenides (TMCs),[38,45] bismuth oxychalcogenides,[46] metal phosphorus trichalcogenides (MPTs)[47,48] and other ternary chalcogenides.[49,50] Of these, systems exhibiting low dimensionality are considered prime candidates for intercalation.

1.2.2 Correlated systems

In certain systems the strong interactions between electrons play a major role in determining the physical properties of the system, known as highly correlated systems. These states include superconductors, excitonic insulators, charge density waves (CDW) and topological insulators.

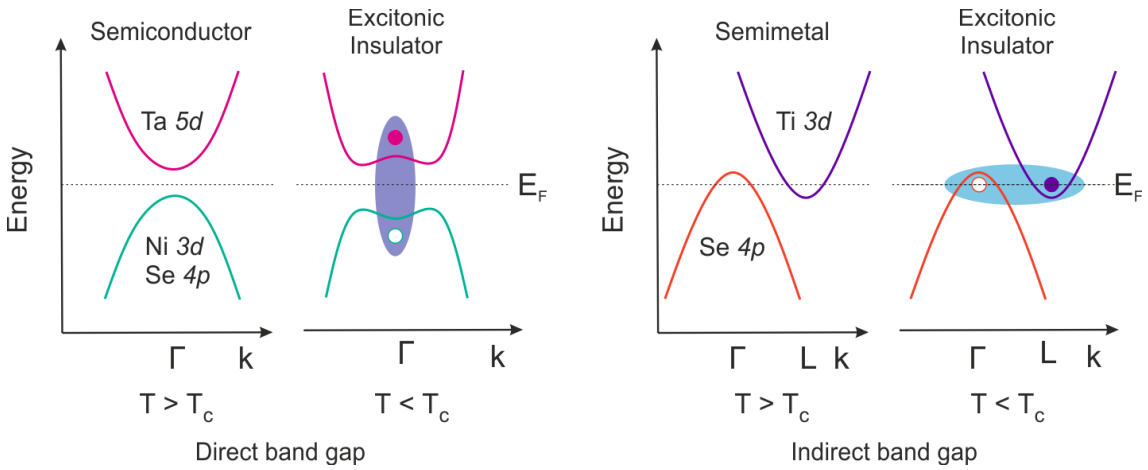

Figure 1.2: Band dispersion schematic of **left** a direct band gap semiconductor and **right** an indirect band gap semimetal, and their corresponding excitonic insulator states. The shaded area represents the bound electron-hole pair.

An excitonic insulator[51,52] is a proposed state arising in narrow-band-gap semiconductors, excitons are formed spontaneously if the exciton binding energy is less than the band gap, and because the electron and hole pair are strongly bound, the state is insulating and may be thought of as an unconventional insulating state. Since the formation of the excitonic insulating phase arises from the formation of strongly bound charge-neutral pairs, the transition can be understood as a Bose-Einstein Condensation (BEC). The band dispersion of the excitonic insulator state in systems with direct and indirect band gaps are shown in Figure 1.2. Some examples

of excitonic insulators are GaAs,[53] V_2O_3,[54] and $1T-TiSe_2$.[55] The intercalation of excitonic insulator candidate Ta_2NiSe_5 is discussed in Chapter 3.[56]

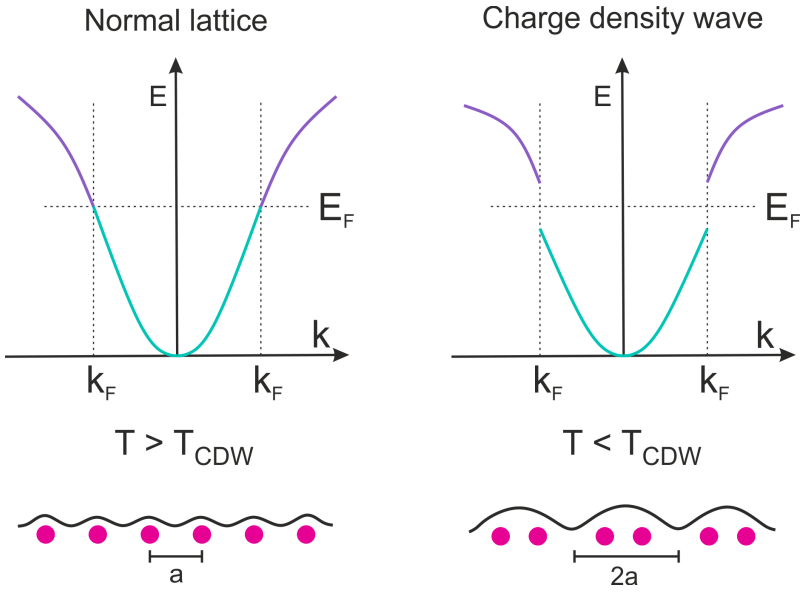

Figure 1.3: Band dispersion schematic and lattice periodicity **left** before, and **right** after a periodic lattice distortion (CDW) in a hypothetical one-dimensional metal.

Another correlated system is a Charge Density Wave (CDW), which can be described as the static modulation of conduction electrons in a metal which opens up a band gap at the Fermi Level and which is accompanied by a periodic distortion of the crystal structure. Unlike excitonic insulators, CDWs are driven by the formation of a gap at the Fermi level, rather than the formation of excitons. Peierls[57] suggested that a simple one-dimensional metal is unavoidably susceptible to a lattice distoriton which lowers the total energy of the system and opens a gap at the Fermi level.[58] Further work by Overhauser[59,60] and Wilson[61] formalise this; since the lattice has doubled in real space, a new band gap will appear at $\pm\frac{\pi}{2a}$ in k-space, which lowers the energy of the top of the valence band, shown in Figure 1.3. CDWs are

more commonly found in lower dimensional crystal systems, some examples include potassium intercalated MoS_2,[62] $CeTe_3$,[63] and $NbSe_2$.[64]

1.3 Intercalation Chemistry

The recent advances in low dimensional materials (described above) has caused a resurgence in intercalation as a powerful synthetic tool. Intercalation can be used to modify both physical and electronic structures, through doping and changing interlayer interactions. We will discuss the methods of intercalation and review the applications of materials synthesised by this method.

In general, intercalation is the insertion of foreign ions or molecules into a host lattice. 2D materials are considered ideal candidates due to the van der Waals gap (essentially a sheet of vacant interstitials) and the relatively weak interlayer attractions. However other structure types are also viable candidates. This is demonstrated by the intercalation of potassium into fullerenes. For example, potassium is able to occupy the O_h and T_d holes in the CCP array of C_{60} molecules.[65,66]

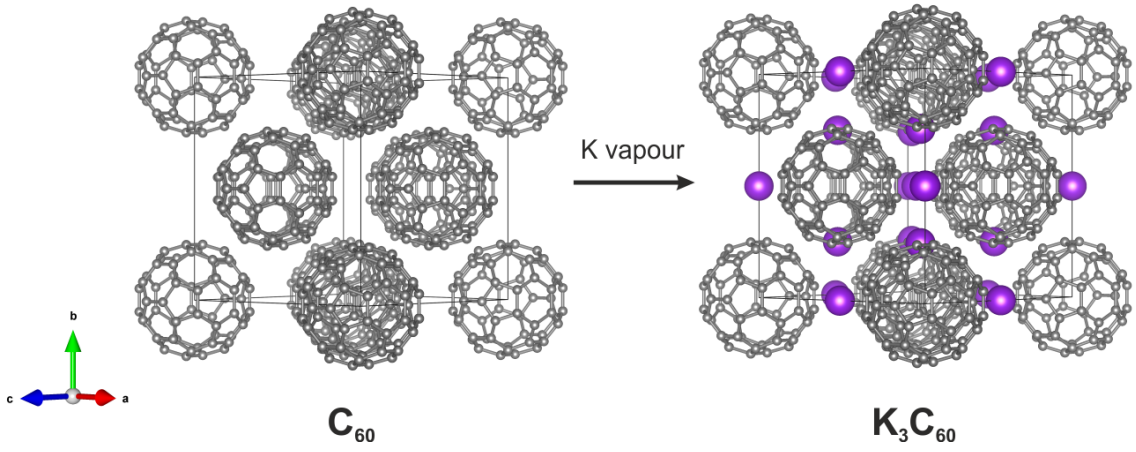

Figure 1.4: Reaction schematic of the potassium intercalation into fullerene, C_{60}.

One major advantage of intercalation is that is usually requires ambient reaction conditions. Unlike ceramic synthesis, which employs high temperatures to overcome the low ion mobility of solids, intercalation syntheses can often be performed at room temperature and allows access to novel metastable phases.

1.3.1 Intercalation methods

Several intercalation methods exist including chemical intercalation from vapour[67,68] or liquid[67,69] phases, or electrochemically using solid[70,71] or liquid[72–74] electrolytes, shown in Figure 1.5.

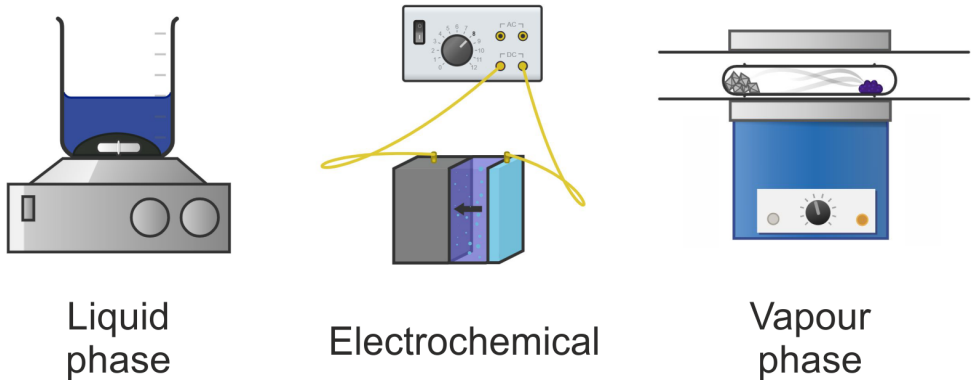

Figure 1.5: Experimental setup schematics of **left to right** liquid phase, electrochemical and vapour phase intercalation methods

Liquid phase

Liquid phase intercalation is performed by suspending the host solid material in a liquid or solution that contains the intercalant species, and the reaction can be spontaneous at room or slightly elevated temperatures. The liquid intercalant source can be a solution containing intercalants[67,75–77] or be a molten state of an intercalant.[69,78] Liquid ammonia and some organic solvents like methylamine and tetrahydrofuran dissolve alkali and alkaline earth metals[76] and make effective intercalation reagents due to their high reduction potential, a consequence of the solvation of the alkali metal valence electrons. Examples of materials that have been intercalated using

this method include graphene[76], MoS_2,[79] and black phosphorus (BP), which produces superconducting phases M_xBP (M = Li, K, Rb, Cs, Ca) which have a universal superconducting T_C of 3.8 K.[80]

Molten metals or metal salts can be used as intercalant reaction mediums, like the intercalation of Ca into graphene using molten Li-Ca alloys,[69,78] for example. This method requires high temperatures so a degree of kinetic control is lost. It is also harder to control the composition of the final product as the intercalant is always in excess. Liquid phase reactions however are a favourable method for less electronically conductive materials, relative to electrochemical intercalation methods.

Electrochemical

Electrochemical intercalation on the other hand requires host materials and intercalant species that are reasonably conductive. The process is driven by an applied external current in a typical electrochemical cell set up, shown in Figure 1.5, in which the anode and cathode are the intercalant and host species respectively. The electrochemical cell requires either a solid or liquid electrolyte, which is not the source of the guest species, and an external current is required.

The use of electrochemistry offers much greater control of the final composition by the means of the applied potential, as the amount of charge transferred can be controlled. Alkali and alkali earth metals are common anode materials and are widely reported electrochemical intercalants into layered materials.[81–84]

Vapour phase

Vapour phase intercalation is one of the earliest and most common mechanisms. It utilises temperature gradients to control the transport of the intercalant is the gas phase. Usually both precursors are heated in a sealed vessel to create a high vapour pressure inside the system. As excess of intercalant is usually used to drive the reaction to completion, it can be difficult to control the end composition. In order to vaporise the guest species, elevated temperatures are usually required.

Many alkali metal (Na, K, Rb, Cs),[85] transition metal (Cu, Cd, Hg)[86] and post transition metal (Sn, Pb)[86] intercalates have have been reported using this method. Halogen guest species bromine[87] and iodine[88,89] have also been reported.

1.3.2 Intercalation for electrochemical energy storage

The principles of intercalation chemistry can be applied to electrochemical energy storage. Graphite-like carbon material is often used as the anode material in Li-ion batteries as the layered structure can reversibly accommodate Li ions during charge-discharge cycles.

Other layered materials have been explored as battery materials. Whittingham[90,91] reported that the reversible intercalation of Li into TiS_2 to form Li_xTiS_2 could be used as prototypical secondary battery systems with high energy density Li-ion batteries that are lightweight,[92] have a high metallic conductivity[93,94] and rapid self-diffusion of Li.[95] TaS_2 can also be used as a prototype cathode for Na-ion batteries,[96] although the weight and scarcity of Ta does not make this suitable for widespread commercial use.

Another candidate for electrochemical applications is black phosphorus, due to its high theoretical capacity[97] and low diffusion barrier for Li ions.[98] Its large interlayer distance of 5.3 Å allows the intercalation of larger ions[99–101] and makes a promising candidate for the anode materials in both Li-ion and Na-ion battery- a cost effective alternative.[102–107]

1.3.3 Property tuning through intercalation

Intercalation has become one of the most widely used methods to modify the properties of 2D materials. Band engineering can be achieved through the intercalation of both donor or acceptor type intercalants. MoO_3 is a wide band gap material, which can be transformed into a photoactive material through intercalation. Insertion of H^+ results in the formation of unstable H_2O groups, which are then released from solid MoO_3 as gaseous molecular H_2O. The resulting phase is oxygen deficient MoO_{3-x} which has a defect state within the bandgap giving rise to the photoactive state.[108,109]

Magnetic properties can also be tuned exploiting intercalation chemistry by altering lattice parameters, spin-orbit effects and orbital moments. The addition of Mn into $NbSe_2$ to form $MnNb_3Se_6$ by filling the interstitial octahedral holes was found to induce a magnetic phase transition to a chiral magnetic solution state, consisting of helical spin structures.[110] Although this phase is formed using high temperature reactions of elemental precursors, the resulting phase resembles that of an intercalate. Similarly, Cr intercalation to form $CrNb_3Se_6$ results in a fully helimagnetic phase below 127 K.[111]

Correlated systems can also be altered using intercalation. Cu insertion into $TiSe_2$ using vapour-based methods causes the transition temperature of the CDW to decrease whilst a superconducting phase emerges. Both these states are found to co-exist inCu_xTiSe_2 ($0.055(5) \leq x \leq 0.091(6)$).[112,113]

1.3.4 Intercalation-induced structural phase transitions

Structural modifications can be controlled through intercalation. The co-ordination requirements of the guest species can drive the separation of and rearrangement of the adjacent layers, as well as inducing structural phase transitions. Sodium intercalation into black phosphorus[114] proceeds via a two stage mechanism in which the arrangement of the layers is altered, shown in Figure 1.6.

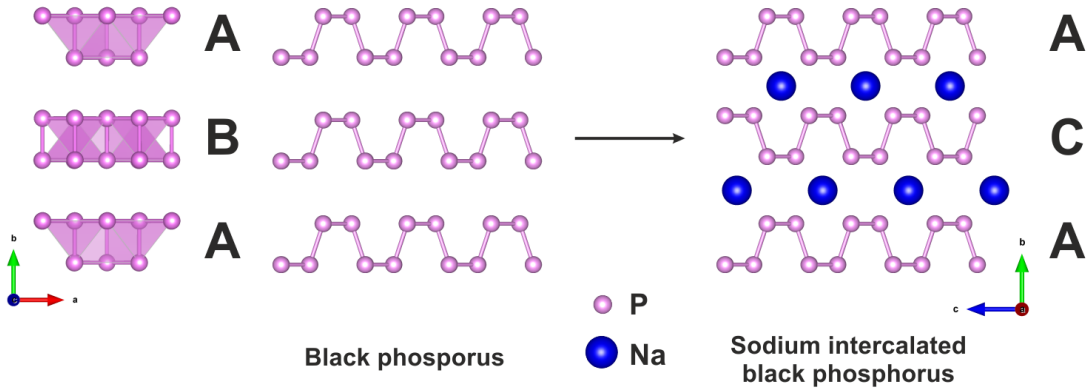

Figure 1.6: Reaction schematic of the sodium intercalation into black phosphorus showing the rearrangement of phosphorus layers.

One heavily studied intercalation-induced structural transition is that of semiconducting 2H-MoS_2 to metallic 1T-MoS_2 upon the insertion of Li. The previously trigonal prismatic MoS_6 site becomes octahedral by sliding one of the co-ordinating sulphur layers, which is driven by lowering the electronic energy upon the addition of electrons.[115] An additional distortion of the Mo positions away from the centre of their octahedra to form the 1T'-MoS_2 phase is observed.[116] Additional experiments have shown this process is reversible by controlling the migration of Li^+ ions using an electric field.[117]

1.4 Magnetism in Solids

Magnetism plays and important part in the functionality of materials. Both crystal and electronic structure contribute to the magnetism observed in solids. For example, the oxidation state of an element controls the number of unpaired spins in a system, and the local geometry can affect how spins interact with one another. This section will provide an overview of the common types of magnetism observed in solids.

1.4.1 Diamagnetism

Diamagnetism is an intrinsic phenomenon common to all materials, in which the circulation of paired electrons around the nucleus in the presence of a magnetic field generates a small current. This in turn generates a magnetic moment which opposes the applied field. This effect can be rationalised using Lenz' Law. The susceptibility of a diamagnet is always negative, due to the direction of the induced moments relative to the field. Diamagnetism is often many orders of magnitude smaller than other magnetic interactions (-10^{-6} – 10^{-4} emu mol^{-1}), and is the only magnetism observed in closed-shell systems such as Bi_2Se_3 and Ta_2PdS_6.[35,118]

1.4.2 Paramagetism

If a material contains electrons with unpaired spins, paramagnetism may be observed. In an applied field, these unpaired spins align parallel to the field and leads to a positive magnetisation. Further classification of paramagnetic materials can be made depending on whether the electrons are localised or itinerant.

Curie Paramagnetism

Most paramagnetic materials with localised unpaired spins that do not interact are found to obey the Curie Law (Equation 1.1), for both extended materials and molecular species.

$$\chi = \frac{C}{T} \tag{1.1}$$

where χ is the magnetic susceptibility and C is the Curie constant given by:

$$C = \frac{N_A \mu_{eff}^2 \mu_B^2}{3k_B} \tag{1.2}$$

where N_A is Avogadro's constant, μ_{eff} is the effective magnetic moment, μ_B is the Bohr magneton, and k_B is the Boltzmann constant. This can be reduced to:

$$\mu_{eff} \simeq 2.84\sqrt{C} \tag{1.3}$$

and used to determine the effective magnetic moment by extracting C from a plot of T vs $1/\chi$. The effective magnetic moment is itself a function of the total angular

momentum of the species given by:

$$\mu_{eff} = g\sqrt{J(J+1)} \tag{1.4}$$

where J is the sum of the spin angular momentum, S, and the orbital momentum, L. g is the Landé factor, given below:

$$g = 1 + \frac{J(J+1) + S(S+1) - L(L+1)}{2J(J+1)} \tag{1.5}$$

Orbital angular momentum of the first-row transition metals is usually quenched by the ligand field splitting of the $3d$ orbitals. In this case, $L = 0$, $J = S$ and $g = 2$. Substitution into Equation 1.4 gives the spin-only effective moment as:

$$\mu_{eff} = 2\sqrt{S(S+1)} \tag{1.6}$$

The number of unpaired electrons can be calculated from the Curie constant by combining Equations 1.3 and 1.6 to give:

$$C \simeq \frac{S(S+1)}{2} \tag{1.7}$$

Magnetic susceptibility values for Curie paramagnets typically fall in the range of 10^{-4} – 10^{-2} emu mol^{-1}. This dominates the opposing effects from core-electron diamagnetism.

Curie Weiss Paramagnetism

When localised unpaired spins in a material interact with one another, the Curie Law has to be adjusted to account for these additional interactions, giving the Curie-Weiss Law:

$$\chi = \frac{C}{T - \theta} \tag{1.8}$$

where θ is the Weiss constant. The magnitude of the Weiss constant reflects the strength of the interactions between magnetic moments, and the sign indicates the type of ordering; parallel spins give positive Weiss constants and antiparallel spins gives a negative Weiss constant. Examples include $BaVO_{2.9}$[119] and MnF_2.[120]

Pauli Paramagnetism

In systems where electrons are not localised (for example in metals), Pauli paramagnetism is observed. When unperturbed by a magnetic field, there is an equal proportion of spin-up and spin-down electrons in the conduction band. When an external field is applied the degeneracy of the spin states is lost as the spin aligned parallel with the field is energetically more favourable and the populations are no longer equal. This leaves a net positive magnetisation, however this is only a small effect as it only arises from spins close to the Fermi level. Pauli paramagnetism is usually of similar magnitude to core-electron diamagnetism, several orders of magnitude weaker than Curie paramagnetism. Examples include almost all metals, Rh_2O_3 and $CeCu_2Si_2$.[121,122]

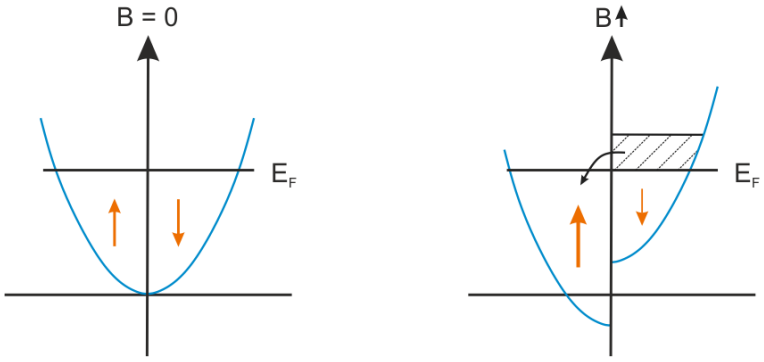

Figure 1.7: Distribution of electron density of a Pauli paramagnet in **left** zero field, and **right** an applied field.

Temperature Independent Paramagnetism (TIP)

Systems with closed shells are only expected to exhibit diamagnetism. However, some systems, such as permanganate[123] have an unpopulated low lying excited state which can mix with the ground state, and results in a paramagnetic contribution. The magnitude of the TIP contribution is independent of temperature. Pauli paramagnetism is also temperature independent but should not to be confused with TIP.

1.4.3 Ferromagnetism

Ferromagnetism arises in materials where there is a concentrated array of strongly interacting spins. This can occur in itinerant spin-polarised systems (like elemental iron or CrO_2) where one spin state is energetically preferred at the Fermi level so is more populated. Alternatively, localised moment systems such as Au_4Mn or Pd_2MnSn display ferromagnetism when it is energetically favourable for neighbouring spins to align parallel to one another. Moments in these systems are locally grouped into domains, which randomly orientate to form a lower energy state giving a net magnetic moment of zero. In the presence of an applied field, the domains align with the field to give a large (typically 10^{-2} – 10^{0} emu mol^{-1}) positive magnetisation. Above the Curie temperature, the thermal energy is sufficient to disrupt the interactions between spins and the material behaves like a paramagnet. Due to the stability of the magnetic state, ferromagnets normally saturate in much lower external fields than paramagnets.

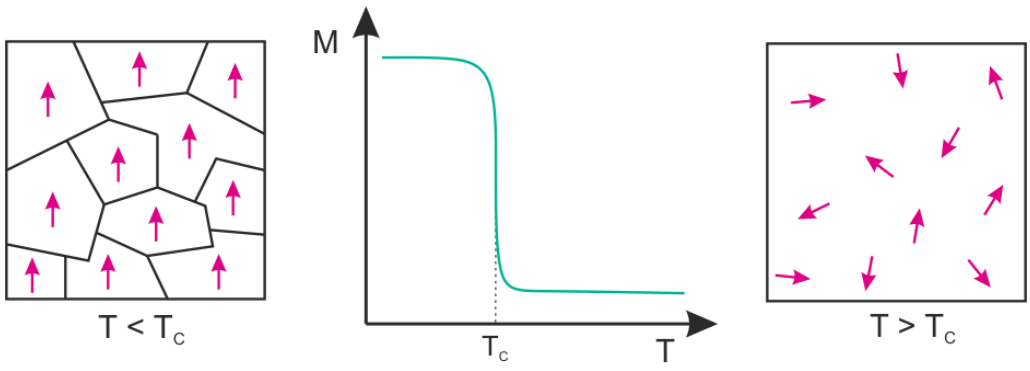

Figure 1.8: Magnetisation vs temperature curve of a typical ferromagnet. The domain alignment and paramagnetic behaviour is shown on either side of the transition temperature.

Magnetisation isotherms (also called hysteresis loops) are typically measured by magnetising a sample before reversing the direction of the applied field, then reapplying the positive field. Typical isotherms are shown in Figure 1.9.

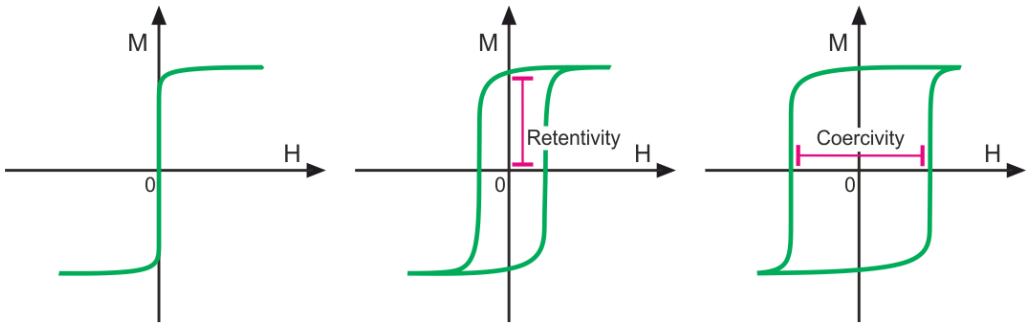

Figure 1.9: Magnetisation isotherms of ideal **left to right** soft, intermediate and hard ferromagnets.

Different ferromagnets exhibit different behaviour and can be characterised by their coercivity - the amount of opposing magnetic field must be applied to cancel the remnant magnetisation after being saturated, and by their retentivity - the material's ability to retain residual magnetisation after the applied field is removed. The coercivity can be quantified by taking the difference of the x- intercepts, and the retentivity is the magnetisation at $H = 0$, shown in Figure 1.9.

Since the susceptibilities of ferromagnets are generally $2 - 4$ orders of magnitude larger than diamagnets or Pauli paramagnets, even small ferromagnetic impurities are evident in magnetisation data. Figure 1.10a shows the ideal behaviour of pure samples as functions of applied field. Figure 1.10b shows the behaviour of different magnetic systems with ferromagnetic impurities present.

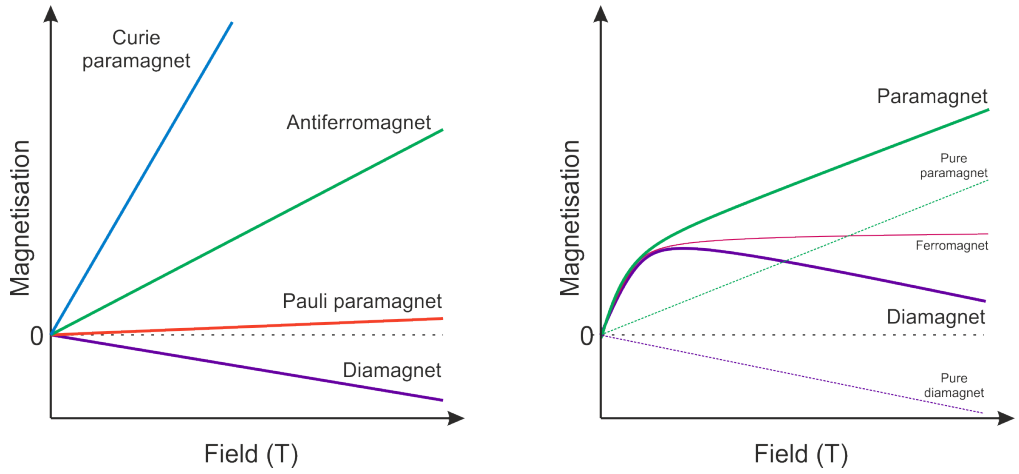

(a) Ideal curves **(b)** With ferromagnetic impurities

Figure 1.10: Magnetisation vs field plots for a range of magnetic systems.

Samples with impurities will display both components; the low field saturation curve of the ferromagnet and the linear behaviour of the sample at higher fields. In order to determine the susceptibility of the bulk sample, the gradient of the M v H curve can be taken in the linear region above the saturation field of the ferromagnet.

Ferrimagnetism

If the magnitude of the magnetic moments of antiparallel aligned spins differ, ferrimagnetism can occur as a result. Although spins exhibit antiferromagnet ordering, a net moment is observed, and the behaviour is ferromagnetic-like. Famous examples of ferrimagnetic materials are spinels such as Fe_3O_4,[124] and $NiCo_2O_4$,[125] in which Ni^{3+} dominates the tetrahedral (spin up) site whilst $Ni^{3.5+}$ and $Co^{2.5+}$ share the octahedral (spin down) site.

1.4.4 Antiferromagnetism

Antiferromagnetism is another form of long-range ordering, in which adjacent spins align anti-parallel to one another below the Néel temperature, T_N. The results in a net magnetic moment of zero, shown in Figure 1.11. Approaching T_N from high temperatures, the decreasing thermal energy lowers the fluctuation of moments and so the sample is more susceptible to the external field. Approaching T_N from low temperatures, the increasing thermal fluctuation destroys the antiferromagnetic state and so the magnetic susceptibility increases. Some examples of antiferromagnets include MnO[126] and $BaCa_2Fe_2O_5Cu_2S_2$.[127]

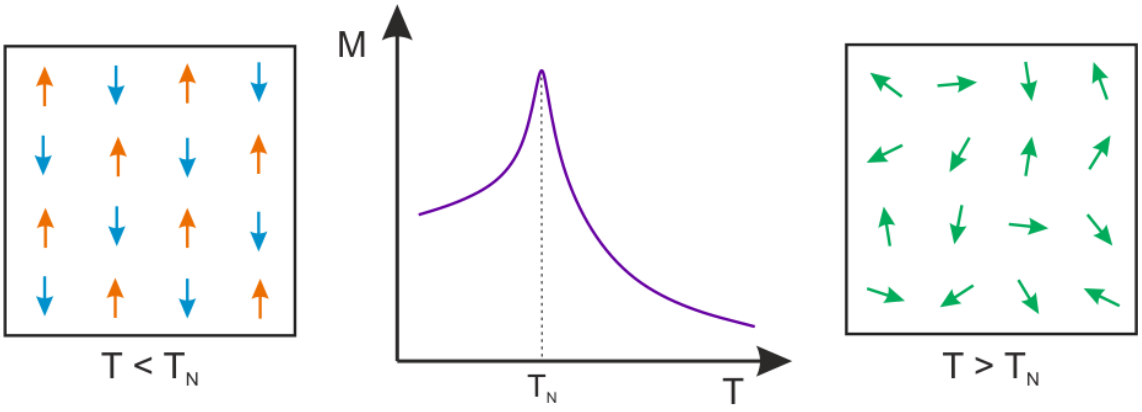

Figure 1.11: Magnetisation vs temperature curve of a typical antiferromagnet. Corresponding spin alignments are represented on either side.

1.4.5 Frustrated Magnetism

Frustrated magnetism can occur in magnetic systems where there are competing interactions. This can be caused by specific geometries such as exchange triangles, shown in Figure 1.12. Spin glasses occur in materials where magnetic frustration is augmented by disorder. In the high temperature regime, there is enough thermal energy to overcome these competing interactions and the material acts like a paramagnet. As the material is cooled, disordered clusters of spins will start to form until all spins become 'frozen' in one of a number of ground state configurations at the freezing temperature, T_g. The frozen configuration depends on the history of the system, and there is no long-range magnetic order. Some examples of spin glasses are $Cu_{1-x}Mn_x$[128] and $BiFeO_3$.[129]

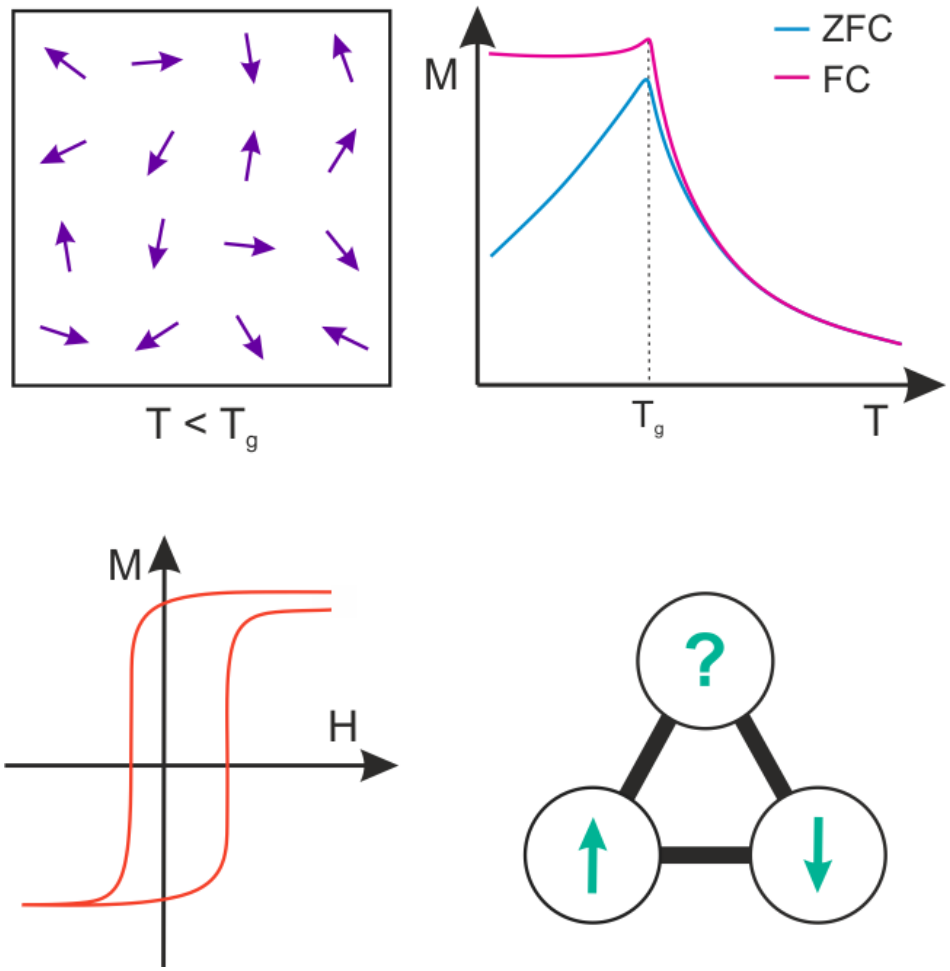

Figure 1.12: Clockwise from top left; spin alignment below the spin glass freezing temperature; typical magnetisation vs temperature curves of a spin glass; an exchange triangle motif; and asymmetric magnetisation isotherms often observed in frustrated systems where there is also disorder.

1.5 Magnetic Exchange

Interactions between magnetic moments can be mediated in a variety of ways. Through-space interactions are long range but are typically weak and generally do not account for magnetic ordering. Through-bond interactions however are much stronger but require orbital overlap, which can be influenced by a variety of factors, including geometry.

1.5.1 Direct exchange

Direct exchange occurs when magnetic ions are close enough to interact directly, i.e. nearest neighbours, and is a very short range interaction. Direct exchange can lead to ferromagnetic or antiferromagnetic coupling, but ions must contain unpaired electrons. This is shown in Figure 1.13.

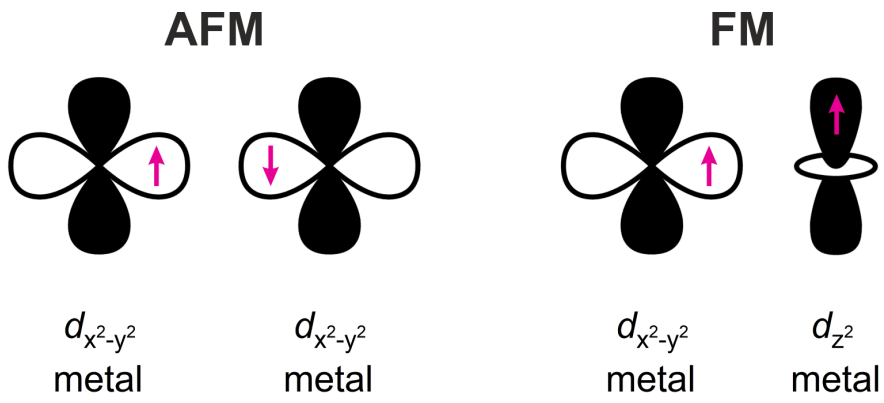

Figure 1.13: Direct exchange of two filled orbitals with antiferromagnetic (AFM) and ferromagnetic (FM) coupling.

1.5.2 Superexchange

Superexchange interactions, shown in Figure 1.14, occur through a mediating non-magnetic ion. When there is donation of electron density from one ion to another to form a covalent bond, there is a preference in the spin state of this electron density depending on the spin state of the recipient ion. Using Hund's rules (electrons in partially filled orbitals must have parallel spins) and the Pauli exclusion principle (that two electrons in the same orbital must have opposite spins) the coupling between two metal centres can be predicted using geometry and electron configurations. This is the basis for the Goodenough-Kanamori rules[130–132] which can be used to predict the most likely dominant magnetic coupling between metals.

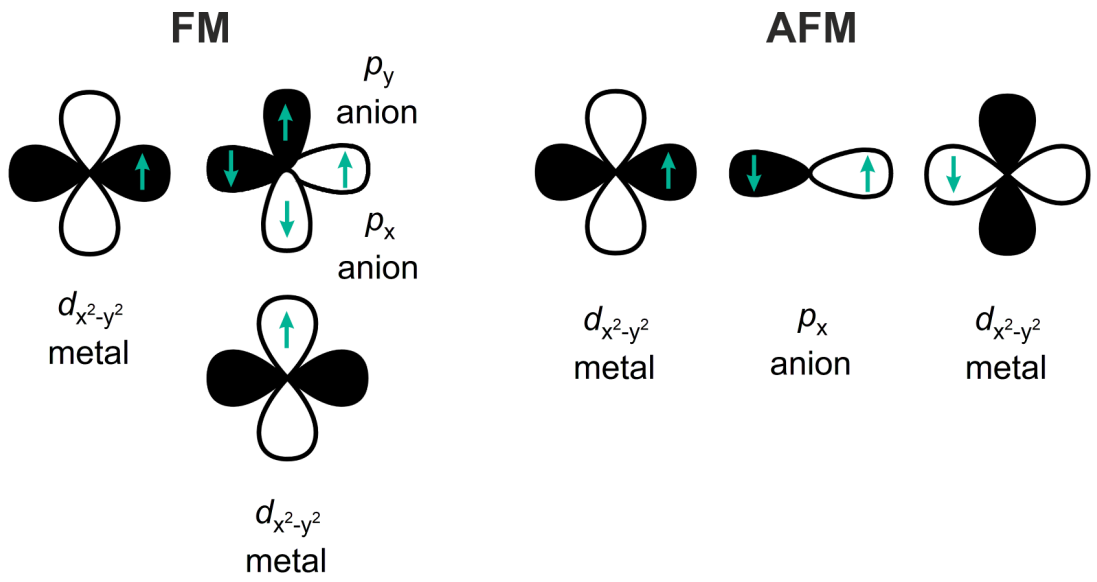

Figure 1.14: Super exchange of two filled orbitals mediated by filled anion orbitals, with antiferromagnetic (AFM) and ferromagnetic (FM) coupling.

1.6 Thesis Aims

This thesis aims to explore the relationship between the structure and properties of new layered chalcogenides synthesised via low temperature soft chemical routes, with a view to developing new functional materials.

Chapter 3 explores the synthesis and characterisation of three new intercalates of the excitonic insulator candidate Ta_2NiSe_5. This section aims to compare and contrast the structure and properties of these intercalates respective to Ta_2NiSe_5, and investigate the effect of insertion of atoms on the excitonic insulator transition. This work is in press in *Inorganic Chemistry*.[56]

Chapter 4 reports the synthesis of the lithium intercalates of Ta_2NiSe_7, which is structurally related to Ta_2NiSe_5. Two different intercalate phases are formed which have different Li site occupancies and display different magnetic properties. This chapter also examines the electrochemical intercalation of Li into Ta_2NiSe_7, and draws comparison between the lithiated phases produced chemically and electrochemically. Complete Li de-intercalation is also examined in this chapter.

Chapter 5 explores the synthesis and characterisation of two new intercalates of room temperature anisotropic ferromagnet Fe_5GeTe_2, synthesised by insertion of potassium or lithium-amide into the interlayer spacing. Both species demonstrate specificity for one interstitial site due to co-ordination requirements. Subtle increases in the Curie temperatures are observed relative to Fe_5GeTe_2 for both intercalates, whilst other magnetic properties remain relatively unchanged.

Chapter 6 reports the potassium intercalation into related layered anisotropic ferromagnet Fe_3GeTe_2. Significant rearrangement of the layers is induced although the intralayer structure of Fe-Ge-Te sheets remains unchanged. In addition, an increase in the Curie temperature of approximately 15 K is observed, and other magnetic properties such as retentivity and coercivity are also affected.

Chapter 7 summarises the work in this thesis as a whole, and reflects on the future outlook of this work.

References

[1] M. Seibald, T. Rosenthal, O. Oekler, W. Schnick, *Critical Reviews in Solid State and Materials Sciences* **2014**, *39*, 215–299.

[2] M. K. Wu, J. R. Ashburn, C. J. Torng, P. H. Hor, R. L. Meng, L. Gao, Z. J. Huang, Y. Q. Wang, C. W. Chu, *Physical Review Letters* **1987**, *58*, 908–10.

[3] K. Nishioka, T. Takamoto, T. Agui, M. Kaneiwa, Y. Uraoka, T. Fuyuki, *Solar Energy Materials and Solar Cells* **2006**, *90*, 57–67.

[4] D. Akinwande, C. Huyghebaert, C. H. Wang, M. I. Serna, S. Goossens, L. J. Li, H. S. P. Wong, F. H. L. Koppens, *Nature* **2019**, *573*, 507–18.

[5] K. Mizushima, P. C. Jones, P. J. Wiseman, J. B. Goodenough, *Solid State Ionics* **1981**, *3-4*, 171–74.

[6] J. Xiao, *Science* **2019**, *366*, 426–27.

[7] L. Prause, *The Material Basis of Energy Transitions*, Academic Press, **2020**, pp. 153–67.

[8] R. Natsui, I. Ikeuchi, S. Ohuchi, K. Nakura, *ECS Meeting Abstracts* **2018**, *MA2018-02*, 202.

[9] A. S. Andersson, J. O. Thomas, B. Kalska, L. Häggström, *Solid State Letters* **2018**, *3*, 66.

[10] I. H. Lee, B. K. Choi, H. J. Kim, M. J. Kim, H. Y. Jeong, J. H. Lee, S.-Y. Park, Y. Jo, C. Lee, J. W. Choi, et al., *ACS Applied Nano Materials* **2021**, *4*, 4810–4819.

[11] U. Lüders, A. Barthelemy, M. Bibes, K. Bouzehouane, S. Fusil, E. Jacquet, J.-P. Contour, J.-F. Bobo, J. Fontcuberta, A. Fert, *Advanced Materials* **2006**, *18*, 1733–1736.

[12] S. Denbaars, D. Feezell, K. Kelchner, S. Pimputkar, C. Pan, C. Yen, S. Tanaka, Y. Zhao, N. Pfaff, R. Farrell, M. Iza, S. Keller, U. Mishra, J. Speck, S. Nakamura, *Acta Materialia* **2013**, *61*, 945–51.

[13] J. Liang, Z. Liang, R. Zou, Y. Zhao, *Advanced Materials* **2017**, *29*, 1701139.

[14] C. D. Wu, M. Zhao, *Advanced Materials* **2017**, *29*, 1605446.

[15] K. S. Novoselov, *Reviews of Modern Physics* **2011**, *83*, 837–49.

[16] S. Z. Butler, S. M. Hollen, L. Cao, Y. Cui, J. A. Gupta, H. R. Gutiérrez, T. F. Heinz, S. S. Hong, J. Huang, A. F. Ismach, E. Johnston-Halperin, M. Kuno, V. V. Plashnitsa, R. D. Robinson, R. S. Ruoff, S. Salahuddin, J. Shan, L. Shi, M. G. Spencer, M. Terrones, W. Windl, J. E. Goldberger, *ACS Nano* **2013**, *7*, 2898–926.

[17] K. M. Price, S. Najmaei, C. E. Ekuma, R. A. Burke, M. Dubey, A. D. Franklin, *ACS Applied Nano Materials* **2019**, *2*, 4085–94.

[18] Y. Lu, T. Chen, G. H. Ryu, H. Huang, Y. Sheng, R.-J. Chang, J. H. Warner, *ACS Applied Nano Materials* **2019**, *2*, 369–78.

[19] A. J. Littlejohn, Z. Li, Z. Lu, X. Sun, P. Nawarat, Y. Wang, Y. Li, T. Wang, Y. Chen, L. Zhang, H. Li, K. Kisslinger, S. Shi, J. Shi, A. Raeliarijaona, W. Shi, H. Terrones, K. M. Lewis, M. Washington, T.-M. Lu, G.-C. Wang, *ACS Applied Nano Materials* **2019**, *2*, 3684–94.

[20] T. Lehnert, M. Ghorbani-Asl, J. Köster, Z. Lee, A. V. Krasheninnikov, U. Kaiser, *ACS Applied Nano Materials* **2019**, *2*, 3262–70.

[21] K. Jaiswal, Y. R. Girish, M. De, *ACS Applied Nano Materials* **2020**, *3*, 84–93.

[22] P. Sutter, E. Sutter, *ACS Applied Nano Materials* **2018**, *1*, 3026–34.

[23] Y. Li, V. Garnier, P. Steyer, C. Journet, B. Toury, *ACS Applied Nano Materials* **2020**, *3*, 1508–15.

[24] R. Han, M. H. Khan, A. Angeloski, G. Casillas, C. W. Yoon, X. Sun, Z. Huang, *ACS Applied Nano Materials* **2019**, *2*, 2830–35.

[25] S. Zhao, S. Shi, K. Xia, T. Wang, M. Chai, Y. Zhang, C. Qu, Q. Zheng, *ACS Applied Nano Materials* **2020**, *3*, 1992–98.

[26] I. Ruiz, T. E. Beechem, S. Smith, P. Dickens, E. A. Paisley, J. Shank, S. W. Howell, R. Sarma, B. L. Draper, M. D. Goldflam, *ACS Applied Nano Materials* **2019**, *2*, 6162–68.

[27] Y.-L. Shi, M.-P. Zhuo, X.-D. Wang, L.-S. Liao, *ACS Applied Nano Materials* **2020**, *3*, 1080–97.

[28] E. A. Schriber, D. C. Popple, M. Yeung, M. A. Brady, S. A. Corlett, J. N. Hohman, *ACS Applied Nano Materials* **2018**, *1*, 3498–508.

[29] O. Y. Posudievsky, N. V. Konoshchuk, A. G. Shkavro, V. L. Karbivskiy, V. G. Koshechko, V. D. Pokhodenko, *ACS Applied Nano Materials* **2018**, *1*, 4145–55.

[30] A. Puthirath Balan, S. Radhakrishnan, R. Neupane, S. Yazdi, L. Deng, C. A. de los Reyes, A. Apte, A. B. Puthirath, B. M. Rao, M. Paulose, R. Vajtai, C.-W. Chu, A. A. Martí, O. K. Varghese, C. S. Tiwary, M. R. Anantharaman, P. M. Ajayan, *ACS Applied Nano Materials* **2018**, *1*, 6427–34.

[31] K. Karmakar, D. Maity, D. Pal, K. Mandal, G. G. Khan, *ACS Applied Nano Materials* **2020**, *3*, 1223–31.

[32] P. A. Madden, M. Wilson, *Chemical Society Reviews* **1996**, *25*, 339–350.

[33] E. W. Liimatta, J. A. Ibers, *Journal of Solid State Chemistry* **1988**, *77*, 141–147.

[34] D. A. Keszler, J. A. Ibers, S. Maoyu, L. Jiaxi, *Journal of Solid State Chemistry* **1985**, *57*, 68–81.

[35] D. A. Keszler, P. J. Squattrito, N. E. Brese, J. A. Ibers, S. Maoyu, L. Jiaxi, *Inorganic Chemistry* **1985**, *24*, 3063–67.

[36] D. A. Keszler, J. A. Ibers, *Journal of the American Chemical Society* **1985**, *107*, 8119–27.

[37] S. A. Sunshine, J. A. Ibers, *Inorganic Chemistry* **1986**, *25*, 4355–58.

[38] S. A. Sunshine, J. A. Ibers, *Inorganic Chemistry* **1985**, *24*, 3611–14.

[39] A. Mar, J. A. Ibers, *Journal of Solid State Chemistry* **1991**, *92*, 352–361.

[40] E. W. Liimatta, J. A. Ibers, *Journal of Solid State Chemistry* **1987**, *3*, 384–89.

[41] W. Tremel, *Angewandte Chemie* **1991**, *103*, 900–903.

[42] J. M. Voorhoeve, N. van den Berg, M. Robbins, *Journal of Solid State Chemistry* **1970**, *1*, 134–137.

[43] S. Ali, S. van Smaalen, *Zeitschrift für Anorganische und Allgemeine Chemie* **2014**, *640*, 931–934.

[44] F. J. DiSalvo, C. H. Chen, R. M. Fleming, J. V. Waszczak, R. G. Dunn, S. A. Sunshine, J. A. Ibers, *Journal of The Less-Common Metals* **1986**, *116*, 51–61.

[45] Q. Jia, Y. C. Zhang, J. Li, Y. Chen, B. Xu, *Materials Letters* **2014**, *117*, 24–27.

[46] J. Wu, H. Yuan, M. Meng, C. Chen, Y. Sun, Z. Chen, W. Dang, C. Tan, Y. Liu, J. Yin, Y. Zhou, S. Huang, H. Q. Xu, Y. Cui, H. Y. Hwang, Z. Liu, Y. Chen, B. Yan, H. Peng, *Nature Nanotechnology* **2017**, *12*, 530–34.

[47] J.-U. Lee, S. Lee, J. H. Ryoo, S. Kang, T. Y. Kim, P. Kim, C.-H. Park, J.-G. Park, H. Cheong, *Nano Letters* **2016**, *16*, 7433–38.

[48] M. Cabán-Acevedo, M. L. Stone, J. R. Schmidt, J. G. Thomas, Q. Ding, H. C. Chang, M. L. Tsai, J. H. He, S. Jin, *Nature Materials* **2015**, *14*, 1245–51.

[49] C. Gong, L. Li, Z. Li, H. Ji, A. Stern, Y. Xia, T. Cao, W. Bao, C. Wang, Y. Wang, Z. Q. Qiu, R. J. Cava, S. G. Louie, J. Xia, X. Zhang, *Nature* **2017**, *546*, 265–69.

[50] A. Wochnik, C. Heinzl, F. Auras, T. Bein, C. Scheu, *Journal of Materials Science* **2012**, *47*, 1669–76.

[51] Y. F. Lu, H. Kono, T. I. Larkin, A. W. Rost, T. Takayama, A. V. Boris, B. Keimer, H. Takagi, *Nature Communications* **2017**, *8*, 14408.

[52] K. Okazaki, Y. Ogawa, T. Suzuki, T. Yamamoto, T. Someya, S. Michimae, M. Watanabe, Y. Lu, M. Nohara, H. Takagi, N. Katayama, H. Sawa, M. Fujisawa, T. Kanai, N. Ishii, J. Itatani, T. Mizokawa, S. Shin, *Nature Communications* **2018**, *9*, 4322.

[53] R. T. Payne, *Physical Review Letters* **1968**, *21*, 284–88.

[54] H. Capellmann, *Physica Status Solidi B* **1975**, *70*, 63–69.

[55] F. J. DiSalvo, D. E. Moncton, J. V. Waszczak, *Physical Review B* **1976**, *14*, 4321–28.

[56] P. A. Hyde, J. Cen, S. J. Cassidy, N. H. Rees, P. Holdship, R. I. Smith, B. Zhu, D. O. Scanlon, S. J. Clarke, *Inorganic Chemistry* **2023**, *62*, 12027–37.

[57] R. Peierls, *Quantum Theory of Solids*, Oxford University Press, London, **1975**.

[58] H. K. D. H. Bhadeshia, C. M. Wayman, *Physical Metallurgy (fifth edition)*, Elsevier, **2015**.

[59] A. W. Overhauser, *Physical Review* **1968**, *167*, 691–98.

[60] A. W. Overhauser, *Physical Review B* **1971**, *3*, 3173–82.

[61] J. Wilson, F. DiSalvo, S. Mahajan, *Advances in Physics* **1975**, *24*, 117–201.

[62] M. K. Bin Subhan, A. Suleman, G. Moore, P. Phu, M. Hoesch, H. Kurebayashi, C. A. Howard, S. R. Schofield, *Nano Letters* **2021**, *21*, 5516–21.

[63] E. DiMasi, M. Aronson, J. Mansfield, B. Foran, S. Lee, *Physical Review B* **1995**, *52*, 14516–25.

[64] B. Ricco, *Solid State Communications* **1977**, *22*, 331–33.

[65] P. Stephens, L. Mihaly, P. L. Lee, R. L. Whetten, S. M. Huang, *Nature* **1991**, *351*, 632–34.

[66] M. J. Rosseinsky, *Journal of Materials Chemistry* **1995**, *5*, 1497–513.

[67] M. S. Stark, K. L. Kuntz, S. J. Martens, S. C. Warren, *Advanced Materials* **2019**, *31*, 1808213.

[68] M. S. Dresselhaus, G. Dresselhaus, *Advanced Physics* **2002**, *51*, 139–326.

[69] S. Pruvost, P. Berger, C. Herold, P. Lagrange, *Carbon* **2004**, *42*, 2049–56.

[70] R. Bissessur, S. F. Scully, *Solid State Ionics* **2007**, *178*, 877–82.

[71] D. Zhou, R. Liu, Y. B. He, F. Li, M. Liu, B. Li, Q. H. Yang, Q. Cai, F. Kang, *Advanced Energy Materials* **2016**, *6*, 1502214.

[72] M. Rajapakse, R. Musa, U. O. Abu, B. Karki, M. Yu, G. Sumanasekera, J. B. Jasinski, *Journal of Physical Chemistry C* **2020**, *124*, 10710–10718.

[73] K. Xu, *Chemical Reviews* **2004**, *104*, 4303–4417.

[74] H. H. Zheng, K. Jiang, T. Abe, Z. Ogumi, *Carbon* **2006**, *44*, 203–210.

[75] M. Burrard-Lucas, D. G. Free, S. J. Sedlmaier, J. D. Wright, S. J. Cassidy, Y. Hara, A. J. Corkett, T. Lancaster, P. J. Baker, S. J. Blundell, S. J. Clarke, *Nature Materials* **2013**, *12*, 15–19.

[76] B. G. Márkus, P. Szirmai, S. Kollarics, B. Náfrádi, L. Forró, J. C. Chacón-Torres, T. Pichler, F. Simon, *Physica Status Solidi B* **2019**, *256*, 1900324.

[77] O. Mashtalir, M. Naguib, V. N. Mochalin, Y. Dall'Agnese, M. Heon, M. W. Barsoum, Y. Gogotsi, *Nature Communications* **2013**, *4*, 1716.

[78] N. Emery, C. Hérold, M. d'Astuto, V. Garcia, C. Bellin, J. F. Marêché, P. Lagrange, G. Loupias, *Physical Review Letters* **2005**, *95*, 087003.

[79] R. Zhang, I.-L. Tsai, J. Chapman, E. Khestanova, J. Waters, I. V. Grigorieva, *Nano Letters* **2016**, *16*, 629–636.

[80] R. Zhang, J. Waters, A. K. Geim, I. V. Grigorieva, *Nature Communications* **2017**, *8*, 15036.

[81] X. L. Li, Y. D. Li, *Journal of Physical Chemistry B* **2004**, *108*, 13893–900.

[82] L. Q. Sun, M. J. Li, K. Sun, S. H. Yu, R. S. Wang, H. M. Xie, *Journal of Physical Chemistry C* **2012**, *116*, 14772–79.

[83] J. Morales, J. Santos, J. L. Tirado, *Solid State Ionics* **1996**, *83*, 57–64.

[84] V. Shokhen, D. Zitoun, *FlatChem* **2019**, *14*, 100086.

[85] G. Abellán, C. Neiss, V. Lloret, S. Wild, J. C. Chacón-Torres, K. Werbach, F. Fedi, H. Shiozawa, A. Görling, H. Peterlik, T. Pichler, F. Hauke, A. Hirsch, *Angewandte Chemie International Edition* **2017**, *56*, 15267–73.

[86] F. J. DiSalvo, G. W. Hull, L. H. Schwartz, J. M. Voorhoev, J. V. Waszczak, *Journal of Physical Chemistry C* **1973**, *59*, 1922–29.

[87] M. Endo, H. Yamanashi, G. L. Doll, M. S. Dresselhaus, *Journal of Applied Physics* **1988**, *64*, 2995–3004.

[88] L. Kumari, V. Prasad, S. V. Subramanyam, *Carbon* **2003**, *41*, 1841–46.

[89] A. Fujiwara, Y. Koike, K. Sasaki, M. Mochida, T. Noji, Y. Saito, *Journal of Physics C* **1993**, *208*, 29–37.

[90] M. S. Whittingham, *Materials Research Bulletin* **1974**, *9*, 1681–90.

[91] M. S. Whittingham, *Journal of the Electrochemical Society* **1974**, *12*, C101.

[92] Whittingham M.S., *Science* **1976**, *192*, 1126–1127.

[93] A. H. Thompson, *Physical Review Letters* **1975**, *35*, 1786–89.

[94] A. H. Thompson, Gamble, F. R., C. R. Symon, *Materials Research Bulletin* **1975**, *10*, 915–19.

[95] M. S. Whittingham, *Progress in Solid State Chemistry* **1978**, *12*, 41–99.

[96] W. B. Johnson, W. L. Worrell, *Synthetic Metals* **1982**, *4*, 225–48.

[97] J. Qian, X. Wu, Y. Cao, X. Ai, H. Yang, *Angewandte Chemie International Edition* **2013**, *52*, 4633–36.

[98] J. Dai, X. C. Zeng, *Journal of Physical Chemistry Letters* **2014**, *5*, 1289–93.

[99] X. Wang, A. M. Jones, K. L. Seyler, V. Tran, Y. Jia, H. Zhao, H. Wang, L. Yang, X. Xu, F. Xia, *Nature Nanotechnology* **2015**, *10*, 517–21.

[100] S. Ge, L. Zhang, P. Wang, Y. Fang, *Scientific Reports* **2016**, *6*, 27307.

[101] L. F. Gao, J. Y. Xu, Z. Y. Zhu, C. X. Hu, L. Zhang, Q. Wang, H. L. Zhang, *Nanoscale* **2016**, *8*, 15132–36.

[102] W. Li, S. Hu, X. Luo, L. Z., X. Sun, M. Li, F. Liu, Y. Yu, *Advanced Materials* **2017**, *29*, 1605820.

[103] H. Hou, Q. Xu, Y. Pang, L. Li, J. Wang, C. Zhang, C. Sun, *Advanced Science* **2017**, *4*, 1700072.

[104] J. Luo, S. Sun, J. Peng, B. Liu, Y. Huang, K. Wang, Q. Zhang, Y. Li, Y. Jin, Y. Liu, Y. Qiu, Q. Li, J. Han, Y. Huang, *ACS Applied Materials and Interfaces* **2017**, *9*, 25317–22.

[105] Y. Xu, Q. Wei, C. Xu, Q. Li, Q. An, P. Zhang, J. Sheng, L. Zhou, L. Mai, *Advanced Energy Materials* **2016**, *6*, 1600389.

[106] M. Sheng, F. Zhang, B. Ji, X. Tong, Y. A. Tang, *Advanced Energy Materials* **2017**, *7*, 1601963.

[107] M. S. Balogun, Y. Luo, W. Qiu, P. Liu, Y. Tong, *Carbon* **2016**, *98*, 162–78.

[108] M. M. Y. A. Alsaif, A. F. Chrimes, T. Daeneke, S. Balendhran, D. O. Bellisario, Y. Son, M. R. Field, W. Zhang, H. Nili, E. P. Nguyen, K. Latham, J. van Embden, M. S. Strano, J. Z. Ou, K. Kalantar-zadeh, *Advanced Functional Materials* **2016**, *26*, 91–100.

[109] J. Z. Ou, J. L. Campbell, D. Yao, W. Wlodarski, K. Kalantar-zadeh, *The Journal of Physical Chemistry C* **2011**, *115*, 10757–63.

[110] Y. Dai, W. Liu, Y. Wang, J. Fan, L. Pi, L. Zhang, Y. Zhang, *Journal of Physics: Condensed Matter* **2019**, *31*, 195803.

[111] H. Han, L. Zhang, D. Sapkota, N. Hao, L. Ling, H. Du, L. Pi, C. Zhang, D. G. Mandrus, Y. Zhang, *Physical Review B* **2017**, *96*, 094439.

[112] E. Morosan, H. W. Zandbergen, B. S. Dennis, J. W. G. Bos, Y. Onose, T. Klimczuk, A. P. Ramirez, N. P. Ong, R. J. Cava, *Nature Physics* **2006**, *2*, 544–50.

[113] A. Kogar, G. A. de la Pena, S. Lee, Y. Fang, S. X.-L. Sun, D. B. Lioi, G. Karapetrov, K. D. Finkelstein, J. P. C. Ruff, P. Abbamonte, S. Rosenkranz, *Physical Review Letters* **2017**, *118*, 027002.

[114] Y. Cheng, Y. Zhu, Y. Han, Z. Liu, B. Yang, A. Nie, W. Huang, R. Shahbazian-Yassar, F. Mashayek, *Chemistry of Materials* **2017**, *29*, 1350–56.

[115] M. A. Py, R. R. Haering, *Canadian Journal of Physics* **1983**, *61*, 76–84.

[116] K. Leng, Z. Chen, X. Zhao, W. Tang, B. Tian, C. T. Nai, W. Zhou, K. P. Loh, *ACS Nano* **2016**, *10*, 9208–15.

[117] X. Zhu, D. Li, X. Liang, W. D. Lu, *Nature Materials* **2019**, *18*, 141–148.

[118] E. Dönges, *Zeitschrift für anorganische und allgemeine Chemie* **1951**, *265*, 56–61.

[119] G. Liu, J. E. Greedan, *Journal of Solid State Chemistry* **2013**, *110*, 274–89.

[120] L. Corliss, Y. Delabarre, N. Elliott, *Journal of Chemical Physics* **1950**, *18*, 1256.

[121] H. Leiva, R. Kershaw, K. Dwight, A. Wold, *Materials Research Bulletin* **1982**, *17*, 1539–1544.

[122] F. Steglich, J. Aarts, C. D. Bredl, W. Lieke, D. Meschede, W. Franz, H. Schäfer, *Physical Review Letters* **1979**, *43*, 1892–96.

[123] Carrington, A, *Molecular Physics* **1960**, *3*, 271–275.

[124] M. A. Willard, Y. Nakamura, D. E. Laughlin, M. E. McHenry, *Journal of the American Chemical Society* **1999**, *82*, 3342–46.

[125] J. F. Marco, J. R. Gancedo, M. Gracia, J. L. Gautier, E. I. Rios, H. M. Palmer, C. Greaves, F. J. Berry, *Journal of Materials Chemistry* **2001**, *11*, 3087–3093.

[126] C. G. Shull, W. A. Strauser, E. O. Wollan, *Physical Review* **1951**, *83*, 333–345.

[127] R. D. Smyth, J. A. D. Wilson, P. Manuel, S. J. Clarke, *Journal of Solid State Chemistry* **2022**, *307*, 122841.

[128] M. Rots, L. Hermans, J. Van Cauteren, *Physical Review B* **1984**, *30*, 3666.

[129] M. K. Singh, W. Prellier, M. P. Singh, R. S. Katiyar, J. F. Scott, *Physical Review B* **2008**, *77*, 144403.

[130] J. Goodenough, *Physical Review* **1955**, *100*, 564–573.

[131] J. Goodenough, *Journal of Physics and Chemistry of Solids* **1958**, *6*, 287–297.

[132] J. Kanamori, *Journal of Physics and Chemistry of Solids* **1959**, *10*, 87–98.

'What's a Pawley refinement?'

- Simon Cassidy

2

Experimental

Contents

2.1 Synthetic Methods

2.1.1 Ceramic Synthesis

The traditional route of solid state synthesis involves the grinding together of stoichiometric quantities of reagents in an agate pestle and mortar, then heating to high temperatures for anywhere between a few hours to a few weeks in a reaction vessel. The process of grinding promotes the formation of the target phase by homogenising the mixture and reducing the particle size to maximise the contact between particles. Synthesis temperatures typically range from 500 – 1500 °C in order overcome the large kinetic barrier caused by the low mobility of ions in the solid state. Depending on the ionic mobility, unreacted crystallites may be re-introduced to one another by subsequent re-grinding and pelletisation at a force of between 1 – 5 tonnes to maximise grain contact. Since chalcogenides have relatively high ionic mobilities, this additional step is not always required. Using a reagent with a melting point lower than the synthesis temperature to form a 'melt' is another effective way of increasing ion mobility, as the liquid phase itself is highly mobile and acts as a carrier for other species. Cooling methods also influence the products formed, slow cooling is often use to promote crystal formation whereas instantaneous quenching from the reaction temperature can be used to trap metastable phases or disordered states.

2.1.2 Air-Sensitive Materials

All the intercalated phases described in this thesis are highly air and moisture sensitive. Handling of these materials requires additional steps to facilitate inert conditions. All samples and reagents were prepared, handled and stored in a Glovebox Technologies Ltd argon-filled dry glovebox. Argon is recirculated through a copper catalyst and molecular sieve bed to remove O_2 and H_2O respectively. The O_2 concentration was monitored by an integrated sensor and was kept below 1 ppm under normal working conditions. To maintain these conditions all equipment is dried in an oven prior to being transferred into the glove box via an antechamber. Monthly regeneration of both the copper catalyst and molecular sieve bed was also performed.

If pelletisation was required the pellet die containing the reagent mixture would be sealed inside two polyethylene bags to provide a protective atmosphere before being removed from the glovebox, pressed and swiftly returned. The reagent powder or pellet is then loaded into a dried silica tube, after which a brass end cap fitted with a Young's tap is secured to the open end of the tube. The tap is then closed and the apparatus is removed from the glovebox and fitted to a vacuum line. The tube is then evacuated and sealed using a methane-oxygen blowtorch under dynamic vacuum. Silica ampoules are placed directly into the furnace and can be heated to around 1200 °C before the integrity of the tube starts to diminish. High temperature reactions can also be carried out by heating under a flow of inert gas such as N_2 or Ar, however for most reactions closed system reaction conditions are more effective.

2.1.3 Solution Based Intercalation Methods

Redox chemistry is commonly the driving force behind intercalation and deintercalation reactions. Materials that are structurally predisposed to topochemical manipulation often have much lower kinetic barriers and consequently reactions take place at or around room temperature by stirring the reagent powder in a solution of appropriate oxidant or reductant, such as n-butyllithium.

Reactions of this type were facilitated by use of dry solvents under a dry nitrogen or argon atmosphere. Reagent material was loaded into a dried vessel in the dry argon-filled glovebox, and sealed before removing to a standard nitrogen-vacuum Schlenk line. Standard Schlenk line techniques were employed and allowed for transfer of liquids between vessels. Post-reaction, excess solvent was removed using a filter-paper-covered cannula, followed by a washing step in which fresh solvent was added then filtered off. Drying under dynamic vacuum was then performed to eliminate residual solvent before being transferred back to the glovebox. A schematic of the reaction setup is shown in Figure 2.1.

2.1.4 Metal-Ammonia Intercalation Methods

A modified Schlenk line was assembled to facilitate metal-ammonia intercalation syntheses. The vacuum line was similar to the usual Schlenk line set up, however the inert gas line was connected to a cylinder of ammonia. The reaction vessel was connected to the Schlenk line in the usual fashion, and cooled to approximately – 78 °C in a bath of isopropanol and dry ice. All glassware and tubing between the sample and ammonia cylinder was evacuated. The cold trap and vacuum pump were then isolated before the line was opened to the ammonia cylinder. Approximately 10 cm^3 of ammonia was condensed over the reagents before closing the cylinder, disconnecting it from the Schlenk line and purging the cylinder regulator with N_2. The suspension was left to stir until all the ammonia had evaporated then the remaining solid was dried under dynamic vacuum for 20 minutes. As ammonia is volatile and toxic, the syntheses were performed in a fume hood and at all times the liquid-ammonia containing vessel was linked to a mercury bubbler to avoid pressures exceeding 1 bar in the reaction vessel. A schematic of the reaction setup is shown in Figure 2.1.

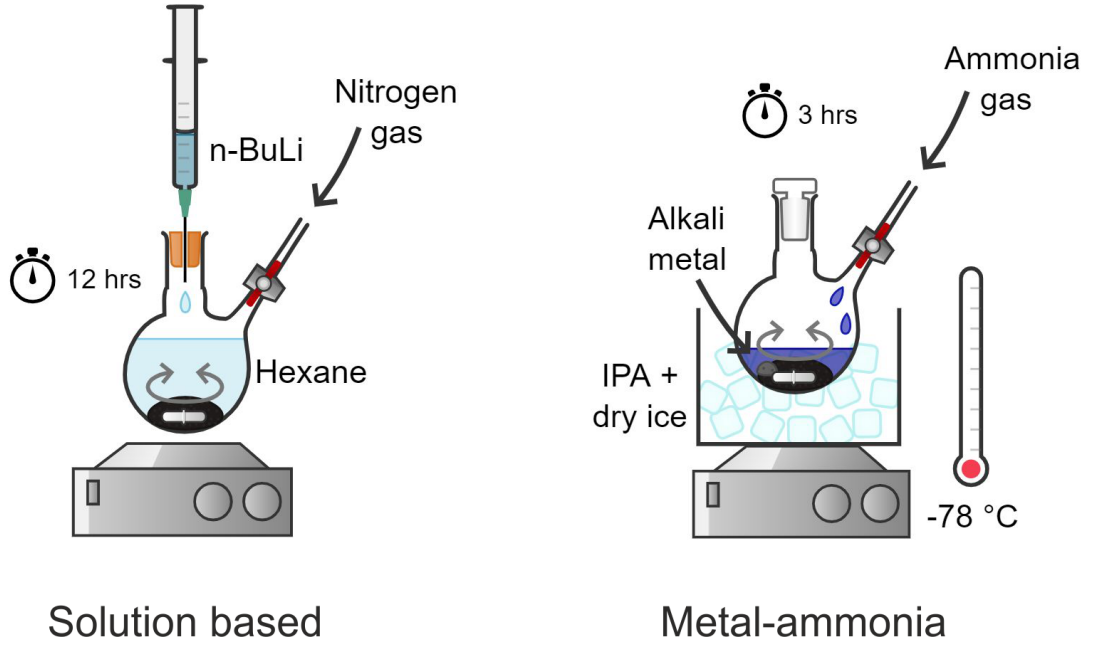

Figure 2.1: A schematic showing the experimental setup of solution based (specifically using n-butyllithium) and metal-ammonia intercalation methods.

2.2 Characterisation Methods

2.2.1 Crystal Symmetry and Diffraction

Crystals are formed of periodic arrays of atoms and are generated by the translational repetition of structural motifs at each lattice point. The crystal itself can be described using a unit cell containing atoms which can generate the crystal structure through translation alone in three dimensions. The unit cell is a parallelpiped with edges labelled a, b and c, and angles between each pair of edges labelled α, β and γ. These are known as lattice parameters. For the case where $a \neq b \neq c$ and $\alpha \neq \beta \neq \gamma$, only 1-fold rotation axes present and the system is known as triclinic. A total of seven different crystal systems are generated through the addition of symmetry elements of higher order in certain allowed combinations[1].

A single unit cell can contain several lattice points. Unit cells that contain one lattice point are known as primitive and are given the space group symbol P, otherwise units cells are referred to as centred. In body-centred (I) systems, there are lattice points located at the origin and at $(\frac{1}{2}, \frac{1}{2}, \frac{1}{2})$ in the unit cell. Face-centred (F) systems have additional lattice points in the centre of each face of the unit cell. Systems where additional lattice points are found only on one pair of opposite faces are labelled A, B or C depending on which face contains the lattice point (C-centring means centring on the ab face). There are 14 Bravais lattices generated through combining the 4 different centring types with the seven different crystal systems. By combining these 14 Bravais lattices with all combinations of symmetry elements we arrive at

the 230 unique three-dimensional space groups[2].

The inherent periodicity of crystalline solids allows for characterisation by diffraction methods. Incident radiation, of similar wavelength to the interatomic spacing in a material (0.3 - 3 Å), is scattered by the constituent atoms which act as a point source. Coherent scattering results in constructive interference which may be detected as beams of intensity in certain directions allowed by the crystal symmetry.

2.2.2 X-ray Diffraction

Several processes occur when an incident beam of X-rays interact with a crystal. Scattering of X-rays occurs through Coulombic interaction of the electrons of an atom with the oscillating electric field of an X-ray. Scattering can be both elastic and inelastic, if the electron emits an electromagnetic wave of the same frequency as the incident radiation, then the scattering is said to be elastic. This process generates the Bragg scattering which is the basis for crystallography.

Max von Laue developed the first theory of X-ray diffraction by electrons in crystals in 1912, for which he later won the Nobel Prize for Physics in 1914. He considered the crystal as a three-dimensional lattice with rows of regularly spaced atoms along each axis. The theory can be more simply illustrated by a one-dimensional row of equally spaced atoms, shown in Figure 2.2.

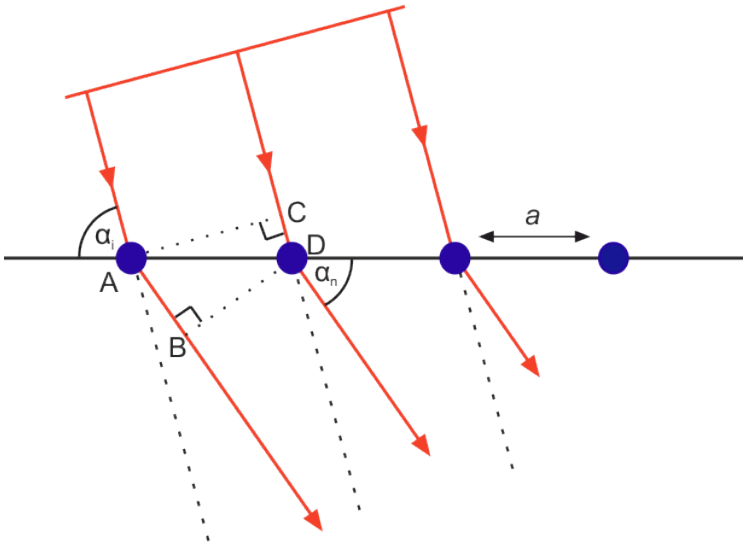

Figure 2.2: A schematic showing the derivation of the Laue equation. The 1D chain of atoms is shown in blue. Incident and diffracted X-rays are shown in orange.

Incident X-rays hit a row of atoms with an incident angle, α_i and are diffracted at an angle of α_n. Maximum constructive interference occurs when path lengths differ by an integer number (n) of wavelengths (λ) such that:

$$AB - CD = a(\cos\alpha_n - \cos\alpha_i) = n\lambda \tag{2.1}$$

This is the first Laue equation and is true for a one-dimensional system. If we also consider the y and z axes as additional one-dimensional systems, we can derive the second and third Laue equations:

$$b(\cos\beta_n - \cos\beta_i) = n_y\lambda \tag{2.2}$$

$$c(\cos\gamma_n - \cos\gamma_i) = n_z\lambda \tag{2.3}$$

Whilst this approach gives a mathematically rigorous model, the solution requires the determination of 12 variables and limits the practicality of this approach to crystallography. Father and son, W. H. and W. L. Bragg, proposed an alternative approach, considering diffraction as the reflection of X-rays from planes of atoms within a crystal, known as Miller planes. These planes are defined by Miller indices h, k and l which intercept the unit cell axes at $\frac{a}{h}$, $\frac{b}{k}$ and $\frac{c}{l}$ respectively. Constructive interference will occur when the additional distance travelled by beams scattered by different Miller planes is equal to an integer number of wavelengths. Figure 2.3 shows the relationship between the distance between planes (d_{hkl}) and the incident angle (θ) of the radiation relative to the planes. The total scattering angle is given by 2θ.

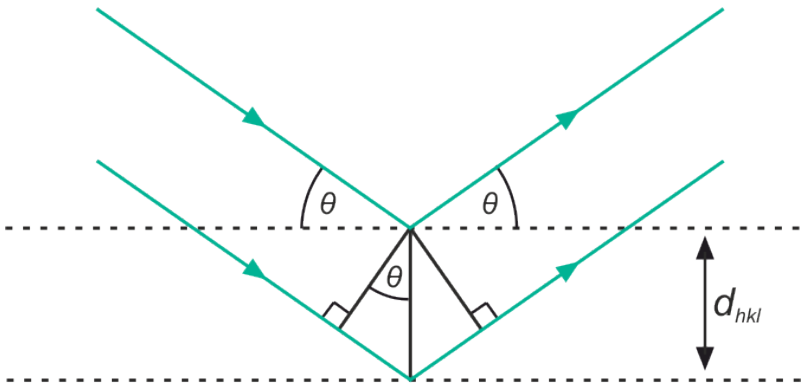

Figure 2.3: X-ray scattering from Miller planes in one dimension showing the derivation of Bragg's Law. Incident and diffracted X-rays are shown in green.

The quantitative relationship is given by Bragg's Law:

$$n\lambda = 2d_{hkl}\sin\theta \tag{2.4}$$

where λ is the radiation wavelength. This relation is the basis for X-ray diffraction experiments. By using a monochromatic beam of incident radiation, a detector can measure the intensity of diffracted beams as a function of 2θ. Indexing is the process of assigning *hkl* values to observed reflections and is used to determine the cell parameters and crystal system. Systematic absences arise from translational symmetry in the unit cell so can be used to deduce any centring and other translational symmetry operations in the cell, from which the Bravais lattice type and a shortlist of space groups may be determined.

Whilst reflection positions can provide dimensional and symmetrical information about the unit cell, the intensities contain the information about the arrangement of atoms within the cell. In an ideal crystal, the intensity, I_{hkl}, of each reflection is given by:

$$I_{hkl} = sLp|F_{hkl}|^2 \tag{2.5}$$

where s is a scaling factor, L is the Lorentz factor (instrument geometry) and p is the polarisation correction. The structure factor, F_{hkl}, is dependent on the structure of the cell and dominates the equation such that:

$$I_{hkl} \propto |F_{hkl}|^2 \tag{2.6}$$

The structure factor is a function describing both the amplitude and phase wave diffracted by the Miller planes with indices $h\ k\ l$ and is given by:

$$F_{hkl} = \sum_{n=1}^{N} f_n(\theta) \exp[2\pi i(hx_n + ky_n + lz_n)] \cdot q \tag{2.7}$$

where $f_n(\theta)$ is the atomic form factor, which gives the scattering amplitude of atom n at a given θ. x_n, y_n, z_n are the co-ordinates of atom n in the unit cell and $\boldsymbol{q}$ is the temperature-dependent Debye-Waller factor. This equation can also be expressed in terms of the real and imaginary components:

$$F_{hkl} = \left(\sum_{n=1}^{N} f_n(\theta)[\cos 2\pi(hx_n + ky_n + lz_n)] + i \sum_{n=1}^{N} f_n(\theta)[\sin 2\pi(hx_n + ky_n + lz_n)] \right) \cdot q \tag{2.8}$$

Given that in centrosymmetric crystals identical atoms lie at (x, y, z) and $-$(x, y, z), and using the trigonometric identity $\sin(-x) = -\sin(x)$, the equation can be reduced to the real component of F_{hkl}:

$$F_{hkl} = \sum_{n=1}^{N} f_n(\theta)[\cos 2\pi(hx_n + ky_n + lz_n)] \cdot q \tag{2.9}$$

For X-ray diffraction, the atomic form factor, $f_n(\theta)$, is given by summing over the contributions of all electrons of an atom, which can be taken to mean that the scattering amplitude is dependent on the atomic number, Z, and θ. This allows us to generate a simplified expression:

$$f_n(\theta) \propto \frac{Z}{2}(1 + cos2\theta) \tag{2.10}$$

Two important implications for the analysis of X-ray data can be gleaned from this relationship. Firstly, heavy atoms scatter X-rays more strongly than lighter atoms and so dominate the diffraction pattern which can make it difficult to locate light atoms, which has particular relevance to this thesis is Chapters 3, 4 and 5. The second is that atoms with similar atomic numbers, thus similar numbers of electrons, are difficult to distinguish using X-ray diffraction.

The angular dependence of the atomic form factor arises due to the finite size of the electron cloud relative to the wavelength of radiation used. This means that photons can be scattered from different regions of the same atom and emerge with slightly different path lengths causing some degree of destructive interference which increases with θ. Mathematically, the form factor is the Fourier transform of the spatial distribution of the scatterer, so follows a Gaussian distribution for X-rays.

The Debye-Waller factor, q, models the thermal displacement of atoms from their equilibrium positions at finite temperature, and also contributes to the structure factor. As temperature increases, so does the effective dispersion of electron density caused by increased atomic vibrations. This effect causes a faster rate of intensity drop off with increasing θ. U_{iso} and B_{iso} are experimentally-determined isotropic temperature factors.

$$q_{iso} = \exp\left[-2\pi^2 U_{iso} r^{*2} \right] \tag{2.11}$$

$$q_{iso} = \exp\left[-\frac{B_{iso} \sin^2 \theta}{\lambda^2} \right] \tag{2.12}$$

2.2.3 Neutron Diffraction

The de Broglie equation expresses the idea of wave-particle duality by relating particle momentum (p) to its wavelength (λ), shown below:

$$\lambda = \frac{h}{p} \tag{2.13}$$

where h is Planck's constant. This means particles of a suitable energy will be diffracted by a crystal, much like X-rays. Whilst the conditions for diffraction are the same, the mechanism by which neutron beams interact with the lattice is different. Since neutrons are scattered by the nucleus, the coherent scattering length is not proportional to atomic number. Consequently, there is variation between isotopes and scattering lengths over increasing atomic number which is often described as 'sawtooth' like. This offers more scope to probe materials where X-rays may fall short, such as differentiating between transition metals with similar atomic numbers, which consequently have similar X-ray scattering lengths. Additionally, because of the smaller size of the nucleus it behaves as a point scatterer, the form factor does not decrease with angle as with X-ray diffraction and so more structural information at higher 2θ values can be obtained. Both methods are often used to complement one another to allow for confirmation of a structural model and for additional information to be extracted, such as the position of light atoms and magnetic information which are obtained from the neutron diffraction experiment.

Another key characteristic of neutrons is that they are spin $-\frac{1}{2}$ particles, which means they can be diffracted by ordered arrays of magnetic moments. The diffracted intensity is proportional to the square of the magnetic scattering factor, which is proportional to the magnitude of the ordered moment. Consequently, when a neutron beam irradiates a magnetically ordered crystalline sample the resulting pattern is the superimposition of the structural component and the magnetic one. Ferromagnetic materials have magnetic structures that are commensurate with their nuclear structure, so magnetic reflections appear at the same positions as the nuclear reflections. Conversely, antiferromagnets give additional reflections if the magnetic structure cannot be described in the structural unit cell, shown in Figure 2.4. Magnetic scattering form factors exhibit strong angle dependence, as the valence electrons are responsible for magnetic scattering. This dependence is greater than in X-ray diffraction, and generally only low angle magnetic Bragg reflections are visible.

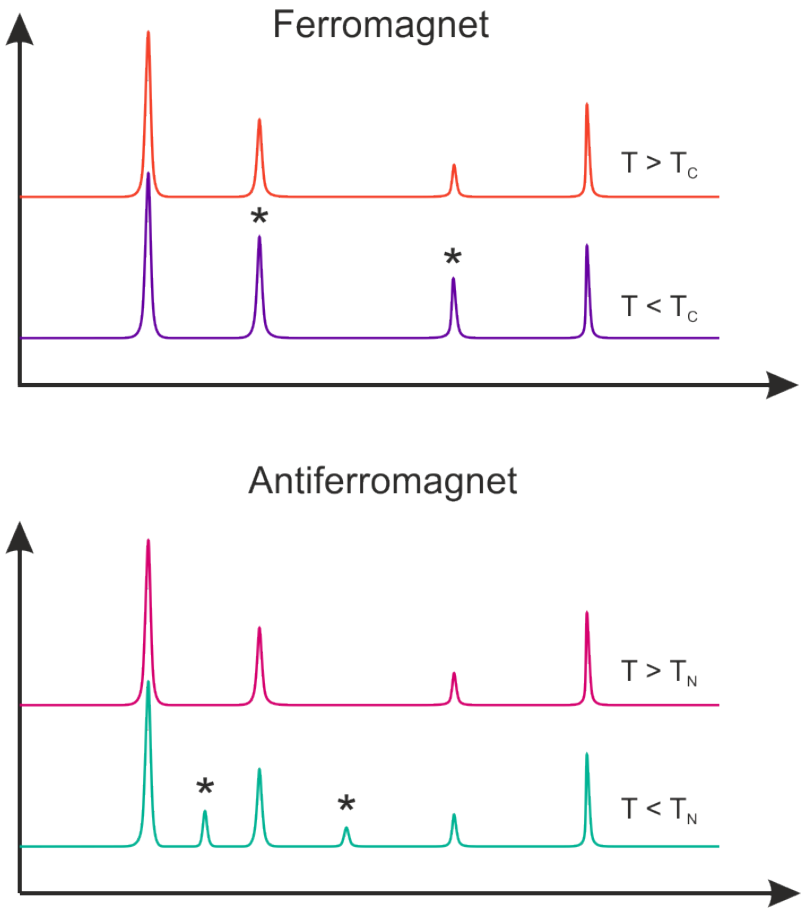

Figure 2.4: Schematic PND patterns of **top** a ferromagnetic sample above and below the Curie temperature, and **bottom** an antiferromagnetic sample above and below the Néel temperature. Magnetic reflections have been marked with an asterisk(*).

2.2.4 Powder Diffraction

Typical powder diffraction experiments involve the irradiation of polycrystalline samples which contain a large number of randomly orientated crystallites. When the beam hits the sample, all Miller planes are illuminated simultaneously and therefore diffract over all angles. This generates Debye-Scherrer cones of diffracted intensity (see Figure 2.5). Depending on the experimental set-up, part of the base of the cone is intercepted and measured, or the entire cone can be integrated as a function of angle, 2θ.

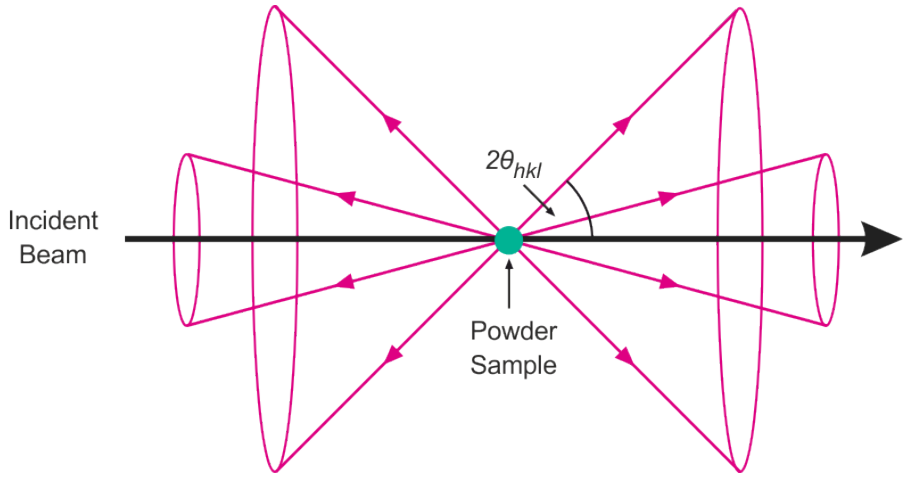

Figure 2.5: The Debye-Scherrer cones of diffracted intensity.

The data are displayed as a one-dimensional pattern of intensity vs 2θ, which is used for structural refinement. However, several problems are encountered due to this presentation. Reflections with the same d-spacing are coincident, meaning if several peaks with different (hkl) values have the same d-spacing they will contribute intensity to the same peak resulting in a loss of information. The finite peak width

of reflections add further complexity as considerable overlap of peaks with similar d-spacings can occur which can lead to difficulties assigning intensities to individual reflections.

Since $I_{hkl} \propto F_{hkl}^2$ (Equation 2.6), the amplitude can be extracted from intensity data, however the 'phase' (the term in the structure factor which contains the atomic positions) cannot. This is known as 'the phase problem' and makes structure determination from diffraction data complex. Therefore, powder diffraction is often used as a fingerprinting tool to assess the phase in comparison to a known powder pattern. That being said when suitably high-quality data is available, methods such as direct methods[3] and charge-flipping[4] can be used to determine the crystal structure *ab initio* (as in a single-crystal experiment). Alternatively, the Rietveld method can be used starting from an approximate model to refine structural parameters.

The average crystallite size can be found from powder diffraction patterns using the Scherrer equation:

$$D = \frac{K\lambda}{\beta cos\theta} \tag{2.14}$$

where D is the mean particle size, K is the shape factor, a standard value of 0.9 has been used for the calculations in this thesis, λ is the radiation wavelength, β is the peak broadening at half the maximum intensity (Full-width-at half-maximum or FWHM), and θ is the Bragg angle of the reflection. FWHM were calculated by fitting well resolved reflections with a Gauss function using the OriginPro software.[5] This is a useful way of quantifying the crystallinity of powder samples.

2.2.5 The Rietveld Method

One technique which allows the refinement of a structural model against experimental powder diffraction data is the Rietveld method, developed by H. M. Rietveld in the late 1960s.[6] Although useful structural information can be derived, it relies on having a good starting model (to avoid having to solve the phase problem) from which a theoretical pattern is produced and is not a structural solution technique. Parameters are refined using a least-squares minimisation to give a best fit to the observed diffraction data.

Since all crystals exhibit some degree of overlap of *hkl* reflections it is difficult to identify the relative contribution of each Bragg reflection to an observed peak, and thus assign the correct intensities to each. Instead of using integrated peak intensities as observables, the Rietveld method uses the intensity of each data point as an observable, of which there are around 2000 in a typical powder diffraction experiment.

The calculated intensity y_{ci} of each data point, y_i, is determined by summing over all the contributions from Bragg reflections for the structure factor F_{hkl} for the structural model input in a fixed range:

$$y_{ci} = y_{bi} + s \sum_{hkl} L_{hkl} P_{hkl} A |F_{hkl}|^2 \phi(2\theta_i - 2\theta_{hkl}) \tag{2.15}$$

where y_{bi} is the background intensity (generated by a separate polynomial function), s is a scale factor, L_{hkl} is the Lorentz polarisation term, P_{hkl} is used to describe any

preferred orientation, A is a term describing absorption, F_{hkl} is the structure factor, and ϕ is the reflection profile function.

The residual function, S_y, gives the difference between the observed and calculated patterns:

$$S_y = \sum_i w_i (y_i - y_{ci})^2 \tag{2.16}$$

where w_i is the normalisation factor, y_i is the observed intensity and y_{ci} is the calculated intensity.

Different R-factors are designed to quantify the fit of a refinement. The weighted profile R-factor, R_{wp}, is given by:

$$R_{wp} = \sqrt{\frac{\sum_i w_i (y_i - y_{ci})^2}{\sum_i w_i y_i^2}} = \sqrt{\frac{S_y}{\sum_i w_i y_i^2}} \tag{2.17}$$

The statistically expected R-factor, R_{exp}, is given by:

$$R_{exp} = \sqrt{\frac{N_{obs} - N_{var}}{\sum_i w_i y_i^2}} \tag{2.18}$$

where N_{obs} and N_{var} are the number of observables and refined variables respectively. The goodness-of-fit parameter, χ, is given by the ratio of the R-values defined above.

$$\chi = \frac{R_{wp}}{R_{exp}} = \sqrt{\frac{S_y}{N_{obs} - N_{var}}} \tag{2.19}$$

All refinements in this thesis were carried out using the TOPAS Academic software.[7]

Rigid Body Refinements

In certain cases where a good starting model is not available, a rigid body approach may be employed if the predicted structure is layered. Rearrangement of layers relative to one another is not uncommon during reactions such as intercalation, resulting in a change of symmetry relative to the parent phase which can no longer be used as a starting model. In this method, the structure of the starting material is built in a cell with lattice parameters obtained through indexing and with $P1$ symmetry imposed. Atoms are then constrained by which layer they occupy in the unit cell so the x, y and z positions of the atoms cannot refine relative to one another within that layer. During the refinement, one layer is fixed in the unit cell whilst the other layer(s) freely refine as one object, shown in Figure 2.6. The relative displacement of each layer is output and by considering the new atomic positions, symmetry elements can be added back into the cell. This method relies heavily on the reasonable assumption that the intra-layer arrangement of atoms remains unchanged, but has the advantage that it is carried out with only a few refined structural variables in the initial stages.

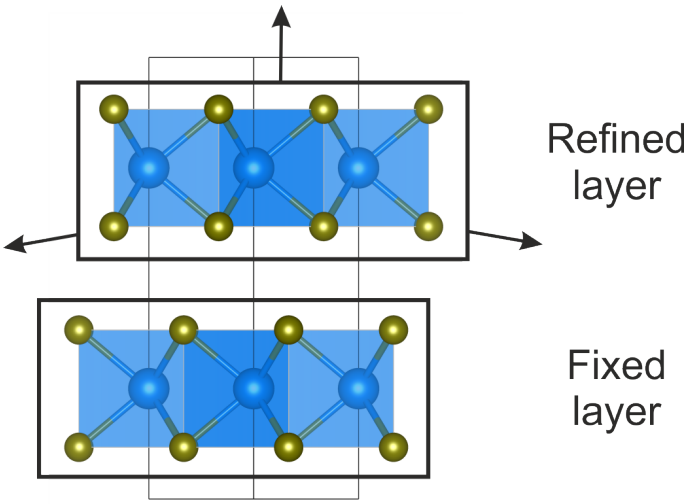

Figure 2.6: A schematic of a rigid body refinement demonstrated for a two layer system. The positions of atoms in the 'fixed layer' are not allowed to refine. The atoms in the 'refined layer' are grouped together and refine along x, y and z directions as one object.

Preferred Orientation

Preferred orientation occurs when crystallites have a tendency to align in certain directions according to a preferred crystallographic plane. Since PXRD relies on the random orientation of crystallites in a sample, this results in additional intensity of certain reflections, depending on their Miller indices and the orientation of their respective Miller plane respective to the favoured crystallographic plane. This can be due to the shape of the crystallites, and is not uncommon in layered materials. Some scenarios are given in Figure 2.7. During the preparation of sample capillaries used for synchrotron measurements, samples are mixed with ground glass to try and lessen this effect, as well as reducing the absorption of the beam by the sample.

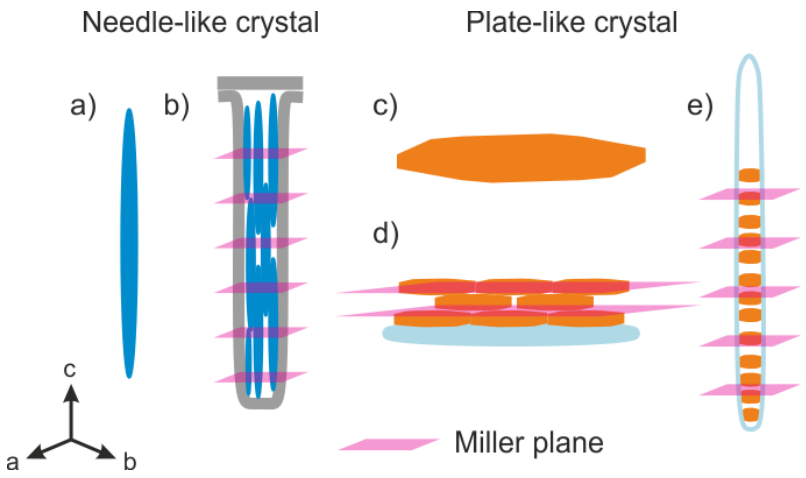

Figure 2.7: A schematic demonstrating the favourable crystal orientations in different sample environments. **a)** the shape of a needle-like crystal **b)** the preferential packing of these crystallites in a cylindrical neutron can **c)** the shape of a plate-like crystal and the preferential packing of these crystallites on **d)** a glass laboratory PXRD slide and in **e)** a cylindrical glass capillary used on the I11 beamline.

Experimentally, the change in intensity profile can be accounted for by including an additional function in the model, which accounts for relative intensity mis-match. Refinements in this thesis uses the March-Dollase model in TOPAS Academic,[7] where appropriate.

2.2.6 X-ray Sources

The X-ray sources described in this thesis can be categorised into either in-house (or laboratory) diffractometers or synchrotron sources. Generally in-house instruments were used for initial characterisation and phase analysis before measuring selected samples using synchrotron radiation.

The laboratory instruments described here produce X-rays by firing electrons at a copper target. This process causes the ionisation of the Cu $1s$ electron. This hole is then filled by a $2p$ or $3p$ electron during the relaxation process to a lower energy state, which is accompanied by the emission of a photon of the same energy. Since two different electron shells are used for the relaxation process, photons of two different energies are produced. The $2p \rightarrow 1p$ transition produces K_α photons ($\lambda \backsim$ 1.54 Å) and the $3p \rightarrow 1p$ transition produces K_β photons ($\lambda \backsim$ 1.39 Å). Only K_α radiation is used since a monochromatic incident beam is required.

The K_a wavelength is produced as a doublet as a consequence of spin-orbit coupling of the excited state. This causes two states to arise, $^2P_{3/2}$ and $^2P_{1/2}$ which are populated in a 2:1 ratio and give wavelengths $K_{\alpha 1}$ ($\lambda \backsim$ 1.54051 Å) and $K_{\alpha 2}$ ($\lambda \backsim$ 1.54433 Å) respectively. This process is shown in Figure 2.8.

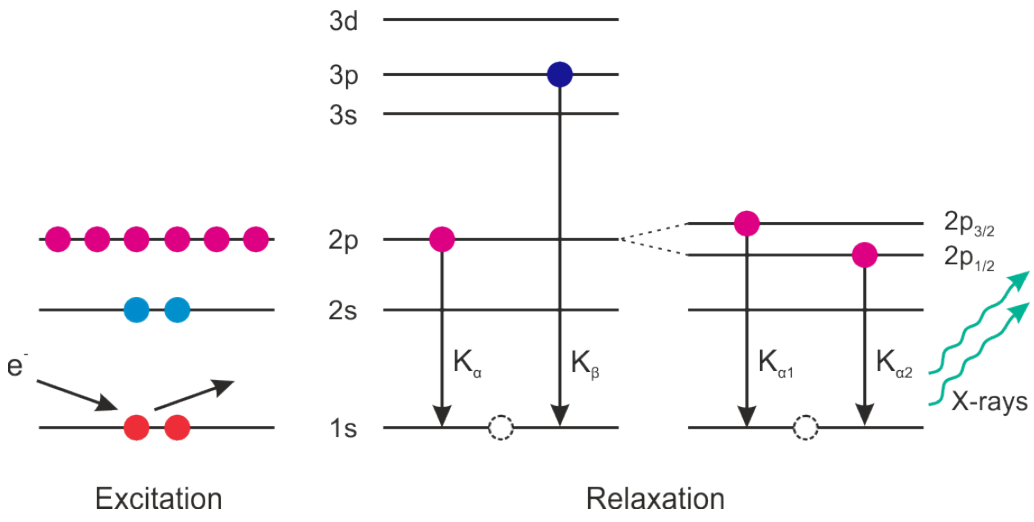

Figure 2.8: The process in which X-rays are generated by laboratory instruments.

In-house samples were prepared by coating the powdered sample on a lightly greased glass slide which was then secured inside an airtight holder. The holders have windows covered in Mylar through which the incident beam can irradiate the sample. Static (non-spinning) measurements were taken when airtight holders were used.

Synchrotrons differ greatly from in-house sources both in setup and the radiation they produce. Synchrotrons are able to produce highly collimated X-ray beams that can be tuned to a specific wavelength, and allows for highly precise data collection. X-rays are generated when electrons are forced to change direction when travelling close to the speed of light. Magnetic fields are used to control the direction of electrons as they travel around a ring. Three processes occur in order to produce the X-ray beam: generation of electrons, acceleration of electrons and generation of radiation.

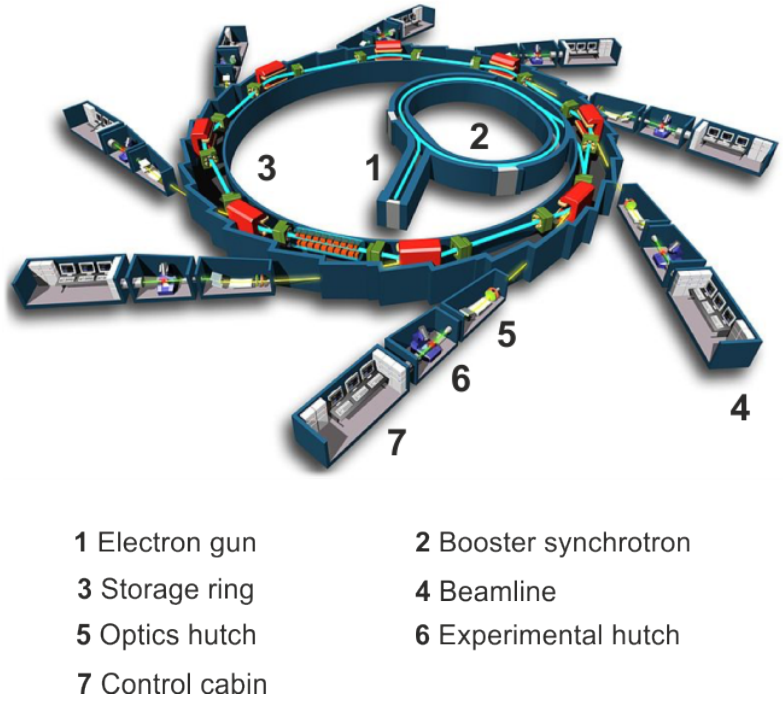

Figure 2.9: A schematic of a synchrotron radiation facility, showing X-ray generation and storage, and the experimental beamlines. (Adapted from: Copyright © EPSIM 3D/JF Santarelli, Synchrotron Soleil)

The electron gun produces a beam of electrons by heating a high voltage cathode in a vacuum. The electron beam is then fed into a linear accelerator before entering the booster ring. Here, the electron beam is further accelerated to the GeV range using bending magnets. From there the electron beam is fed into the storage ring. By this point, the electrons are travelling at close to the speed of light. The emitted synchrotron light spans the whole electromagnetic spectrum. The radiation is then directed down the beamlines into the optics hutch, where the appropriate wavelength(s) for the experiment are selected. The experimental hutch is where the radiation interacts with the sample on the specific instrument- which is controlled from the control cabin. A schematic of a synchrotron is shown in Figure 2.9.

Bruker D8 ADVANCE ECO Diffractometer

The Bruker D8 ADVANCE ECO diffractometer is a laboratory instrument and operates in a Bragg-Brentano geometry with a fixed sample position and moving X-ray source and detector. This instrument is primarily used for collecting high intensity data over a short period of time- approximately 25 minutes for a scan over $5 \leq 2\theta(^{\circ}) \leq 70$. This is because it is not fitted with a Cu $K_{\alpha 2}$-excluding monochromator, so both Cu K_{α} wavelengths contribute to the incident beam intensity. The inclusion of both wavelengths however lowers the resolution of the data collected. This instrument is also fitted with an energy discriminating detector which filters out K_{β} radiation and aides in suppression of fluorescence. This is most often observed in samples with a high density of $3d$ transition metals which adds to the noise in a diffraction experiment.

PANalytical X'Pert Empyrean Diffractometer

The PANalytical X'Pert Empyrean diffractometer is another laboratory instrument and also operates a Bragg-Brentano set-up, but with a fixed X-ray source and moving sample and detector. This instrument is fitted with a germanium crystal-based monochromator which eliminates the Cu $K_{\alpha 2}$ contribution. As a result, the peak-shape and resolution are improved, but the beam intensity is reduced. This instrument generally requires longer measurements but is useful for detecting more subtle changes between samples.

I11 Beamline- Diamond Light Source, Oxfordshire, UK

The I11 beamline[8] is a high-resolution powder diffraction beamline at the Diamond Light Source, a synchrotron facility. A white beam of radiation is produced by an in-vacuum undulator, a single wavelength is then selected using a cryogenically cooled double-crystal Si (111) monochromator and harmonic rejection mirrors. The resulting beam is highly monochromated and generally in the range of 0.8 – 0.9 Å.

The instrument employs Debye-Scherrer geometry and features two detectors- the Mythen position sensitive detector (PSD) and the higher resolution MAC detector. The PSD features a 90 ° aperture and is capable of collecting a full diffraction pattern in a few seconds. The MAC detector is comprised of 45 individual detectors separated across 5 arms which are preceded by Si(111) analyser crystals to reduce background. The resulting diffraction pattern is very high resolution and scans typically take 30 minutes. Samples for all measurements were loaded into 0.5 mm borosilicate capillaries which were spinning during data collection. "Quartz" (i.e. fused silica) capillaries were used for high temperature data collection.

2.2.7 Neutron Sources

There are two commonly used methods of generating neutrons: accelerator-based 'spallation' and steady-state reactor-based methods. Sources using both of these methods have been used in this thesis.

Reactor sources use the fission of ^{235}U nuclei to produce neutrons which are slowed in D_2O or cold methane to generate a beam with a flux suitable for neutron diffraction experiments. The white beam is usually monochromated before reaching the experimental beamlines where the diffracted intensity is measured as a function of angle, much like PXRD data. The Institut Laue-Langevin (ILL) and Australian Centre for Neutron Scattering (ACNS) both use reactor-sourced neutrons.

Spallation is the process of producing pulses of neutrons by firing charged particles at a heavy metal target. Moderators are then used to slow down the neutron beam to give a suitable range of wavelengths for a diffraction experiment. In contrast to reactor sources, time of flight (ToF) diffraction experiments measure intensity as a function of the arrival times, or time of flight (t), of scattered neutrons to the detectors. Since the distance from the source to the detector is a fixed length (L), the de Broglie equation can be used to find the wavelength of diffracted neutrons.

$$\lambda = \frac{h}{m_n v} = \frac{ht}{m_n L} \tag{2.20}$$

By combining Bragg's Law with the de Broglie equation, the d-spacings of diffracted beams can be calculated:

$$n\lambda = \frac{nht}{m_n L} = 2d_{hkl}sin\theta \tag{2.21}$$

The equation can be simplified by substitution of Planck's constant (h) and the mass of a neutron (m_n) :

$$t = 505.56Lsin\theta d_{hkl} \tag{2.22}$$

ToF diffractometers typically group together multiple detectors into banks which cover a fixed range of scattering angles (θ), and therefore only cover a specific range of d-spacings. During refinement, the model is refined against all data banks simultaneously.

GEM- ISIS, Oxfordshire, UK

GEM[9] is the GEneral Materials diffractometer on target station 1 at ISIS - a spallation neutron and muon source. The instrument receives neutrons from a cold methane moderator covers a d-spacing range of 0.4 – 25 Å and is capable of reasonable resolution measurements over a short period of time. The six detector banks are positioned at 9 °, 17 °, 35 °, 62 °, 92 ° and 146 °. The detector banks positioned at higher angles cover shorter d-spacings and have a higher resolution.

D2B- ILL, Grenoble, France

The D2B[10] instrument is a high intensity diffractometer at the ILL, a steady-state reactor source. D2B operates in a Debye-Scherrer geometry and uses a Ge (115) monochromator to give a single wavelength. The monochromator can be rotated to access different wavelengths by illuminating different $h\ k\ l$ values. Measurements in this thesis were performed using a wavelength of 1.594 Å or 2.398 Å. The detector setup can measure across an angular range of $5 \leq 2\theta(^{\circ}) \leq 165$ and is comprised of 128 ^{3}He tubes set at intervals of 1.25 °.

Echidna- ACNS, Sydney, Australia

Echidna[11] is the high-resolution powder diffractometer at the ACNS, which also utilises reactor sourced neutrons. Like D2B, Echidna is set up in a Debye-Scherrer geometry and uses a variable angle monochromator, but instead Ge (335) crystals. The detector is comprised of 128 linear position sensitive detectors which cover a range of $5 \leq 2\theta(^{\circ}) \leq 145$. The wavelength used for experiments described in this thesis is 1.622 Å.

2.2.8 SQUID Magnetometry

Magnetic samples were characterised using a Quantum Design MPMS SQUID magnetometer. A Superconducting QUantum Interference Device, or SQUID,[12,13] consists of a closed loop intersected by two Josephson junctions, thin strips of insulating material separating two superconducting materials. When a small current is applied across the device, Cooper pairs tunnel through the junctions allowing zero resistance conduction across the detector coil. When the applied current exceeds the critical current of these junctions, the resistivity becomes finite and a voltage is generated across the device. This current can be modified by an external magnetic field so the voltage output is related to the magnitude of the field.

To allow the SQUID to operate accurately it must be shielded from fluctuating external fields and so is housed away from the sample and protected by a superconducting shield. The sample is mounted on a long stick and lowered down into the induction coils and magnetised by a helium-cooled superconducting magnet. Once the sample has been magnetised, a current is induced in the detector coil by vertical translation of the sample. This detector coil is coupled to another, larger input coil which is then coupled to the SQUID which generates an output voltage proportional to the magnetic moment of the sample.

To reduce any magnetic signal from the sample environment, the sample is contained in a gelatin capsule secured inside a plastic drinking straw. The sample chamber is kept under an inert helium atmosphere which can be cooled to 1.8 K and the superconducting magnet can produce fields of up to $\pm$ 7 T, allowing the magnetic

moment of a sample to be measured as a function of temperature or applied field.

DC measurements

Direct-current magnetic susceptibility measurements were performed both as a function of field (H) and temperature (T). Typically, low field (10 - 1000 Oe) measurements were performed as a function of temperature upon warming twice, once having cooled the sample in the absence of a magnetic field (zero field-cooled (ZFC)), the other with an applied field (field-cooled (FC)). The differences in these curves can used to gain additional insight into the magnetic behaviour of the sample. In some cases, units of Bohr magnetons per ion, μ_B/ion, were used when evaluating the saturation moment of magnetic ions. The conversion is given below:

$$\mu_B/ion = \frac{\mu}{n_{ion} N_a \mu_B} \tag{2.23}$$

where μ is the magnetic moment, n is number of moles, H is the field, N_a is Avogadro's constant and μ_B is the Bohr magneton.

Magnetisation isotherms (also known as hysteresis loops) were also measured, typically in the range $-7 \leq H(\mathrm{T}) \leq 7$. In this thesis, these measurements were used to probe ferromagnetic behaviour. Two measurements were typically performed at 2 K and 300 K, an additional measurement was made at 350 K for samples with a Curie temperature, $\mathrm{T_C}$, near room temperature. This allowed the ferromagnetic properties to be quantified, and for comparison to the paramagnetic state.

2.2.9 Nuclear Magnetic Resonance Spectroscopy

Nuclear magnetic resonance exploits the intrinsic spin of neutrons and protons. Atomic nuclei with a non-zero spin have a magnetic moment are considered NMR-active and can be studied using the technique.

In the absence of a magnetic field spins are randomly oriented throughout a material. Once an external field, B_0, is applied to a sample, nuclei align with (lower energy) or against (higher energy) the field. This lifting of degeneracy is known as Zeeman splitting, and is demonstrated in Figure 2.10a). The Zeeman splitting is dependant on the magnetic field at the nucleus.

During the experiment, spin flipping occurs from one energy state to another which requires a quanta of energy, and atoms in different electronic environments will require different frequencies to cause a spin flip. The Fourier transform of the NMR signal gives a spectrum given as a function of chemical shift, δ, relative to a known standard. Each peak corresponds to a different chemical environment, and the area under the peaks in a spectrum is directly proportional to the number of nuclei in that environment, as shown in Figure 2.10b).

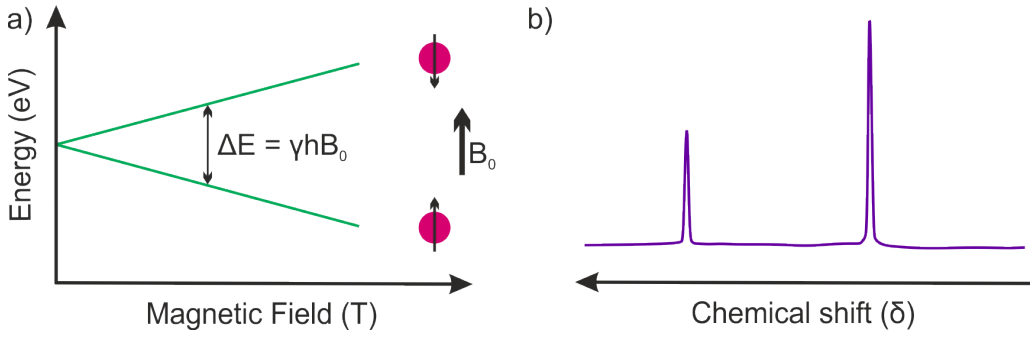

Figure 2.10: a) The Zeeman splitting of energy levels as a function of the external magnetic field, B_0. **b)** An NMR spectrum showing signals from atoms in two chemical environments.

Solid-state NMR usually requires experimental additional considerations. In solution, rapid random tumbling of molecules allows for averaging of any anisotropic NMR interactions. In the solid state however, broad spectra are often observed due to these interactions. Magic-angle spinning (MAS), is a technique which introduces artificial motion. The sample is tightly packed into a rotor and spun at 54.74 ° (the magic angle) with respect to the applied field. This angle comes from the term $(3cos^2\theta - 1)$ found in the expressions for both quadrupolar broadening and chemical shift anisotropy, which reduces to zero when $\theta = 54.74$ °.

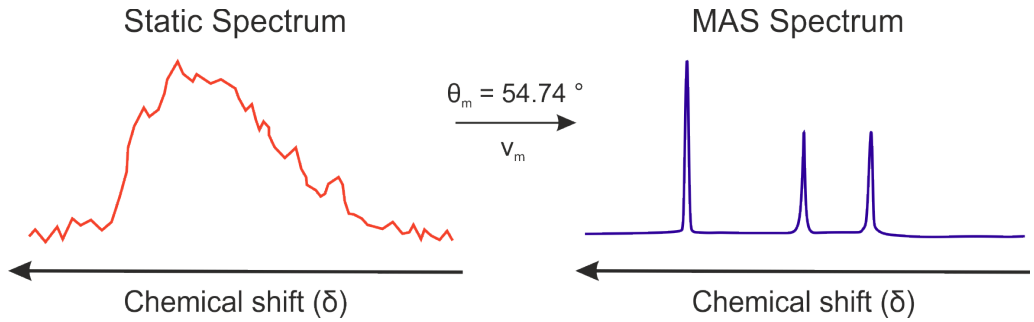

Figure 2.11: The solid-state NMR spectra of **Left.** a static sample and **Right.** the same sample spinning at the magic angle.

Sometimes a significant shift in the NMR frequency for atoms in a metal is observed compared to the same atoms in a nonmetallic environment. This is referred to as a Knight shift,[14] and is due to the conduction electrons in metals. The size of the shift is proportional to the density of states at the Fermi level. Depending on the electronic structure, the Knight shift may also be temperature dependant.

The NMR studies in this thesis were performed by either Dr. Nick Rees, Department of Chemistry, University of Oxford, or Dr. Sunita Dey under the guidance of Prof. Clare Grey, University of Cambridge.

2.2.10 Computational Studies

Density-functional theory, or DFT, is a method of computation quantum mechanical modelling. Primarily used in physics, chemistry and materials science, it is used to investigate the electronic or nuclear structure of many-body systems using functionals - functions of other functions. In the case of DFT, functionals are of spatially dependent electron density.

In many-body structure calculations, the nuclei are treated as fixed and electrons are moving in a static potential. The stationary electronic state can then be described by a wavefunction which satisfies the many-electron time-dependent Schrödinger equation. Sophisticated methods for solving the many-body Schrödinger equations, such as the Hartree-Fock method, rely on expansion of the wavefunction and require a large computational input and cannot be applied efficiently to larger systems. DFT offers an attractive alternative and works on the basis of mapping a many-body problem, onto a single body problem.

For a specified system, the energy functional can be minimised with respect to $n(\boldsymbol{r})$, the probability density that any of the N electrons is at the position $\boldsymbol{r}$, to yield the ground-state density, from which all other ground-state observables can be extracted.

DFT and density of states (DOS) calculations in this thesis were performed by Jiayi Cen under the supervision of Prof. David Scanlon, University College London.

2.2.11 Mössbauer Spectroscopy

Mössbauer spectroscopy relies on the a phenomenon called the Mössbauer effect.[15] The conservation of momentum requires a nucleus to recoil during the emission or absorption of a gamma ray. However, for nuclei in a solid lattice energy can be lost through discrete lattice vibrations, or phonons, referred to as 'recoil free events'. Any integer number of phonons can be emitted, including zero, which are referred to as 'recoil free' events. Subtle differences in electric and magnetic fields can be detected by measuring the energies of these 'recoil free' events.

During the experiment, the sample is irradiated by a beam of gamma rays and the transmission is measured. The energy of the gamma ray is perturbed by accelerating the source over a range of velocities, using the Doppler effect to create a range of energies. When the energy of the emitted gamma ray is equal to the absorption energy of the sample a drop in transmission is observed.

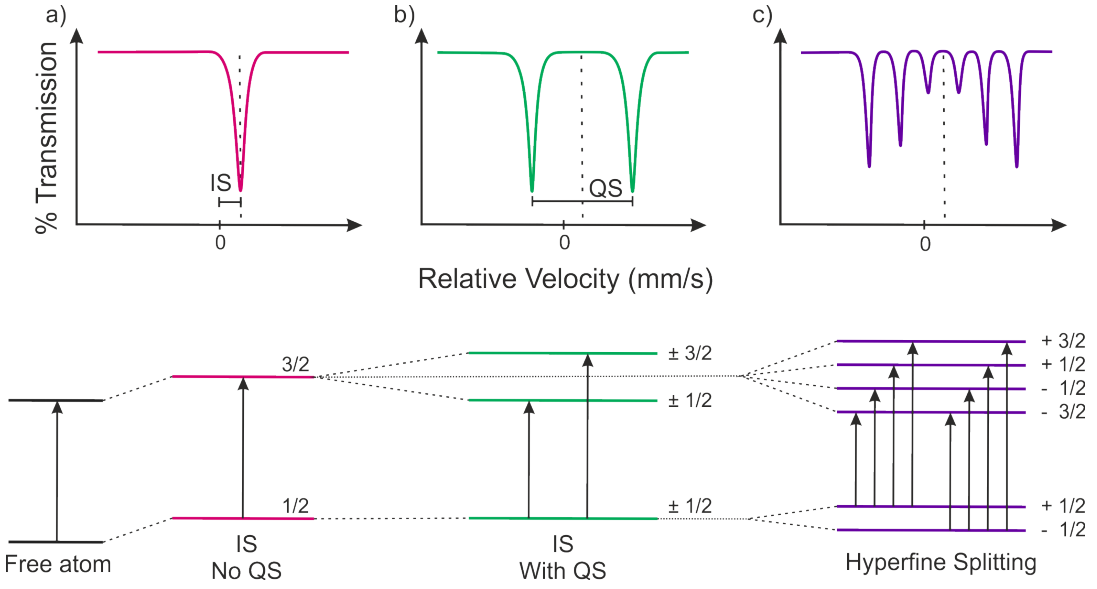

Figure 2.12: The resulting Mössbauer spectra when **a)** only the isomer shift is observed **b)** quadrupolar splitting is observed **c)** hyperfine splitting is observed. Below each spectrum shows the splitting of energy levels and absorption processes in each regime.

Absorption velocities (energies) are dependant several factors such as site symmetry (QS, quadrupole splitting) and distribution of charge/oxidation state (CS, centre shift (related to IS, isomer shift)). Hyperfine splitting is indicative of magnetic ordering between nuclei. These effects are shown in Figure 2.12.

All Mössbauer measurements in this thesis were carried out by Dr. Alex Scrimshire under the direction of Prof. Paul Bingham at Sheffield Hallam University.

2.2.12 ICP-MS

Inductively Coupled Plasma Mass Spectroscopy (ICP-MS) is used to quantify the constituent elements of a sample. Inductively coupled plasma is an ionisation source that decomposes a sample into its elements then ionises them. The plasma acts as a carrier gas for the sample. The resulting ions are diverted from neutral particles using charged plates. The reduced ion beam is them filtered by mass to charge ratio (m/z) by the mass spectrometer. Most instruments use a quadrupolar mass spectrometer which consists of two pairs of charged rods which generate an electric field in the space between them. This can be finely controlled and changed rapidly to allow for measurement of several elements over a short time period.

Samples were prepared by dissolving approximately 5 mg of powdered solid in 1 mL of 12M HCl with 19 mL HNO_3. This solution was then diluted by a factor of 50 with deionised water before being added to the instrument.

The ICP-MS measurements in this thesis were carried out by either Philip Holdship, Department of Earth Sciences, University of Oxford, or Trang To, School of Geography, University of Oxford.

2.2.13 Combustion Analysis

Also known as CHNS analysis, combustion analysis is another method of quantifying the elements C, H, N and S in a sample. This method relies on the combustion of a sample in the presence of oxygen to produce gaseous by-products such as CO_2, NO, SO_2 and H_2O. The gas mixture is then separated by gas chromatography and quantified using thermal conductivity detection. Combustion analysis referred to in this thesis was performed by Elemental Microanalysis Ltd, Okehampton, UK.

References

[1] G. Burns, A. Glazer, *Space Groups for Solid State Scientists*, Elsevier, **1990**.

[2] IUCr, T. Hahn, *International Tables for Crystallography Volume A: Space-group symmetry*, Wiley, **2002**.

[3] H. Hauptman, *Science* **1986**, *233*, 178.

[4] G. Oszlanyi, A. Süto, *Acta Crystallographica* **2004**, *60*, 134.

[5] OriginLab Corporation, *OriginPro*, version 2020.

[6] H. M. Rietveld, *Physica Scripta* **2014**, *89*, 098002.

[7] A. A. Coelho, *Journal of Applied Crystallography* **2018**, *51*, 210–218.

[8] S. P. Thompson, J. E. Parker, J. Potter, T. P. Hill, A. Birt, T. M. Cobb, F. Yuan, C. C. Tang, *Review of Scientific Instruments* **2009**, *80*, 075107.

[9] W. G. Williams, R. M. Ibberson, P. Day, J. E. Enderby, *Physica B: Condensed Matter* **1997**, *241-243*, 234–236.

[10] E. Suard, A. Hewat, *Neutron News* **2001**, *12*, 30.

[11] M. Avdeev, J. R. Hester, *Journal of Applied Crystallography* **2018**, *51*, 1597–1604.

[12] R. L. Fagaly, *Review of Scientific Instruments* **2006**, *77*, 101101.

[13] R. Kleiner, D. Koelle, F. Ludwig, J. Clarke, *Proceedings of the IEEE* **2004**, *92*, 1534.

[14] W. D. Knight, *Physical Review* **1949**, *76*, 1259–1260.

[15] N. N. Greenwood, T. C. Gibb in *Mössbauer Spectroscopy*, Springer Netherlands, Dordrecht, **1971**.

'You can't break anything if you don't

do any experiments...'

- Rob Smyth

3

Intercalation Chemistry of Ta_2NiSe_5

Contents

3.1 Introduction

The narrow-band-gap semiconductor, Ta_2NiSe_5, is a candidate for being an excitonic insulator.[1,2] In such a proposed state arising in narrow-band-gap semiconductors, excitons are formed spontaneously if the exciton binding energy is less than the band gap and because the electron and hole pair are strongly bound, the state is insulating and may be thought of as an unconventional insulating state. Because the formation of the excitonic insulating phase in narrow-gap semiconductors arises from the formation of strongly bound charge-neutral pairs, the transition to the excitonic insulating state can be understood as a Bose-Einstein Condensation (BEC). A schematic of the band dispersion of both states[3] is shown in Figure 3.1c). Structurally, Ta_2NiSe_5 is a layered material constructed from Ta_2NiSe_5 layers stacked along the b axis and related by the C-centring translation so that an AB-type stacking results[4], as shown in Figure 3.1a – b).

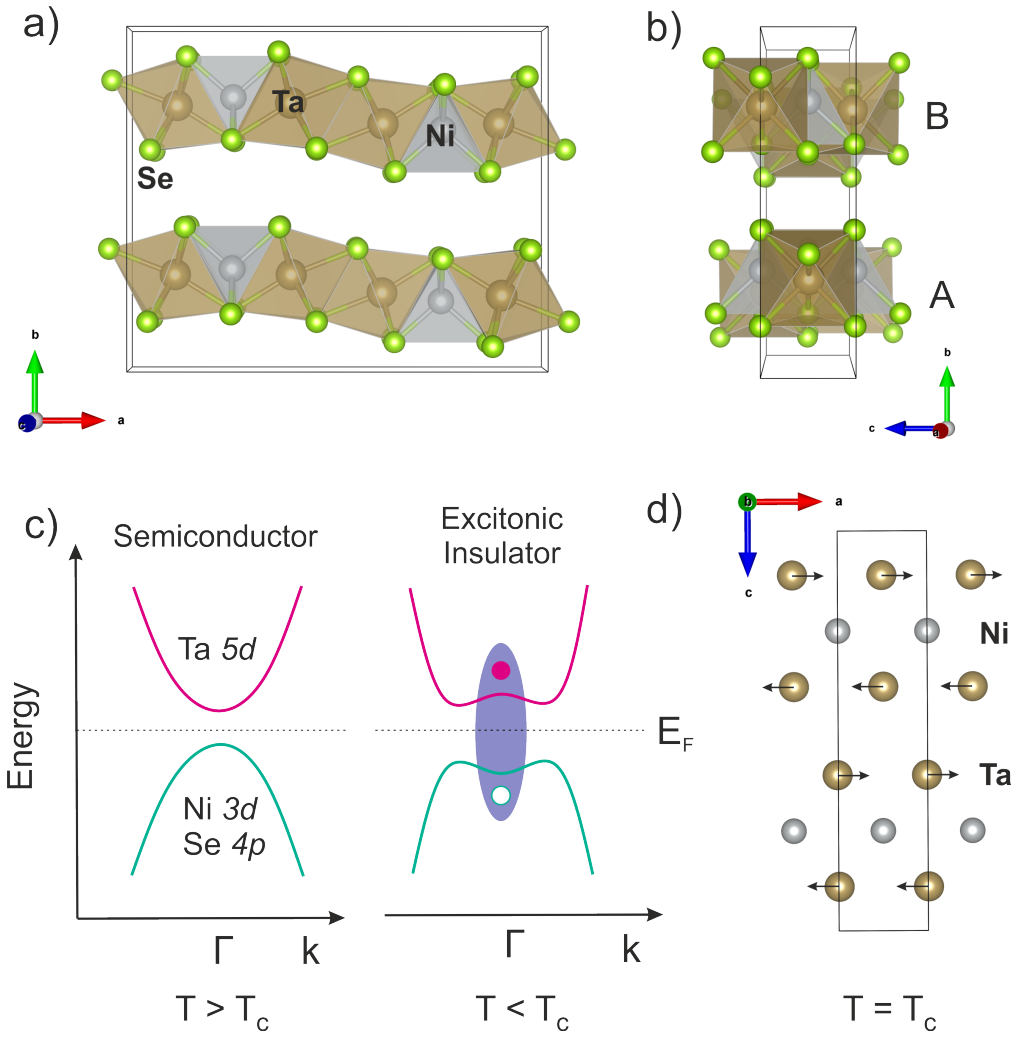

Figure 3.1: a) The structure of Ta_2NiSe_5 viewed along the c-axis **b)** Ta_2NiSe_5 viewed along the a-axis demonstrating the AB-layer stacking which are offset from one another long the c-axis. **c)** A schematic of the band dispersion of Ta_2NiSe_5 in the semiconducting state and as an excitonic insulator. The purple shaded area shows the bound hole-electron pair. **d)** Schematic representation showing the lattice distortion of the 1-D Ta chains relative to the Ni chains corresponding to the orthorhombic to monoclinic phase transition.

The layers comprise octahedral $TaSe_6$ and tetrahedral $NiSe_4$ polyhedra joined via edge sharing. The layers are gently corrugated along the c direction, and along the a direction there are ribbons of double-thickness edge-shared $TaSe_6$ octahedra linked by chains of vertex-linked $NiSe_4$ tetrahedra. Resistivity measurements reveal semiconductor behaviour at room temperature and a gradual transition to a state where the resistivity behaves like that of a metal above 550 K.[5] An additional feature at 328 K is accompanied by a structural phase transition from *Cmcm* symmetry above this temperature to $C2/c$ below. Structurally this is equivalent to the shearing of the Ta chains against the Ni chains, shown in Figure 3.1d). Chemically, the composition is intriguing with the possibility of Ta(IV)/Ni(II) versus Ta(V)/Ni(0) configurations seeming plausible. Chemical intuition would argue for the former, but the observed diamagnetism and the fact that there is no evidence for a charge density wave (CDW) distortion associated with the Ta(IV) $5d^1$ configuration that would account for the insulating behaviour seemingly arguing for the former. Tight binding band structure calculations of the *Cmcm* structure indicate Ta_2NiSe_5 has a direct gap at the Γ point of the Brillouin zone.[6,7] The conduction band is largely configured by the Ta $5d_{xy}$ chain giving a quasi-1D dispersion, whilst the top of the valence band also has a quasi-1D dispersion and is composed of well-hybridised Ni $3d_{xz}$ and Se $4p_y$ orbitals. There is no mixing of the states at the top of the Ni/Se based valence band and the Ta-based conduction band because the states belong to different irreducible representations at Γ,[8] and the appropriate formulation is Ta(V) and Ni(0). Canadell and Whangbo[6] point out that the Ta–Ta separations

are long (consistent with Ta(V)), while the Ta-Ni separation is short suggesting that the Ni(0) oxidation state is stabilised by donation to the Ta(V) acceptor orbitals analogous to the stabilisation of Ni(0) in molecules such as $Ni(CO)_4$. Kaneko *et al.*[8] account for the phase transition from the *Cmcm* phase to the $C2/c$ phase as driven by the BEC of excitonic electron-hole pairs. This symmetry-lowering distortion accompanying the formation of the excitonic insulator phase allows mixing of the conduction and valence bands at Γ and this mixing is proposed[9] to account for the observation of flattening of the bands around Γ in ARPES experiments, and the interpretation of the ARPES data using an electronic description which is suggestive of a Ta(IV) d^1 state and an oxidised Ni $3d^9$/Se-ligand hole state.[8–10] Further experiments devoted to fully understanding the transition are the topic of current research[11]. High pressure experiments[12] on Ta_2NiSe_5 reveal the sensitivity of the structure to applied pressure. The ambient-temperature and pressure phase crystallising in $C2/c$, assigned as the excitonic insulator phase, transforms to the *Cmcm* phase under applied hydrostatic pressure at about 2 GPa at ambient temperature. The *Cmcm* phase is the high-temperature/ambient-pressure phase, and it transforms at about 3GPa at ambient temperature to a *Pmnm* phase related to the *Cmcm* phase by a relative sliding of the layers to produce an AA stacking with the loss of lattice centring. This high-pressure orthorhombic phase also undergoes a transition on cooling at high pressure to a monoclinic phase in $P2/n$, and Nakano *et al.*[12] suggest that this may also be an excitonic insulator phase. Chemical transformation by intercalation of lithium into Ta_2NiSe_5 has previously been reported by

Squattrito *et al.*[13] using n-butyllithium to reportedly produce $Li_2Ta_2NiSe_5$. However, the PXRD pattern was not successfully indexed due to low crystallinity of the product. Hyde[14] reported the structural characterisation of the phase $LiTa_2NiSe_5$ in 2019 through refinement of high resolution PXRD data, and located a tentative Li site using PND. The intercalation results in significant structural and electronic changes compared with the host. Here we present further characterisation of this compound using a revised fit to PND data, computational studies and NMR, and the synthesis and characterisation of two additional intercalates of Ta_2NiSe_5.

3.2 Synthesis of Ta_2NiSe_5

Polycrystalline samples of Ta_2NiSe_5 were synthesised by grinding together tantalum powder (Alfa Aesar, 99.97 %), nickel powder (Alfa Aesar, 99.9 %) and selenium powder (Alfa Aesar, 99.999 %) in stoichiometric amounts using an agate pestle and mortar until homogeneous. The mixture was then sealed inside an evacuated silica tube and heated at 750 °C for 7 days (ramping rate of 5 °C min^{-1}) before being allowed to cool naturally. The resulting powder was reground and pressed into a pellet before reheating to 700 °C for 48 hours and cooling at the natural rate of the furnace. This second step was found to improve the crystallinity of the precursor Ta_2NiSe_5. The Rietveld fit against PXRD data of Ta_2NiSe_5 can be found in Figure 3.2.

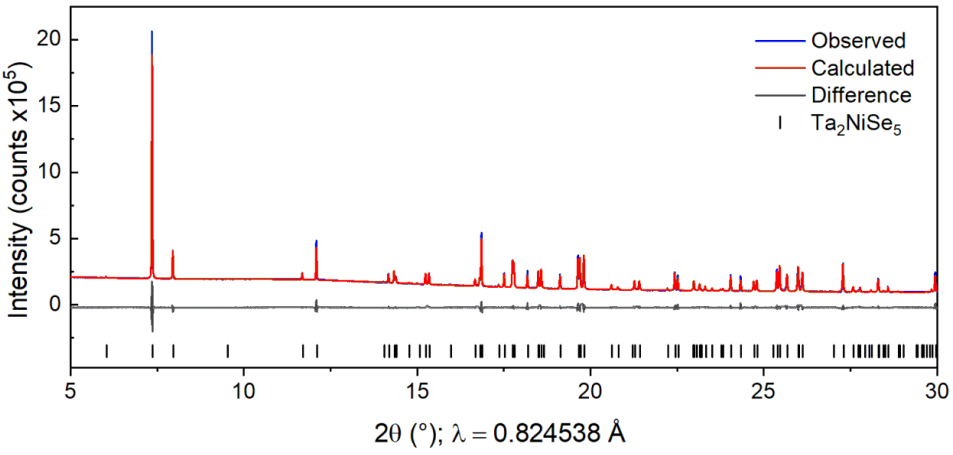

Figure 3.2: Rietveld fit against PXRD data of Ta_2NiSe_5 ($C2/c$) collected using the PSD detector on the I11 beamline. R_{wp} = 2.23 %.

3.3 Lithium Intercalated Ta_2NiSe_5

The synthesis of $LiTa_2NiSe_5$ was described by Hyde[14] but has been reproduced here for completeness.

The reductive intercalation of Ta_2NiSe_5 was performed using the n-butyllithium method. An amount between 0.3 - 2 g of polycrystalline Ta_2NiSe_5 was loaded into a Schlenk tube, along with a magnetic stirrer bar under an Ar atmosphere and sealed. Using a nitrogen Schlenk line, approximately 10 - 20 cm^3 of dry hexane was added to the Schlenk tube, after which a 1:1 stoichiometric volume of 1.6 M n-butyllithium in hexane solution was added to the vessel using a N_2-purged air-tight needle and syringe. The mixture was then removed from the Schlenk line and left to stir overnight at room temperature. The resulting suspension was then left to settle before filtering off the supernatant. The remaining solid was then washed by adding fresh dry hexane to the Schlenk tube, stirring for 30 seconds, and then removing the solvent by filtration. The resulting grey powder was dried under dynamic vacuum for one hour then stored in an Ar atmosphere glovebox for later use.

3.3.1 Powder X-ray Diffraction

The PXRD data show a notable reduction in crystallinity between Ta_2NiSe_5 and $LiTa_2NiSe_5$, which has been attributed to reduction in particle size during the intercalation step. Grain sizes calculated using the Scherrer equation are 150(5) nm and 100(4) nm for Ta_2NiSe_5 and $LiTa_2NiSe_5$ respectively. The ratio of full-width-half-maxima (FWHM) of well resolved $h0l$ and $0k0$ reflections were found to be 1.13 and 0.95 for Ta_2NiSe_5 and $LiTa_2NiSe_5$ respectively, indicating the peak broadening is fairly isotropic and that there is little stacking disorder in both phases. This further supports our hypothesis that peak broadening is an effect of the reduced particle size.

Additional phases using a 2:1 ratio of n-butyllithium to Ta_2NiSe_5 were synthesised to replicate the method used by Squattrito[13]. This sample had poor crystallinity as reported, however the lattice parameters for samples prepared using 1 or 2 equivalents of n-butyllithium were found to be similar within error. We hypothesise that both methods produce the same phase, possibly with slightly different Li contents. However excess reagent evidently causes reduced crystallinity. This is shown in Figure 3.3.

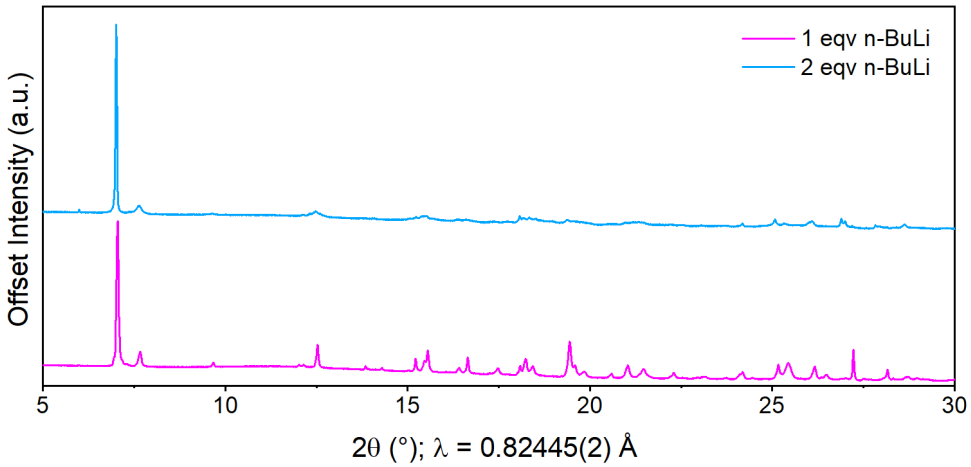

Figure 3.3: The PXRD patterns of Li intercalates of Ta_2NiSe_5 synthesised using a 1 molar equivalents of n-BuLi (pink) and 2 molar equivalents of n-BuLi (blue), collected using the PSD on the I11 beamline at Diamond.

The structural solution is reported in the MChem thesis of Hyde, 2019[14] so will not be discussed in depth here, but is summarised in Appendix I. The solution utilised a rigid body approach in which the relative positions of the Ta-Ni-Se slabs were refined, and it was found that a significant rearrangement of the Ta-Ni-Se layers had taken place, with a relative displacement of (0.5, 0, -0.1372(3)). This is visually demonstrated in Figure 3.5.

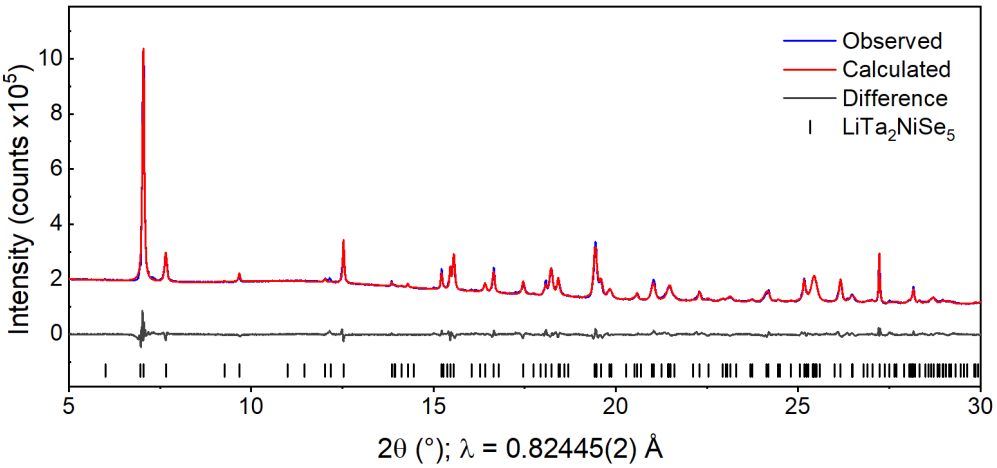

Figure 3.4: Rietveld fit against PXRD data of $LiTa_2NiSe_5$ (*Pmnb*) collected using the PSD detector on the I11 beamline. R_{wp} = 1.76 %.

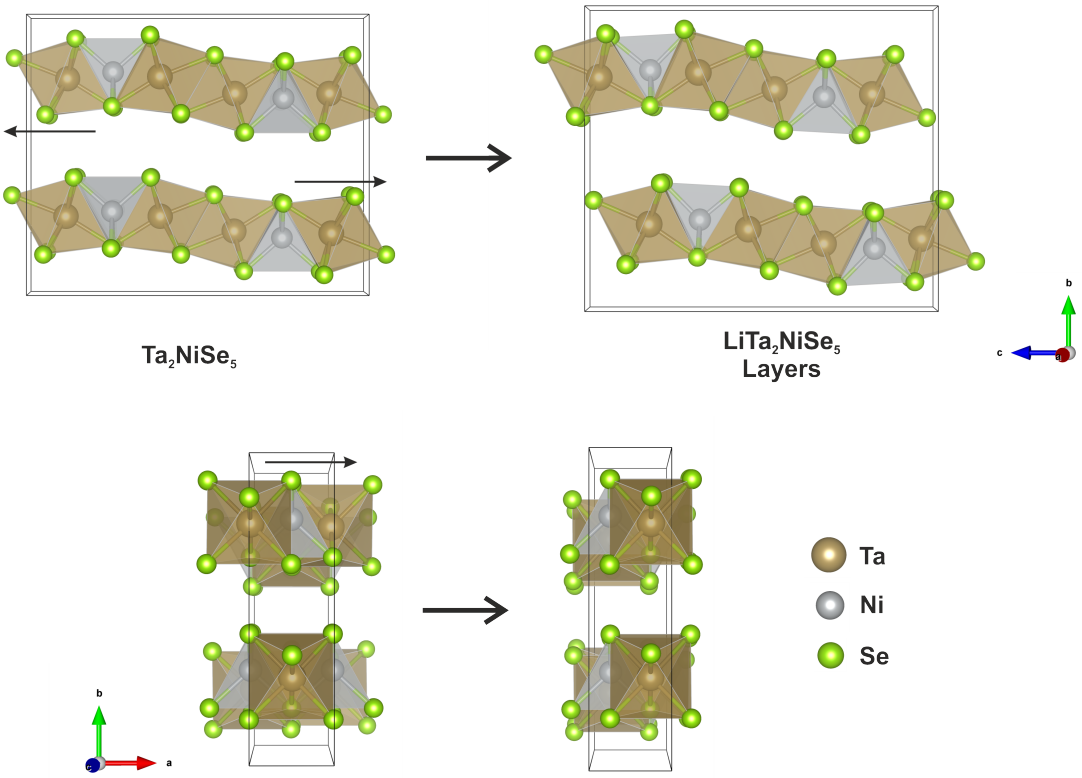

Figure 3.5: Left The crystal structure of Ta_2NiSe_5. **Right** The crystal structure of the Ta-Ni-Se slabs of the Li intercalate in *Pmnb*. Small black arrows represent the displacement of the alternate layers upon intercalation.

The final structure occupies an orthorhombic cell with lattice parameters a = 3.50247(3) Å, b = 13.4053(4) Å, c = 15.7396(2) Å, in space group *Pmnb* (No. 62). The Rietveld fit against PXRD data is shown in Figure 3.4. The refinement parameters have been complied with those obtained from refinement of PND data, shown on page 98, for comparison and are given in Table 3.1.

3.3.2 Powder Neutron Diffraction

Room temperature PND experiments were performed in order to attempt to locate the light Li atoms, and were described in the MChem thesis of Hyde, 2019.[14] A tentative Li site was located at (0.25, 0.515(2), 0.332(3)), however the Li occupancy could not be refined to a sensible value and was fixed at 1 based on the reaction stoichiometry.

Further new work to improve the fit to the experimental PND data using a modified model to account for preferred orientation due to the needle-like crystallite shape, discussed in Chapter 2, has been carried out since. This resulted in improved fit which allowed the Li occupancy to be refined to 1.04(7), which is consistent with the stoichiometry of the reaction, the high phase purity of the intercalate product, and the results of ICP-MS measurements of the washed solid sample which gave a Li:Ni ratio of 0.96(4). The stoichiometry has been assigned as $LiTa_2NiSe_5$ on this basis and is consistent with the PND model. The thermal displacement of Li from the refinement is 0.180(19) $Å^2$, larger than any other atom in the model by one order of magnitude. This could be a result of high mobility of Li, or due to a combination of the low scattering length of Li (-1.90 fm), compared with those of the other atoms (Ta: 6.91 fm, Ni: 10.3 fm, Se: 7.97 fm) and the large number of parameters required to fully describe the structure. This has been seen in similar systems in the literature.[15] The fit of the simultaneous Rietveld refinement against banks 1 - 6 of PND data is shown in Figure 3.6, with refinement parameters given in Table 3.1.

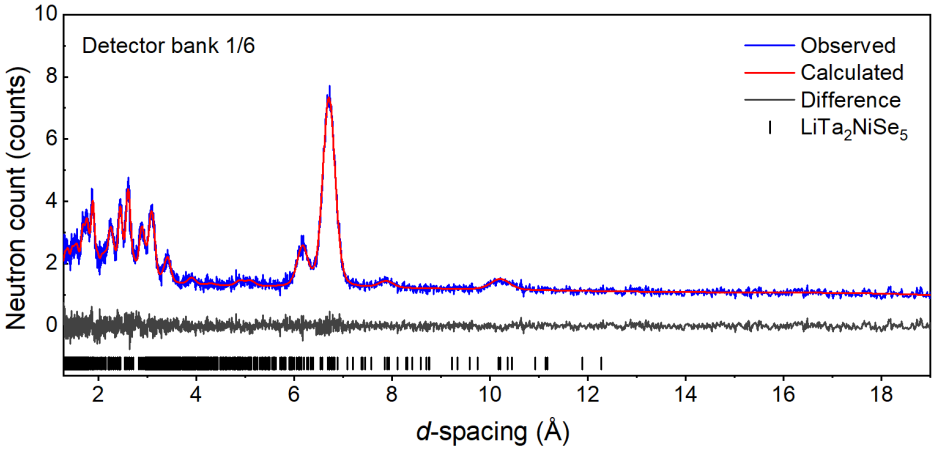
Detector bank 1/6
Observed
Calculated
Difference
LiTa2NiSe5
Neutron count (counts)
d-spacing (Å)

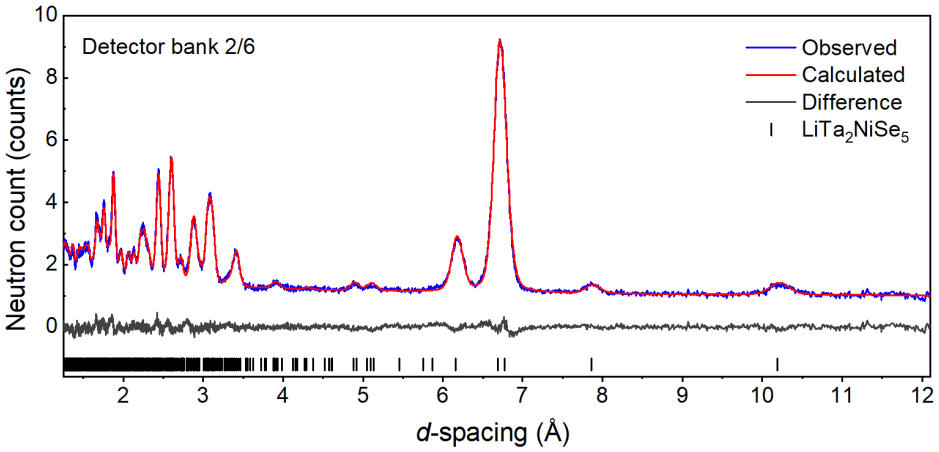
Detector bank 2/6
Observed
Calculated
Difference
LiTa2NiSe5
Neutron count (counts)
d-spacing (Å)

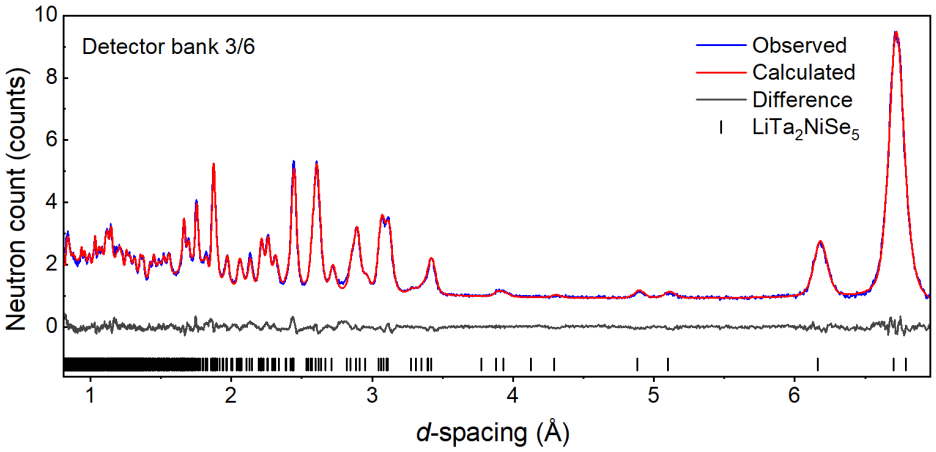
Detector bank 3/6
Observed
Calculated
Difference
LiTa2NiSe5
Neutron count (counts)
d-spacing (Å)

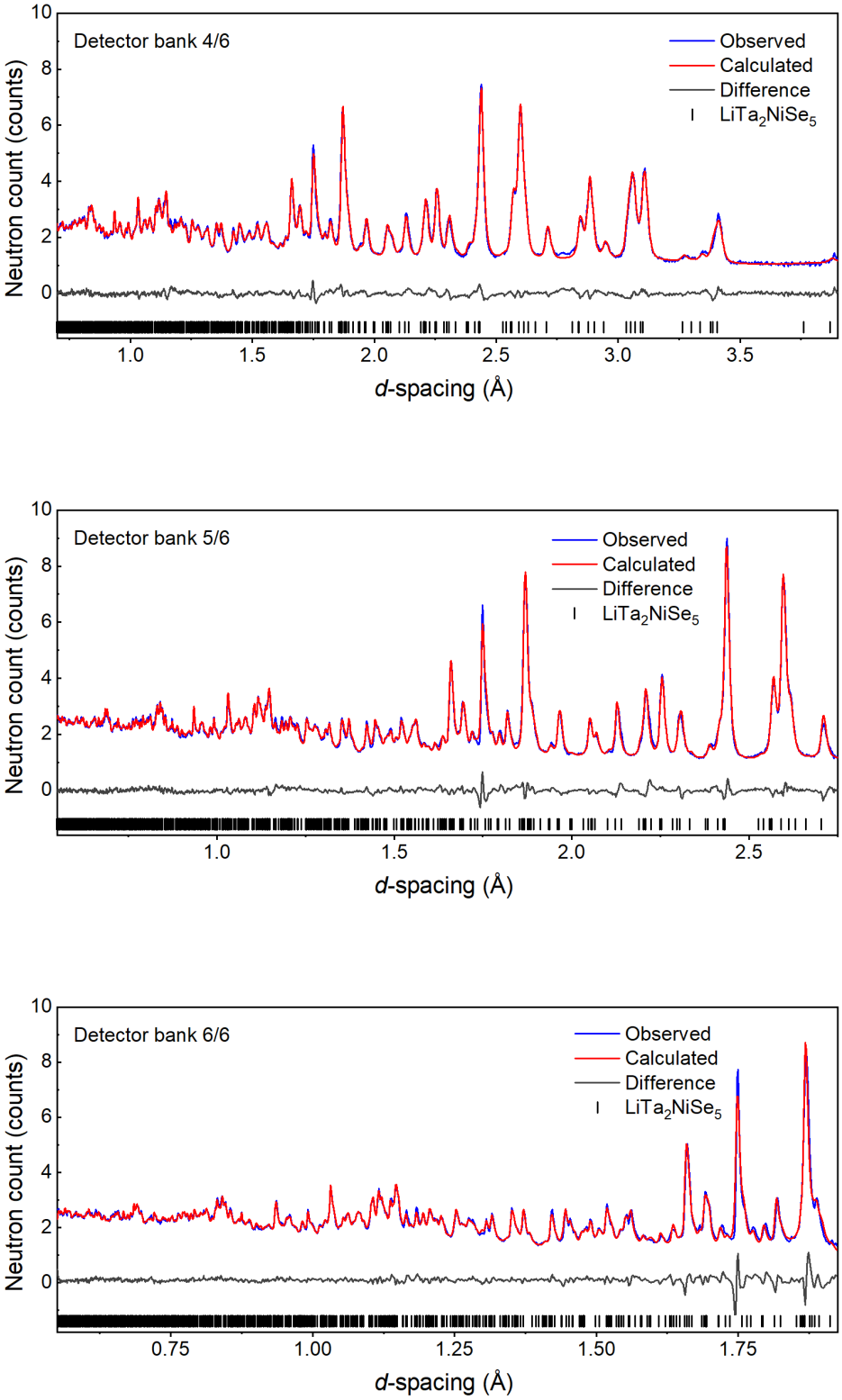

Figure 3.6: Rietveld fits against PND data of $LiTa_2NiSe_5$ (*Pmnb*) collected on banks 1-6 on the GEM instrument at ISIS. R_{wp} = 4.58 %.

Table 3.1: Refinement parameters from PXRD data of $LiTa_2NiSe_5$, parameters obtained from PND data (simultaneous refinement of banks 1 – 6) are given in parentheses ().

$LiTa_2NiSe_5$ RMM = 822.33 g mol^{-1}, Z = 4						
Diffractometer			I11(PSD) (GEM (ISIS))			
Wavelength (Å)			0.825395 (White beam TOF)			
Temperature (K)			300			
Space group			*Pmnb* (62)			
a (Å)			3.50247(3) (3.49523(6))			
b (Å)			13.4053(4) (13.3681(3))			
c (Å)			15.7396(2) (15.7015(4))			
V (Å^3)			739.00(3) (733.64(3))			
Atom	Site	x	y	z	Occ	U_{iso} (Å^2)
Ta1	4c	0.25	0.2304(2) (0.2256(3))	0.0389(2) (0.0404(3))	1	0.0206(9) (0.0133(11))
Ta2	4c	0.25	0.2072(2) (0.2089(3))	0.3213(2) (0.3204(3))	1	0.0148(7) (0.0075(9))
Ni	4c	0.25	0.2999(4) (0.3051(2))	0.6850(5) (0.6803(2))	1	0.0050(16) (0.0109(7))
Se1	4c	0.25	0.9081(4) (0.9073(3))	0.9411(3) (0.9388(2))	1	0.0270(19) (0.0067(8))
Se2	4c	0.25	0.9245(4) (0.9279(3))	0.7099(3) (0.7082(2))	1	0.0237(21) (0.0118(9))
Se3	4c	0.25	0.1592(4) (0.1639(3))	0.8752(3) (0.8776(2))	1	0.0073(18) (0.0060(8))
Se4	4c	0.25	0.1502(4) (0.1415(3))	0.4800(3) (0.4814(2))	1	0.0150(19) (0.0122(9))
Se5	4c	0.25	0.3136(3) (0.3139(3))	0.1847(4) (0.1858(2))	1	0.0048(13) (0.0098(8))
Li	(4c)	(0.25)	(0.506(9))	(0.308(7))	(1.04(7))	(0.180(19))

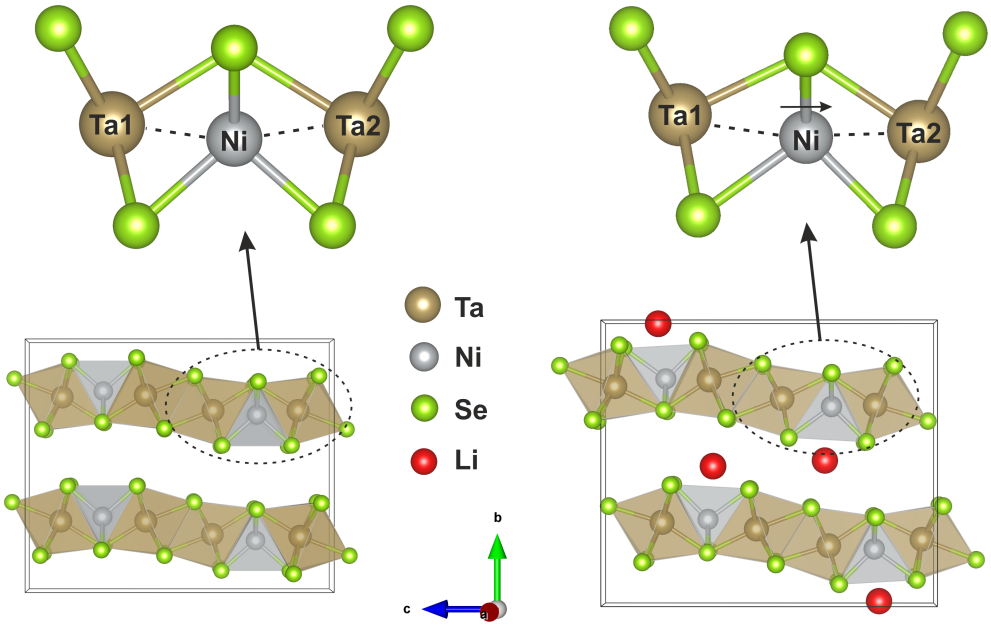

Figure 3.7: The co-ordination environment surrounding Ni in **left** Ta_2NiSe_5 and **right** $LiTa_2NiSe_5$. Ta1-Ni and Ta2-Ni distances have been represented with the dashed line.

The refined metal-metal separations for Ta_2NiSe_5 and $LiTa_2NiSe_5$ are listed in Table 3.2. The values obtained for Ta_2NiSe_5 from PXRD data are within the uncertainty of those reported by Sunshine *et al.* from single crystal XRD data.[4] Canadell and Whangbo[6] comment on the long Ta–Ta and short Ta–Ni separations in Ta_2NiSe_5 supporting the Ta(V)/Ni(0) oxidation state configuration. Both Ta1–Ni and Ta2–Ni distances in Ta_2NiSe_5 are approximately equal at 2.8037(8) Å and 2.8131(8) Å respectively. In $LiTa_2NiSe_5$, the structural refinements and the computation both suggest that the Ta1–Ni separation is somewhat elongated relative to the Ta2–Ni separation, although the difference is only significant in the PXRD data (2.947(7) Å and 2.740(7) Å respectively). This may be because Ni makes a relatively weak contribution to the scattering compared with the PND data, so this may be an artefact. The partial density of states calculated for each Ta site (Figure 3.12,

page 113) suggests both sites are reduced equally and the subtle differences in band structure are due to the different local co-ordination around the two Ta sites.

Table 3.2: Refined bond distances of Ta_2NiSe_5 and $LiTa_2NiSe_5$ from PXRD, PND and computed models determined in this work. Atomic labels of Se atoms for Ta_2NiSe_5 data in space group $C2/c$ are given in square brackets, for comparison to $LiTa_2NiSe_5$ in space group *Pmnb*.

Distances	Ta_2NiSe_5	$LiTa_2NiSe_5$		
(Å)	PXRD	PXRD	PND	Computation
Ta1-Ta1	3.496(1)	3.503(1)	3.495(1)	3.4781
Ta1-Ta2	3.903(1)	3.943(4)	3.969(6)	3.9268
Ta1-Ni	2.804(1)	2.947(7)	2.837(5)	2.8479
Ta2-Ni	2.813(1)	2.740(7)	2.816(5)	2.7890
Ta1-Se1	2.523(1) [Se1]	2.587(6)	2.512(5)	2.5650
Ta1-Se3	2.678(1) [Se2]	2.761(6)	2.686(6)	2.6798
Ta1-Se4	2.588(1) [Se2]	2.546(5)	2.659(5)	2.6173
Ta1-Se5	2.570(1) [Se3]	2.572(7)	2.570(6)	2.5662
Ta2-Se2	2.581(1) [Se1]	2.529(5)	2.569(5)	2.5602
Ta2-Se3	2.661(1) [Se2]	2.660(5)	2.598(5)	2.6078
Ta2-Se4	2.678(1) [Se2]	2.628(6)	2.684(6)	2.6787
Ta2-Se5	2.570(1) [Se3]	2.553(7)	2.537(6)	2.5428
Ni-Se1	2.339(2) [Se1]	2.456(9)	2.365(3)	2.3329
Ni-Se2	2.339(2) [Se1]	2.348(9)	2.400(5)	2.3590
Ni-Se5	2.381(2) [Se3]	2.335(5)	2.365(3)	2.3893

3.3.3 Li NMR Spectroscopy

Variable temperature MAS ^{6}Li NMR measurements (Figure 3.8a) indicate a single Li environment at 298 K, observable on the NMR timescale, which agrees with our previous Li analysis. However low temperature measurements reveal the appearance of a second asymmetric peak between 253 – 233 K which contains the majority of the Li and becomes extremely broad upon cooling. This could be due to a second Li environment, although none of the higher energy Li sites located computationally refined to non-zero occupancies outside the uncertainty in the parameters in the PND structure refinements. The nature of the splitting is unusual, one peak shifts and broadens significantly relative to the other. This could indicate a temperature dependent Knight shift usually observed in metallic compounds arising from the Pauli paramagnetism of conduction electrons,[16,17] which is proportional to the electronic density of states at the Fermi level.

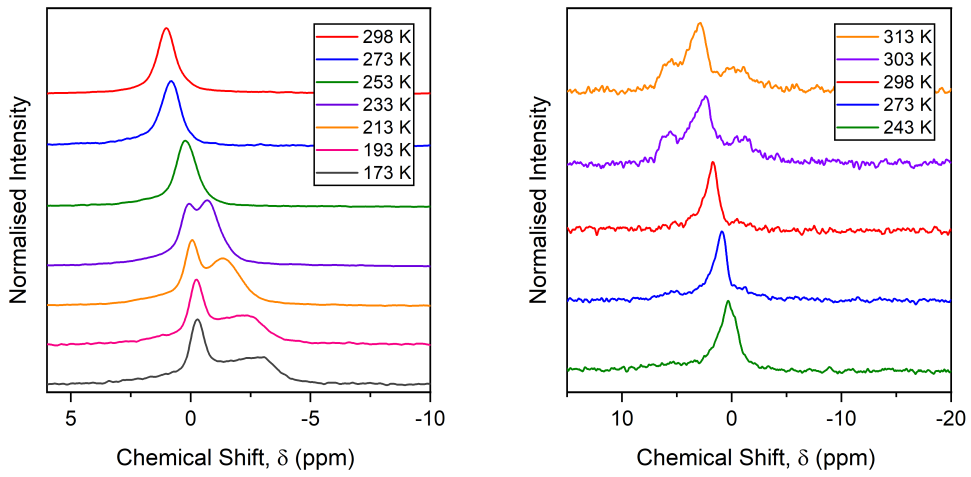

(a) Low temperature measurements made between 173 – 298 K.

(b) High temperature measurements made between 298 – 313 K.

Figure 3.8: Variable temperature MAS ^{6}Li NMR spectra. The two ranges are presented separately as they were performed as two measurements.

Above room temperature (Figure 3.8b) two additional peaks appear which could indicate the appearance of a conductive phase above 298 K, as indicated by spinning problems and changes in probe tuning, although no structural transition or decomposition is apparent in the variable temperature PXRD data until much higher temperatures, as described above. Variable temperature conductivity measurements are hampered by the air sensitivity of this compound, although the calculations and a crude resistivity measurement, described in the magnetometry section, do suggest metallic behaviour for this intercalate.

3.3.4 Computational Studies

To locate other possible Li sites and calculate their relative energies in the expanded structure, DFT calculations were performed on $LiTa_2NiSe_5$ by Jiayi Cen at University College London under the supervision of Prof. David Scanlon. Plane wave density functional theory (DFT) code Vienna Ab initio Simulation Package (VASP)[18–20] (version 5.4.4) was used to determine lithium site energies. A plane wave cut-off energy of 600 eV and Γ-centered Monkhorst-Pack (MP) grids with a maximum spacing of 0.043 2π Å^{-1} were used with projector-augmented wave[21,22] (PAW) pseudopotentials from dataset PBE.54 (Li_sv, Ta_pv, Ni_pv and Se). The PBEsol[23] generalised gradient approximation (GGA) and dispersion corrected[24] PBEsol + D3 functionals were used to model the exchange and correlation effects. Tolerances of 10^{-6} eV and 10^{-2} eV Å^{-1} were applied to total energy and forces during electronic minimisation and geometry optimisation, respectively. The electronic densities of states (DOS) were computed using denser k-point grids with a maximum spacing of 0.025 2π Å^{-1}. Analysis of the DOS were conducted using the SUMO[25] python package. Input files for lithium site calculations were prepared using the DOPED[26,27] python package with a 32-atom supercell. Force tolerance was raised to 2×10^{-2} eV Å^{-1} for lithium interstitials during relaxations, with fixed lattice parameters. The PYMATGEN[28] and ASE[29] python packages were used to manipulate structures and to assist with the symmetry analysis of the lithium sites.

22 symmetry inequivalent interstitial positions were identified, and each Li interstitial was subject to relaxation in the host Ta_2NiSe_5 supercell with *Pmnb* symmetry

using the PBEsol functional. All Li interstitials were relaxed to one of 5 different clusters of sites. The sites within each cluster have marginally different positions relative to one another but were found to be within 0.015 Å of each other along any given axis, a distance comparable to the uncertainty in a refined interatomic distance. 21 of the individual sites were located on $4c$ sites of m site symmetry in the experimental *Pmnb* model. One additional site corresponded to a general position in *Pmnb* but was close to a mirror plane. Co-ordinates of all sites can be found in Table 3.3. The Li site identified independently from the PND measurements with co-ordinates (0.25, 0.515(2), 0.332(3)), corresponds to the lowest energy Li cluster, labelled as Cluster 1. On this basis, the Li site identified through PND was accepted as the final model, shown in Figure 3.10 on page 110, and is consistent with the refinement and the chemical analysis.

Table 3.3: Parameters of relaxed interstitial sites output by DFT calculations. The site marked with an asterisk (*) was the only site not located on a mirror plane in the *Pmnb* model and the symmetry was reduced to $P2_1/c$ to allow it to fully occupy a site of 4-fold multiplicity. ΔE is the total energy difference relative to the lowest energy cluster model.

Defect name	ΔE (eV)	Site	Site co-ordinates		
			x	y	z
Cluster 1					
Int Li 14	0	4*c*	0.25	0.50114	0.33392
Int Li 2	0	4*c*	0.25	0.48885	0.33518
Int Li 12	0	4*c*	0.25	0.49714	0.33272
Int Li 16	0	4*c*	0.25	0.50199	0.33267
Int Li 18	0	4*c*	0.25	0.49362	0.33384
Int Li 17	0	4*c*	0.25	0.49384	0.33157
Int Li 15	0	4*c*	0.25	0.50124	0.33008
Int Li 13	0.01	4*c*	0.25	0.49654	0.32908
Cluster 2					
Int Li 8	0.08	4*c*	0.25	0.46758	0.07313
Int Li 9	0.08	4*c*	0.25	0.46977	0.07400
Int Li 7*	0.08	4*e*	0.25735	0.46595	0.07039
Int Li 6	0.08	4*c*	0.25	0.46429	0.06736
Int Li 5	0.08	4*c*	0.25	0.46220	0.06621
Cluster 3					
Int Li 10	0.15	4*c*	0.25	0.50076	0.92858
Int Li 4	0.15	4*c*	0.25	0.50964	0.92808
Int Li 3	0.15	4*c*	0.25	0.50484	0.92916
Int Li 19	0.15	4*c*	0.25	0.49277	0.92998
Int Li 11	0.15	4*c*	0.25	0.50017	0.92949
Cluster 4					
Int Li 21	0.46	4*c*	0.25	0.57913	0.74604
Int Li 20	0.46	4*c*	0.25	0.58248	0.74324
Int Li 22	0.46	4*c*	0.25	0.57631	0.74609
Cluster 5					
Int Li 1	0.68	4*c*	0.25	0.54079	0.51680

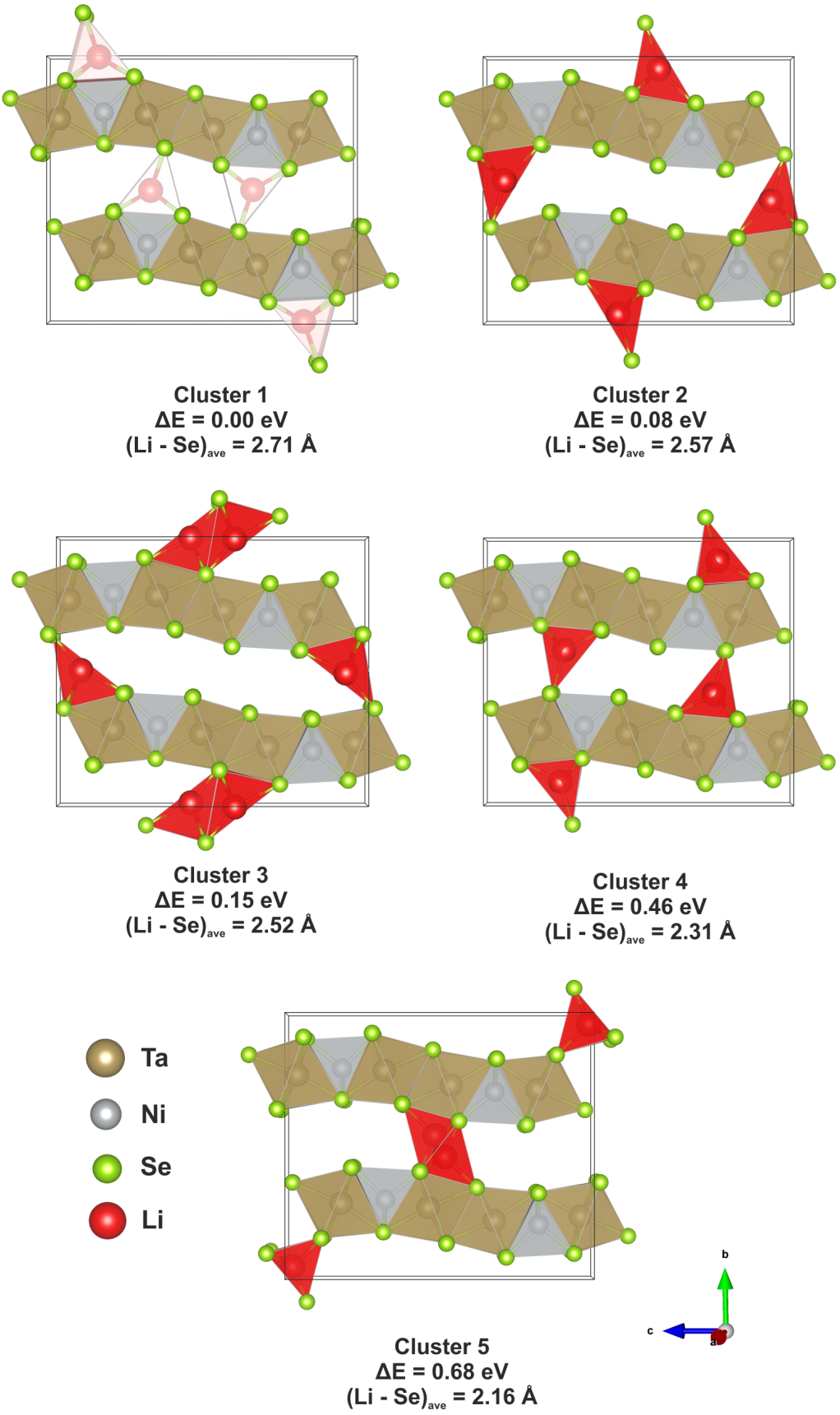

Figure 3.9: A schematic showing the five distinct clusters of Li sites determined by the plane wave DFT analysis and their relative energies.

The final structural model for $LiTa_2NiSe_5$ is shown in Figure 3.10. Li atoms lie in 6 co-ordinate distorted triangular prisms of Se with an average Li–Se bond length of 2.724(2) Å, determined from the PND measurement. This is consistent with Li–Se bond length values reported in the literature, which range from 2.61 Å for the tetrahedral environment in Li_2Se[30] to 2.93 Å for 6 co-ordinate Li sites in $LiMnSe_2$.[31] An additional Se atom lies at a distance of 3.322(4) Å, which has not been formally included in the co-ordination sphere of Li since it lies far outside of this range. The co-ordination environment of Li is detailed in Figure 3.10, which gives the Li–Se bond distances and the angles of the $LiSe_6$ polyhedra- indicating the degree of distortion away from a regular triangular prism. The stacking rearrangement of the Ta-Ni-Se is most likely driven by the co-ordination requirements of the Li ions, which could not be fulfilled in the original layer configuration.

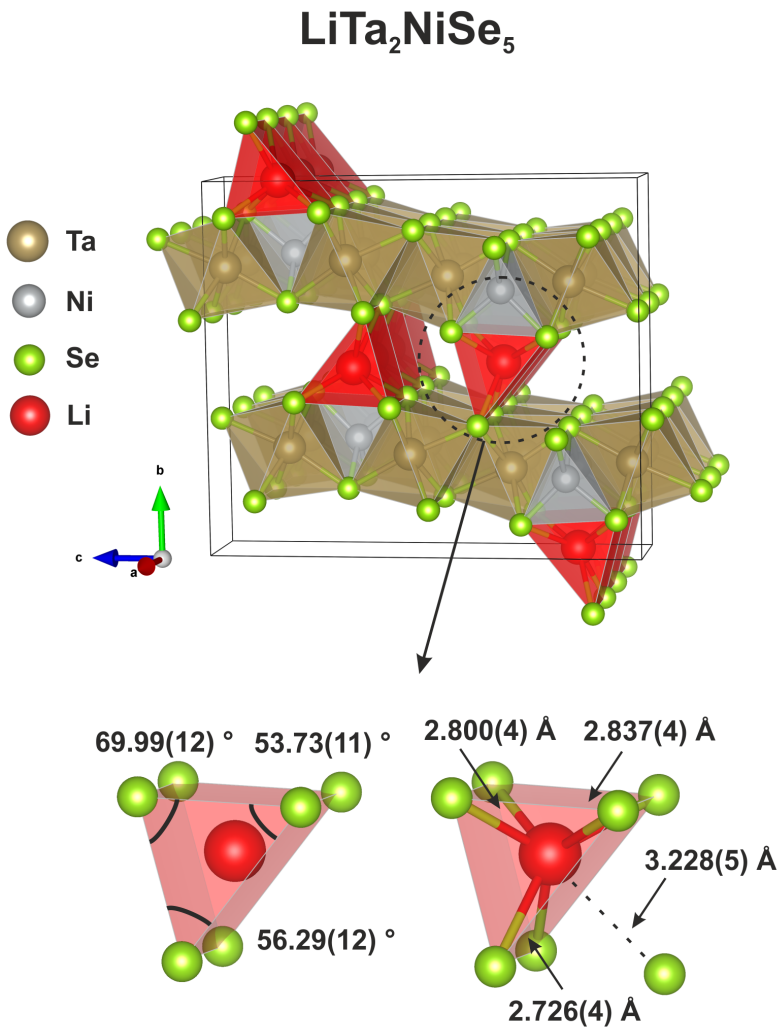

Figure 3.10: Final structural model of $LiTa_2NiSe_5$ from refinement of PXRD and PND and confirmed by computational prediction of the Li position. Bond lengths and angles are derived from refinement of PND data.

The electronic density of states (DOS) and band dispersion of $LiTa_2NiSe_5$ were calculated using the lowest energy Li site given by DFT calculations, and are shown in Figure 3.11. The band dispersion shows no band gap and suggests that $LiTa_2NiSe_5$ is metallic. The DOS shows that the Ta $5d$ bands dominate the conduction band and are partially filled upon intercalation, which is consistent with partial reduction of Ta(V). Partial densities of states for the Ta1 and Ta2 (Figure 3.12a and 3.12b) sites show no significant difference between the two sites in the positions of the various

bands relative to the Fermi Level, suggesting that reduction of Ta is not specific to one site. The small differences in partial densities of states presumably arise from the small difference in local co-ordination between the two Ta sites discussed previously. The band structure and DOS of Ta_2NiSe_5 in both orthorhombic and monoclinic symmetries were calculated using the dispersion-corrected functionals PBEsol + D3 and are given in Figure 3.13, confirming the narrow-gap behaviour is quite different from the intercalate. It should noted that the differences observed in the band structures and DOS between the parent phase and $LiTa_2NiSe_5$ are not simply due to changing the Fermi Level by adding electrons donated from the intercalated Li, but also due to the structural change that occurs during intercalation.

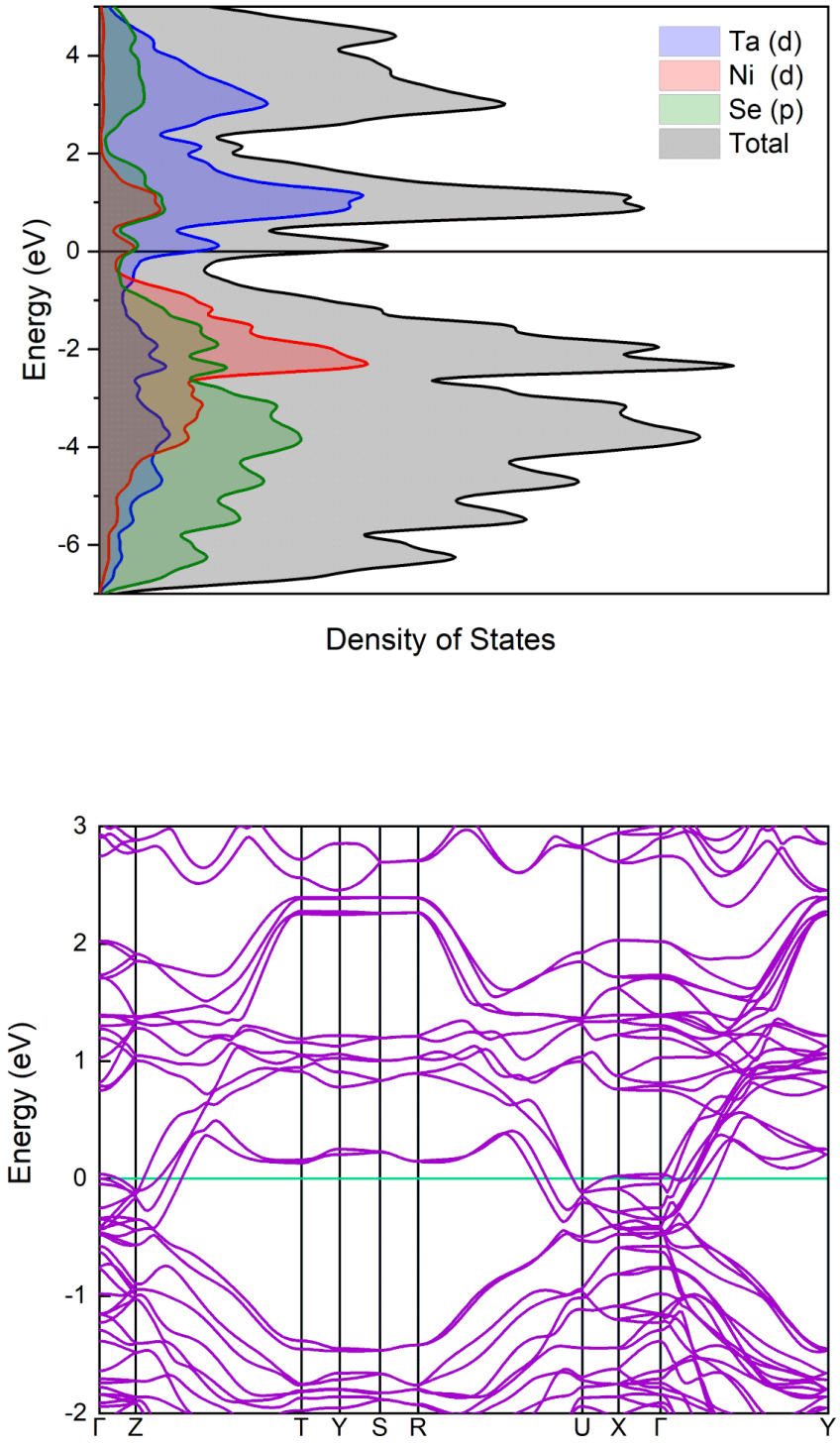

Figure 3.11: Top. The density of states and **bottom**. the band dispersion of $LiTa_2NiSe_5$ calculated using the PBEsol functional.

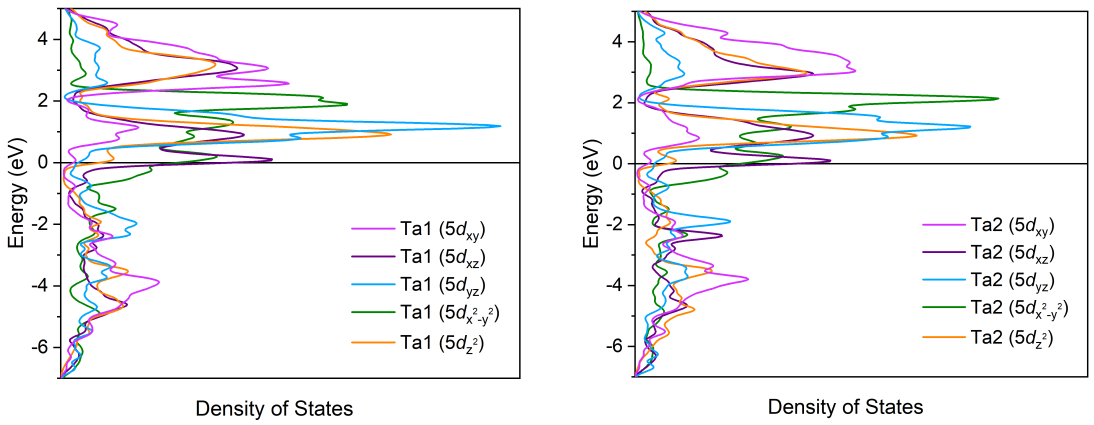

(a) PDOS of the Ta1 site.

(b) PDOS of the Ta2 site.

Figure 3.12: The partial density of states (PDOS) calculated for the two Ta sites in $LiTa_2NiSe_5$ using the PBEsol functional.

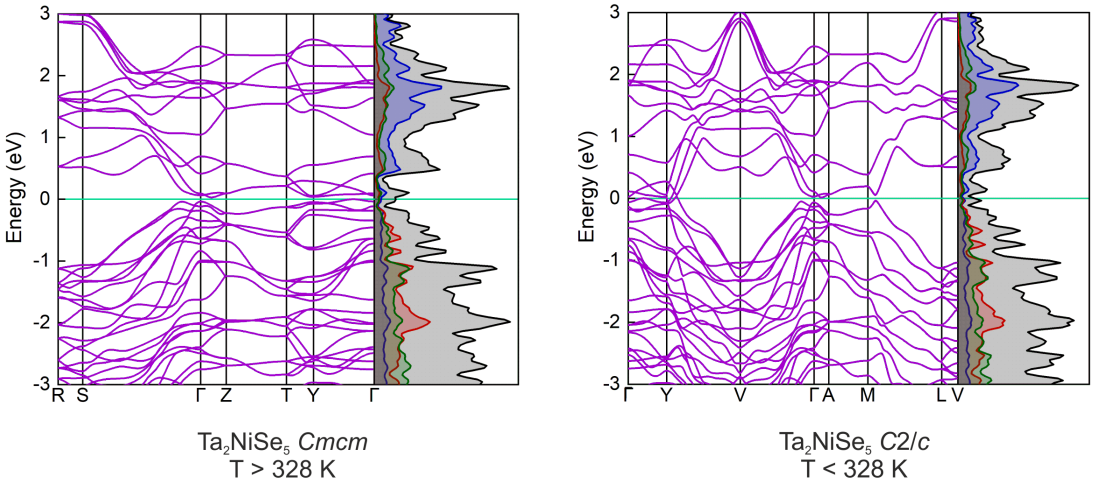

(a) Ta_2NiSe_5 in *Cmcm* symmetry.

(b) Ta_2NiSe_5 in $C2/c$ symmetry.

Figure 3.13: The band dispersion and density of states for Ta_2NiSe_5 computed using dispersion corrected PBEsol + D3 functionals.

Due to the lack of implementation on computing the NMR shifts for metallic systems using *ab initio* methods, attempts were made to calculate the NMR shifts with the gauge-including projector augmented wave, an approach designed for non-metallic crystalline systems.[32–34] These calculations were unsuccessful due to the metallic nature of the compound.

3.3.5 Variable Temperature PXRD

Temperature resolved PXRD measurements between 100 K and 300 K approximately every 2 K were performed on $LiTa_2NiSe_5$ to probe for any structural distortions analogous to the monoclinic distortion observed in Ta_2NiSe_5 at 328 K. These high-resolution measurements revealed no peak splitting down to 100 K, indicating that there was no comparable distortion in $LiTa_2NiSe_5$ down to this temperature. The lattice parameters and unit cell volume output from the sequential refinement of PXRD patterns indicated no structural transitions or anomalies, shown in Figure 3.14.

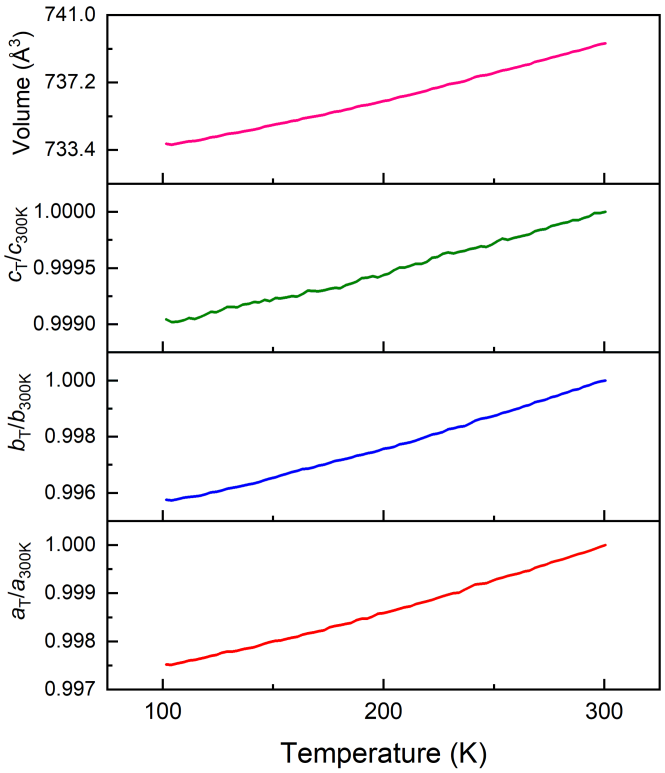

Figure 3.14: Lattice parameter variation of $LiTa_2NiSe_5$ from temperature resolved PXRD data measured from 100 – 300 K, using the PSD detector on the I11 beamline.

An additional measurement between 303 K and 1173 K was performed to assess the decomposition of $LiTa_2NiSe_5$. The film plot in Figure 3.15 shows decomposition occurs at approximately 700 – 800 K with the disappearance of the high intensity reflection at $2\theta \approx 7.1$ °. Beyond this temperature two new low angle reflections emerge at $2\theta \approx 6$ ° and 6.7 °. From the changes in scattering around this transition there is evidence for a possible intermediate phase and some unusual changes in peak positions are evident. This requires further examination.

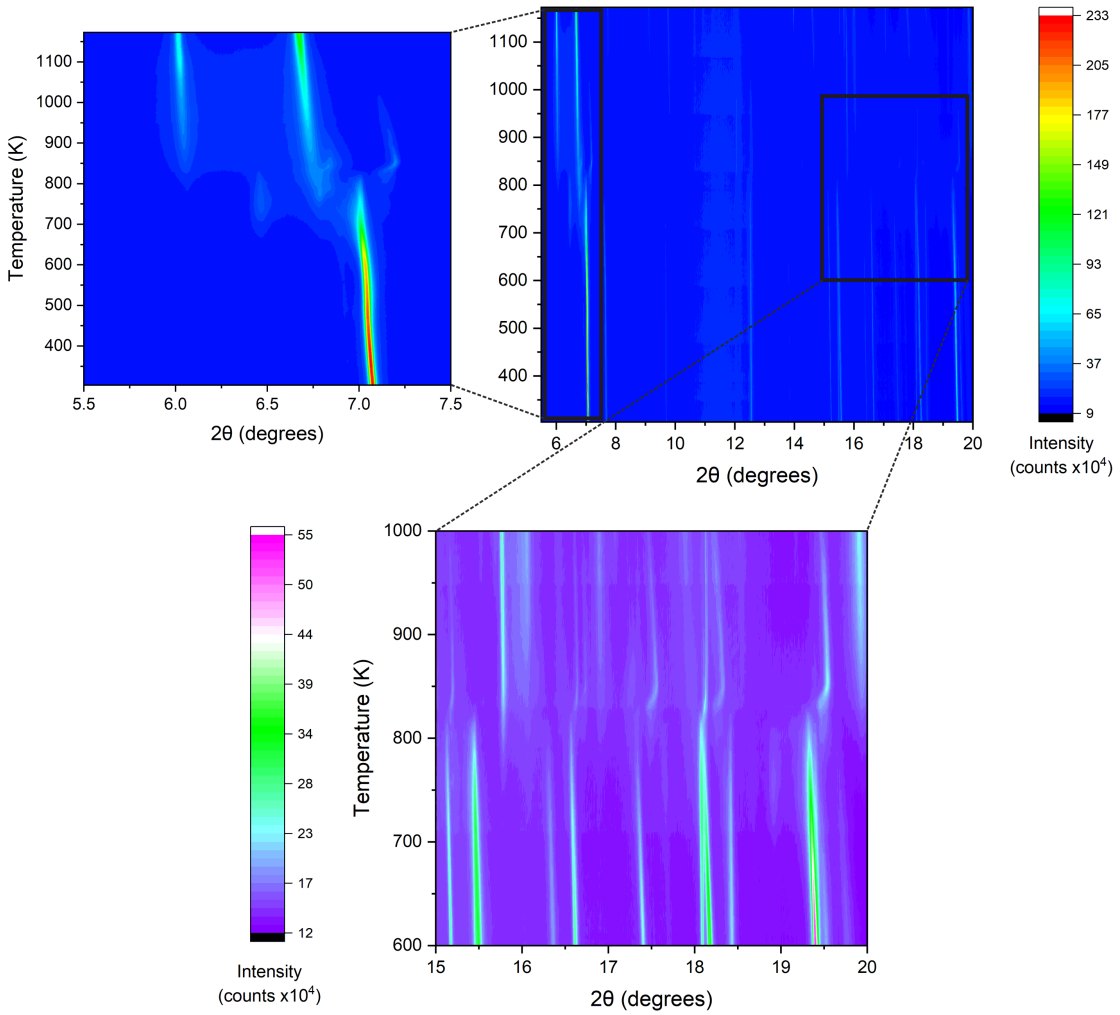

Figure 3.15: Temperature resolved PXRD patterns collected on the I11 beamline between 303 – 1173 K over 211 temperatures.

The PXRD pattern collected at 1173 K, shown in Figure 3.16, cannot be fitted using $LiTa_2NiSe_5$, Ta_2NiSe_5 or any other ternary or binary phases made up of the constituent elements of the intercalated phase. This indicates the pattern is dominated by some high temperature phase or a set of unknown decomposition products. Upon cooling, the new pattern persists which means that the change is not reversible, and the $LiTa_2NiSe_5$ intercalate is metastable. The pattern collected at 300 K after heating shows a significant thermal contraction relative to the pattern collected at 1173 K. Attempts were made to index the PXRD pattern of the high temperature phase, however no sensible lattice parameters were found. This high temperature change is subject to further investigation.

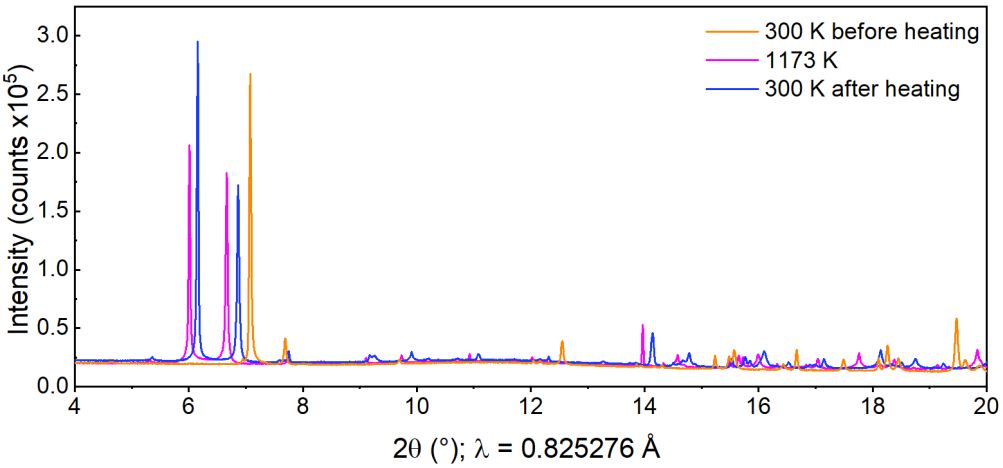

Figure 3.16: PXRD patterns of $LiTa_2NiSe_5$ measured at 300 K, 1173 K and at 300 K after heating using the PSD detector on the I11 beamline.

To assess the air stability of $LiTa_2NiSe_5$, a portion of the sample was left to oxidise in air overnight. The resulting phase was found to be almost exclusively Ta_2NiSe_5, with slightly diminished crystallinity compared to fresh Ta_2NiSe_5, from analysis of synchrotron PXRD data. Additional side phases could not be identified, however there is most likely a lithium-containing amorphous phase resulting from the aerial deintercalation of Li. Considering the layer rearrangement between the two phases is significant, this indicates high mobility of the Ta-Ni-Se layers. The Rietveld refinement of the PXRD data can be found in Figure 3.17.

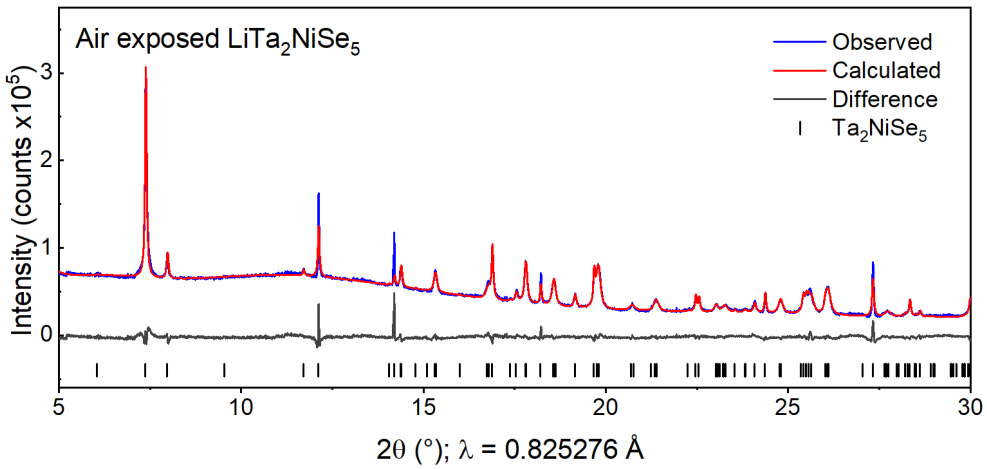

Figure 3.17: Rietveld refinement of air exposed $LiTa_2NiSe_5$ collected using the PSD detector on the I11 beamline. The majority phase is Ta_2NiSe_5 (*Pmnb*). R_{wp} = 4.69 %.

3.3.6 Magnetometry

Ambient temperature magnetisation isotherms measured using SQUID magnetometry reveal that the parent and intercalate compounds are bulk diamagnets. At low fields both isotherms reveal small positive magnetisations from 0 – 1 T. This is indicative of a small ferromagnetic impurity and has been attributed to the presence of elemental Ni in trace amounts (0.0205(8) % and 0.0106(2) % respectively) below the detection limit of X-ray powder diffraction. The susceptibility was determined as a function of temperature by performing measurements at two fields above the saturation field of the ferromagnetic impurity.

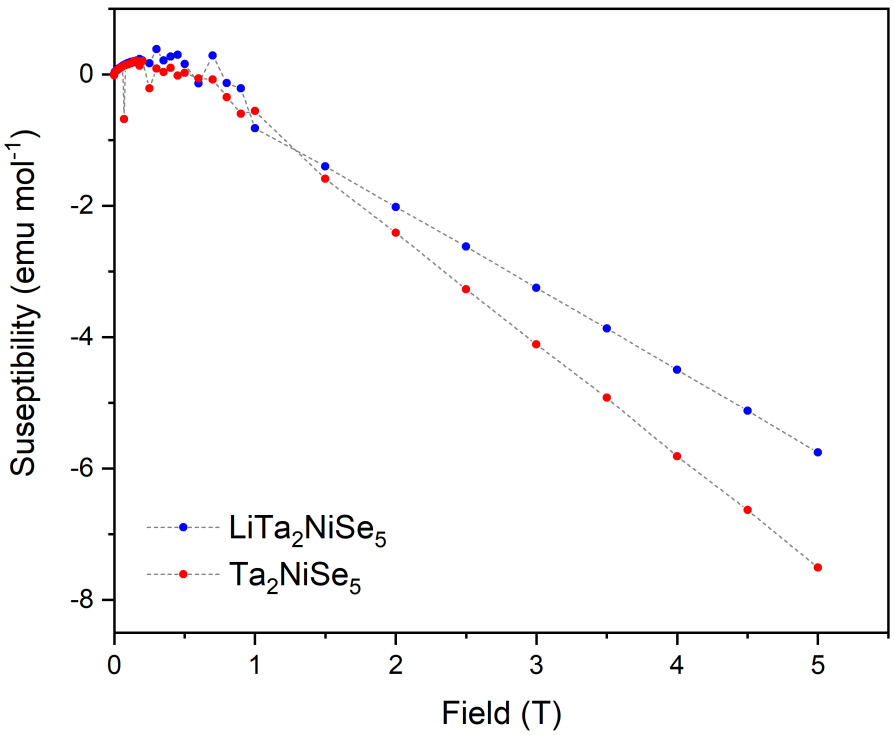

Figure 3.18: Magnetisation vs field for Ta_2NiSe_5 and $LiTa_2NiSe_5$ at 300 K. Magnetic impurities attributed to elemental Ni can be seen at low field but saturate above 1.5 T.

Figure 3.18 shows a 30 % reduction in the diamagnetic susceptibility, from $-1.695(7)$ x10^{-4} emu mol^{-1} in Ta_2NiSe_5 (DiSalvo *et al.* report a susceptibility of -1.028 x10^{-4} emu mol^{-1} for Ta_2NiSe_5 at 300 K[5]) to $-1.254(4)$ x10^{-4} emu mol^{-1} in $LiTa_2NiSe_5$, upon intercalation. Subtraction of the magnetisation vs temperature curve measured at 2.5 T from that measured at 3.5 T (Figure 3.19) for $LiTa_2NiSe_5$ eliminates the effect of the minuscule ferromagnetic impurity and gives the intrinsic susceptibility which is temperature independent, consistent with opposing temperature independent diamagnetic and paramagnetic contributions.

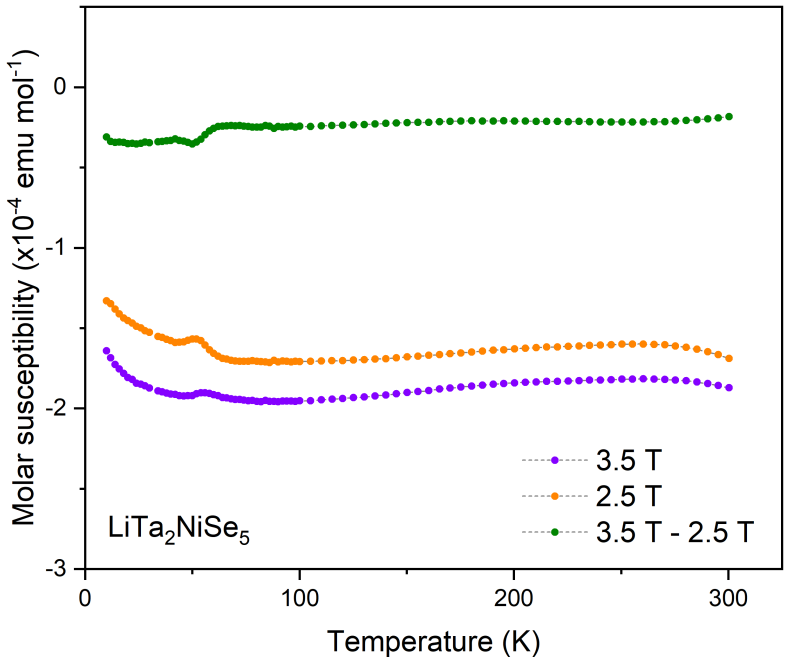

Figure 3.19: Molar susceptibility vs temperature curves collected at 2.5 T and 3.5 T after being cooled in zero field. The green curve is the subtraction of the data points collected at 3.5 T from those collected at 2.5 T. The hump at approximately 50 K has been attributed to a trace amount of oxygen contamination.

The core diamagnetic contributions calculated from standard tables[35] are -2.8 x10^{-4} emu mol^{-1} and -2.81 x10^{-4} emu mol^{-1} for Ta_2NiSe_5 and $LiTa_2NiSe_5$ respectively. However, the experimental susceptibilities are approximately half these values. This suggests that there is a small-temperature independent paramagnetism in the parent Ta_2NiSe_5, and that the intercalate is a Pauli paramagnet with a temperature independent susceptibility enhanced by the injection of electrons from the intercalated Li to increase the density of states at the Fermi Level. This is consistent with the clear conclusion from the calculations that the intercalated phase $LiTa_2NiSe_5$ is metallic. Conductivity measurements on Ta_2NiSe_5 have been reported previously by DiSalvo *et al.*[5] Similar measurements of $LiTa_2NiSe_5$ were hampered by the air sensitivity of the sample. A room temperature measurement was made under non-ideal conditions inside a glove box by sandwiching a 5 mm diameter pellet of $LiTa_2NiSe_5$ between two steel contacts of the same diameter, connected to a multimeter via an electronics feedthrough, which gave a value of $\rho = 2.1(1)$ Ω cm, a value consistent with a metallic sample measured under such conditions.

No superconductivity was observed in $LiTa_2NiSe_5$ down to 2 K (the lower limit of the instrument) at ambient pressure in an applied field of 50 Oe. Whilst the arrangement of the layers in $LiTa_2NiSe_5$ is similar to that in the high-pressure form of Ta_2NiSe_5, which exhibits superconductivity below 1.2 K at a pressure of 8 GPa,[36] the intercalation provides additional electrons to raise the Fermi level. Whether superconductivity is present in $LiTa_2NiSe_5$ below 2 K, at high pressure, or with different Li contents is not predictable, and may be the subject of further experiments.

The work in this chapter up until this point has been published in *Inorganic Chemistry.*[37]

* * *

3.4 Lithium and Ammonia Intercalated Ta_2NiSe_5

Lithium-ammonia intercalates were synthesised by adding Ta_2NiSe_5 powder and an amount of Li metal (Sigma Aldrich; 99 %) to give the stoichiometry $LiTa_2NiSe_5$, to a Schlenk tube under an Ar atmosphere. The reaction vessel was then sealed and attached to a Schlenk line along with a cylinder of ammonia (BOC; 99.98 %). The Schlenk tube was placed in a bath of isopropanol and dry ice, and all glassware/tubing between the sample and the ammonia cylinder was evacuated. Approximately 10 cm^3 of NH_3 was then condensed over the reagents. The suspension was left to stir until all the ammonia had evaporated via the mercury manometers contained in a fume hood. The resulting grey solid was then dried under dynamic vacuum for 20 minutes and stored in an Ar filled glovebox for later use.

3.4.1 Powder X-ray Diffraction

The PXRD patterns of the intercalated phases had visual similarities to that of the parent compound Ta_2NiSe_5 with a change in intensity profile, possibly due to strong preferred orientation from sample packing in the capillary. The pattern shows a good degree of crystallinity, shown in Figure 3.20, with an estimated crystallite size of 90(5) nm calculated using the Scherrer equation, given in Chapter 2. The pattern of the lithium-ammonia intercalate could be well indexed to an orthorhombic unit cell, a = 3.5175(1) Å, b = 18.7828(7) Å, c = 15.7520(3) Å, in space group *Pmnb*, which has similar a and c parameters to the parent but have significantly elongated b parameters relative to the of the parent, which gives an increased unit cell volume of 48 %.

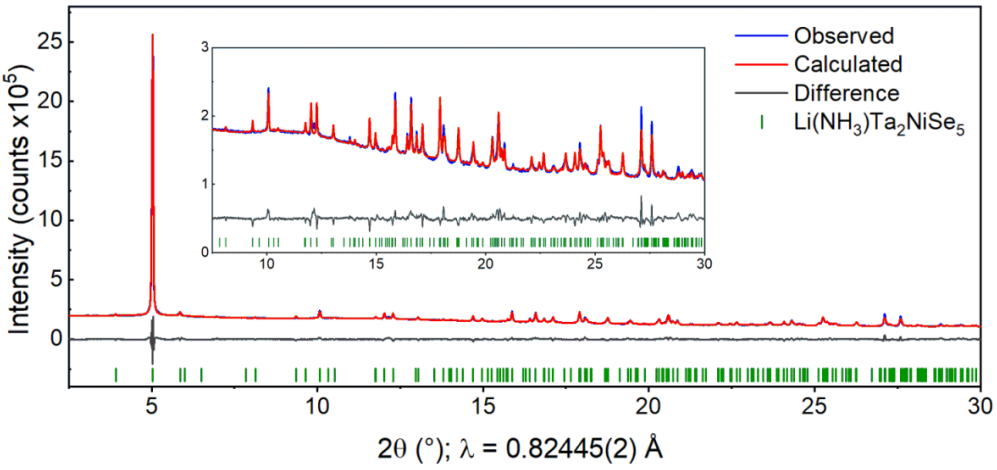

Figure 3.20: Rietveld fit against PXRD data of $Li(NH_3)Ta_2NiSe_5$ (*Pmnb*) collected using the PSD detector on the I11 beamline. R_{wp} = 2.11 %.

Like the structural solution of $LiTa_2NiSe_5$, a rigid body approach was adopted to take advantage of the layered nature of the structure, assuming that the layers would remain intact during the low temperature intercalation experiments. A model resembling the parent phase in terms of the arrangement of the atoms and the interatomic distances was built in $P1$ symmetry inside a unit cell with parameters obtained from the indexing described above. The atoms were then divided into two groups according to which layer they occupied, and constrained so there was no refinement of atomic positions within each layer. One layer was kept fixed and the other allowed to refine its position in the x, y and z directions relative to the other. The displacement in x (i.e. along the short axis) is within error of 0.5 and was assumed to be so for the purpose of this model, so there is a substantial relative shift in this direction. The small displacement in y was fixed to zero so that the relationship between the two layers remains that they are displaced along the b axis, which is the stacking direction, by $\frac{1}{2}b$, consistent with the expectation that they remain equally spaced. The layers are significantly displaced relative to one another along the c direction. The final displacement of the layers relative to one another is given by (0.5, 0, $-0.1885(3)$). The resulting structure obtained from this rigid-body refinement in $P1$ can then be described in $Pmnb$ (a setting of space group No. 62), which is the same space group assigned to the Li intercalate $LiTa_2NiSe_5$ described previously. The final model was thus produced by lifting the rigid body constraints and allowing atomic positions to freely refine in the $Pmnb$ cell. Due to the large number of parameters required to describe the structure and the relative

low intensity of the pattern in the region $2\theta > 6$ °, atomic displacements parameters of all Se sites were constrained to be equal to give sensible values. These values are marked with an asterisk (*) in Table 3.4 on page 130.

3.4.2 Powder Neutron Diffraction

PND experiments were performed in order to locate the light atoms; Li, N and H. The Rietveld refinement against room temperature data from Echidna (ACNS) was consistent with the *Pmnb* model generated from the PXRD data given in Table 3.4 on page 130. Two interlayer scattering centres were identified at (0.25, 0.516(1), 0.683(3)) and (0.25, 0.034(3), 0.662(2)) using TOPAS-generated Fourier maps. Both scattering centres visually appeared to have similar scattering amplitudes. Given the fairly low visual resolution of the Fourier map, this observation may be due to the superimposition of the neutron scattering of both N and H atoms, which lie approximately 1 Å from one another. This collectively would give a scattering length of −1.86 fm for NH_3 (N: 9.36 fm, H: −3.74 fm) which is similar to Li (−1.90 fm). Two models, each with a different moiety solely occupying the interlayer sites, were produced and allowed to refine against the data. Only one arrangement resulted in a physically sensible structure. In addition, inspection of the two sites showed that one had a clear co-ordination environment to 6 six surrounding Se atoms at a distance of approximately 3.7 Å. Given that lithium-ammonia intercalates of FeSe[38] and Bi_2Se_3[39] report H–Se and N–H distances of approximately 2.7 Å and 1 Å respectively, this site satisfied the co-ordination requirements of NHx (x = 2, 3).

H sites were then added at several different positions surrounding N and allowed to refine. Initially the H positions were allowed to freely refine, however the addition of a soft constraint to give an approximate N–H bond length of 1 Å was found to result in a more structurally sensible model. The occupancies of Li, N and H (averaged over the three sites) refined to 1.08(9), 1.09(9) and 0.55(4) respectively.

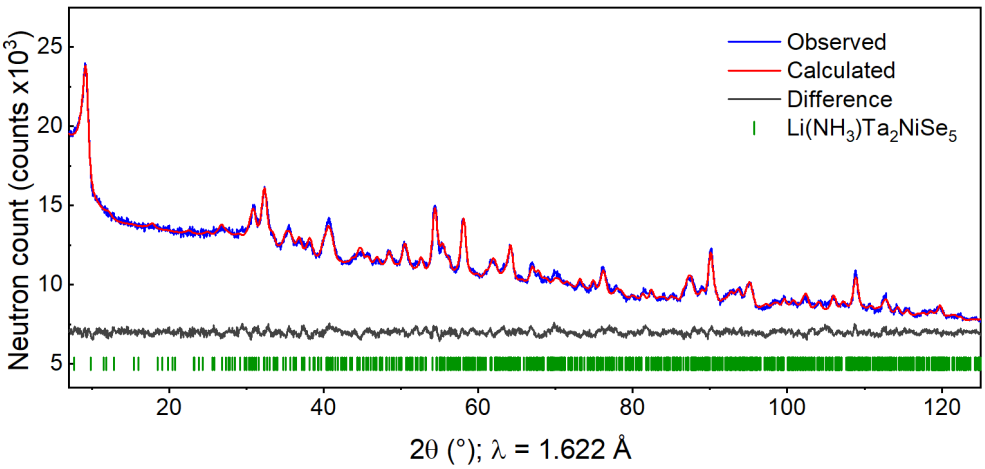

Figure 3.21: Rietveld fit against PND data collected for $Li(NH_3)Ta_2NiSe_5$ (*Pmnb*) using the Echidna instrument at ACNS. R_{wp} = 1.53 %.

An alternative model in which Li and NH_3 moieties share a crystallographic site to mimic disorder across the two sites was refined against the PND pattern. Unlike the Li-ammonia intercalates of Bi_2Se_3,[39] where either moiety could occupy one of two geometrically identical sites within each layer, we were unable to refine Li or H to chemically sensible positions using this model. This supports our observation that the two sites have different co-ordination geometries which favour different moieties. The final structural model is shown in Figure 3.22, with refinement parameters given in Table 3.4.

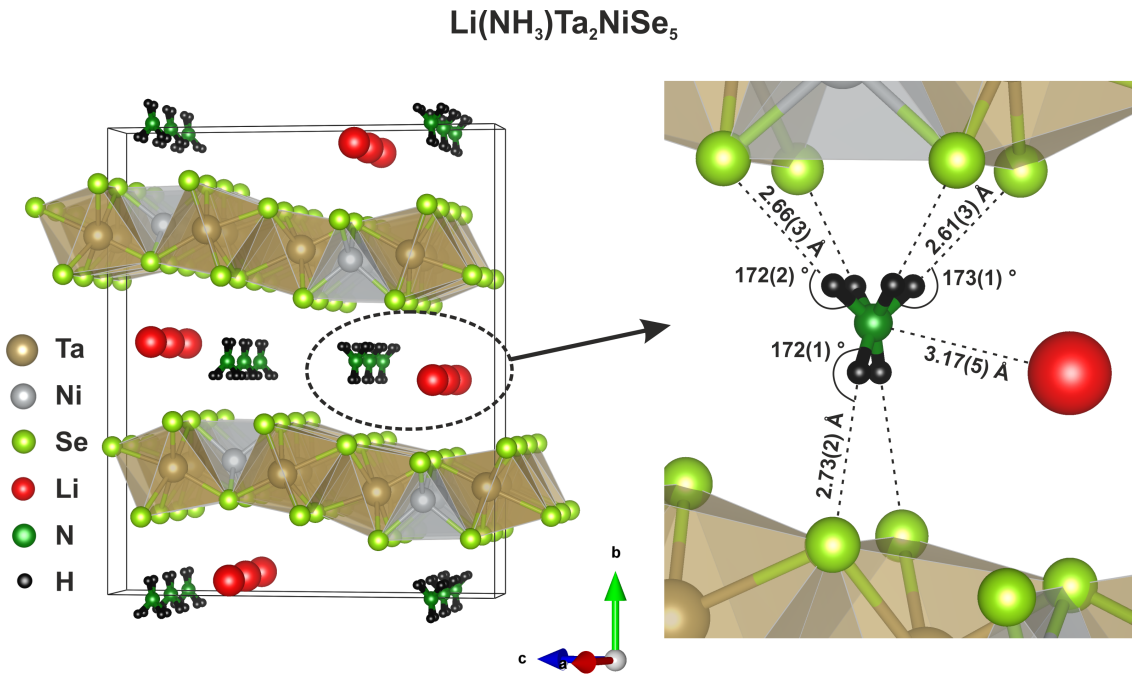

Figure 3.22: Structural model of $Li(NH_3)Ta_2NiSe_5$.

Independent refinement of Li, N and H positions resulted in a Li–N distance of 3.17(5) Å and an average N–H bond length of 1.04(8) Å. The H–Se hydrogen bonds are found to range from 2.61(3) – 2.73(2) Å and the average N–H–Se angle is 172(2) °. All bond distances/angles are consistent the lithium-ammonia intercalates of FeSe[38] and Bi_2Se_3,[39] the latter of which reports weak H–Se bonds of approximately 2.8 Å and a near linear N–H–Se angle. The N–Li distance was found to be 3.17(5) Å, which is significantly longer than the Li–N bond length in crystalline $LiNH_2$ of 2.35 Å[40] suggesting there is little bonding between the two species; Li^+ and NH_3.

Combustion analysis gives the N:H ratio as 2.62(7), which indicates a mixture of ammonia and amide species are present. Refinement of the model against the PND pattern gives average refined occupancy of the H sites as 0.55(4), and 6 H positions per N are generated in the model. This indicates NH_3 is the majority species.

The combustion analysis can be used in conjunction to the ICP-MS result described earlier, by assuming the remaining mass of the sample not attributed to N or H in the combustion analysis is made up of Li, Ta, Ni and Se in the ratio 1:2:1:5. Combining these results gives an overall stoichiometry of $Li_{1.1}(NH_{2.62})Ta_2NiSe_5$. Since the PND refinement gives a stoichiometry of $Li_{1.1}(NH_{3.3})TaNiSe_5$, this phase has been assigned as $Li(NH_3)Ta_2NiSe_5$ for simplicity.

Table 3.4: Refinement parameters from PXRD data of $Li(NH_3)Ta_2NiSe_5$, parameters from PND data are given in parentheses. *, •, † or ‡ indicate parameters constrained to refine to the same value.

$Li(NH_3)Ta_2NiSe_5$ RMM = 838.35 g mol^{-1}, $Z = 4$						
Diffractometer			I11(PSD) (Echidna (ACNS))			
Wavelength (Å)			0.82445(2) (1.622)			
Temperature (K)			300			
Space group			*Pmnb* (62)			
a (Å)			3.51753(5) (3.5146(3))			
b (Å)			18.7828(7) (18.799(4))			
c (Å)			15.7520(3) (15.712(1))			
V (Å^3)			1040.72(5) (1038.2(3))			
Atom	Site	x	y	z	Occ	U_{iso} (Å^2)
Ta1	4c	0.25	0.2297(4) (0.235(2))	0.0158(3) (0.024(1))	1	0.0097(18) (0.026(5))
Ta2	4c	0.25	0.2219(3) (0.224(2))	0.2957(2) (0.293(1))	1	0.0046(16) (0.019(4))
Ni	4c	0.25	0.2795(6) (0.289(1))	0.6604(9) (0.658(1))	1	0.0052(31) (0.044(4))
Se1	4c	0.25	0.8550(6) (0.868(1))	0.9593(7) (0.9606(7))	1	0.0041(13)* (0.004(1))†
Se2	4c	0.25	0.8682(7) (0.874(1))	0.7319(6) (0.7293(7))	1	0.0041(13)* (0.004(1))†
Se3	4c	0.25	0.1803(5) (0.1759(1))	0.8555(7) (0.8514(8))	1	0.0041(13)* (0.004(1))†
Se4	4c	0.25	0.1871(6) (0.180(1))	0.4544(6) (0.4496(7))	1	0.0041(13)* (0.004(1))†
Se5	4c	0.25	0.3018(5) (0.291(1))	0.1578(7) (0.1496(8))	1	0.0041(13)* (0.004(1))†
Li	(4c)	(0.25)	(0.516(1))	(0.683(3))	1.08(9)	(0.049(31))
N	(4c)	(0.25)	(0.034(3))	(0.662(2))	1.09(9)	(0.054(13))
H1	(8d)	(0.64(1))•	(0.533(5))	(0.641(2))	(0.52(3))	(0.064(10))‡
H2	(8d)	(0.64(1))•	(0.482(5))	(0.682(5))	(0.42(3))	(0.064(10))‡
H3	(8d)	(0.64(1))•	(0.482(5))	(0.612(7))	(0.72(4))	(0.064(10))‡

Whilst both data sets that describe the bond lengths in $Li(NH_3)Ta_2NiSe_5$ (Table 3.5) are in relatively good agreement with one another, there are some subtle changes between when compared to Ta_2NiSe_5. The same skew of Ni towards the Ta2 site, as described in detail for $LiTa_2NiSe_5$, is observed in the PXRD data and not in the PND data. There is some lengthening of Ta–Se bond lengths compared to Ta_2NiSe_5 in both data sets which reflects the partial reduction of Ta upon intercalation. Some bonds show a greater increase than others, namely Ta1–Se1, Ta1–Se5 and Ta2–Se3. This distortion away from perfect octahedral symmetry may be a consequence of the co-ordination requirements of the intercalated NH_3 molecules, which now form H bonds to the Se atoms which comprise these Ta-centred octahedra.

Table 3.5: Refined bond distances of Ta_2NiSe_5 and $Li(NH_3)Ta_2NiSe_5$ from PXRD and PND determined in this work. Atomic labels of Se atoms for Ta_2NiSe_5 data in space group $C2/c$ are given in square brackets, for comparison to $Li(NH_3)Ta_2NiSe_5$ in space group *Pmnb*.

Distances	Ta_2NiSe_5	$Li(NH_3)Ta_2NiSe_5$	
(Å)	PXRD	PXRD	PND
Ta1-Ta1	3.496(1)	3.5175(1)	3.5146(3)
Ta1-Ta2	3.903(1)	3.994(6)	4.07(3)
Ta1-Ni	2.804(1)	2.88(1)	2.79(3)
Ta2-Ni	2.813(1)	2.78(1)	2.80(2)
Ta1-Se1	2.523(1) [Se1]	2.50(1)	2.74(4)
Ta1-Se3	2.678(1) [Se2]	2.70(1)	2.88(3)
Ta1-Se4	2.588(1) [Se2]	2.55(1)	2.51(3)
Ta1-Se5	2.570(1) [Se3]	2.62(1)	2.48(3)
Ta2-Se2	2.581(1) [Se1]	2.48(1)	2.44(3)
Ta2-Se3	2.661(1) [Se2]	2.71(1)	2.82(3)
Ta2-Se4	2.678(1) [Se2]	2.58(1)	2.58(3)
Ta2-Se5	2.570(1) [Se3]	2.64(1)	2.63(3)
Ni-Se1	2.339(2) [Se1]	2.36(2)	2.38(3)
Ni-Se2	2.339(2) [Se1]	2.38(2)	2.50(3)
Ni-Se5	2.381(2) [Se3]	2.33(1)	2.40(2)

3.4.3 NMR Spectroscopy

NMR experiments were performed to probe the local environments the light atoms, H, Li and N, of $Li(NH_3)Ta_2NiSe_5$. Spectra are shown in Figure 3.23.

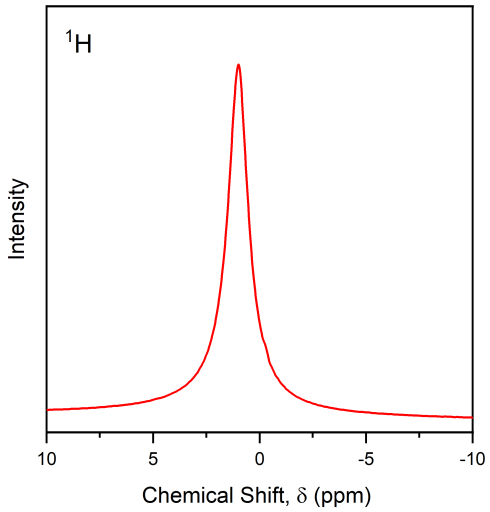

(a) Magic angle spinning ^{1}H

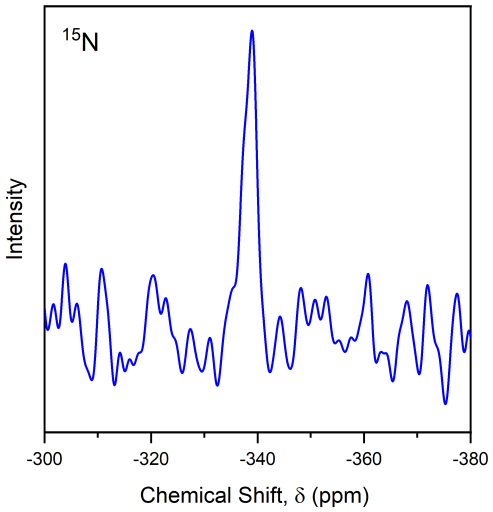

(b) Static ^{15}N

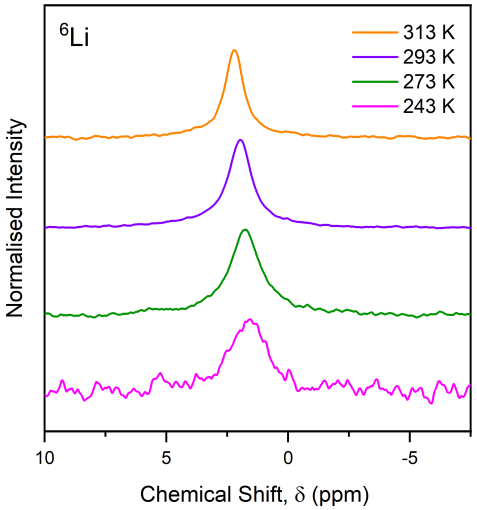

(c) Variable temperature MAS ^{6}Li

Figure 3.23: NMR spectra of $Li(NH_3)Ta_2NiSe_5$.

The magic angle spinning (MAS) ^{1}H and static ^{15}N NMR spectra (Figures 3.23a and 3.23b) both show single proton and N environments, on the NMR timescale. This agrees with our analysis of PND data, which reveals a single NH_3 site. Since the NH_3 molecules are tumbling rapidly on the NMR timescale, the three static H sites in the structural model appear as a single resonance.

Variable temperature MAS ^{6}Li NMR measurements (Figure 3.23c) indicate a single Li environment at 298 K, observable on the NMR timescale, which agrees with our previous Li analysis. As with the $LiTa_2NiSe_5$ intercalate, low temperature measurements show a subtle peak shift to lower δ, indicative of a temperature dependant Knight shift which is proportional to the density of states at the Fermi level. Compared to $LiTa_2NiSe_5$, which has an approximate Knight shift of 2 ppm between 243 – 313 K, $Li(NH_3)Ta_2NiSe_5$ has an approximate shift of 0.5 ppm over the same temperature range. This could be due to the structural differences between $Li(NH_3)Ta_2NiSe_5$ and $LiTa_2NiSe_5$ resulting in an altered band structure than that computed for $LiTa_2NiSe_5$, and so the density of states at the Fermi level may differ.

Unlike $LiTa_2NiSe_5$, no additional resonances appear at high temperatures in the ^{6}Li NMR spectra of $Li(NH_3)Ta_2NiSe_5$, and no spinning problems were encountered. This indicates no electronic transitions occur across the temperature range 243 – 313 K, and could be due to differences in electronics or band structure as described above.

3.4.4 Magnetometry

The ambient temperature magnetisation isotherm measured using SQUID magnetometry reveals that the lithium-ammonia intercalate is a bulk diamagnet, which shows a small positive magnetisation from 0 – 1 T. Again, this was attributed to the presence of elemental Ni in trace amounts.

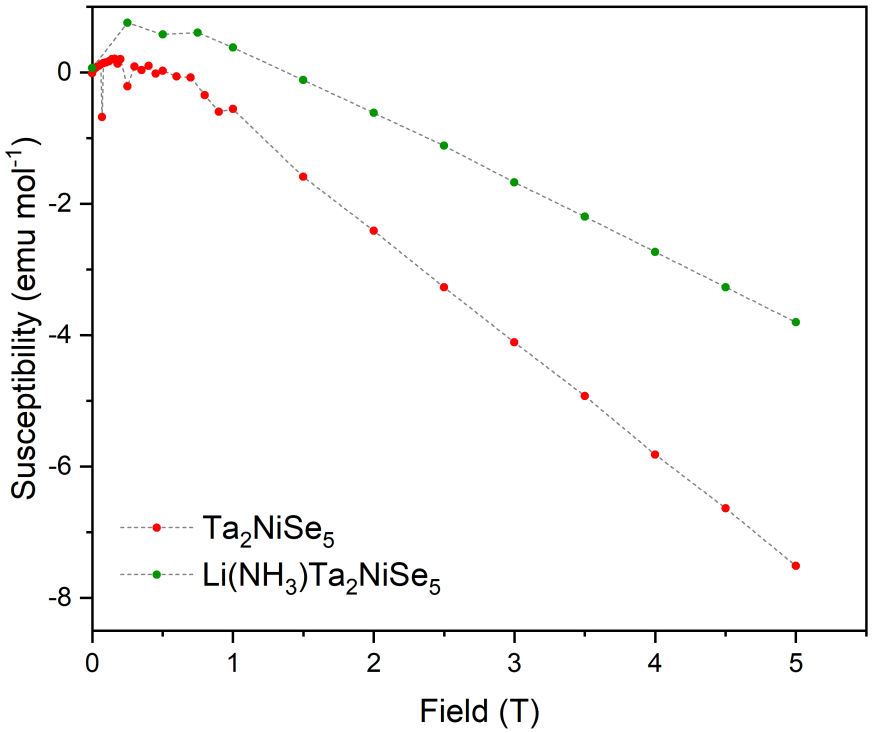

Figure 3.24: Magnetisation vs field for Ta_2NiSe_5 and $Li(NH_3)Ta_2NiSe_5$ at 300 K.

Figure 3.24 shows a 37 % reduction in the diamagnetic susceptibility, from $-1.695(7)$ x10^{-4} emu mol^{-1} in Ta_2NiSe_5 to $-1.071(2)$ x10^{-4} emu mol^{-1} in $Li(NH_3)Ta_2NiSe_5$, upon intercalation. The core diamagnetic contribution calculated from standard tables[35] is -2.99 x10^{-4} emu mol^{-1} for $Li(NH_3)Ta_2NiSe_5$. However, the experimental susceptibility is approximately one third of this value. As discussed previously, we

hypothesise some temperature independent paramagnetism is present in Ta_2NiSe_5, and the lithium-ammonia intercalate is a Pauli paramagnet with a temperature independent susceptibility enhanced by the injection of electrons from the intercalated Li to increase the density of states at the Fermi Level. Comparison to other intercalates of Ta_2NiSe_5 will be discussed later in the chapter.

3.5 Potassium Intercalated Ta_2NiSe_5

Potassium intercalates were synthesised by adding Ta_2NiSe_5 powder and an amount of K metal (Sigma Aldrich; 99 %) to give the stoichiometry KTa_2NiSe_5, along with a magnetic stirrer bar, to a Schlenk tube under an Ar atmosphere and sealed. This was then attached to a Schlenk line along with a cylinder of ammonia (BOC; 99.98 %). The Schlenk tube was placed in a bath of isopropanol and dry ice, and all glassware/tubing between the sample and the ammonia cylinder was evacuated. Approximately 10 cm^3 of NH_3 was then condensed over the reagents. The suspension was left to stir until all the ammonia had evaporated via the mercury manometers contained in a fume hood. The resulting grey solid was then dried under dynamic vacuum for 20 minutes and stored in an Ar filled glovebox for later use.

3.5.1 Powder X-ray Diffraction

The PXRD patterns of the potassium intercalated phase had visual similarities to that of the parent compound Ta_2NiSe_5, with a similar change in intensity profile as described for $Li(NH_3)Ta_2NiSe_5$, shown in Figure 3.25. The estimated crystallite size was 91(4) nm calculated using the Scherrer equation, which is comparable to the other intercalates discussed in this chapter. As with the previously discussed intercalates of Ta_2NiSe_5, the pattern could be well indexed to an orthorhombic unit cell, $a = 3.592$ Å, $b = 16.053$ Å, $c = 15.876$ Å, in space group *Pmnb*. This gives an increased unit cell volume of 31 % and an increase of 1.610 Å per interlayer spacing, compared to Ta_2NiSe_5.

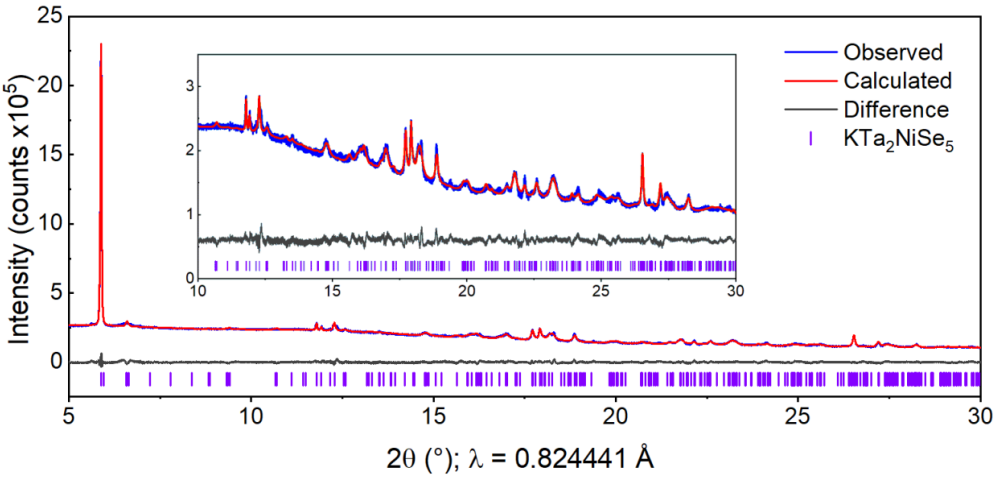

Figure 3.25: Rietveld fit of the PXRD pattern of KTa_2NiSe_5 (*Pmnb*) collected using the PSD detector on the I11 beamline. $R_{wp} = 2.74$ %.

Again, the rigid body approach to the structure solution was adopted as described for $Li(NH_3)Ta_2NiSe_5$ on page 123. The resulting displacement of the two layers relative to their positions in the parent structure refined to (0.5, 0, −0.1703(7)).

The final model of the Ta–Ni–Se layers was thus produced by lifting the rigid body constraints and allowing atomic positions to freely refine in the *Pmnb* cell.

Given the similarities to the previously discussed intercalates of Ta_2NiSe_5, K was added to the model at approximately (0.25, 0.5, 0.3), which coincided with a positive scattering centre in the TOPAS-generated Fourier map. This position was allowed to freely refine and gave an occupancy of 1.05(6), which is consistent with the reaction stoichiometry. Due to the large number of parameters required to describe the structure and the relative low intensity of the pattern in the region $2\theta > 7$ °, atomic displacement parameters of all Se sites were constrained to be equal to give sensible values. The Ni position was also fixed during the refinement to prevent a chemically unrealistic position in the unit cell being returned. This can be justified since Ni only makes a relatively weak contribution to the scattering compared with Ta and Se which are more abundant and are better scatterers, and the low intensity of the data. The final structural model is shown in Figure 3.26.

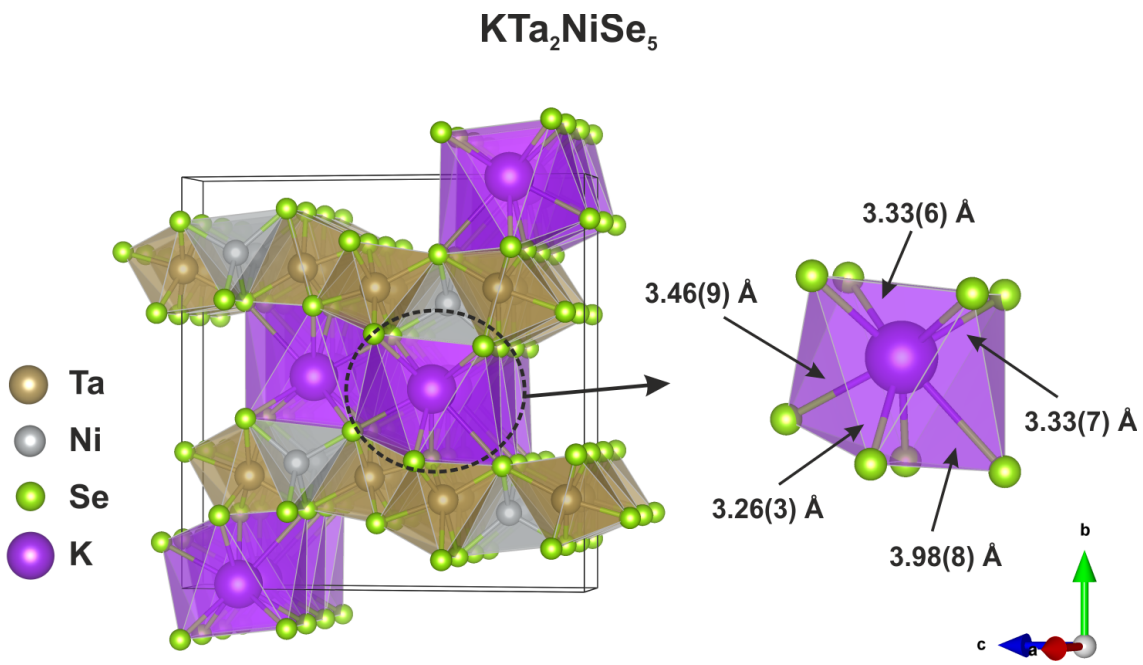

Figure 3.26: Structural model of KTa_2NiSe_5 from refinement of PXRD data.

The general structure of the Ta–Ni–Se layers is maintained during the intercalation of potassium to form KTa_2NiSe_5. Potassium is found to occupy 8 co-ordinate bi-capped trigonal prism sites with an average K-Se bond length of 3.41(3) Å. This is consistent with K-Se bond length values reported in the literature, which range from 3.33 Å for the tetrahedral environment in K_2Se[30] to 3.42 – 3.53 Å for the 8 co-ordinate K sites in $KFeSe_2$.[41]

There is one long K–Se bond which has been included in the formal co-ordination sphere with a bond distance of 3.98(8) Å, as reports of long K–Se bond lengths exist in the literature, especially for more unusual co-ordination geometries. For example, bonds of up to 3.95 Å have been reported for $K_3(FeSe_2)_2$.[42] The co-ordination environment of K is detailed in Figure 3.26.

Table 3.6: Refinement parameters from the Rietveld fit against PXRD data of KTa_2NiSe_5. * indicates fixed parameters. † denotes values that were constrained to be equal.

KTa_2NiSe_5 RMM = 854.49 g mol^{-1}, Z = 4						
Diffractometer				I11(PSD)		
Wavelength (Å)				0.824441		
Temperature (K)				300		
Space group				*Pmnb* (62)		
a (Å)				3.5928(1)		
b (Å)				16.0497(1)		
c (Å)				15.8774(8)		
V (Å^3)				915.55(7)		
Atom	Site	x	y	z	Occ	U_{iso} (Å^2)
Ta1	4c	0.25	0.2207(4)	0.0193(4)	1	0.0170(9)
Ta2	4c	0.25	0.2027(4)	0.3204(5)	1	0.0127(12)
Ni	4c	0.25	0.3099*	0.6750*	1	0.079(8)
Se1	4c	0.25	0.8971(9)	0.9521(10)	1	0.0112(12)†
Se2	4c	0.25	0.9199(10)	0.7101(9)	1	0.0112(12)†
Se3	4c	0.25	0.1790(8)	0.8628(9)	1	0.0112(12)†
Se4	4c	0.25	0.1620(9)	0.4767(10)	1	0.0112(12)†
Se5	4c	0.25	0.2957(12)	0.1699(15)	1	0.0112(12)†
K	4c	0.25	0.488(2)	0.331(8)	1.05(6)	0.0863(18)

Table 3.7: Refined bond distances of Ta_2NiSe_5 and KTa_2NiSe_5 obtained by refinement of PXRD data. Atomic labels of Se atoms for Ta_2NiSe_5 data in space group $C2/c$ are given in square brackets, for comparison to $LiTa_2NiSe_5$ in space group *Pmnb*.

Distance (Å)	Ta_2NiSe_5	KTa_2NiSe_5
Ta1-Ta1	3.496(1)	3.5928(1)
Ta1-Ta2	3.903(1)	3.8370(1)
Ta1-Ni	2.804(1)	3.0954(1)
Ta2-Ni	2.813(1)	2.9327(1)
Ta1-Se1	2.523(1) [Se1]	2.6473(2)
Ta1-Se3	2.678(1) [Se2]	2.5739(1)
Ta1-Se4	2.588(1) [Se2]	2.6893(1)
Ta1-Se5	2.570(1) [Se3]	2.6783(1)
Ta2-Se2	2.581(1) [Se1]	2.7091(2)
Ta2-Se3	2.661(1) [Se2]	2.6994(1)
Ta2-Se4	2.678(1) [Se2]	2.5668(2)
Ta2-Se5	2.570(1) [Se3]	2.8178(1)
Ni-Se1	2.339(2) [Se1]	2.4559(1)
Ni-Se2	2.339(2) [Se1]	2.5400(1)
Ni-Se5	2.381(2) [Se3]	2.4719(1)

Inspection of the bond lengths of KTa_2NiSe_5 relative to Ta_2NiSe_5 in Table 3.7, shows elongation of both Ta–Se and Ni–Se bonds, indicating the partial reduction of Ta and of Ni, which is consistent with our previous analysis. Some anomalies, namely the contraction of Ta1–Se3 and Ta2–Se5, have been attributed to the distortion of the $TaSe_6$ octahedra driven by the co-ordination requirements of K which is bonded to the Se atoms of the adjacent layers.

3.5.2 Magnetometry

The ambient temperature magnetisation isotherm measured using SQUID magnetometry reveals that the potassium intercalate is a bulk diamagnet, which shows a small positive magnetisation from 0 – 1 T. Again, this was attributed to the presence of elemental Ni in trace amounts.

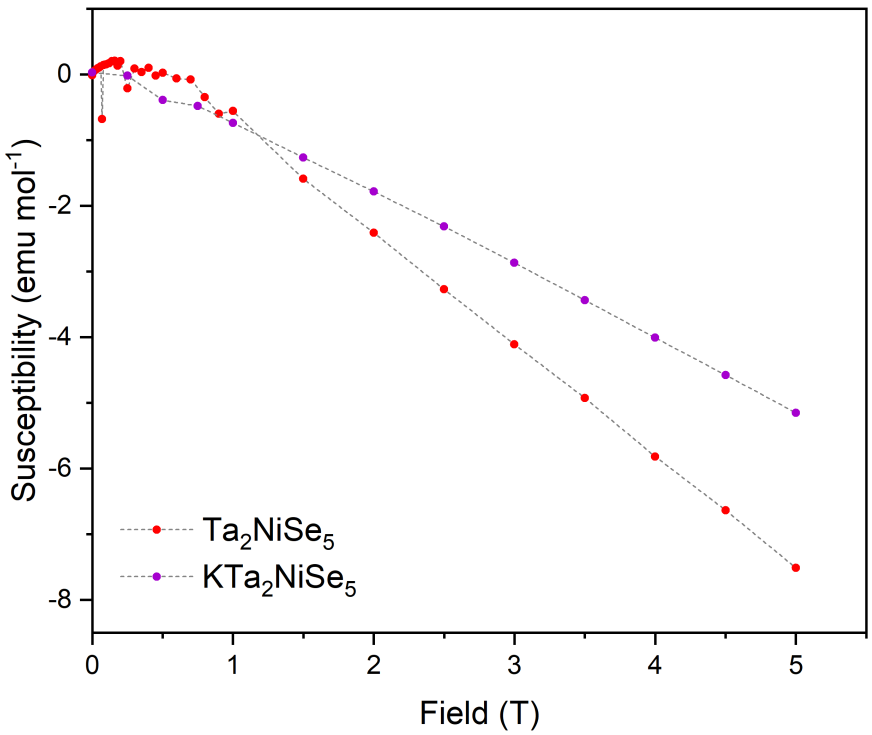

Figure 3.27: Magnetisation vs field for Ta_2NiSe_5 and KTa_2NiSe_5 at 300 K.

Figure 3.27 shows a 34 % reduction in the diamagnetic susceptibility, from $-1.695(7)$ x10^{-4} emu mol^{-1} in Ta_2NiSe_5 to $-1.126(6)$ x10^{-4} emu mol^{-1} in KTa_2NiSe_5, upon intercalation. The core diamagnetic contribution calculated from standard tables[35] is -2.95 x10^{-4} emu mol^{-1} for KTa_2NiSe_5. As previously discussed, the experimental susceptibility is approximately one third of this value, which has been attributed

to enhanced temperature independent Pauli paramagnetism from the addition of electrons and an increased density of states at the Fermi level.

3.6 Discussion

Structurally, all three intercalated compounds reported here have similarities and some differences. Table 3.8 compares the lattice parameters of Ta_2NiSe_5 and its intercalates. Whilst a and c are fairly consistent across the series, the b lattice parameter increases with the size of the intercalated species, to increase the size of the interlayer spacing, given by ΔW. Perhaps the most significant change is the rearrangement of the Ta–Ni–Se layers, which is common to all intercalates, and creates a larger cavity for the intercalated species to occupy.

Table 3.8: Refined lattice parameters at 300 K and relative offset of alternating layers along the c axis of Ta_2NiSe_5 and its intercalates reported in this chapter. ΔW is the change in interlayer spacing relative to Ta_2NiSe_5.

	Ta_2NiSe_5	$LiTa_2NiSe_5$	KTa_2NiSe_5	$Li(NH_3)Ta_2NiSe_5$
Space group	$C2/c$		$Pmnb$	
a (Å)	3.4945(1)	3.5025(1)	3.5928(1)	3.5175(1)
b (Å)	12.8294(1)	13.4053(4)	16.0497(1)	18.7828(7)
c (Å)	15.6431(3)	15.7396(2)	15.8774(8)	15.7520(3)
β (°)	90.53(1)	90	90	90
V (Å^3)	701.29(1)	739.00(3)	915.55(7)	1040.72(5)
Layer offset	0	0.1372(3)	0.1703(7)	0.1885(3)
ΔW (Å)	0	0.2880	1.6102	2.9767

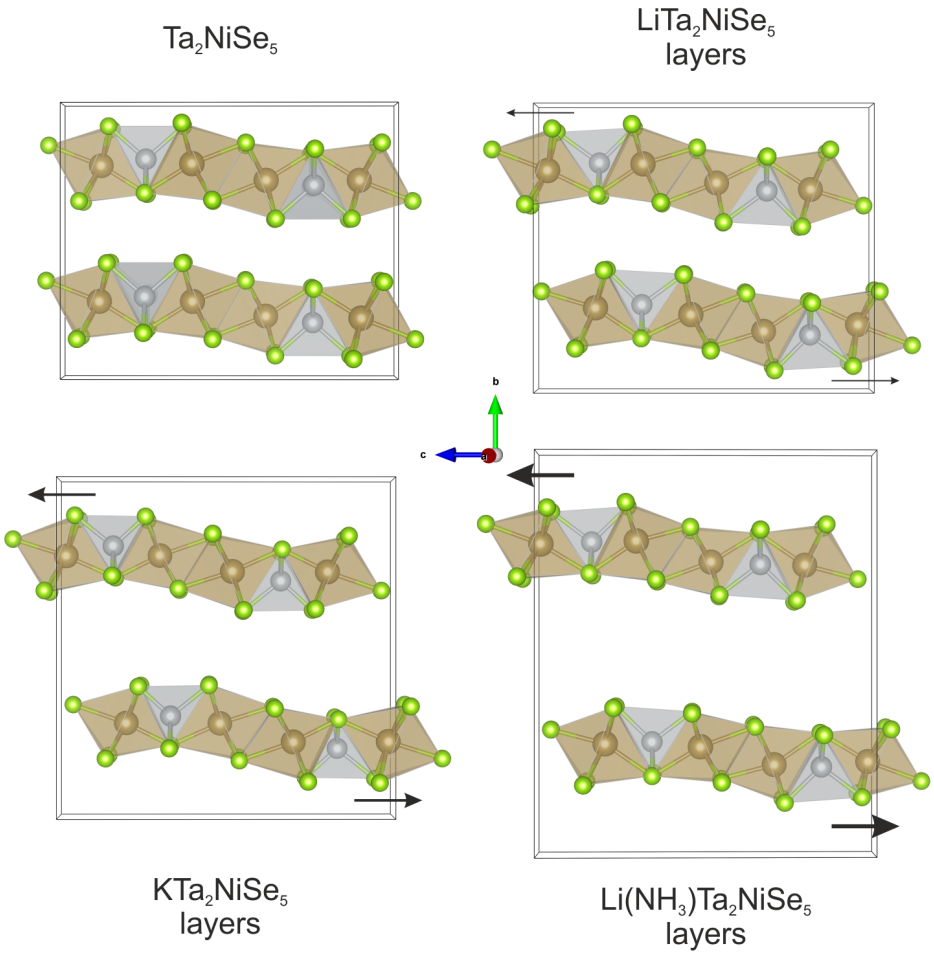

Figure 3.28: Structure of the Ta–Ni–Se layers of Ta_2NiSe_5 and the intercalates reported here. The weight of the black arrows represents the degree of layer offset relative to Ta_2NiSe_5.

The relative offset of alternating layers also controls the size of this cavity, so is also correlated with the size of the intercalant. Figure 3.28 compares the structural changes of the corrugated Ta–Ni–Se layers of the parent phase and each intercalate.

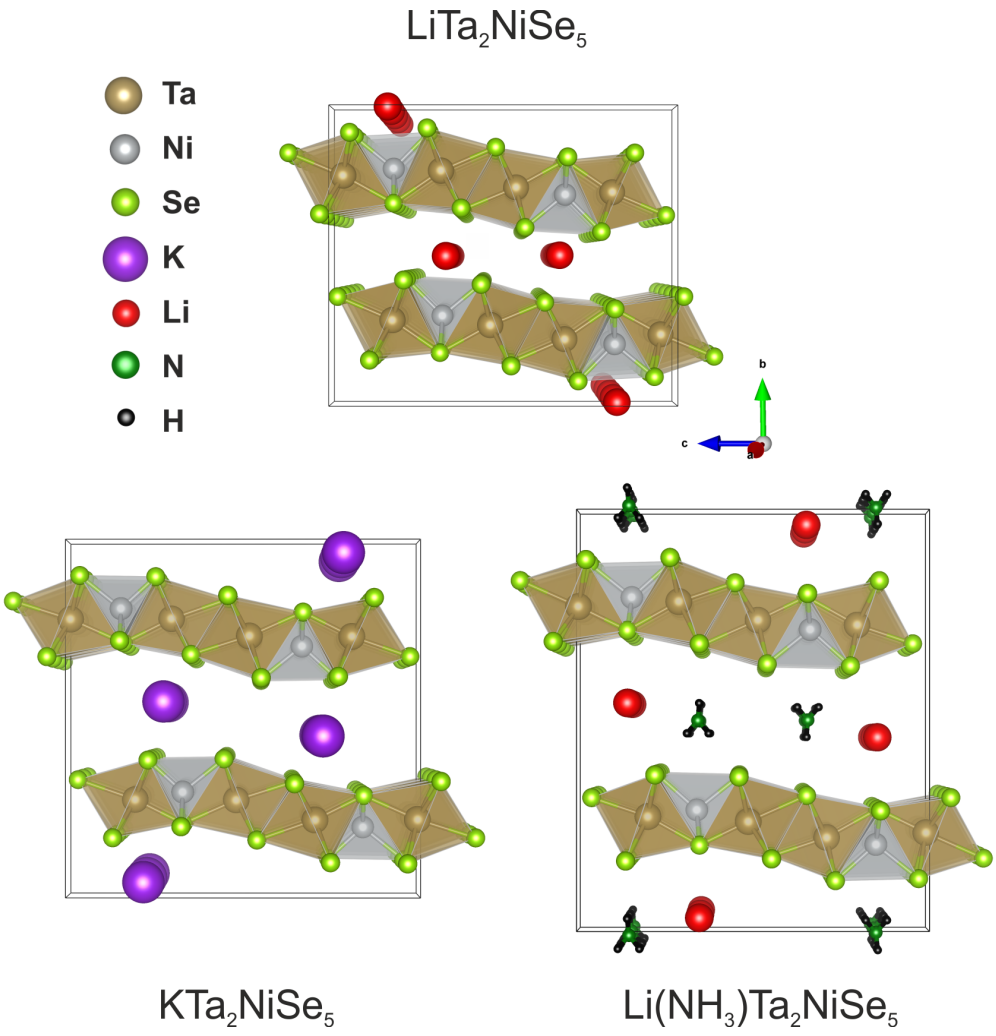

Figure 3.29: Structural models of the intercalates of Ta_2NiSe_5.

Figure 3.29 shows the structural models of all three intercalates of Ta_2NiSe_5. The guest species all occupy similar regions of the unit cell. In the case of $Li(NH_3)Ta_2NiSe_5$, the NH_3 moiety solely occupies this region as it is both larger than the co-intercalated Li ion, and the co-ordination requirements of the approximately linear N–H–Se bonds are satisfied, whilst maintaining a chemically sensible structure of the NH_3 molecule itself. Although potassium in KTa_2NiSe_5 is shown to occupy an 8 co-ordinate site which includes two long K–Se bonds, the formal co-ordination number depends on where the boundary of the co-ordination sphere is defined.

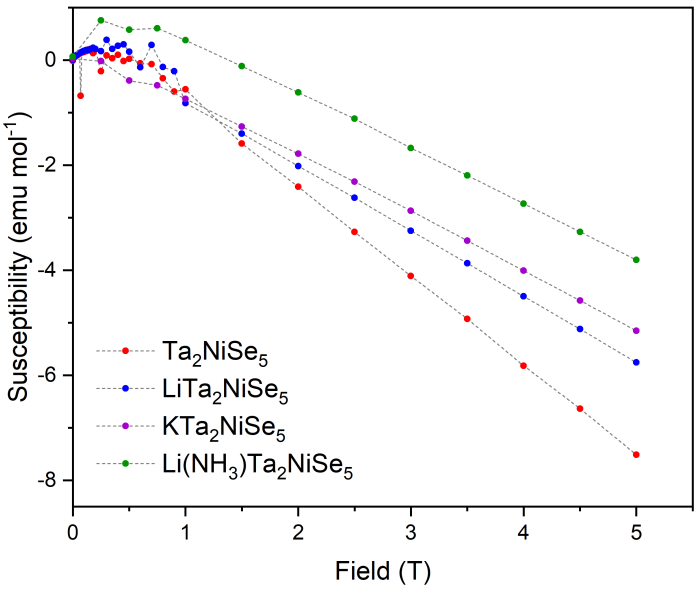

Figure 3.30: Magnetisation vs field for Ta_2NiSe_5, $LiTa_2NiSe_5$, KTa_2NiSe_5 and $Li(NH_3)Ta_2NiSe_5$ at 300 K.

The three intercalated phases also show comparable magnetic properties. Figure 3.30 shows the ambient temperature magnetisation isotherms of Ta_2NiSe_5 and its intercalates. Collectively, the magnetic susceptibilities of all the intercalated phases show a similar reduction in diamagnetic susceptibility relative to Ta_2NiSe_5, resulting from increased density of states at the Fermi level. Extracted magnetic susceptibility values are given in Table 3.9. Zero-field-cooled measurements of all intercalates using a field of 50 Oe revealed no superconducting transition down to 2 K.

Table 3.9: Magnetic susceptibilities of Ta_2NiSe_5, $LiTa_2NiSe_5$, KTa_2NiSe_5 and $Li(NH_3)Ta_2NiSe_5$ at 300 K.

Compound	Magnetic susceptibility (emu mol^{-1})
Ta_2NiSe_5	–1.695(7) x10^{-4}
$LiTa_2NiSe_5$	–1.254(4) x10^{-4}
KTa_2NiSe_5	–1.126(6) x10^{-4}
$Li(NH_3)Ta_2NiSe_5$	–1.071(2) x10^{-4}

3.7 Summary and Conclusions

Here we have presented the synthesis and characterisation of three intercalates of the excitonic insulator candidate Ta_2NiSe_5. PXRD shows that the three phases are closely structurally related, all crystallising in orthorhombic space group *Pmnb*. All phases exhibit rearrangement of alternating Ta_2NiSe_5 layers by $a/2$, and a varying shift along c which correlates with the size of the intercalated species. No evidence of the monoclinic distortion can be found down to 100 K. PND has been used to locate the positions of light atoms in $LiTa_2NiSe_5$ and $Li(NH_3)Ta_2NiSe_5$ and NMR experiments confirm these analyses. Computational studies have further confirmed the Li position in $LiTa_2NiSe_5$, and DOS computations of $LiTa_2NiSe_5$ have shown this compound to be metallic, which agrees with our preliminary ambient temperature resistivity measurements.

All three intercalated species, Li^+, K^+ and NH_3, occupy similar sites in the same region of the unit cell. The degree of layer offset, as well as the unit cell expansion along b, controls the size of this interstitial site to size match the resident ion/molecule.

All intercalated phases retain their bulk diamagnetism, but show increased Pauli paramagnetism through increasing the density of states at the Fermi level of these metallic systems by injecting electrons. This work could be extended by attempting to intercalate larger ions or small molecules, such as Cs or ethylenediamine, to assess the limit of layer rearrangement ability of Ta_2NiSe_5. The Li/NH_3 intercalate

of Ta_2NiSe_5 could be the subject of *in situ* PXRD experiments to see if there is evidence for an ammonia-rich phase formed when the sample is in contact with liquid ammonia or is under a high partial pressure of NH_3 at low temperatures. This is seen for the Li-ammonia intercalates of FeSe and Bi_2Se_3.[38,39] The reversibility could be further investigated by attempting chemical deintercalation, and experiments to see if the electrochemical intercalation of Li induces the same structural changes could be performed. Intermediate phases $Li_xTa_2NiSe_5$ ($0 < x < 1$) could also be synthesised to control the electronic properties, both chemically and electrochemically.

References

[1] Y. F. Lu, H. Kono, T. I. Larkin, A. W. Rost, T. Takayama, A. V. Boris, B. Keimer, H. Takagi, *Nature Communications* **2017**, *8*, 14408.

[2] K. Okazaki, Y. Ogawa, T. Suzuki, T. Yamamoto, T. Someya, S. Michimae, M. Watanabe, Y. Lu, M. Nohara, H. Takagi, N. Katayama, H. Sawa, M. Fujisawa, T. Kanai, N. Ishii, J. Itatani, T. Mizokawa, S. Shin, *Nature Communications* **2018**, *9*, 4322.

[3] Y. Tomio, K. Honda, T. Ogawa, *Physical Review B* **2006**, *73*, 235108.

[4] S. A. Sunshine, J. A. Ibers, *Inorganic Chemistry* **1985**, *24*, 3611–14.

[5] F. J. DiSalvo, C. H. Chen, R. M. Fleming, J. V. Waszczak, R. G. Dunn, S. A. Sunshine, J. A. Ibers, *Journal of The Less-Common Metals* **1986**, *116*, 51–61.

[6] E. Canadell, M. H. Whangbo, *Inorganic Chemistry* **1987**, *26*, 3974–76.

[7] T. Kaneko, T. Toriyama, T. Konishi, Y. Ohta, *Journal of Physics: Conference Series* **2012**, *400*, 032035.

[8] T. Kaneko, T. Toriyama, T. Konishi, Y. Ohta, *Physical Review B* **2013**, *87*, 35121.

[9] K. Seki, Y. Wakisaka, T. Kaneko, T. Toriyama, T. Konishi, T. Sudayama, N. L. Saini, M. Arita, H. Namatame, M. Taniguchi, N. Katayama, M. Nohara, H. Takagi, T. Mizokawa, Y. Ohta, *Physical Review B - Condensed Matter and Materials Physics* **2014**, *90*, 155116.

[10] Y. Wakisaka, T. Sudayama, K. Takubo, T. Mizokawa, M. Arita, H. Namatame, M. Taniguchi, N. Katayama, M. Nohara, H. Takagi, *Physical Review Letters* **2009**, *103*, 026402.

[11] K. Kim, H. Kim, J. Kim, C. Kwon, J. S. Kim, B. J. Kim, *Nature Communications* **2021**, *12*, 1969.

[12] A. Nakano, K. Sugawara, S. Tamura, N. Katayama, K. Matsubayashi, T. Okada, Y. Uwatoko, K. Munakata, A. Nakao, H. Sagayama, R. Kumai, K. Sugimoto, N. Maejima, A. Machida, T. Watanuki, H. Sawa, *IUCrJ* **2018**, *5*, 158–165.

[13] P. Squattrito, S. Sunshine, J. A. Ibers, *Solid State Ionics* **1986**, *22*, 53–63.

[14] P. Hyde, MChem thesis, University of Oxford, **2019**.

[15] G. Hyett, O. Rutt, Z. Gál, S. Denis, M. A. Hayward, S. J. Clarke, *Journal of the American Chemical Society* **2004**, *126*, 1980–91.

[16] L. Bennett, R. Watson, G. Carter, *Journal of research of the National Bureau of Standards. Section A Physics and chemistry* **1970**, *74A*, 569.

[17] W. D. Knight, *Physical Review* **1949**, *76*, 1259–1260.

[18] G. Kresse, J. Hafner, *Physical Review B* **1993**, *47*, 558.

[19] G. Kresse, J. Furthmüller, *Physical Review B* **1996**, *54*, 11169.

[20] G. Kresse, J. Furthmüller, *Computational Materials Science* **1996**, *6*, 15–50.

[21] P. E. Blöchl, *Physical Review B* **1994**, *50*, 17953.

[22] G. Kresse, D. Joubert, *Physical Review B* **1999**, *59*, 1758.

[23] J. P. Perdew, A. Ruzsinszky, G. I. Csonka, O. A. Vydrov, G. E. Scuseria, L. A. Constantin, X. Zhou, K. Burke, *Physical Review Letters* **2008**, *100*, 136406.

[24] S. Grimme, J. Antony, S. Ehrlich, H. Krieg, *The Journal of Chemical Physics* **2010**, *132*, 154104.

[25] A. M. Ganose, A. J. Jackson, D. O. Scanlon, *Journal of Open Source Software* **2018**, *3*, 717.

[26] S. Kavanagh, GitHub - SMTG-UCL/doped: Collection of Python modules & functions to perform and process solid-state defect calculations, `https://github.com/SMTG-UCL/doped`.

[27] D. Broberg, B. Medasani, N. E. Zimmermann, G. Yu, A. Canning, M. Haranczyk, M. Asta, G. Hautier, *Computer Physics Communications* **2018**, *226*, 165–179.

[28] S. P. Ong, W. D. Richards, A. Jain, G. Hautier, M. Kocher, S. Cholia, D. Gunter, V. L. Chevrier, K. A. Persson, G. Ceder, *Computational Materials Science* **2013**, *68*, 314–319.

[29] A. H. Larsen, J. J. Mortensen, J. Blomqvist, I. E. Castelli, R. Christensen, M. Dułak, J. Friis, M. N. Groves, B. Hammer, C. Hargus, E. D. Hermes, P. C. Jennings, P. B. Jensen, J. Kermode, J. R. Kitchin, E. L. Kolsbjerg, J. Kubal, K. Kaasbjerg, S. Lysgaard, J. Bergmann Maronsson, T. Maxson, T. Olsen, L. Pastewka, A. Peterson, C. Rostgaard, J. Schiøtz, O. Schütt, M. Strange, K. S. Thygesen, T. Vegge, L. Vilhelmsen, M. Walter, Z. Zeng, K. W. Jacobsen, *Journal of Physics: Condensed Matter* **2017**, *29*, 30.

[30] E. Zintl, A. Harder, B. Dauth, *Zeitschrift für Elektrochemie und angewandte physikalische Chemie* **1934**, *40*, 588–593.

[31] J. Kim, C. Wang, T. Hughbanks, *Inorganic Chemistry* **1988**, *37*, 1428–29.

[32] C. J. Pickard, F. Mauri, *Physical Review B* **2001**, *63*, 245101.

[33] C. Bonhomme, C. Gervais, F. Babonneau, C. Coelho, F. Frédé, F. Pourpoint, T. Azaïs, S. E. Ashbrook, J. M. Griffin, J. R. Yates, F. Mauri, C. J. Pickard, *Chemical Reviews* **2012**, *112*, 5733–5779.

[34] M. D'Avezac, N. Marzari, F. Mauri, *Physical Review B* **2007**, *76*, 165122.

[35] G. F. Bain, J. F. Berry, *Journal of Chemical Education* **2008**, *85*, 532.

[36] K. Matsubayashi, H. Okamura, T. Mizokawa, N. Katayama, A. Nakano, H. Sawa, T. Kaneko, T. Toriyama, T. Konishi, Y. Ohta, H. Arima, R. Yamanaka, A. Hisada, T. Okada, Y. Ikemoto, T. Moriwaki, K. Munakata, A. Nakao, M. Nohara, Y. Lu, H. Takagi, Y. Uwatoko, *Journal of the Physical Society of Japan* **2021**, *90*, 074706.

[37] P. A. Hyde, J. Cen, S. J. Cassidy, N. H. Rees, P. Holdship, R. I. Smith, B. Zhu, D. O. Scanlon, S. J. Clarke, *Inorganic Chemistry* **2023**, *62*, 12027–37.

[38] M. Burrard-Lucas, D. G. Free, S. J. Sedlmaier, J. D. Wright, S. J. Cassidy, Y. Hara, A. J. Corkett, T. Lancaster, P. J. Baker, S. J. Blundell, S. J. Clarke, *Nature Materials* **2013**, *12*, 15–19.

[39] M. E. Kamminga, S. J. Cassidy, P. P. Jana, M. Elgaml, N. D. Kelly, S. J. Clarke, *Dalton Transactions* **2021**, *50*, 11376.

[40] R. Juza, K. Opp, *Zeitschrift für anorganische und allgemeine Chemie* **1951**, *266*, 313–24.

[41] W. Bronger, A. Kyas, P. Müller, *Journal of Solid State Chemistry* **1986**, *70*, 262.

[42] W. Bronger, H. S. Genin, P. Müller, *Zeitschrift für anorganische und allgemeine Chemie* **1999**, *625*, 274.

'Half of this stuff was taken from the ark'

- Mahmoud Elgaml

4

Intercalation Chemistry of Ta_2NiSe_7

Contents

4.1 Introduction

Ta_2NiSe_7 is a layered ternary chalcogenide first reported in 1986 by Sunshine *et al.*[1] which undergoes an incommensurate charge density wave (CDW) transition, or the static modulation of conduction electrons,[2] at 52.5 K.[3] Structurally, Ta_2NiSe_7 crystallises in space group $C2/m$ with lattice parameters a = 13.594(3) Å, b = 3.482(1) Å, c = 18.577(4) Å, and β = 108.80(1) °. It can be described as a quasi-1D material, and consists of double rows of 8 co-ordinate $TaSe_8$ bicapped trigonal prisms and double rows of $TaSe_6$ octahedra, linked by 1-D chains of highly distorted $NiSe_6$ octahedra.[1] Adjacent layers are related by the C-centring translation resulting in AB stacking along the a direction. The crystal structure is shown in Figure 4.1. The corrugated structure draws structural likenesses to $FeNb_3Se_{10}$,[4] which also exhibits a CDW at 140 K.[5]

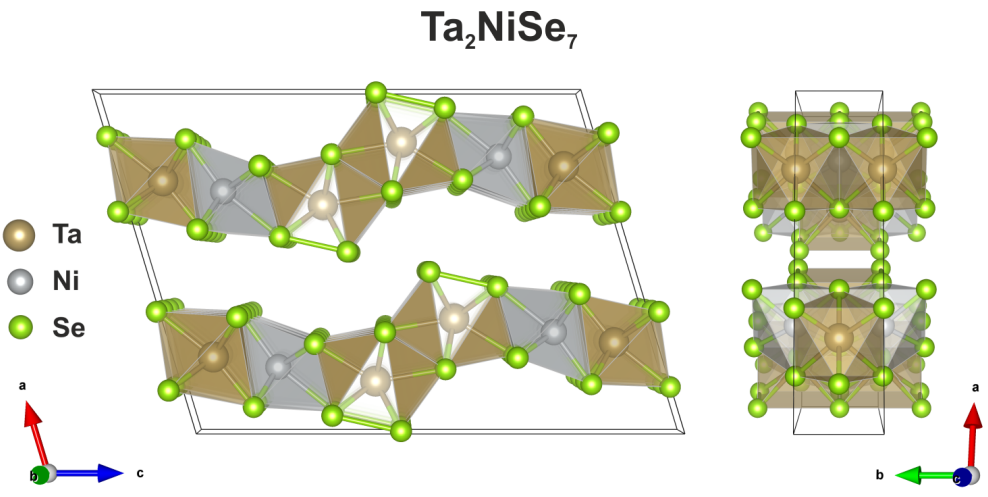

Figure 4.1: Crystal structure of Ta_2NiSe_7.

It is difficult to describe this compound in simple valence terms. Although the formal oxidation states $(Ta^{5+})_2(Ni^{2+})(Se^{2-})_5(Se_2)^{2-}$ would suggest semiconducting properties for Ta_2NiSe_7, resistivity measurements show metallic behaviour.[3] Canadell and Whangbo[6] rationalise that the metallic state originates from the fact that the bottom of the *d*-block band overlaps with the top of the Se *p*-block band, causing some charge transfer from the Se-Se dimer to the neighbouring Ta^{5+} ions in the bicapped trigonal prisms.[1] Although Ta_2NiSe_7 is reported to be a bulk diamagnet, Sunshine *et al.* propose that the Pauli paramagnetism arising from the partially filled band (indicated by the electrical conductivity) is small when compared to the core diamagnetism.[1] This suggests Ni^{2+} is in a low spin state, which is consistent with the highly distorted octahedral co-ordination environment of Ni in which the energy of the $3d_{z^2}$ orbital is lowered, leaving the $3d_{x^2-y^2}$ vacant. This indicates significant covalency between Ni and Se, like in Ta_2NiSe_5 where the Ni $3d$ and Se $4p$ states are well hybridised.

Structural characterisation of the CDW transition at 16 K, reported by Spijkerman *et al.*[7] describes the modulation as a variation of interatomic distances of Se2-Se5 and Ni-Se2, with a modulation wave vector $\mathbf{q}$ = (0, 0.483, 0). They also report that Ta_2NiSe_7 retains its *C*-centring, which contrasts the finding by Dai *et al.* which reports the loss of *C*-centring at low temperature through STM imaging.[8] Unlike in Ta_2NiSe_5, the loss of *C*-centring is not due to a layer rearrangement. The CDW inTa_2NiSe_7 has been found to be highly sensitive to defects[3,9] and can cause CDW domain pinning and jeopardise the formation of long-range structural

changes.[9] Polarised Raman spectroscopy was used in conjunction to angle resolved photoelectron spectroscopy (ARPES) to study the momentum-dependent electron-phonon coupling in this system.[10] The band dispersion has been calculated[10] and the density of states[11] shows some mixing of the Ta *d*-block and Se *p*-block bands as previously reported.[6]

No soft chemical transformations of Ta_2NiSe_7 have been reported to date. Here, the reduced phases $Li_xTa_2NiSe_7$ ($0.4 < x < 1.5$) synthesised by the intercalation of Li both chemically and electrochemically are investigated, and characterised using high resolution PXRD, neutron diffraction, SQUID magnetometry and ^{7}Li NMR spectroscopy.

4.2 Synthesis of Ta_2NiSe_7

Poly-crystalline samples of Ta_2NiSe_7 were synthesised by grinding together tantalum powder (Alfa Aesar 99.97 %), nickel powder (Alfa Aesar 99.9 %) and selenium powder (Alfa Aesar 99.999 %) in stoichiometric amounts using an agate pestle and mortar until homogeneous. The mixture was then sealed inside an evacuated silica tube and heated at 750 °C for 7 days (ramping rate of 5 °C min^{-1}) before being allowed to cool naturally. The resulting powder was reground and pressed into a pellet before reheating to 700 °C for 48 hours and was then left to cool at the natural rate of the furnace. This second step was often required to improve the crystallinity of the samples. The Rietveld refinement against PXRD data can be found in Figure 4.2.

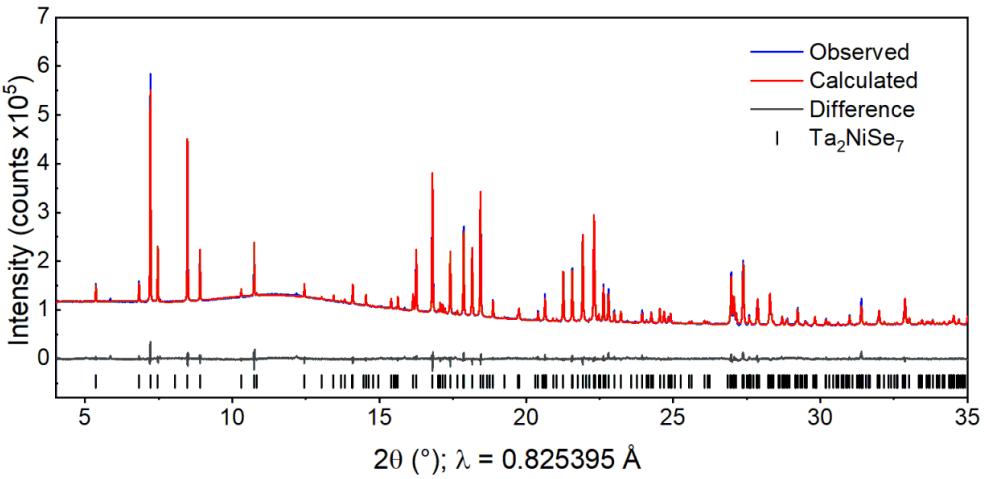

Figure 4.2: Rietveld refinement against PXRD data of Ta_2NiSe_7 ($C2/m$) collected using the PSD on the I11 beamline. R_{wp} = 1.32 %.

4.3 Lithium Intercalated Ta_2NiSe_7

Lithium intercalates were synthesised by adding Ta_2NiSe_7 powder and a magnetic stirrer bar into a Schlenk tube in the glove box. Approximately 20 cm^3 of dry hexane was then added to the vessel using a Schlenk line. Various stoichiometric volumes of n-butyllithium solution (1.6 M in hexanes; Alfa Aesar) to give various target phases $Li_xTa_2NiSe_7$ (x = 0.4 – 1.5) were added using a nitrogen-purged needle and syringe. The suspension was left to stir overnight before filtering off the supernatant whilst attached to a Schlenk line. The solid was then washed by adding fresh dry hexane to the Schlenk tube, stirring for 30 seconds, and removing the solvent by filtration. This procedure was repeated twice. The remaining solid was left to dry under dynamic vacuum for 1 hour, and stored in an Ar-filled glovebox.

4.3.1 Powder X-ray Diffraction

The PXRD patterns of the intercalates of all compositions were visually similar to that of the parent compound Ta_2NiSe_7. All intercalates appeared single phase when measured on laboratory instruments, however high-resolution synchrotron measurements revealed two phases were present for reaction stoichiometries x = 0.5, 1.0. This is shown by the presence of two 200 reflections, shown in Figure 4.3. Pure phases with reaction stoichiometries x = 0.4 and x = 1.5 were denoted as 'Li poor' and 'Li rich' phases respectively. Chemical analysis of the Li and Ni contents using ICP-MS was performed by Trang To, Department of Geography. The resulting compositions were found to be x = 0.36, 0.54, 0.96 and 1.45.

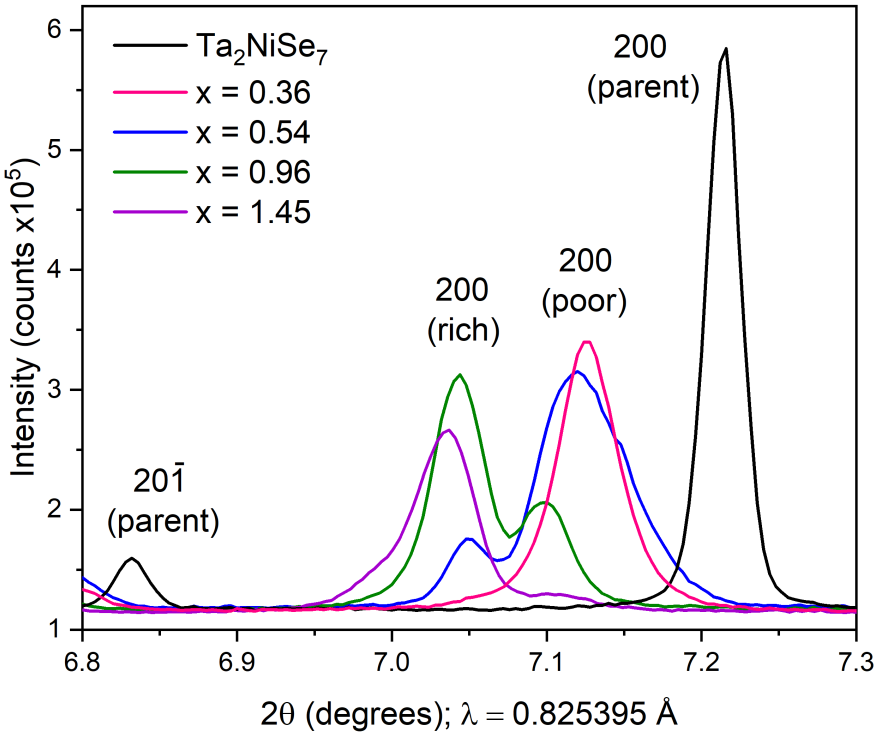

Figure 4.3: PXRD patterns of Ta_2NiSe_7 and lithium intercalates in the region around the 200 reflection, collected at 300 K using the PSD on the I11 beamline.

The patterns of the Li poor and Li rich phases could be well indexed to monoclinic unit cells, $a = 13.964$ Å, $b = 3.488$ Å, $c = 18.808$ Å, $\beta = 107.92$ ° and $a = 14.056$ Å, $b = 3.493$ Å, $c = 19.098$ Å, $\beta = 106.78$ °. Both have very similar shapes to that of Ta_2NiSe_7, but with an increase in unit cell volume of 2.16 % and 5.22 % respectively. Due to the subtle volume increase, the unit cell of Ta_2NiSe_7 in $C2/m$ with expanded lattice parameters of both intercalate phases were used as starting models. All atomic positions were then allowed to refine, final Rietveld refinements are shown in Figure 4.4 with refinement parameters given in Tables 4.1 and 4.2. Subtle variation in lattice parameters of both rich and poor phases in the mixed phase samples is observed, which indicates there are also slight variations in composition in the Li-poor and Li-rich phases, in addition to the change in proportions of each phase (i.e. the Li-poor and Li-rich phases seem to exist with a range of Li contents).

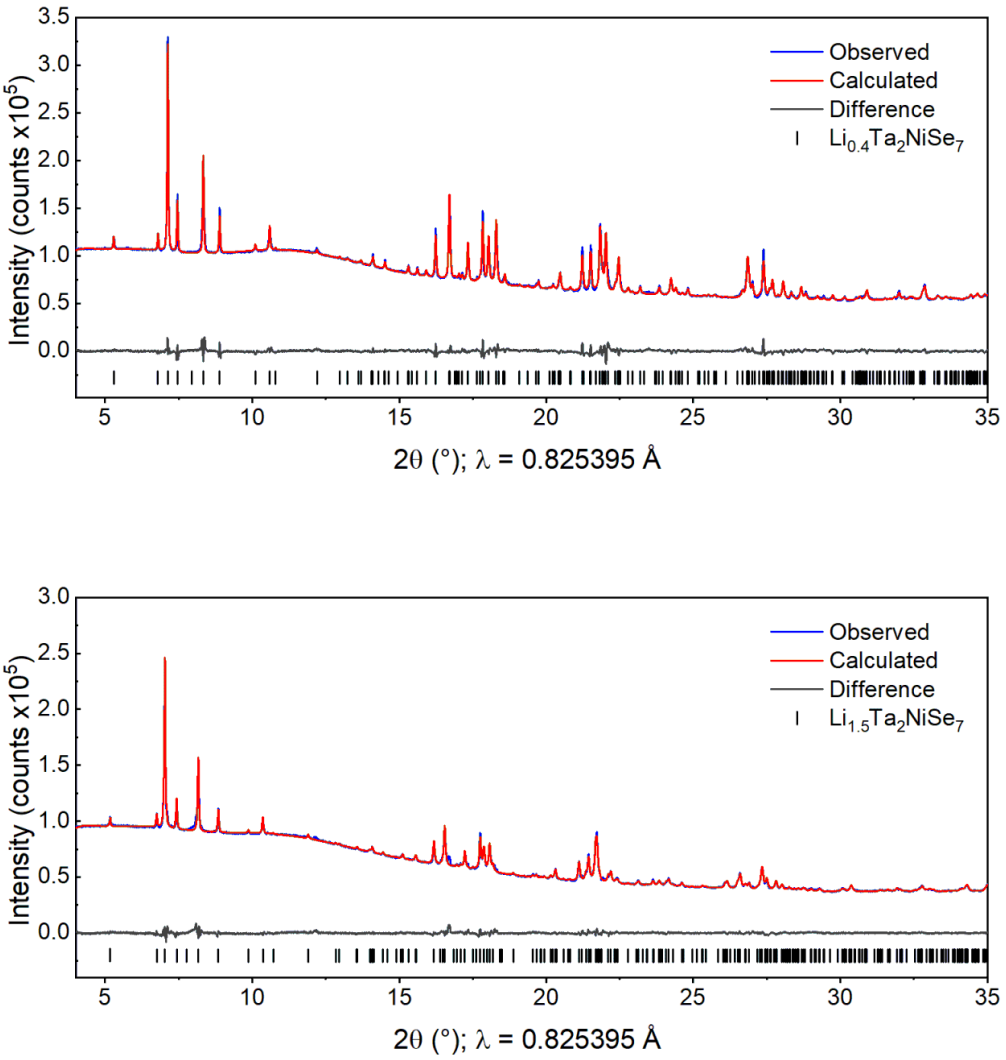

Figure 4.4: Rietveld refinements against PXRD data of **top** $Li_{0.4}Ta_2NiSe_7$ ($C2/m$) and **bottom** $Li_{1.5}Ta_2NiSe_7$ ($C2/m$) measured at 300 K using the PSD on the I11 beamline. R_{wp} = 1.22 % and 1.74 % respectively.

4.3.2 Powder Neutron Diffraction

PND experiments were performed in order to locate the light Li atoms in both phase pure Li-rich and Li-poor samples of $Li_xTa_2NiSe_7$. The Rietveld refinements against room temperature data were consistent with the models for the Ta–Ni–Se layers fit against the PXRD data, parameters are given in Tables 4.1 and 4.2. In the Li-rich phase, with measured Li content x = 1.45, two scattering centres with negative scattering amplitude were located at (0, 0, 0) and (0.424(3), 0.5, 0.337(2)), $2a$ and $4i$ sites respectively, both located in the interlayer spacing. The site at (0, 0, 0) is an octahedral site and the other site is an 8 co-ordinate bi-capped triangular prism formed by Se atoms of adjacent Ta_2NiSe_7 layers. The lithium occupancies were refined to 1.0(1) and 0.99(7) respectively, which is consistent with the stoichiometry of the reaction and the results of ICP-MS measurements, which gave a Li:Ni ratio of 1.45(5). The stoichiometry has been assigned as $Li_{1.5}Ta_2NiSe_7$ on this basis. Both Li sites were added to the Rietveld refinement of the Li poor phase, however no scattering amplitude could be identified on the bi-capped trigonal prism site. The octahedral site at (0, 0, 0) gave a refined Li occupancy of 0.82(18). This gives a stoichiometry of approximately $Li_{0.4}Ta_2NiSe_7$, which is consistent with the reaction of the stoichiometry and the ICP-MS Li:Ni ratio of 0.36(5).

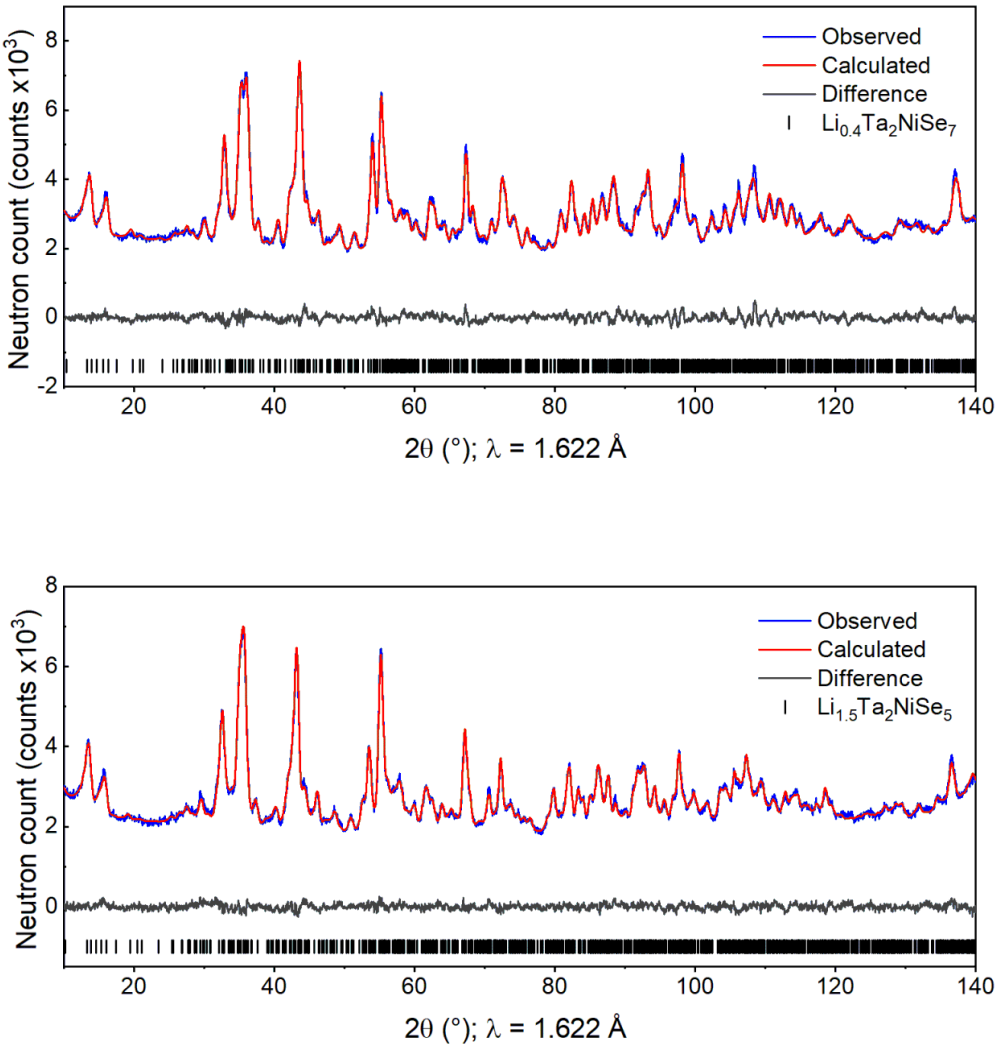

Figure 4.5: Rietveld refinements against PND data of **top** $Li_{0.4}Ta_2NiSe_7$ ($C2/m$) and **bottom** $Li_{1.5}Ta_2NiSe_7$ ($C2/m$) measured at 300 K using the Echidna instrument at ACNS. R_{wp} = 3.16 % and 2.68 % respectively.

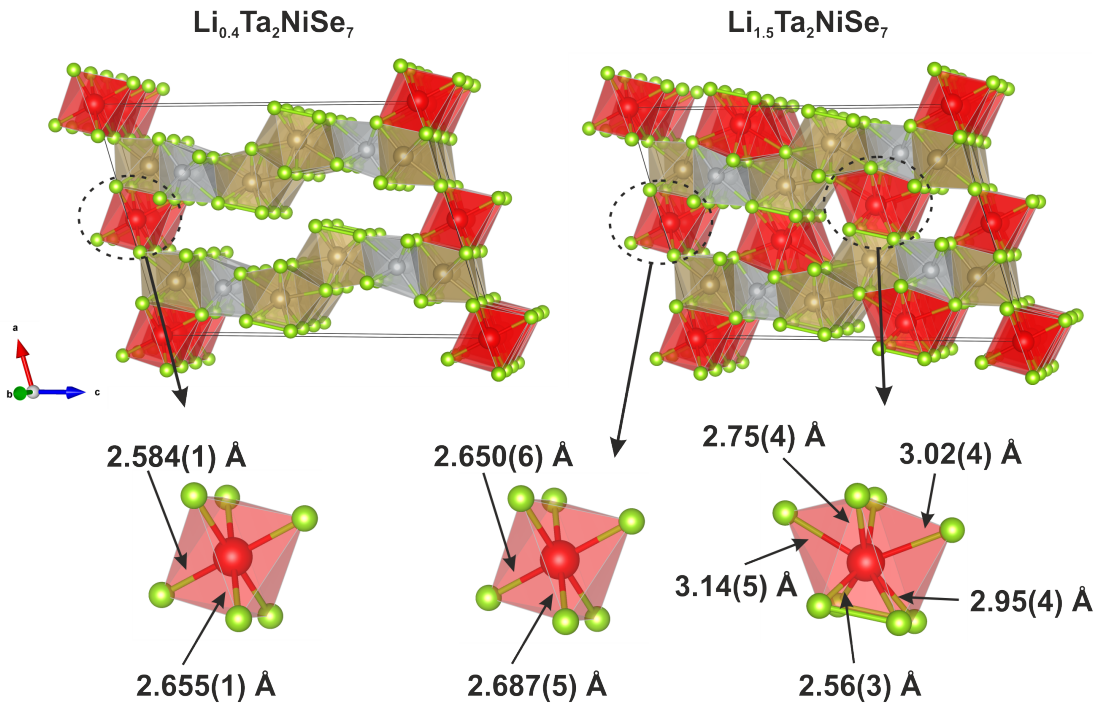

Figure 4.6: Structural models of **left** $Li_{0.4}Ta_2NiSe_7$ and **right** $Li_{1.5}Ta_2NiSe_7$ from refinement of PXRD and PND data. Li- Se bond lengths are derived from the refinement of PND data.

The emergence of two distinct phases in different ratios depending on the reaction stoichiometry suggests that filling of the two sites occurs sequentially. First the octahedral site is filled and when this site nears full occupancy, the bi-capped trigonal prism sites start to be filled. The refined Li occupancy of the Li poor phase and the emergence of the Li rich phase when the reaction stoichiometry is increased to x = 0.5, which theoretically could fully occupy the octahedral site exclusively, suggests the filling of the octahedral site is not complete before filling of the alternative site begins. This may be due to the entropic balance between fully occupying the lower energy octahedral site, which offers a better size match to Li, and filling the larger higher energy site. Disorder favours filling both Li sites simultaneously, but is opposed by the lower energy of the octahedral site. However as the octahedral site is filled, unfavourable Li–Li repulsions cause filling of the second Li site before

filling of the octahedral site is complete. The exact nature of the phase coexistence in the multiphase samples is difficult to deduce as the characterisation techniques used here are bulk techniques, and there may also be an electronic reason for the compositional gap between Li rich and poor phases.

Table 4.1: Refined parameters of $Li_{0.4}Ta_2NiSe_7$ from the Rietveld fit against PXRD data. Values given in parentheses () were obtained from PND data.

$Li_{0.4}Ta_2NiSe_7$ RMM = 975.39 g mol^{-1}, $Z = 4$						
Diffractometer			I11 (PSD) (Echidna(ACNS))			
Wavelength (Å)			0.825395 (1.622)			
Temperature (K)			300 (300)			
Space group			$C2/m$ (12)			
a (Å)			13.9641(2) (13.9619(8))			
b (Å)			3.4876(1) (3.4847(1))			
c (Å)			18.8079(3) (18.8272(9))			
β (°)			107.915(1) (107.757(5))			
V (Å^3)			871.55(2) (872.36(8))			
Atom	Site	x	y	z	Occ	U_{iso} (Å^2)
Ta1	4i	0.1561(2) (0.1554(5))	0	0.4008(2) (0.3999(4))	1	0.0165(11) (0.0093(16))
Ta2	4i	0.2345(2) (0.2384(6))	0	0.0923(2) (0.0943(4))	1	0.0097(11) (0.0121(14))
Ni	4i	0.2034(6) (0.1987(4))	0.5	0.2145(4) (0.2154(3))	1	0.0040(22) (0.0041(9))
Se1	4i	0.3656(6) (0.3603(4))	0	0.0088(5) (0.0096(3))	1	0.0080(9) (0.0041(6))
Se2	4i	0.0649(5) (0.0664(5))	0.5	0.2971(4) (0.2982(3))	1	0.0161(13) (0.0104(9))
Se3	4i	0.0872(5) (0.0901(5))	0	0.1416(4) (0.1449(3))	1	0.0080(9) (0.0041(6))
Se4	4i	0.3458(5) (0.3503(4))	0.5	0.1710(4) (0.1727(3))	1	0.0080(9) (0.0041(6))
Se5	4i	0.0256(6) (0.0265(7))	0.5	0.4215(4) (0.4207(3))	1	0.0161(13) (0.0104(9))
Se6	4i	0.3072(4) (0.3025(4))	0.5	0.4489(3) (0.4487(3))	1	0.0080(9) (0.0041(6))
Se7	4i	0.2611(4) (0.2634(4))	0	0.3032(4) (0.3004(3))	1	0.0080(9) (0.0041(6))
Li	(2a)	(0)	(0)	(0)	(0.8(2))	(0.101(29))

Table 4.2: Refined parameters of $Li_{1.5}Ta_2NiSe_7$ from the Rietveld fit against PXRD data. Values given in parentheses () were obtained from PND data.

$Li_{1.5}Ta_2NiSe_7$ RMM = 983.72 g mol^{-1}, Z = 4						
Diffractometer				I11 (PSD) (Echidna(ACNS))		
Wavelength (Å)				0.825395 (1.622)		
Temperature (K)				300 (300)		
Space group				$C2/m$ (12)		
a (Å)				14.0559(2) (14.0529(8))		
b (Å)				3.4928(1) (3.4916(1))		
c (Å)				19.0981(4) (19.0840(9))		
β (°)				106.779(1) (106.881(5))		
V (Å^3)				897.69(3) (896.05(8))		
Atom	Site	x	y	z	Occ	U$_{iso}$ (Å^2)
Ta1	4i	0.1592(2) (0.1605(5))	0	0.4019(2) (0.4015(4))	1	0.0041(10) (0.0086(14))
Ta2	4i	0.2322(3) (0.2327(6))	0	0.0936(2) (0.0933(4))	1	0.0072(12) (0.0073(14))
Ni	4i	0.2018(6) (0.2014(4))	0.5	0.2148(4) (0.2132(3))	1	0.0061(27) (0.0172(11))
Se1	4i	0.3576(5) (0.3580(4))	0	0.0046(5) (0.0074(3))	1	0.0142(9) (0.0060(5))
Se2	4i	0.0727(5) (0.0695(5))	0.5	0.3008(4) (0.2972(3))	1	0.0111(14) (0.0129(9))
Se3	4i	0.0899(5) (0.0900(5))	0	0.1442(4) (0.1428(3))	1	0.0142(9) (0.0060(5))
Se4	4i	0.3483(6) (0.3464(4))	0.5	0.1711(4) (0.1717(3))	1	0.0142(9) (0.0060(5))
Se5	4i	0.0312(4) (0.0289(5))	0.5	0.4245(4) (0.4236(3))	1	0.0111(14) (0.0129(9))
Se6	4i	0.3059(4) (0.3025(4))	0.5	0.4472(3) (0.4514(3))	1	0.0142(9) (0.0060(5))
Se7	4i	0.2650(5) (0.2662(4))	0	0.3055(5) (0.3024(3))	1	0.0142(9) (0.0060(5))
Li1	(2a)	(0)	(0)	(0)	(1.0(1))	(0.028(12))
Li2	(4i)	(0.424(3))	(0.5)	(0.337(2))	(0.89(7))	(0.040(11))

4.3.3 Li NMR

To further investigate the Li environments in each phase, ^{7}Li magic-angle spinning (MAS) NMR experiments were performed by Dr Sunita Dey under the guidance of Prof. Clare Grey, University of Cambridge. A Bruker Avance 300 MHz (7.05 T) spectrometer operating at a Larmor frequency of 116.6 MHz employing a 2.5 mm Bruker probe was used. Samples were packed into a 2.5 mm ZrO_2 rotor inside the glove box and spun at speeds between 25 and 35 KHz. A rotor-synchronized Hahn echo sequence (90°-τ-180°-τ-acquisition) with a $\pi/2$ pulse length of 1.0 μs and recycle delay of 0.1 s was used. The spectra were referenced to a standard LiOCl at 1 ppm. Bruker Topspin (version 4.0.7)[12] was used for raw data processing.

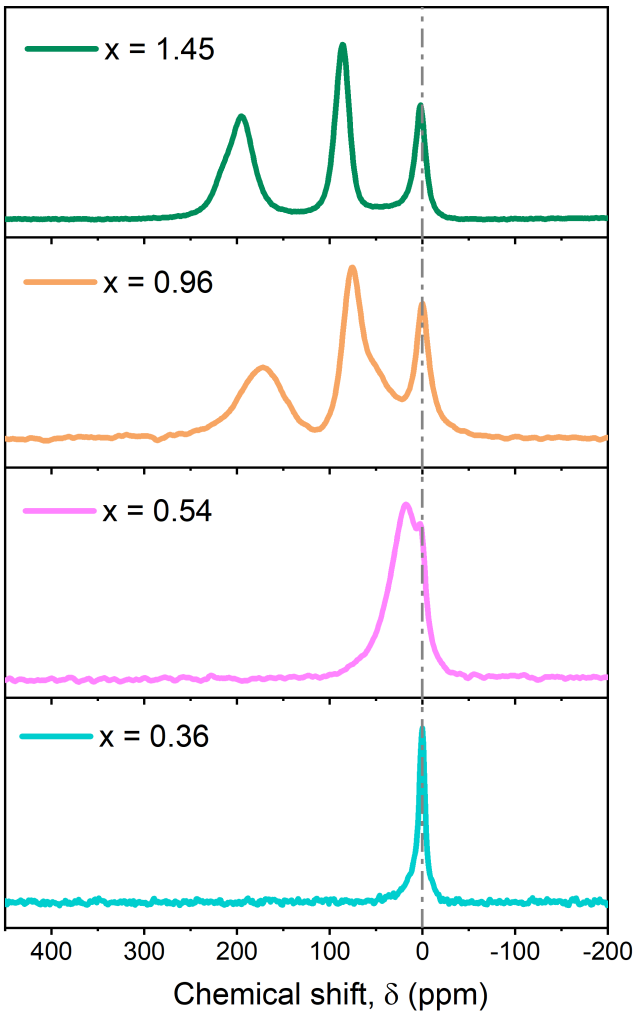

Figure 4.7: Normalised MAS ^{7}Li NMR spectra of $Li_xTa_2NiSe_7$.

All samples have a resonance at 0 ppm, which is indicative of diamagnetic phases. The spectrum of the sample x = 0.36 only displays this resonance, indicating only one Li environment is present which is consistent with our PND analysis. The appearance of this resonance at 0 ppm indicates that this phase is diamagnetic- which is consistent with our magnetometry data presented later in this chapter. At higher values of x, additional resonances appear, which is consistent with filling the second Li site. At x = 0.54, the resonances are not well resolved, but the emergence of a resonance from a paramagnetic phase is indicated by the Knight shift (discussed

in Chapter 2) of the second resonance. By x = 0.96, three well resolved resonances are observed, one a 0 ppm resonance attributed to the diamagnetic Li poor phase, and two from the paramagnetic Li rich phase which has two Li sites. The spectrum of the sample x = 1.45 is similar to that of the sample x = 0.96. The 0 ppm resonance is found to persist with reduced relative intensity, indicating at least a portion of the Li poor phase is consumed. The PXRD data indicates that a very small amount of the diamagnetic Li poor phase may still be present in the sample x = 1.45, shown by the broad, low intensity reflection at $2\theta = 7.1\ ^\circ$ in Figure 4.3. A significant paramagnetic Knight shift to higher ppm is also observed to increase across the series as more electrons are filling the conduction band of Ta_2NiSe_7, increasing the density of states at the Fermi level.

4.3.4 Magnetometry

Ambient temperature magnetisation isotherms are shown in Figure 4.8, measured using SQUID magnetometry. At low fields all isotherms reveal positive non-linear magnetisations from 0 - 2 T. This is indicative of a ferromagnetic impurities, such as elemental Ni. The positive magnetisation in this region is significantly larger for the intercalates of Ta_2NiSe_7 than for Ta_2NiSe_7 itself, which may suggest a tiny amount of elemental Ni or other ferromagnetic impurity is extruded during the intercalation process, which would be expected to vary from sample to sample.

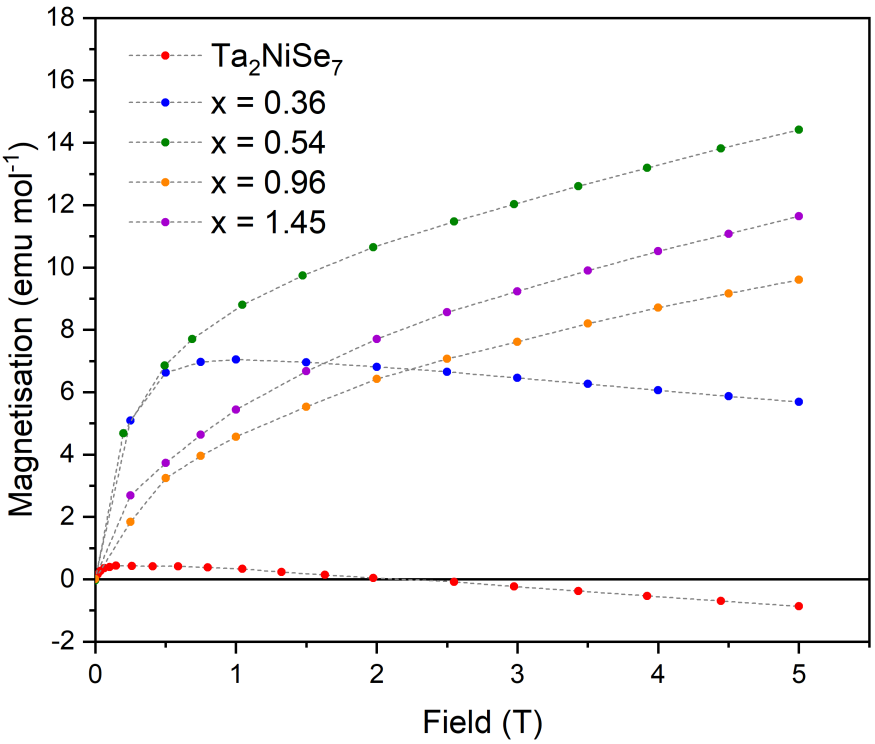

Figure 4.8: Magnetisation vs magnetic field curves of Ta_2NiSe_7 and lithium intercalates, $Li_xTa_2NiSe_7$.

Magnetic susceptibilities extracted from the high field region of the isotherms are given in Table 4.3, and reveal the parent and Li-poor phases compounds are bulk diamagnets. Samples x = 0.54, 0.96 and 1.45, which all contain the Li-rich phase in varying amounts, show bulk paramagnet behaviour. This agrees with the ^{7}Li NMR discussed above, which shows a correlation between the presence of the Knight shift, and whether the sample is diamagnetic or paramagnetic at the fields used in the NMR spectrometer. The large difference in susceptibilities between the samples which contain the Li rich phase and those that do not, suggest that either Ta(V) has been reduced to Ta(IV), or the $[Se–Se]^{2-}$ unit has been partially reduced, or a combination of both. This would give rise to the Pauli paramagnetism in the fully lithiated phase. Although the Li poor phase also has injected electrons, there is no increase in paramagnetism relative to Ta_2NiSe_7. Since the core diamagnetism dominates the Pauli contribution in Ta_2NiSe_7, the small increase in Pauli paramagnetism from the reduction of either species is insufficient to overcome the core diamagnetism at low Li amounts. This could also be due to the low concentration of injected electrons filling any holes in the selenide band before reducing the Ta(V).

Table 4.3: Room temperature magnetic susceptibilities of Ta_2NiSe_7 and lithium intercalates, $Li_xTa_2NiSe_7$.

Sample	Magnetic susceptibility (emu mol^{-1})
Ta_2NiSe_7	–3.14(2) x10^{-5}
x = 0.36 (single phase)	–3.87(4) x10^{-5}
x = 0.54 (mixed phase)	1.18(2) x10^{-4}
x = 0.96 (mixed phase)	1.00(4) x10^{-4}
x = 1.45 (single phase)	1.19(3) x10^{-4}

Subtraction of the magnetisation vs temperature curves were measured at 3 T from that measured at 4 T (Figure 4.9) for the diamagnetic samples, which eliminates the effect of the minuscule ferromagnetic impurity and gives the intrinsic susceptibility which is temperature independent, consistent with opposing temperature independent diamagnetic and paramagnetic contributions. The core diamagnetic contributions calculated from standard tables[13] are -3.76 x10^{-4} emu mol^{-1} and -3.77 x10^{-4} emu mol^{-1} for Ta_2NiSe_7 and $Li_{0.4}Ta_2NiSe_7$ respectively. However, the experimental susceptibilities are approximately 10 % of these values. This suggests there is a Pauli paramagnetism in both the parent and Li poor phase, as discussed in the introduction of this chapter.

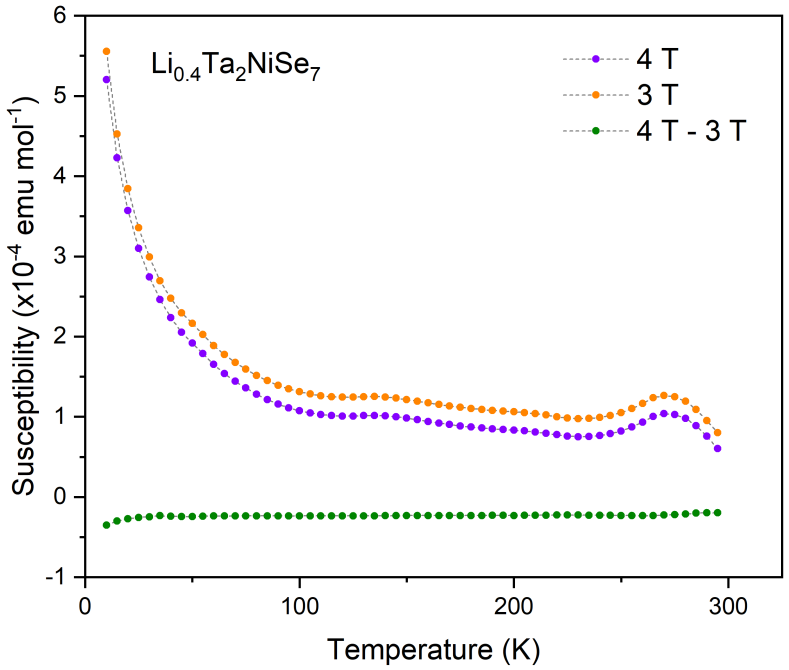

Figure 4.9: Magnetic susceptibility vs temperature of $Li_{0.4}Ta_2NiSe_7$ measured at 3 T and 4 T. Subtraction of the data points measured at these two fields is given in green.

4.4 De-intercalation of $Li_{1.5}Ta_2NiSe_7$

Chemical deintercalation of Li was attempted to assess the reversibility of the intercalation process. This was performed by adding $Li_xTa_2NiSe_7$ powder and a magnetic stirrer bar into a Schlenk tube in a glove box. Various stoichiometric amounts of I_2 were added to another Schlenk tube outside the glove box, along with a magnetic stirrer bar. Using a Schlenk line, the air atmosphere was replaced with N_2, then approximately 20 cm^3 of dry acetonitrile was added to the vessel and left to stir until the iodine had dissolved. This solution was then transferred to the Schlenk tube containing $Li_xTa_2NiSe_7$ powder. The suspension was left to stir over night before filtering, washing with fresh dry acetonitrile and drying under dynamic vacuum for 1 hour.

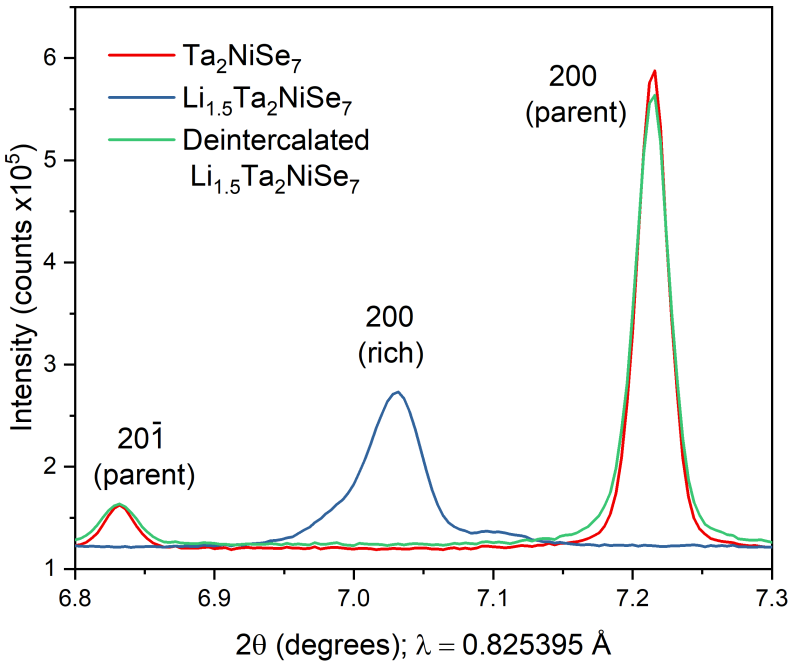

Figure 4.10: PXRD patterns of Ta_2NiSe_7, $Li_{1.5}Ta_2NiSe_7$ and deintercalated $Li_{1.5}Ta_2NiSe_7$ in the 200 region.

PXRD patterns of samples of $Li_{1.5}Ta_2NiSe_7$ treated with I_2 show almost pristine Ta_2NiSe_7 is returned, as shown in Figure 4.10. Both excess and stoichiometric amounts of iodine solutions were used, along with a variety of reaction times from 5 minutes to 25 hours. $Li_{0.4}Ta_2NiSe_7$ was also subjected to the same experiments. All deintercalated samples returned near identical synchrotron PXRD patterns, and indicates high stability of Ta_2NiSe_7 respective to their binary transition metal selenides. The Rietveld refinement of deintercalated $Li_{1.5}Ta_2NiSe_7$ can be found in Figure 4.11. Curiously, the reaction performed with an amount of I_2 less than that needed to remove all the Li also returned the same PXRD pattern, indicating that additional side reactions may be occurring. This is subject to further investigation.

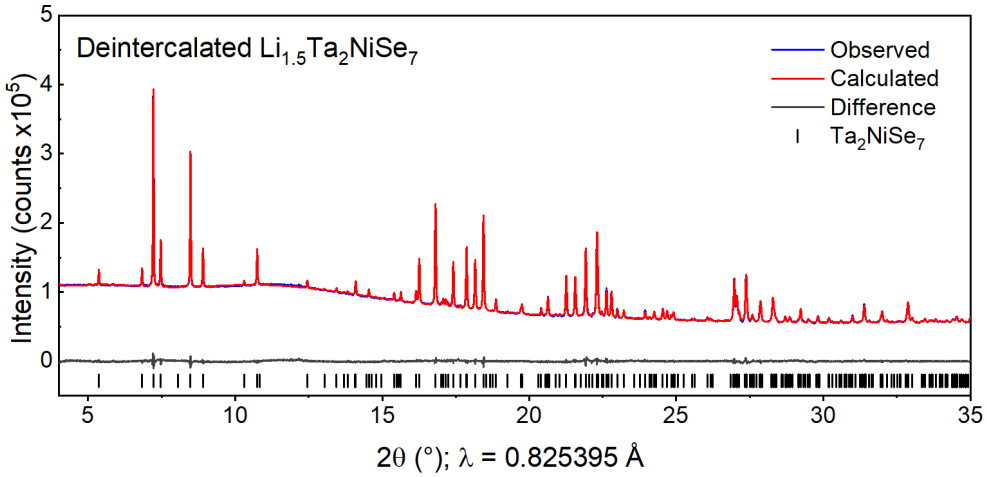

Figure 4.11: Rietveld refinement of deintercalated $Li_{1.5}Ta_2NiSe_7$ ($C2/m$) measured at 300 K using the PSD detector on the I11 beamline. $R_{wp} = 1.03$ %.

To assess the air stability of $Li_{1.5}Ta_2NiSe_7$, a portion of the sample was left to oxidise in air overnight. The resulting phase was found to be crystalline Ta_2NiSe_7 from analysis of synchrotron PXRD data. Additional Li-containing side phases could not be identified, however there is most likely an amorphous hydroxide or carbonate phase present to account for the aerially extruded Li. This further demonstrates the relative high stability of Ta_2NiSe_7. The Rietveld refinement of the PXRD data can be found in Figure 4.12.

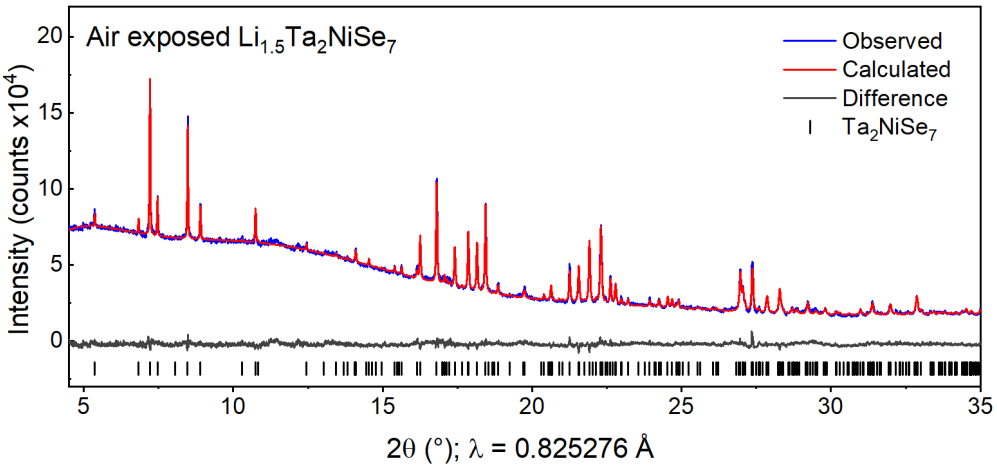

Figure 4.12: Rietveld refinement of air exposed $Li_{1.5}Ta_2NiSe_7$ measured at 300 K using the PSD on the I11 beamline. The majority phase is Ta_2NiSe_7 ($C2/m$). R_{wp} = 2.92 %.

Lattice parameters and bond lengths extracted from the Rietveld refinements of both PXRD and PND data for both phase pure Li intercalates, and PXRD data for Ta_2NiSe_7 and the deintercalated phase is given in Table 4.4. Values given for Ta_2NiSe_7 and deintercalated $Li_{1.5}Ta_2NiSe_7$ are within 3 standard deviations of one another (except for the β angle which lies just outside this range). This confirms our previous assessment that deintercalation of the lithiated phase returns crystalline

Ta_2NiSe_7. Inspection of lattice parameters shows the lattice expansion is dominated by a and c lattice parameters, which both increase the interlayer spacing. The β angle is found to decrease with increasing Li content, which structurally is equivalent to sliding the layers over one another, which increases the volume of the interstitial sites.

Table 4.4: Lattice parameters and bond lengths of Ta_2NiSe_7, both lithiated phases and deintercalated $Li_{1.5}Ta_2NiSe_7$. Bond lengths are given as weighted mean values. Values given in parentheses () were obtained from PND data.

	Ta_2NiSe_7	$Li_{0.4}Ta_2NiSe_7$	$Li_{1.5}Ta_2NiSe_7$	Deintercalated $Li_{1.5}Ta_2NiSe_7$
a	13.8680(1)	13.9641(2)	14.0559(2)	13.8684(1)
		(13.9619(8))	(14.0529(8))	
b	3.48876(1)	3.48758(5)	3.49277(5)	3.48863(2)
		(3.4847(1))	(3.4916(1))	
c	18.6404(1)	18.8272(9)	19.0981(4)	18.6407(1)
		(18.8272(9))	(19.0840(9))	
β (°)	108.923(1)	107.915(1)	106.779(1)	108.923(1)
		(107.757(5))	(106.881(5))	
V (Å^3)	853.13(1)	871.55(2)	897.69(3)	853.13(1)
		(872.36(8))	(896.05(8))	
Ta1-Se	2.653	2.667	2.660	2.649
		(2.649)	(2.667)	
Ta2-Se	2.582	2.582	2.594	2.585
		(2.588)	(2.588)	
Ni-Se	2.470	2.492	2.508	2.476
		(2.465)	(2.492)	
Se dimer	2.534(9)	2.571(9)	2.591(9)	2.523(5)
		(2.532(9))	(2.637(9))	

Comparison of bond lengths show very little change between Ta_2NiSe_7 and the Li poor phase. A greater degree of (but still subtle) bond lengthening can be observed across all distances given in Table 4.4 for the Li rich phase. This observation is expected given that the Li rich phase has a higher concentration of injected electrons. Since the Materials Project[11] reports a well-mixed band structure, and as discussed in the introduction to the chapter there is some mixing between the Se $4p$ and Ta $5d$ bands,[6] it is possible that both species are simultaneously reduced. The length of the Se-Se dimer appears to be increasing the most as a consequence of intercalation, suggesting that some of the Se dimers are fully reduced. This would result in an increased mean Se–Se bond length observed by diffraction. This is also consistent with the magnetometry data. Individual bond lengths have been tabulated in Appendix II.

4.5 Electrochemical intercalation of Li

Due to the high reversibility of chemical intercalation of Li, electrochemical cycling of Li was attempted. Electrochemical Li intercalation was conducted using coin cells (CR2032, Cambridge Energy Solutions) assembled by Dr Sunita Dey in an Ar-filled glove box. The Ta_2NiSe_7 phase was mixed with Super P Carbon (Timcal) and polyvinylidene fluoride (PVDF) binder (weight ratio: 80:10:10) to prepare the cathode. A coin cell was assembled with Ta_2NiSe_7 as the cathode, a borosilicate glass fibre separator (Whatman, 15 mm diameter) soaked with 75 μl of electrolyte, and a Li counter electrode (diameter 13 mm). 1 M $LiPF_6$ in ethylene carbonate (EC):dimethyl carbonate (DMC) (1:1) was used as the electrolyte. Galvanostatic (dis)charge was carried out at room temperature with a Lanhe battery cycler (Wuhan Land Electronics Co. Ltd.) at C/10 rate, where C is defined as the theoretical capacity of the compound and C/10 means fully charging or discharging over 10 hours. Prior to *ex situ* measurements, batteries were disassembled inside the Ar glove box and the electrode mixture was rinsed three times with DMC and dried in the glove box ante-chamber (under vacuum) for 30 mins. Electrochemical lithiation was performed by Dr Sunita Dey under the guidance of Prof. Clare Grey, University of Cambridge.

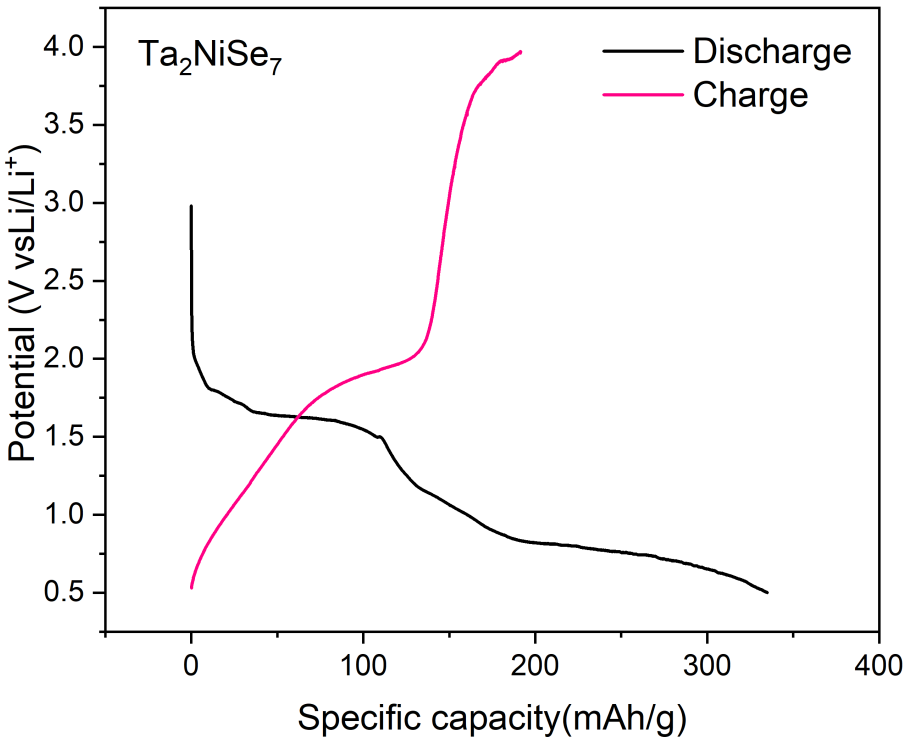

Figure 4.13: Voltage profile against specific capacity of Ta_2NiSe_7.

It was found that the specific capacity on discharging to 0.5 V far exceeds the 41.3 mAh/g required to produce $Li_{1.5}Ta_2NiSe_7$ shown in Figure 4.13. This indicates decomposition of $Li_xTa_2NiSe_7$ to binary or elemental side phases (such as Li_2Se and Ni) is occurring at high capacities, as is sometimes seen in electrochemical intercalation, although the formation of a Li-richer phase as an intermediate cannot be ruled out. Analysis of the fully discharged phase through PXRD is part of the future work of this project. Subsequent electrochemical intercalation of Ta_2NiSe_7 was performed using specific capacities of 11.0, 13.8, 27.5 and 41.3 mAh/g to produce samples $Li_xTa_2NiSe_7$ (x = 0.4, 0.5, 1.0, 1.5) respectively for comparison to samples synthesised chemically. Voltage profiles for synthesis on discharge of samples with

target compositions $LiTa_2NiSe_7$ and $Li_{1.5}Ta_2NiSe_7$ are shown in Figure 4.14. The low starting potential of the discharge curve of $Li_xTa_2NiSe_7$ x = 1.0 is due to crimping of the coin cell, a minor defect in the sample preparation.

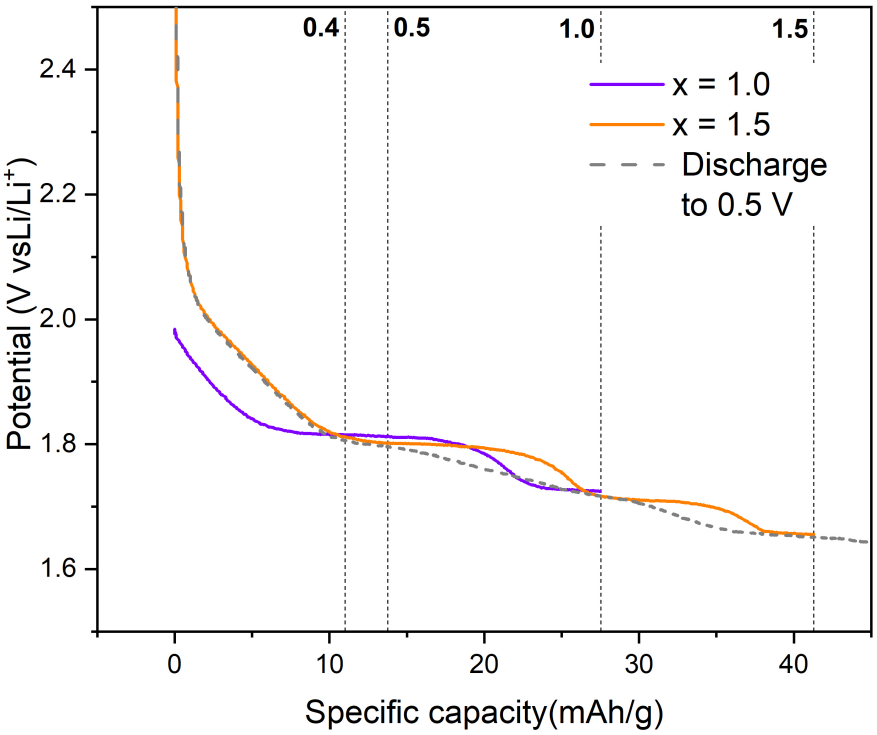

Figure 4.14: Voltage profile against specific capacity of $LiTa_2NiSe_7$ (purple), $Li_{1.5}Ta_2NiSe_7$ (orange) and the total discharge to 0.5 V (grey- see Figure 4.13). Samples x = 0.4 and 0.5 follow the purple curve but have not been shown for clarity. Reference lines mark the capacities which give phases $Li_xTa_2NiSe_7$, x values are given in bold.

The voltage profiles of samples x = 1.0, 1.5 in Figure 4.14 show three plateaus in the range 0 – 41.3 mAh/g. The regions of constant voltage indicate that the chemical potential of the system is not changing. This is consistent with the presence of multiple phases with a changing ratio of the two in this region. The regions of the plot with a negative gradient indicates there is a continuous change in the band filling occurring, and subsequently the Fermi level, hence the chemical potential changes. These regions indicate a single phase with a changing composition is present. Interestingly, the total discharge curve taken from Figure 4.13 and superimposed on Figure 4.14 shows some differences. Most notably, the discharge profile does not appear to have any plateaus, indicating the Li filling in this sample is completely continuous. This could be a consequence of the faster charge rate used for this sample, as a significantly higher capacity is reached in the same amount of time as the other samples (10 hours; the charge rate is C/10 where C is the capacity). This equates to a discharge rate of approximately 35 mAh/g per hour for the full discharge curve versus approximately 4 mAh/g per hour for the sample x = 1.5.

Comparison of the two partial discharge curves shown in Figure 4.14 shows the discharge curve for the lower values of x is offset by approximately 5 mAh/g (0.2 molar equivalents of Li) to lower specific capacities than the discharge curve for the sample x = 1.5, and the full discharge curve. It is speculated that this may be due to a defect in the coin cell preparation as discussed above. This may indicate different samples have undergone a greater degree of discharge than anticipated, resulting in different Li stoichiometries than the target phases. Consequences of this will be discussed later in this chapter. The target Li contents and the estimated Li contents of each sample are shown in Table 4.5. The estimated Li contents were calculated by adding 0.2 molar equivalents (see above) of Li to the target Li contents. The target values of x = 0.4, 0.5 and 1.0 will continue to be used in this chapter for simplicity, although this may be underestimates of the true Li content.

Table 4.5: The target Li contents and the estimated Li contents obtained from comparison of the discharge curves collected during the electrochemical syntheses of $Li_xTa_2NiSe_7$.

Target Li content	Estimated 'true' Li content
x = 0.4	x = 0.6
x = 0.5	x = 0.7
x = 1.0	x = 1.2
x = 1.5	x = 1.5

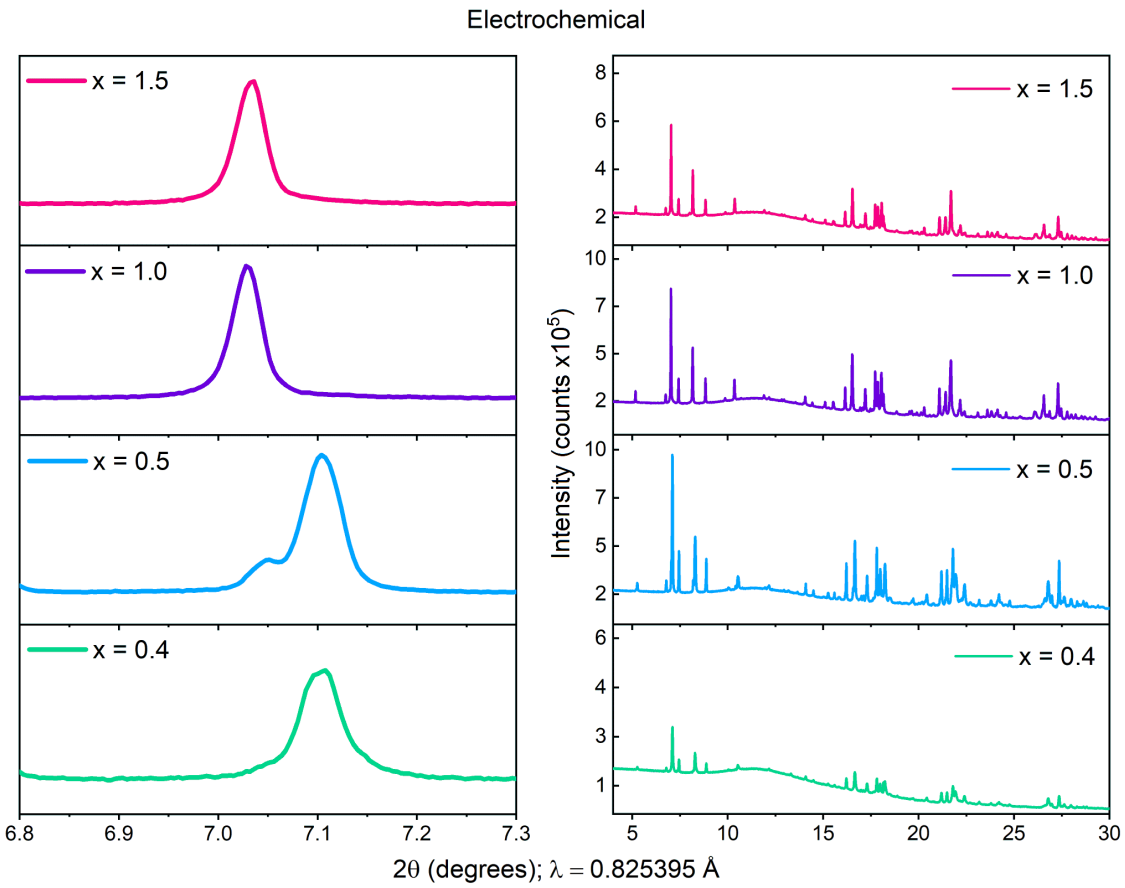

Figure 4.15: Normalised PXRD patterns showing the 200 reflection of $Li_xTa_2NiSe_7$ collected using the I11 beamline at the Diamond Light Source. Patterns given in blue were synthesised chemically, patterns shown in pink and labelled 'EC' were synthesised electrochemically.

High resolution PXRD data of the electrochemical intercalates was collected using the PSD on the I11 beamline, shown in Figure 4.15. Unlike chemically synthesised samples, the electrochemical samples appear to be single phase, with the exception of a small shoulder in the sample for which the target discharge point was x = 0.5. This is consistent with discharging the samples until near the beginning of the plateau regions in the voltage profile plots in Figure 4.14. This could be a consequence of the small sample size (approximately 10 mg) used for electrochemical lithiation, compared to chemical lithiation (approximately 300 mg). Additionally, a slow charge rate was used as described in the method. This allows the Li to equilibrate and

distribute evenly throughout the sample. At x = 0.4, the general intensity of the pattern is lower compared to samples with a higher value of x. This is indicative of the formation of an amorphous coating layer (the solid-electrolyte interphase) as Li adsorbs to the surface of Ta_2NiSe_7. This is a common observation in electrochemical systems at low x values. Rietveld refinements of the electrochemically synthesised samples can be found in Appendix II.

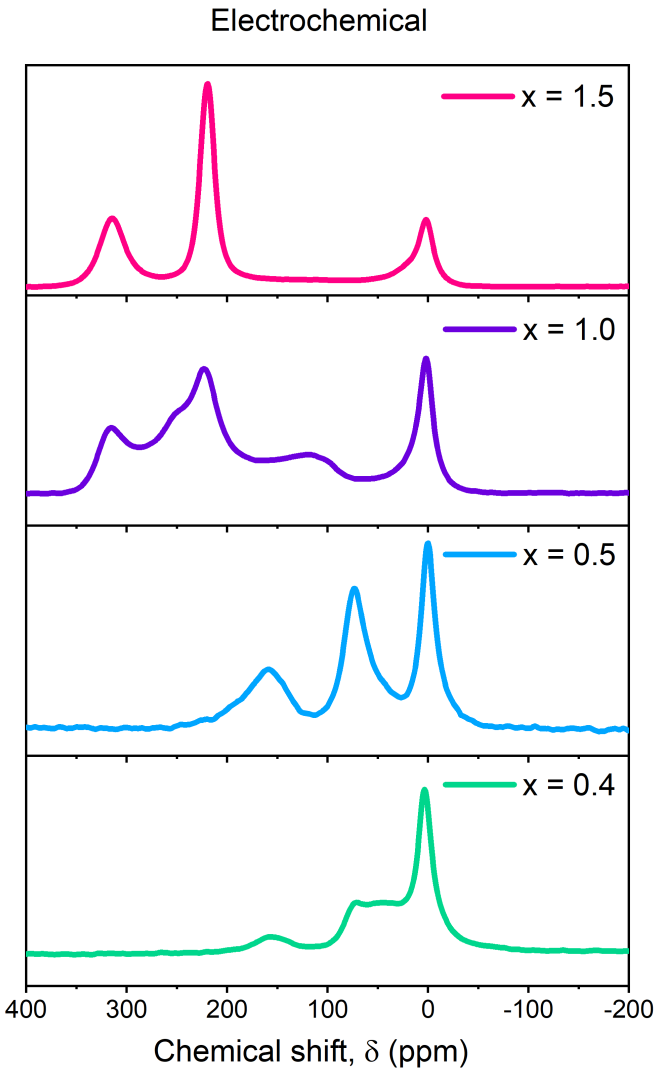

Figure 4.16: Normalised ^{7}Li MAS NMR spectra of $Li_xTa_2NiSe_7$ synthesised electrochemically.

The MAS ^{7}Li NMR spectra, shown in Figure 4.16, of all electrochemical samples feature a sharp resonance at 0 ppm, which diminishes relative to the other resonances with increasing Li content as more of the bulk $Li_xTa_2NiSe_7$ is formed relative to the surface coating. This is consistent with the formation of the solid-electrolyte interphase at low values of x, as previously discussed. The spectrum of sample x = 0.4 has two broad resonances, which can be attributed to the small amount of Li rapidly exchanging between both Li sites, on the NMR timescale. At x = 0.5 these two resonances are more well resolved, and continue to become sharper and shift to a higher ppm by x = 1.5. This suggests less site hopping is occurring as more sites are filled, and a larger Knight shift which is consistent with the addition of more electrons. The spectrum for sample x = 1.0 has some additional resonances however, which suggest some proportion of an intermediate phase may be present.

4.6 Discussion

Figure 4.17 compares the PXRD patterns of $Li_xTa_2NiSe_7$ samples synthesised chemically and electrochemically, over the range 6.8 °$< 2\theta <$ 7.3 °. As previously discussed, the most significant difference is the lack of phase separation observed for the electrochemical samples compared to those synthesised chemically, presumably a consequence of the sample size and synthesis method.

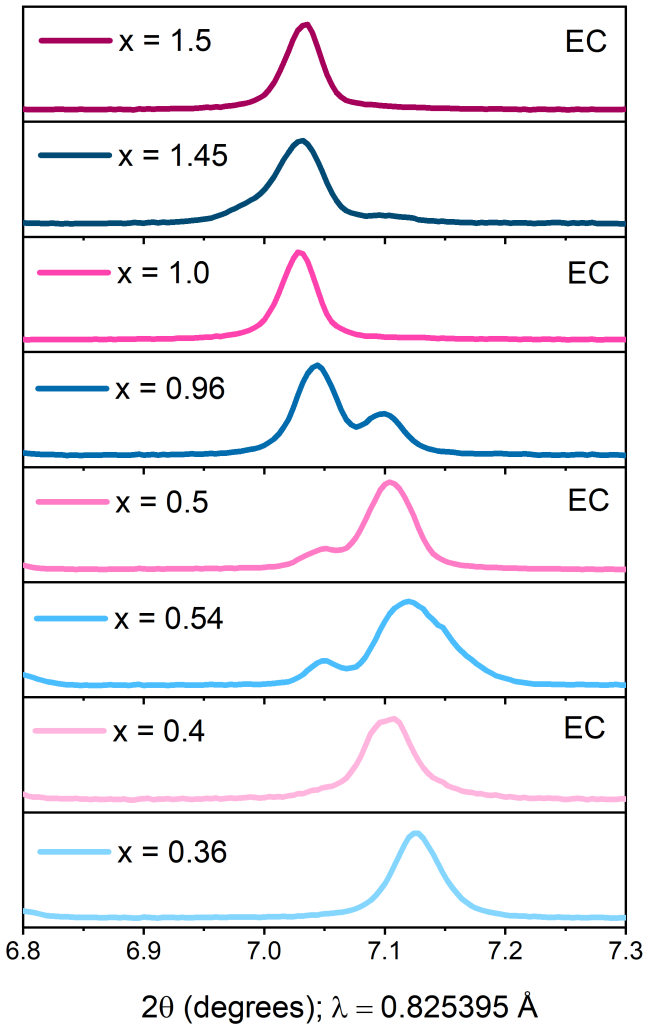

Figure 4.17: Normalised PXRD patterns showing the 200 reflection of $Li_xTa_2NiSe_7$ collected using the I11 beamline at the Diamond Light Source. Patterns given in blue were synthesised chemically, patterns shown in pink and labelled 'EC' were synthesised electrochemically.

Comparison of the patterns at corresponding values of x show that in general, the 002 reflection of samples synthesised electrochemically show a greater shift to lower angle, indicating a greater degree of lattice expansion. This is consistent with the hypothesis that the true Li content is higher than expected for x = 1.0, 0.5 and 0.4 as discussed previously based on the offset of the electrochemical discharge curves. This can also be seen by comparing electrochemical sample x = 1.0 and chemical sample x = 1.45, as their respective 200 reflections lie at approximately the same value of 2θ. Since no further expansion is seen between the electrochemical sample x = 1.0 (estimated Li content x = 1.2) and electrochemical sample x = 1.5, the partial homogeneous filling of Li sites at the lower Li content may be sufficient to fully expand the lattice. Both sites are then completely filled by x = 1.5 without further expansion. Both patterns are visually very similar to the sample x = 1.45 synthesised chemically in this range which supports this conclusion.

Table 4.6: Lattice parameters from Rietveld refinements of $Li_xTa_2NiSe_7$ synthesised chemically and electrochemically. Both Li poor and Li rich phases could be fit at x = 0.96, for all other values of x the lattice parameters of the majority phase is given.

Chemical					
x	0.36	0.54	0.96	0.96	1.45
a (Å)	13.9632(2)	13.9564(4)	13.9803(4)	14.0491(2)	14.0558(2)
b (Å)	3.4874(1)	3.4857(1)	3.4852(1)	3.4895(1)	3.4928(1)
c (Å)	18.8075(3)	18.7998(7)	18.8684(5)	19.0455(4)	19.0978(4)
β (°)	107.916(1)	107.900(2)	107.556(2)	107.015(1)	106.779(1)
V (Å^3)	871.44(2)	870.35(5)	876.54(4)	892.83(3)	897.67(3)
Electrochemical					
x	0.4	0.5	-	1.0	1.5
a (Å)	13.9840(4)	13.9752(3)		14.0576(1)	14.0556(1)
b (Å)	3.4857(1)	3.4860(1)		3.4938(1)	3.4926(1)
c (Å)	18.8606(7)	18.8447(4)		19.0988(2)	19.0834(2)
β (°)	107.596(2)	107.712(1)		106.824(1)	106.900(1)
V (Å^3)	876.31(5)	874.79(3)		897.89(1)	896.38(1)

The lattice parameters from the Rietveld fits of $Li_xTa_2NiSe_7$ synthesised chemically and electrochemically are given in Table 4.6. There is a clear difference in lattice parameters and volume between the Li poor and Li rich phases in chemically synthesised samples, which supports our hypothesis that Li sites are filled sequentially. Electrochemically synthesised samples show a large increase in volume between x = 0.5 – 1.0, and does not increase further as additional Li is inserted, as previously discussed.

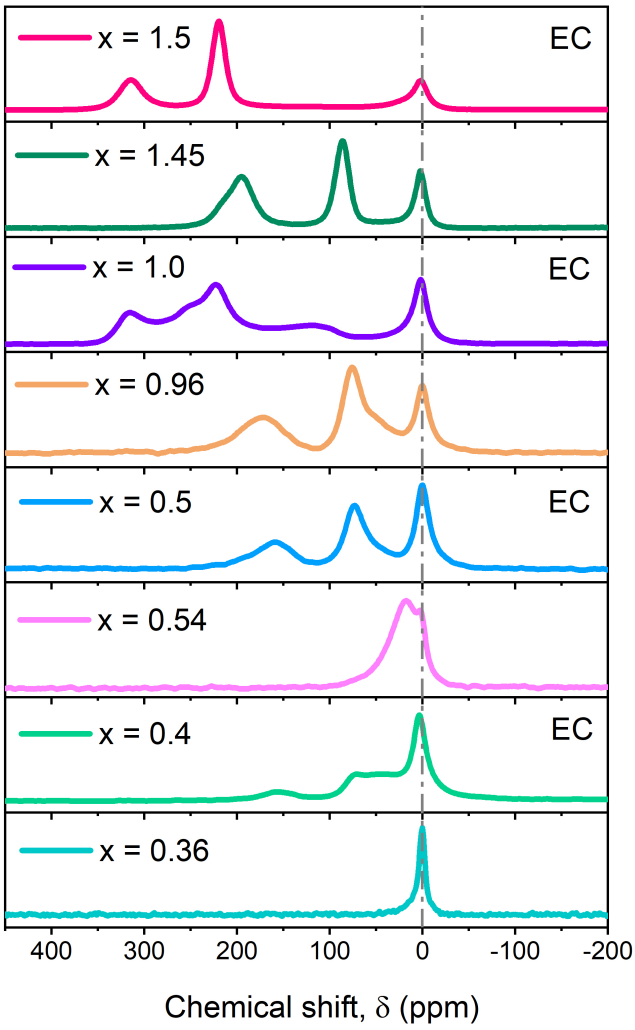

Figure 4.18: Normalised ^{7}Li MAS NMR spectra of $Li_xTa_2NiSe_7$. Spectra labelled 'EC' were from samples synthesised electrochemically. The dashed line is a visual guide to the resonance at 0 ppm.

Comparison of the ^{7}Li NMR spectra of samples synthesised chemically and electrochemically shows some marked differences, shown in Figure 4.18. Whilst the two series can be rationalised individually, the similarity of spectra of the chemical sample x = 0.96 and electrochemical sample x = 0.5 appears contradictory. This is most likely a consequence of the of the offset of discharge curves for the samples x = 1.0, 0.5 and 0.4, which have estimated Li contents x = 1.2, 0.7 and 0.6 respectively, as discussed previously. Another comparison can be drawn between the chemical sample x = 0.96, which shows well resolved resonances, the corresponding electrochemical sample x = 1.0 has some additional broad resonances. The resonances at 300 and 200 ppm can be clearly be attributed to those in the fully lithiated electrochemical sample, which is consistent with the higher estimated Li content of x = 1.2, however the broad resonances are more difficult to assign and might suggest some amorphous intermediate phase is forming.

Another difference is the higher chemical shift of the fully lithiated phase synthesised electrochemically, compared to the sample synthesised chemically. This may indicate the degree of the paramagnetic Knight shift is larger for the electrochemical sample, however more work is required to rationalise this observation.

SQUID magnetometry was not possible on the electrochemical samples due to their small size. However, if the synthesis could be scaled up to reproduce the same PXRD and NMR results, the magnetometry data could provide further insights to the diamagnetic to paramagnetic 'tipping point' with increasing Li composition.

4.7 Summary and Conclusions

The ambient temperature lithium intercalation of Ta_2NiSe_7 has been shown to be topochemical in nature, resulting in very little change to the host structure. Sequential filling of the two different Li sites is a consequence of the different energies of the two sites, and results in the emergence of two distinct phases. Further investigation shows each phase has different magnetic properties, a result of the degree of reduction of Ta(V) and $[Se\text{-}Se]^{2-}$ caused by different amounts of injected electrons. The Li rich phase shows transformation from a diamagnet to a Pauli paramagnet, consistent with reduction to Ta(IV) with the $5d^1$ electronic configuration. It is clear that the diselenide unit is not reduced to a strongly paramagnetic species, however the lengthening of the diselenide unit is observed upon intercalation, consistent with some reduction.

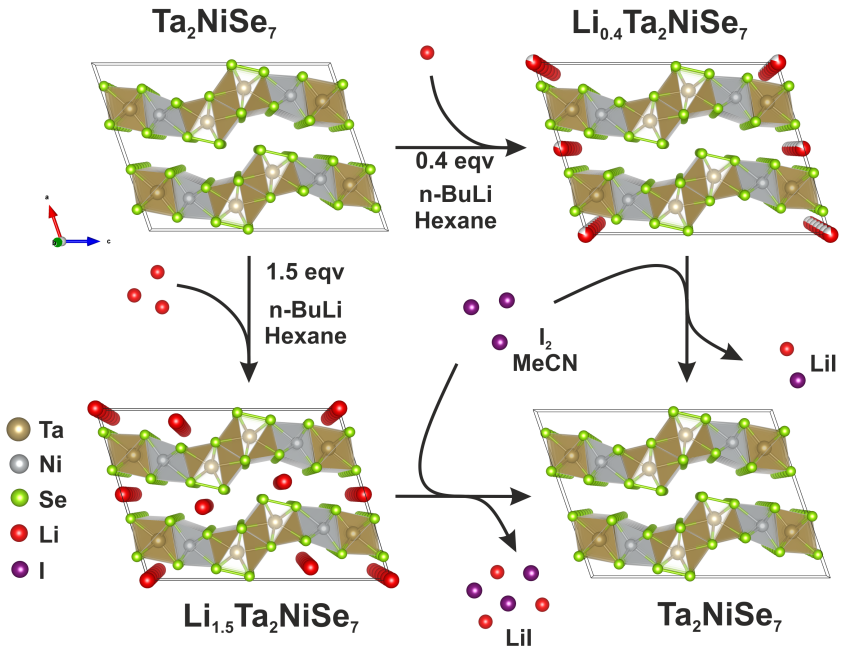

Figure 4.19: A reaction scheme showing the intercalation and deintercalation reactions of Ta_2NiSe_7.

Chemical and aerial deintercalation returns pristine Ta_2NiSe_7 and reflects the stability of this phase. However, Ta_2NiSe_7 is not electrochemically stable and decomposes at high specific capacities. Analysis of these phases should be performed using PXRD, and constitutes further work of this project. Electrochemical intercalates do not show the same phase separation, which could be a result of smaller sample sizes and a slow charge rate.

^{7}Li MAS NMR also shows differences between samples synthesised by the two different methods. Chemically synthesised samples follow the expected observation of one Li resonance from the Li poor phase, and two from the Li rich phase. Electrochemical samples display spectra with higher chemical shifts, possibly due to differences in band structure, but further experiments would be required to investigate this. Computational experiments to calculate the band structures of samples with different Li distributions would be useful to examine this, in addition to computing the NMR spectra of each sample.

All samples show a paramagnetic Knight shift which is consistent with the injection of electrons and the formation of paramagnetic phase, with the exception of the Li poor phase synthesised chemically. Additional work includes the attempt to scale up the electrochemical syntheses to produce large enough samples to collect SQUID magnetometry data to examine the effect of Li distribution on the magnetic properties. Additional work also includes accurately quantifying the Li composition of the electrochemical samples using ICP-MS to account for discrepancies in the PXRD and NMR data compared to the chemically synthesised samples.

Further work also includes the synthesis of more intermediate phases through chemical and electrochemical methods to better understand the formation of each phase presented here and follow the course of the reaction *ex situ*. *In situ* experiments could also be performed using synchrotron radiation, in order to achieve the data resolution required, although this would require a more complex experimental setup.

References

[1] S. A. Sunshine, J. A. Ibers, *Inorganic Chemistry* **1986**, *25*, 4355–58.

[2] H. K. D. H. Bhadeshia, C. M. Wayman, *Physical Metallurgy (fifth edition)*, Elsevier, **2015**.

[3] R. M. Fleming, S. A. Sunshine, C. H. Chen, L. F. Schneemeyer, J. V. Waszczak, *Physical Review B* **1990**, *42*, 4954.

[4] R. Cava, V. Himes, A. Mighell, R. Roth, *Physical Review B* **1981**, *24*, 363–367.

[5] S. J. Hillenius, R. V. Coleman, R. M. Fleming, R. J. Cava, *Physical Review B* **1981**, *23*, 1567.

[6] E. Canadell, M. H. Whangbo, *Inorganic Chemistry* **1987**, *26*, 3974–76.

[7] A. Spijkerman, A. Meetsma, J. L. De Boer, Y. Gao, S. Van Smaalen, *Physical Review B* **1995**, *52*, 3892.

[8] Z. Dai, C. G. Slough, W. W. McNairy, R. V. Coleman, *Physical Review Letters* **1992**, *69*, 1769.

[9] J. Lüdecke, E. Riedl, M. Dierl, S. Hosseini, K.and van Smaalen, *Physical Review B* **2000**, *62*, 7057.

[10] H. Chen, Z. Sun, *Journal of Materials Chemistry C* **2021**, *9*, 5162–66.

[11] A. Jain, S. P. Ong, G. Hautier, W. Chen, W. D. Richards, S. Dacek, S. Cholia, D. Gunter, D. Skinner, G. Ceder, K. A. Persson, *APL Materials* **2013**, *1*, 011002.

[12] Bruker, *TopSpin*, version 4.0.7.

[13] G. F. Bain, J. F. Berry, *Journal of Chemical Education* **2008**, *85*, 532.

'Explored the city a bit this weekend, found a hill to look down on all the plebs'

- Viktoria Falkowski

5

Intercalation Chemistry of Fe_5GeTe_2

Contents

5.1 Introduction

Layered materials with intrinsic functionality have become increasingly popular due to their potential applications in progressive technologies. In spintronics, stable ambient temperature anisotropic ferromagnets with a large magnetisation and high conductivity are ideal candidates. Typically, 2D ferromagnets have relatively low Curie temperatures as a consequence of weak magnetic interlayer coupling across the interlayer gap. However, one such candidate is 2D room temperature ferromagnet Fe_5GeTe_2, first reported in 2019,[1] which has the highest Curie temperature of any van der Waals material to date.

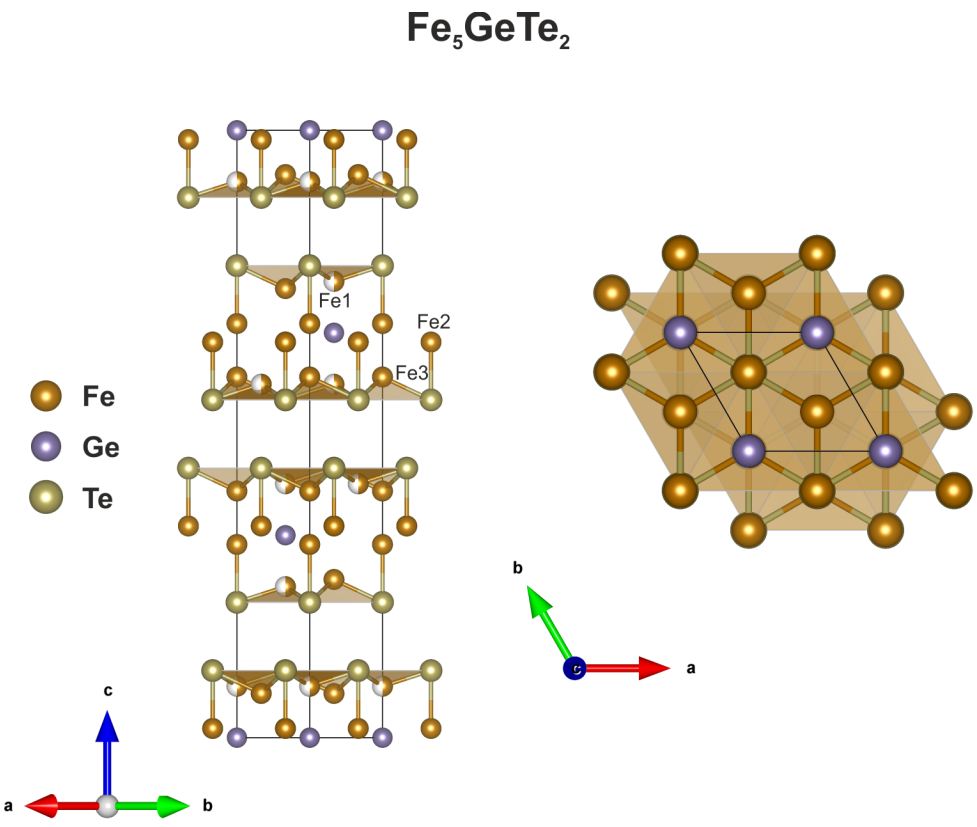

Figure 5.1: Crystal structure of Fe_5GeTe_2.

In bulk Fe_5GeTe_2,[1–3] the Curie temperature, T_C, varies between 270 - 310 K depending on Fe content and the thermal history of the crystals.[3] This temperature can be further enhanced by doping with Co, which also induces a ferromagnetic to antiferromagnetic transition.[4,5] However, due to the complex structure and magnetic properties, no unified description of the temperature dependence of the magnetisation has been reported. Calculated magnetic exchange parameters show the presence of both ferromagnetic and antiferromagnetic exchange between Fe sublattices.[6] Monte Carlo simulations suggest exotic temperature-dependant magnetisation and the presence of significant canting at 0 K, indicating the magnetic order is complex and not strictly collinear.[6] This is further supported by the observation of helimagnetism in Fe_5GeTe_2 crystals.[7] DFT calculations also report some degree of swapping between Fe atoms on the partially occupied Fe1 sublattice which it was claimed could contribute to the unusual magnetism observed in Fe_5GeTe_2.[6]

Fe_5GeTe_2 crystallises in trigonal space group $R\bar{3}m$ with lattice parameters a = 4.04(2) Å and c = 29.19(3) Å. The structure exhibits ABC stacking along the c axis, but has a tendency to form stacking faults.[3] The crystal structure exhibits further complexities; Ge is split between two closely spaced positions with a fractional occupancy of 0.5 each (i.e. a fully-occupied "split site"), caused by the fractional occupancy of the Fe1 site of 0.47(2).[1] This is shown in Figure 5.2.

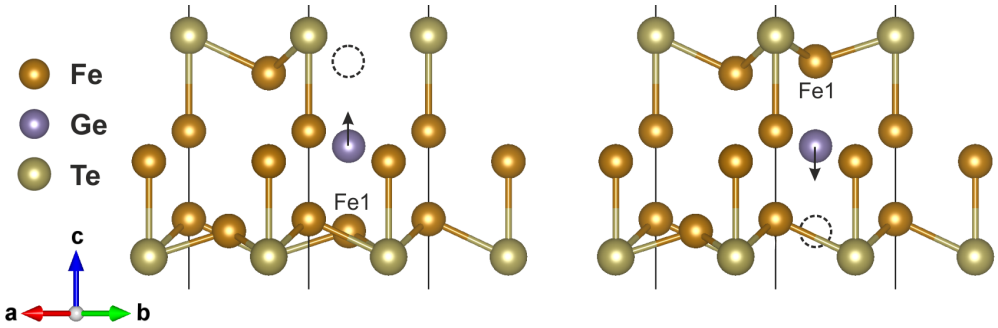

Figure 5.2: A schematic showing the origin of the Ge site splitting caused by the position of the Fe1 atom in each individual layer. The alternative Fe1 position is shown by the dashed circle.

Fe_5GeTe_2 can also be described with less disorder using a 3a× 3a supercell.[1,7] The synthesis method is also found to play a crucial role in determining the Fe content, and quenching was an important step in producing single crystal diffraction data suitable for structural solutions.[3]

To date, there are no reports of intercalation into Fe_5GeTe_2 although its layered structure makes this material an ideal host candidate. Here, the synthesis and characterisation of the potassium and lithium-amide intercalated phases are presented.

5.2 Synthesis of Fe_5GeTe_2

All syntheses were carried out in a Glovebox Technology argon-filled dry glove box with an O_2 content below 1 ppm or on a Schlenk line. Poly-crystalline samples of Fe_5GeTe_2 were synthesised by grinding together iron powder (Alfa Aesar; 99.998 %), germanium powder (Alfa Aesar; 99.99 %) tellurium powder (Alfa Aesar; 99.999 %) in stoichiometric amounts using an agate pestle and mortar until homogeneous. The mixture was then sealed inside an evacuated silica tube and heated at 750 °C for 10 days (ramp rate of 5 °C min^{-1}). Powders were then quenched into an ice/water bath. The Rietveld refinement of Fe_5GeTe_2 can be found in Figure 5.3. No obvious superstructure or stacking faults appear in the powder samples.

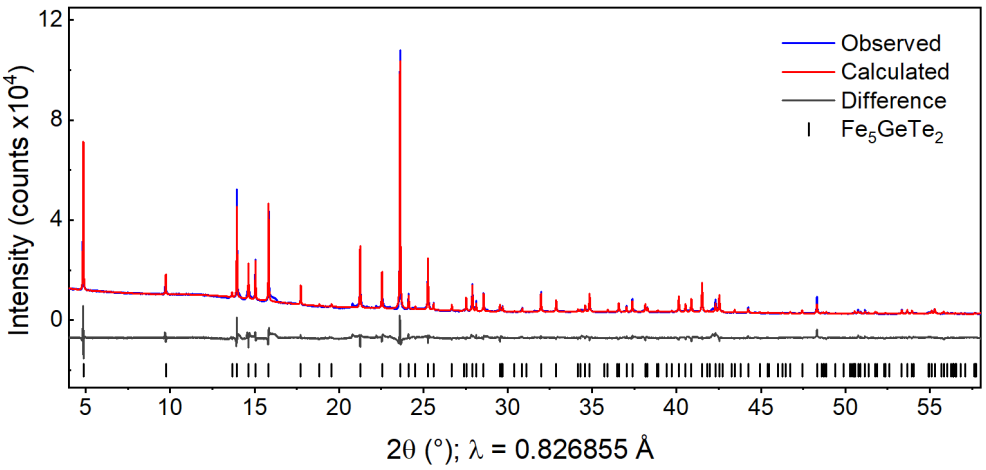

Figure 5.3: Rietveld fit against PXRD data of Fe_5GeTe_2 ($R\bar{3}m$) collected using the PSD on the I11 beamline, Diamond Light Source. R_{wp} = 5.98 %.

5.3 Lithium and ammonia intercalated Fe_5GeTe_2

Lithium-ammonia intercalates were synthesised by adding Fe_5GeTe_2 powder, a magnetic stirrer bar, and an amount of Li metal (Sigma Aldrich; 99 %) to give the stoichiometry $LiFe_5GeTe_2$ to a Schlenk tube. This was then attached to a Schlenk line along with a cylinder of ammonia (BOC; 99.98 %). The Schlenk tube was then placed in a bath of isopropanol and dry ice and cooled to approximately −78 °C, before a small volume (approximately 10 cm^3) of NH_3 was condensed over the reagents. The characteristic blue solution of dissolved electrons was observed, no decolourisation occurs during the first 30 minutes of the reaction. The mixture was then left to stir until the ammonia has evaporated via the manometers of the Schlenk line, typically 3 hours, leaving a powder of the intercalated product. The resulting solid was then dried under dynamic vacuum for 20 minutes.

5.3.1 Powder X-ray Diffraction

Initial powder X-ray diffraction patterns were collected using laboratory diffraction instruments to assess crystallinity and check for phase purity, as described in Chapter 2. PXRD patterns collected sometime after the synthesis of $Li(NH_2)Fe_5GeTe_2$ indicated some decomposition had occurred. Initially this was thought to be the failure of the air-tight seal on the air sensitive PXRD sample holders. However, this observation was found to persist during subsequent measurements, irrespective of sample holder or instrument. To further investigate, a fresh sample of $Li(NH_2)Fe_5GeTe_2$ was synthesised and the PXRD pattern was collected. Subsequent measurements were made at two weeks, three weeks and four weeks after the initial synthesis. These patterns are shown in Figure 5.4. The data collected three weeks post synthesis shows signs of decomposition, and by four weeks the reflections attributed to the intercalated phase has completely diminished. This result is unusual given that all samples were stored in a dry Ar-filled glovebox, yet this decomposition occurs under inert conditions, suggesting a thermal instability.

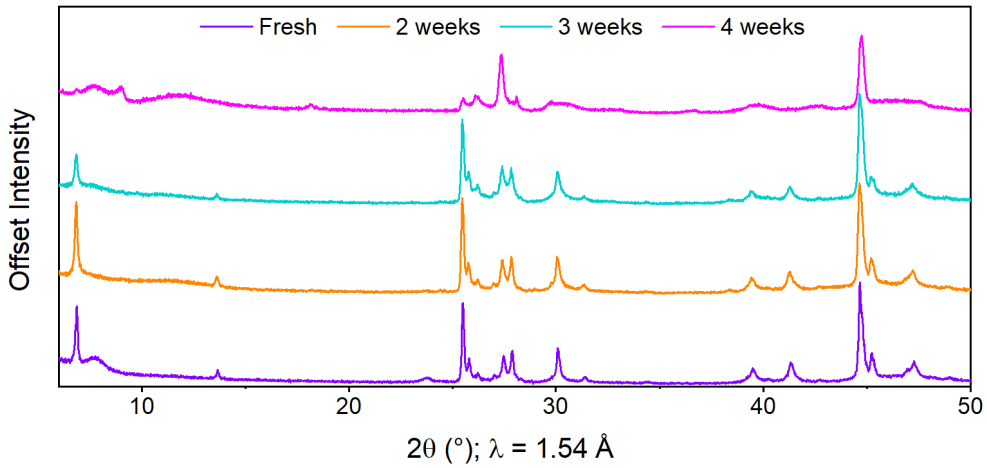

Figure 5.4: PXRD patterns of $Li(NH_2)Fe_5GeTe_2$ collected at various intervals after synthesis.

Numerous attempts at collecting high resolution synchrotron PXRD data were made, however none was successful. Given the high phase instability demonstrated by the degradation under inert conditions, it's possible that either momentary exposure to air or heat during the capillary sealing procedure causes decomposition of the phase, or decomposition occurs through heating by the intense synchrotron beam. Alternative methods of sealing were attempted, by using a small amount of superglue inside a glovebox and by filling the capillary with glass in the region where it is sealed, however these were also unsuccessful. As such, the primary structural characterisation of this phase was performed against data collected on the PANalytical X'Pert Empyrean Diffractometer collected over three hours in an effort to increase the resolution. The high level of background noise has been attributed to fluorescence from the high concentration of Fe in the sample, shown in Figure 5.5. The PXRD pattern shows no obvious signs of superstructure or stacking faults.

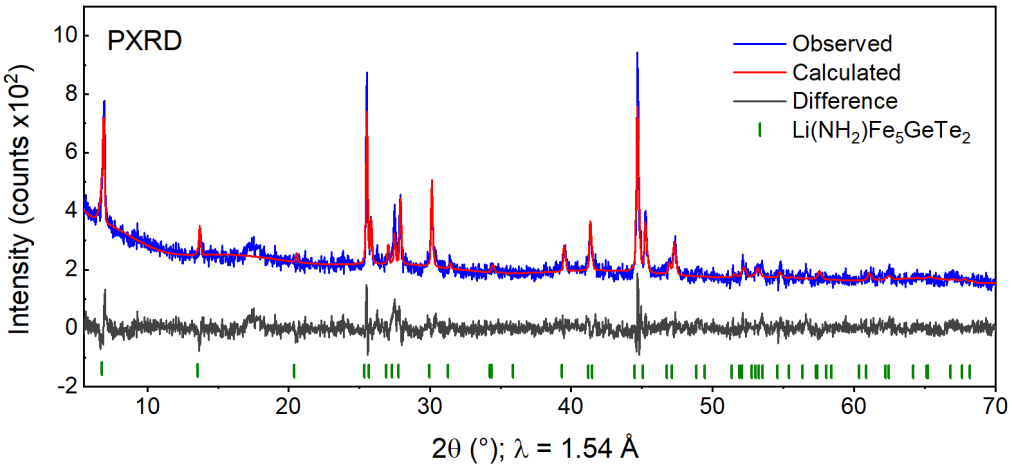

Figure 5.5: Rietveld fit of the PXRD pattern of $Li(NH_2)Fe_5GeTe_2$ ($R\bar{3}m$) collected using the PANalytical Empyrean diffractometer. R_{wp} = 7.96 %.

The PXRD pattern of the intercalate could be well indexed using the auto-indexing routines in the TOPAS Academic V6 software, to a hexagonal unit cell with space group $R\bar{3}m$, a = 4.0641(6) Å and c = 39.094(9) Å, similar to that of the parent with an increase in c of 9.192 Å (30.7 %). Assuming the Fe–Ge–Te layers remain unchanged, this is equivalent to an increase of 3.064 Å per van der Waals gap. Since the crystal radius of Li^+ is only approximately 1 Å in a six co-ordinate site,[8] this indicates that the co-intercalation of NH_3 had occurred.

A preliminary structural model that closely resembled the parent phase in terms of atomic positions and intralayer bond distances was built in a unit cell with unit cell parameters obtained from the indexing described above. After refinement, this model was found to be a good fit to the data and it was concluded that no layer rearrangement had occurred. Refined parameters of the Fe–Ge–Te layers are given in Table 5.1 on page 207.

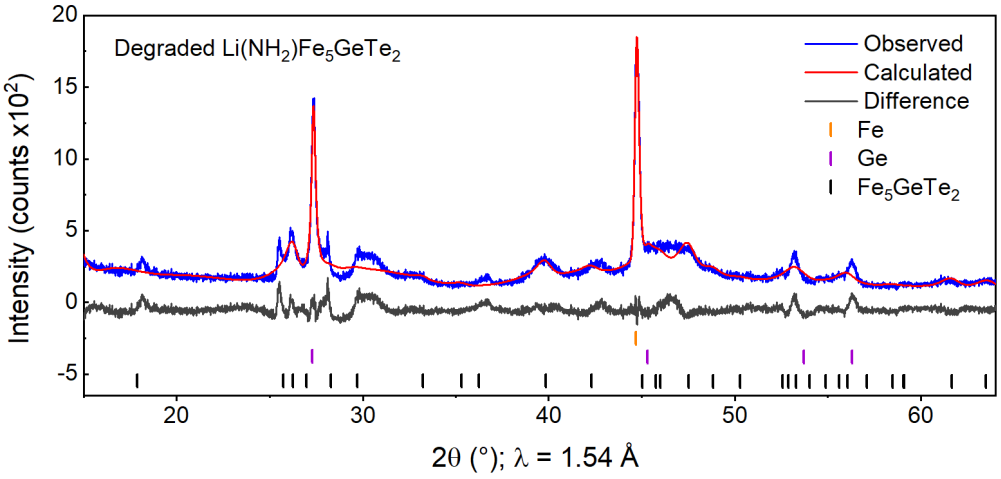

Figure 5.6: Rietveld fit of the PXRD pattern of the decomposition products $Li(NH_2)Fe_5GeTe_2$ under inert conditions, collected using the PANalytical Empyrean diffractometer. R_{wp} = 18.39 %.

A Rietveld fit of the PXRD pattern collected 4 weeks post synthesis was attempted to study the decomposition of $Li(NH_2)Fe_5GeTe_2$. The identifiable impurity phases were Fe, Ge and the parent phase Fe_5GeTe_2. Some additional broad reflections, shown in Figure 5.6, could not be formally assigned but may be phases accounting for the light elements, in addition to some possible amorphous phases.

5.3.2 Powder Neutron Diffraction

In order to locate the light atoms Li, N and H, neutron diffraction was performed using the D2B instrument at the ILL. Since hydrogen containing samples usually have a high background due to the large incoherent scattering length of hydrogen, deuterated samples were measured in addition. The higher scattering length of D compared to H, as well as the opposite sign (6.67 fm and −3.74 fm respectively), is also useful for identifying H/D positions in the unit cell.

Two 2 g samples were synthesised using condensed NH_3 and ND_3. The hydrogenated sample was measured at 300 K, whilst the deuterated sample was measured at 300 K and 10 K to obtain information about the magnetic structure. The preliminary nuclear model obtained from the PXRD data provided a good fit to all three patterns, given that the strong scatterers N and D (scattering lengths 9.36 fm and 6.67 fm respectively) were not yet included in the model.

To complete the structural model, Li, N and H/D sites were added. From inspection, there are two distinct likely crystallographic sites in the interlayer spacing, with different co-ordination environments. Three different models were fitted to the data - two in which Li and NH_2 occupy different sites and one in which Li/NH_2 moieties share a crystallographic site. It was found that Li and NH_2 moieties occupy different sites, primarily driven by the co-ordination requirements of NH_2. The final model is shown in Figure 5.9. The Rietveld fits of this single model against the two PND patterns collected at ambient temperature are shown in Figures 5.7 and 5.8, with extracted parameters given in Table 5.1. To fit the data from the hydrogenated

sample, the parameters of the H atoms had to be constrained to the values obtained from the refinement against the PND pattern of the deuterated sample. This was due to the low neutron scattering length of H compared to D (H: -3.74 fm, D: 6.67 fm), and the higher background when H was present.

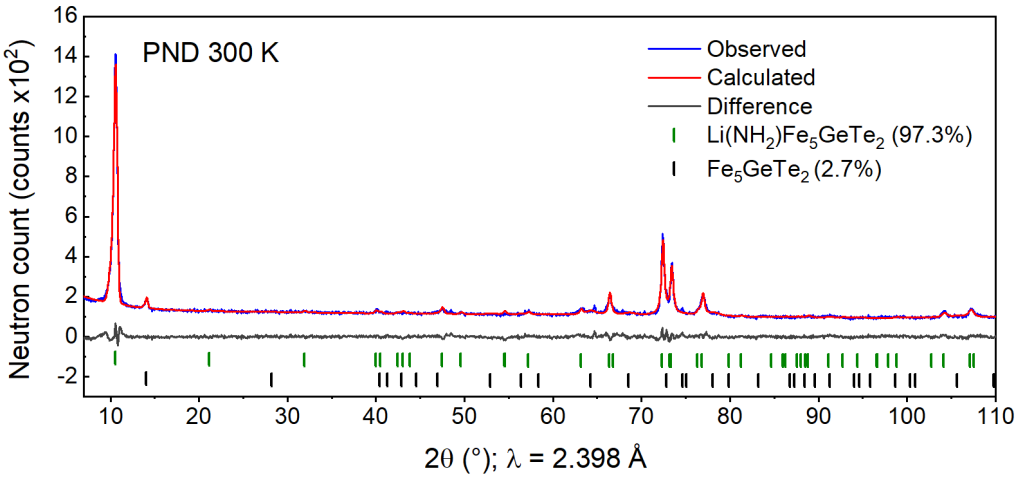

Figure 5.7: Rietveld fit of the PND pattern of $Li(NH_2)Fe_5GeTe_2$ ($R\bar{3}m$) collected at 300 K using the D2B instrument at the ILL. R_{wp} = 4.77 %.

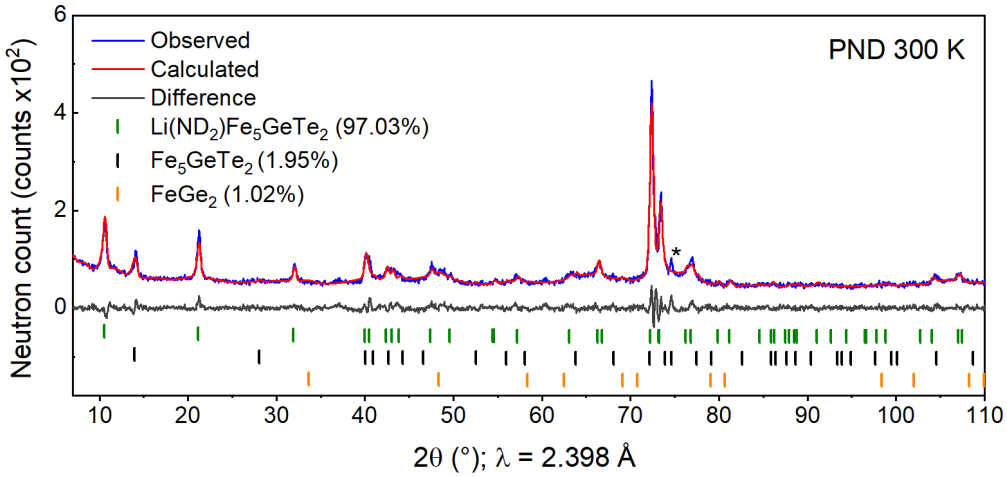

Figure 5.8: Rietveld fit of the PND pattern of $Li(ND_2)Fe_5GeTe_2$ ($R\bar{3}m$) collected at 300 K using the D2B instrument at the ILL. Reflections that could not be assigned is marked by an asterisk (*). R_{wp} = 7.97 %.

Table 5.1: Refinement parameters from the Rietveld fit against PXRD data of $Li(NH_2)Fe_5GeTe_2$. Parameters obtained from PND data is given in parentheses (). * indicates parameters that were fixed.

$Li(NH_2)Fe_5GeTe_2$ RMM = 629.98 g mol^{-1}, Z = 3						
Diffractometer				Empyrean (D2B (ILL))		
Temperature (K)				300		
Space group				$R\bar{3}m$ (166)		
a (Å)				4.0641(6) (4.0654(2))		
c (Å)				39.095(9) (39.222(4))		
V (Å^3)				559.2(2) (561.39(7))		
Atom	Site	x	y	z	Occ	U_{iso} (Å^2)
Fe1	6c	0	0	0.072(10) (0.056(3))	0.47(3) (0.5)*	0.37(4) (0.045(9))
Fe2	6c	0	0	0.320(3) (0.3217(5))	1	0.24(3) (0.051(1))
Fe3	6c	0	0	0.409(2) (0.3829(3))	1	0.28(9) (0.051(1))
Ge	3a	0	0	0	1	0.28(3) (0.051(7))
Te	6c	0	0	0.246(1) (0.2541(9))	1	0.37(3) (0.049(7))
N	(3b)	(0)	(0)	(0.5)	(0.85(9))	(0.094(9))
Li	(6c)	(1/3)	(2/3)	(0.5)	(0.5)*	(0.48(6))
H/D	(18h)	(0.06(1))	(0.94(1))	(0.489(2))	(0.24(6))	(0.022(5))

NH_2 is found to exclusively occupy a six co-ordinate triangular antiprism site, whilst Li is found in an elongated triangular pyramidal site with a partial occupancy of 0.5. This arrangement is driven by the co-ordination requirements of NH_2, which forms hydrogen bonds with Te at a distance of 3.07(8) Å and a N–H–Te bond angle of 178(8) °. The N–H and N–Li bond lengths refined to 0.98(8) Å and 2.345(1)

Å respectively. These values are in agreement with distances reported for Li-NH_2 intercalates of Bi_2Se_3 and FeSe,[9,10] which report N–H and H–Se distances of approximately 1 Å and 2.7 Å respectively, and a N-H-Se bond angle of approximately 180 °. D was found to have an average occupancy of $\frac{1}{3}$ on each of the six sites, suggesting they are randomly orientated between these sites. The refined occupancies of H/D are in good agreement with the combustion analysis which gives a H:N ratio of 2.04(3), and gives an overall stoichiometry of $Li(NH_2)Fe_5GeTe_2$.

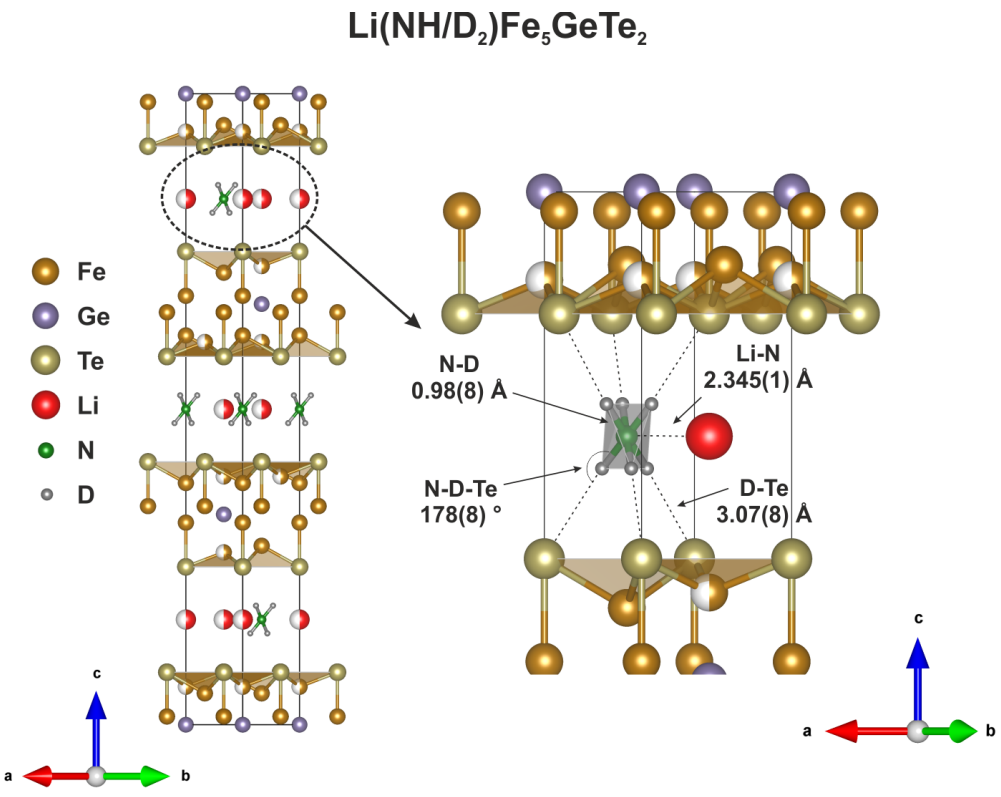

Figure 5.9: Structural model of $Li(NH/D_2)Fe_5GeTe_2$.

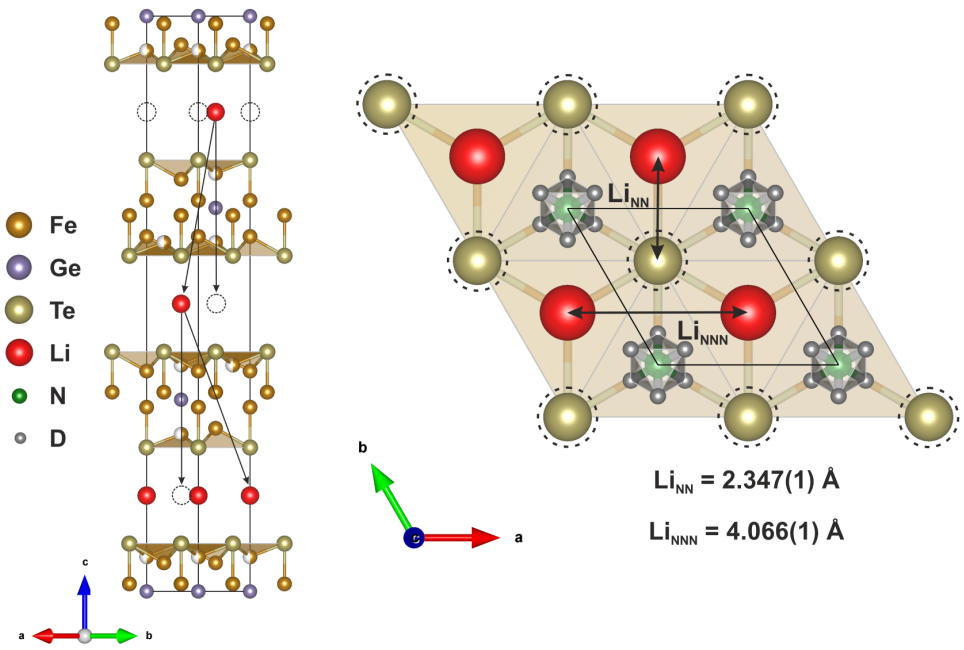

Figure 5.10: Structural model demonstrating the proposed ordering of Li in each layer. Vertical arrows denote the two possible Li sites layer to layer. Li_{NN} denotes the Li-Li nearest neighbour distance, Li_{NNN} denotes the Li-Li next nearest neighbour distance. Dashed circles represent the alternative Li positions.

From the Rietveld refinement against PND data the Li site has an occupancy of 0.5 over the two symmetry-generated positions, which gives a Li:N ratio of 1, since Li and N occupy 6*c* and 3*b* sites respectively. This is in good agreement with the stoichiometry of the reaction and the chemical analysis which gives a Li:Ge ratio of 1.1:1. It is proposed that the Li positions are disordered layer to layer, resulting in the site occupancy averaging, however it is difficult to determine if Li is ordered within each layer or not. The nearest-neighbour and next-nearest-neighbour Li–Li distances are 2.347(1) Å and 4.066(1) Å respectively, shown in Figure 5.10. Since the crystal radius of Li^+ is 0.73 Å,[8] Li atoms could occupy the nearest-neighbour sites in theory, however the closest Li–Li distance in crystalline $LiNH_2$ is 3.58 Å.[11] Therefore, it is reasonable that the Li atoms occupy next-nearest-neighbour sites within each layer.

Table 5.2: Refined lattice parameters and weighted average bond lengths from Rietveld fits of the PXRD pattern of Fe_5GeTe_2 and the PXRD and PND patterns of $Li(NH_2)Fe_5GeTe_2$ and $Li(ND_2)Fe_5GeTe_2$.

	Fe_5GeTe_2	$Li(NH_3)Fe_5GeTe_2$		$Li(ND_3)Fe_5GeTe_2$	
Radiation	PXRD	PXRD	PND	PND	PND
T (K)	300	300	300	300	10
a (Å)	4.04088(3)	4.0641(6)	4.0654(2)	4.067(2)	4.0621(4)
c (Å)	29.2024(3)	39.095(9)	39.222(4)	39.26(4)	38.90(1)
V (Å^3)	412.95(1)	559.2(2)	561.39(7)	562.2(9)	555.8(2)
$(Fe\text{-}Ge)_{ave}$	2.704	2.728	2.675	2.673	2.671
$(Fe\text{-}Te)_{ave}$	2.568	2.640	2.678	2.675	2.672

Inspection of the lattice parameters in Table 5.2 shows that the a lattice parameter remains unchanged, whilst the c lattice parameter increases by approximately 10 Å, which is consistent across all samples. The weighted average bond distances show an increase in the Fe–Te bond distance in all intercalated samples, which could be a result of electrostatic attraction between Te and Li^+, or H-bonding between NH_2^- and Te. Contrary to this, the average Fe-Ge bond distance in the intercalated phases changes relatively little in comparison to Fe_5GeTe_2.

PND data of the deuterated sample was also collected at 10 K, to assess any long-range magnetic ordering through the emergence of magnetic peaks. A comparison of the PND patterns collected at 10 K and 300 K are shown in Figure 5.11.

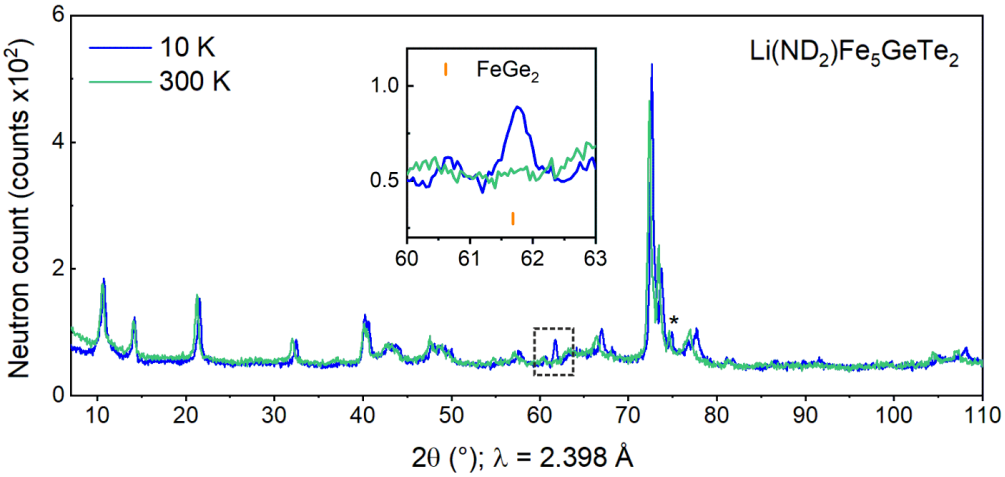

Figure 5.11: PND patterns of $Li(ND_2)Fe_5GeTe_2$ collected at 300 K and 10 K using the D2B instrument at the ILL. The inset shows the reflection with magnetic intensity. Reflections that could not be assigned have been marked with an asterisk (*).

Only one temperature dependent reflection is observed at approximately $2\theta = 62$ °. This was found to be incommensurate with the structural unit cell, or the Fe_5GeTe_2 impurity. A $2a$ x $2a$ unit cell expansion was generated using ISODISTORT.[12,13] This however generated a large number of possible magnetic modes, none of which could be fit to the data and produce a sensible model. Later, this was attributed to $FeGe_2$, an impurity phase identified in the room temperature PND pattern, which is a commensurate antiferromagnet below 263 K.[14] The fit of the data collected at 10 K is shown in Figure 5.12. We conclude that there is no long-range magnetic order observable by powder neutron diffraction.

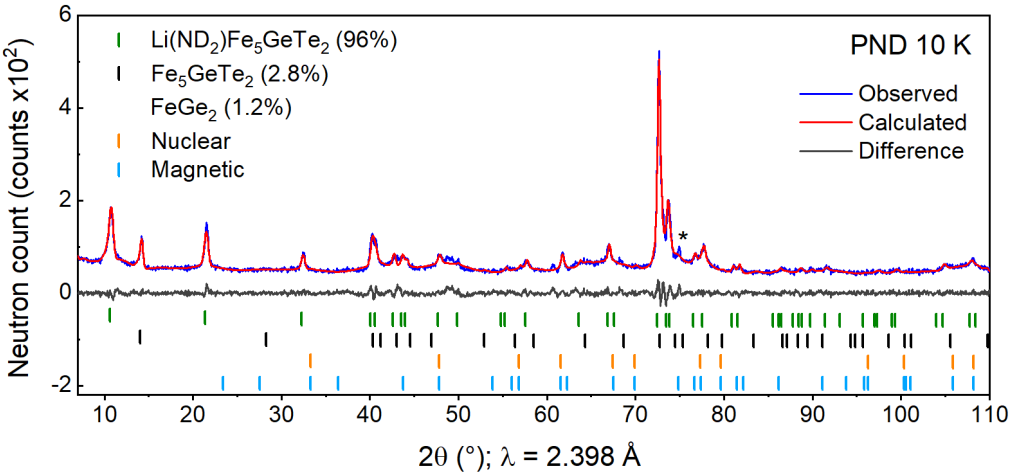

Figure 5.12: Rietveld fit of the PND pattern of $Li(ND_2)Fe_5GeTe_2$ ($R\bar{3}m$) collected at 10 K using the D2B instrument at the ILL. Reflections that could not be assigned is marked by an asterisk (*). $R_{wp} = 9.01$ %.

5.3.3 Magnetometry

The room temperature ferromagnetism exhibited by Fe_5GeTe_2 was one of the motivations for attempting to manipulate this phase through intercalation. Figure 5.13 shows the magnetic susceptibility as a function of temperature of both Fe_5GeTe_2 and $Li(NH_2)Fe_5GeTe_2$, measured in a field 100 Oe. Inspection of the 280 – 330 K region (shown in inset) shows an increase in the Curie temperature by approximately 10 K, from 300 K to 310 K upon intercalation of lithium and ammonia/amide.

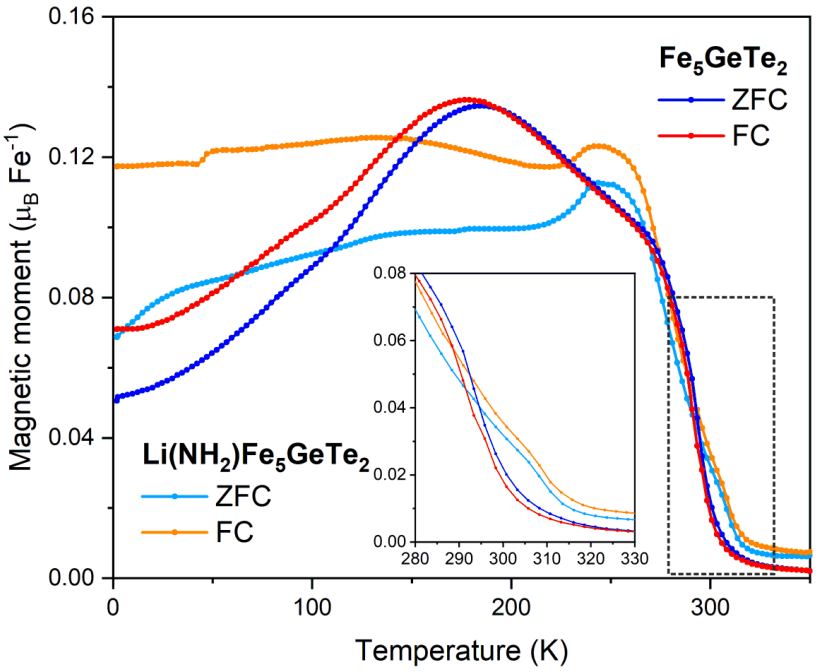

Figure 5.13: Magnetic moment vs temperature of Fe_5GeTe_2 and its lithium-ammonia intercalate, cooled in a field of 100 Oe.

Due to the complex magnetic behaviour described previously[6,7] it is difficult to fully rationalise this observation. However, the separation of the Fe containing layers may reduce any competing magnetic interactions. The general shape of the magnetisation curves also change, implying more complicated magnetic changes are occurring.

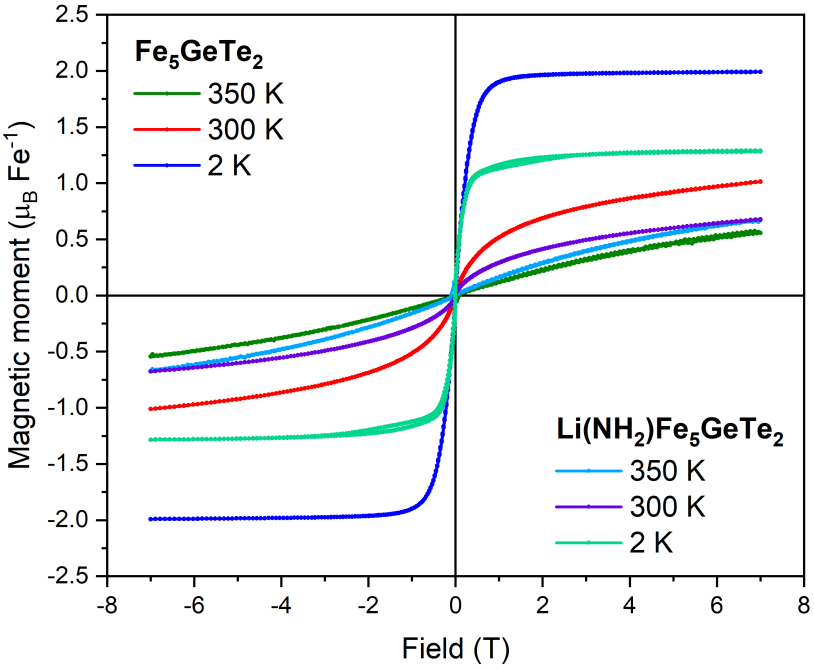

Figure 5.14: Magnetisation isotherms of Fe_5GeTe_2 and $Li(NH_2)Fe_5GeTe_2$ measured at 350 K, 300 K and 2 K over the range ±7 T.

Magnetic isotherms of Fe_5GeTe_2 and $Li(NH_2)Fe_5GeTe_2$ measured at 2 K, 300 K and 350 K between fields of ±7 T are shown in Figure 5.14. The key observation is that both phases reach saturation, but there is significant reduction in the saturation moment of $Li(NH_2)Fe_5GeTe_2$ relative to the parent phase, by approximately 35 % at 2 K. Since these systems exhibit elements of both localised and itinerant ferromagnetism,[15] it is difficult to rationalise this observation without a thorough understanding of the coupling mechanisms in this compound. Remnant ferromagnetic behaviour is observed at 300 K as expected. The data collected at 350 K appear to have a slight curvature, which might indicate superparamagnetism above the Curie temperature.

5.3.4 Mössbauer Spectroscopy

In order to further probe the magnetic ordering, Mössbauer spectroscopy measurements were performed at 300 K, 150 K, 50 K and 10 K. The fitted data can be found in Figure 5.15 with extracted parameters given in Table 5.3.

Table 5.3: Parameters from fitting Mössbauer data of $Li(NH_2)Fe_5GeTe_2$ collected at 300 K, 150 K, 50 K and 10 K.

Site	Label	CS (mm/s)	Δ (δ) (mm/s)	Population (%)
		300 K		
Fe	Doublet 1	0.333(15)	0.334(45)	100
		150 K		
Fe	Doublet 1	0.440(11)	0.777(17)	40.4(15)
	Sextet 1	0.501(32)	-0.034(30)	17.5(63)
	Sextet 2	0.463(18)	-0.003(18)	31.4(62)
	Sextet 3	0.425(17)	-0.052(17)	10.8(17)
		50 K		
Fe	Doublet 1	0.503(50)	1.073(83)	9.8(27)
	Sextet 1	0.551(23)	-0.024(20)	43.3(51)
	Sextet 2	0.467(21)	0.020(21)	32.5(50)
	Sextet 3	0.668(82)	0.096(72)	14.4(39)
		10 K		
Fe	Doublet 1	0.515(37)	1.188(65)	4.2(12)
	Sextet 1	0.523(20)	0.004(19)	43.8(43)
	Sextet 2	0.472(15)	0.020(14)	32.4(38)
	Sextet 3	0.500(56)	0.013(39)	19.6(23)

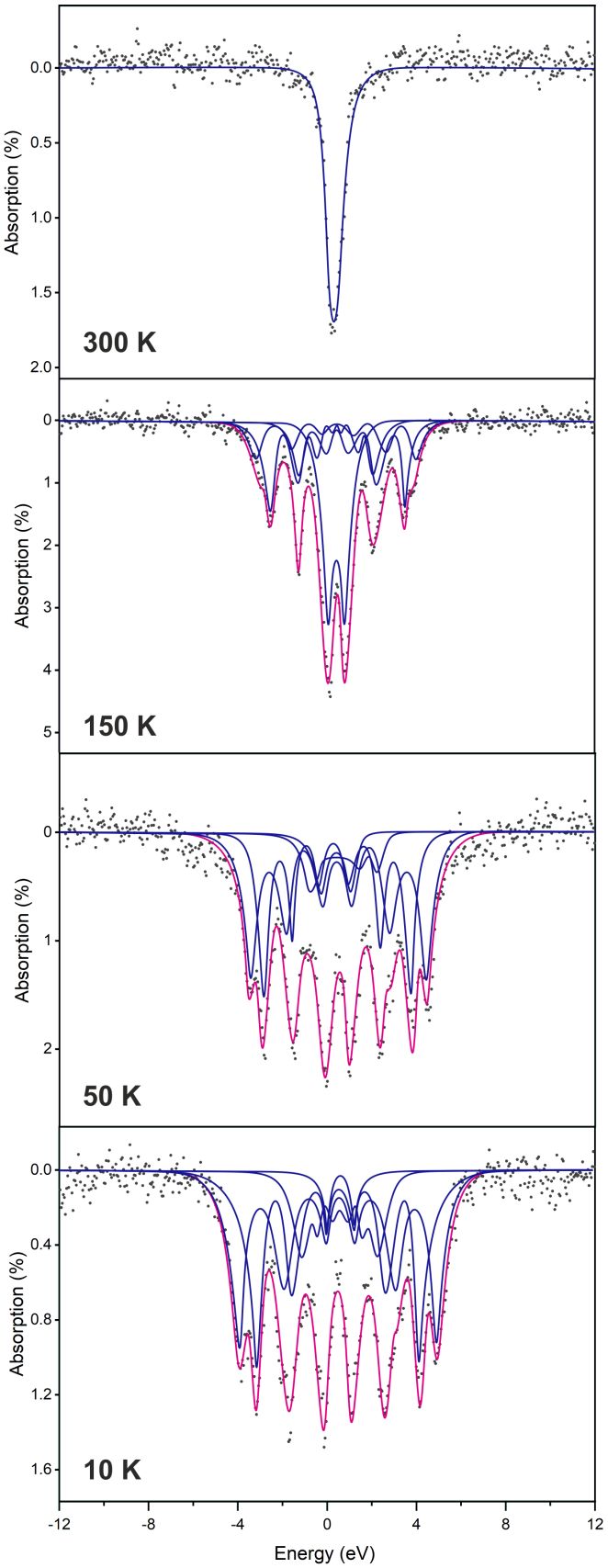

Figure 5.15: Fitted Mössbauer spectra of $Li(NH_2)Fe_5GeTe_2$ at 300 K, 150 K, 50 K and 10 K.

At 300 K, there is no evidence of any Fe ordering and the data can be fit as a single doublet which encompasses all of the Fe sites in the structure. This is contrary to the SQUID magnetometry data, which suggests the Curie temperature is approximately 305 K, However, the measurement temperature is very close to the Curie temperature, and at 300 K the magnetic susceptibility is still relatively small. The signal shown in the SQUID data could plausibly be from a very small subset of Fe ions which is not well resolved in the Mössbauer spectrum.

As predicted, the data collected at 150 K show some magnetic ordering, approximately 60 % of the iron sites. Due to the similar Δ (δ) and centre shift (CS) values of the ordered sites, they could not be assigned to distinct crystallographic Fe sites.

The data collected at 50 K and 10 K are both visually similar and have numerically comparable parameters. This indicates there is very little change in the magnetic ordering between these two temperatures, and leads us to conclude magnetic ordering is complete by 50 K. At both these temperatures, sextet 3 has been assigned to the Fe1 site based on its population, as the theoretical populations of the Fe1, Fe2 and Fe3 sites are 20 %, 40 % and 40 % respectively. Sextets 2 and 3 were assigned to the Fe2 and Fe3 sites on this basis, however the relative assignments could not be concluded from this data. The persistence of a doublet at low temperatures suggests that a small number of the Fe ions do not participate in the magnetic ordering. This is consistent with the low temperature Mössbauer spectrum of the parent Fe_5GeTe_2.[1]

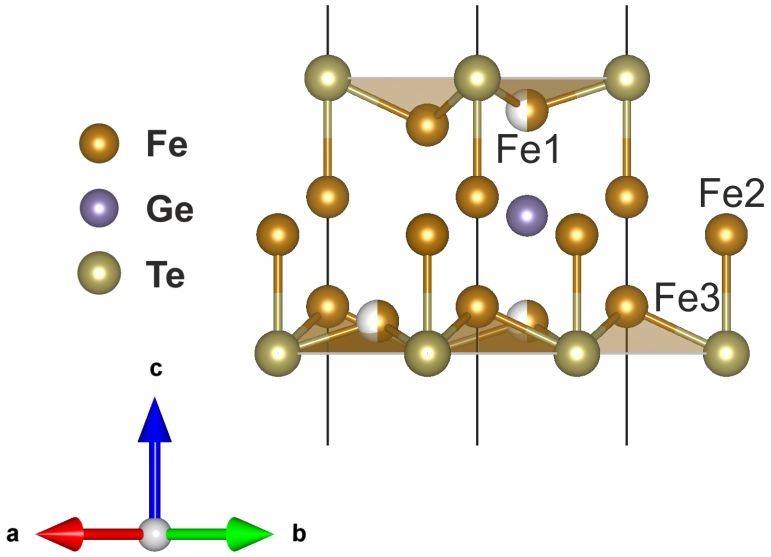

Figure 5.16: Structural model of a layer of Fe_5GeTe_2 showing the three different Fe sites.

The data collected at 150 K follows the assignments of the data at 10 K and 50 K. Since the populations of all three sextets increases between 50 K and 150 K, the doublet at 150 K has been assigned of the unordered proportions of all three Fe sites. Between 10 K and 50 K, the population of the Fe2/3 sites change very little, leading to the conclusion the Fe1 site is the last to order, and the doublet at 50 K has a large proportion of unordered Fe1 atoms. It should be noted however that the doublet has a very low population.

5.4 Potassium intercalated Fe_5GeTe_2

Potassium intercalates were synthesised by adding Fe_5GeTe_2 powder, a magnetic stirrer bar, and an amount of K metal (Sigma Aldrich; 99%) to give the stoichiometry KFe_5GeTe_2 to a Schlenk tube. This was then attached to a Schlenk line along with a cylinder of ammonia (BOC; 99.98%). The Schlenk tube was then placed in a bath of isopropanol and dry ice and cooled to approximately −78 °C, before a small volume (approximately 10 cm^3) of NH_3 was condensed over the reagents, as described in Chapter 2. The characteristic blue solution of dissolved electrons was observed. Decolourisation occurred within two minutes of the condensation of ammonia, in contrast to the intercalation of Li. The mixture was then left to stir until the ammonia had evaporated via the manometers of the Schlenk line, typically 3 hours, leaving a powder of the intercalated product. The resulting solid was then dried under dynamic vacuum for 20 minutes.

5.4.1 Powder X-ray Diffraction

Initial PXRD patterns were collected using laboratory diffractometers to assess crystallinity and phase purity. Figure 5.17 shows the PXRD pattern measured using the PANalytical Empyrean Diffractometer described in Chapter 2.

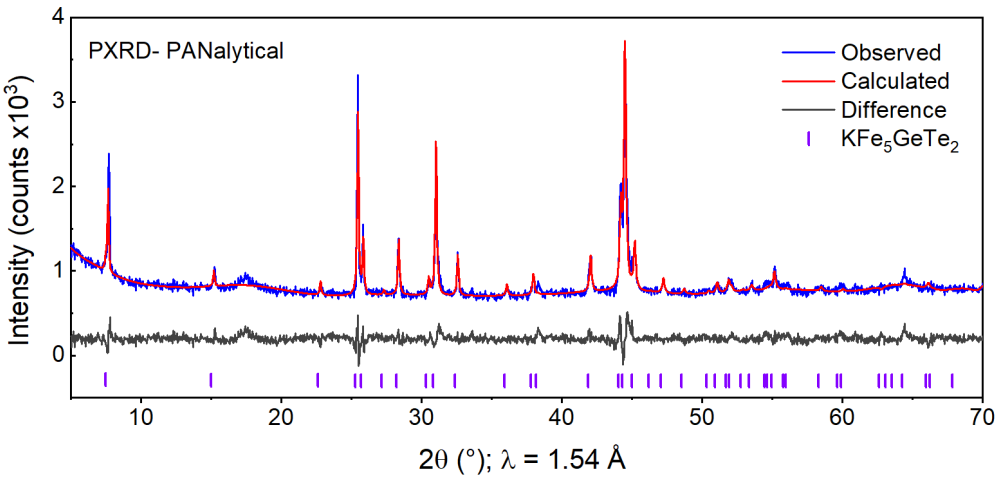

Figure 5.17: Rietveld refinement against the PXRD pattern of KFe_5GeTe_2 ($R\bar{3}m$) collected using the PANalytical Empyrean diffractometer. R_{wp} = 6.65 %.

The laboratory PXRD pattern could be well indexed to a single phase with a hexagonal cell in $R\bar{3}m$ with lattice parameters $a = 4.071(1)$ Å and $c = 34.61(2)$ Å. Although a is comparable to Fe_5GeTe_2, c is found to increase by 18.5 %, and is equivalent to an increase of 1.84 Å per interlayer spacing. This increase is less than the Shannon radius of K (1.4 Å)[8] so it was concluded that no co-intercalation of NH_2 or NH_3 had occurred. This is likely due to the lower charge density of potassium compared to a smaller alkali metal, such as lithium, and has been discussed in relation to the intercalates of Ta_2NiSe_5 in Chapter 3. As with the Li-ammonia intercalate, no obvious signs of stacking faults or superstructure are present in the PXRD pattern.

Since the indexed space group was the same as for Fe_5GeTe_2 and the lattice parameters are clearly related, a preliminary model that closely resembled the parent structure was build inside a unit cell with the lattice parameters and symmetry obtained by indexing. In this model, the bond lengths within each Fe–Ge–Te slab were maintained whilst the van der Waals' gap was allowed to increase.

This model proved to be a good fit to the data, and two potassium sites were visually identified in the interlayer spacing at (0, 0, 1/2) and (1/3, 2/3, 1/2). Inspection of the Fourier map generated using the TOPAS software confirmed a scattering centre present at (0, 0, 1/2) but not at (1/3, 2/3, 1/2). K occupancy was modelled on both sites regardless to confirm this observation. As expected, sensible occupancy and thermal displacement parameters could only be refined on the (0, 0, 1/2) site.

Synchrotron PXRD data were collected to take advantage of the reduced linewidth and improved resolution of the data. However, a significant intensity mismatch was observed between laboratory data, shown in Figure 5.17, and synchrotron data, shown in Figure 5.18. This was hypothesised to be a result of the flat shape of the crystallites in conjunction with the capillary packing procedure and the axial rotation (i.e not 3D tumbling) resulting in the increased intensity of the $00l$ reflections.

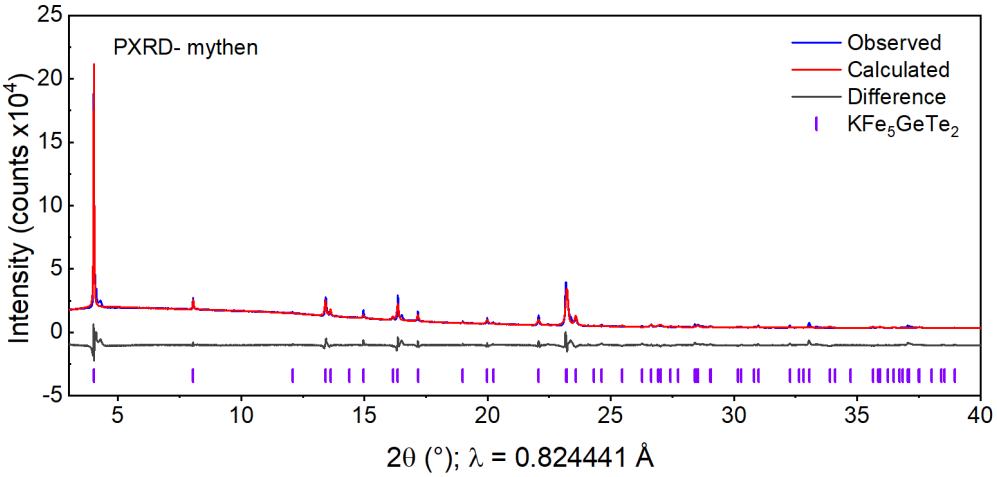

Figure 5.18: Rietveld refinement against the PXRD pattern of KFe_5GeTe_2 ($R\bar{3}m$) collected using the PSD detector on the I11 beamline at Diamond. R_{wp} = 7.39 %.

A Rietveld fit against the synchrotron data was still achieved, however the structure had to be modelled using a significant amount of preferred orientation, discussed in Chapter 2. This was to account for the stacking of the plate-like particles along one direction in the sample capillary, which we propose causes the relative change in intensities. In addition, several constraints on atomic positions were required to produce a suitable model. Because of this, the final model uses parameters from the fit against laboratory data due to the greater intensity of the $hk0$ reflections and fewer constraints built into the model, at the cost of larger errors of the refined parameters. Parameters are given in Table 5.4. Refined parameters from PND data collected at room temperature, discussed later in this chapter, are also included in Table 5.4.

Table 5.4: Refinement parameters from the Rietveld fit against PXRD data of KFe_5GeTe_2. Parameters obtained from PND data is given in parentheses (). * indicates fixed parameters.

KFe_5GeTe_2 RMM = 646.11 g mol^{-1}, Z = 3						
Diffractometer				PANalytical Empyrean (D2B (ILL))		
Wavelength (Å)				1.54 (1.594)		
Temperature (K)				300		
Space group				$R\bar{3}m$ (166)		
a (Å)				4.0858(3) (4.1066(3))		
c (Å)				35.322(5) (35.284(5))		
V (Å^3)				510.7(2) (515.3(1))		
Atom	Site	x	y	z	Occ	U_{iso} (Å^2)
Fe1	6c	0	0	0.0703* (0.070(5))	0.5*	0.95(9) (0.027(2))
Fe2	6c	0	0	0.3175(2) (0.3231(1))	1	0.30(4) (0.010(1))
Fe3	6c	0	0	0.3825(2) (0.3881(1))	1	0.39(7) (0.011(1))
Ge	3a	0	0	0	1	0.31(5) 0.069(4)
Te	6c	0	0	0.2489(5) (0.2442(3))	1	0.58(7) (0.026(3))
K	3b	0	0	0.5	1.09(4) (1.1(1))	0.32(4) (0.035(9))

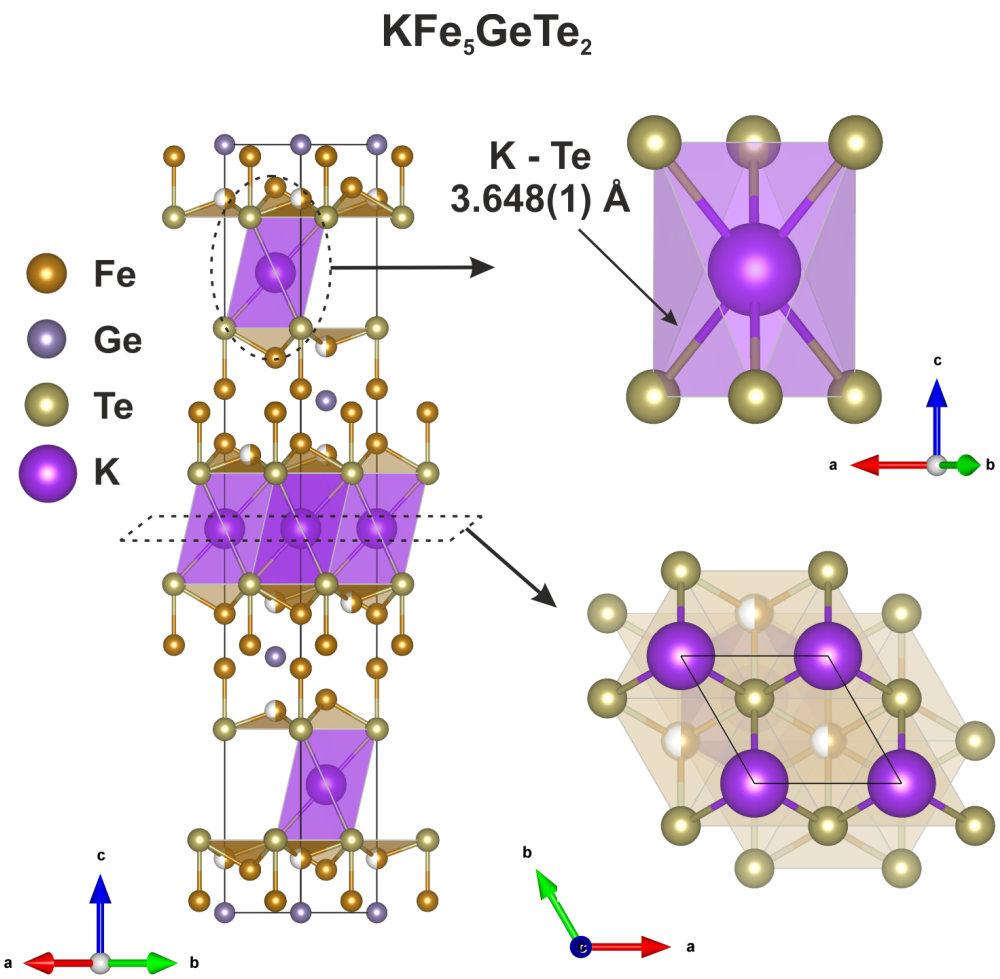

Figure 5.19: Structural model of KFe_5GeTe_2. **Left**. An extended unit cell of KFe_5GeTe_2. **Top right**. The co-ordination environment of potassium. **Bottom right**. KFe_5GeTe_2 viewed along the c-axis.

The structural model of KFe_5GeTe_2 obtained from the refinement of PXRD and PND data is shown in Figure 5.19. The general structure of the Fe–Ge–Te layers and their relative positions are retained, and potassium is found to exclusively occupy one site in the unit cell from two possible symmetry allowed positions in $R\bar{3}m$. The co-ordination geometries of each site fall into one of two categories, shown in Figure 5.20.

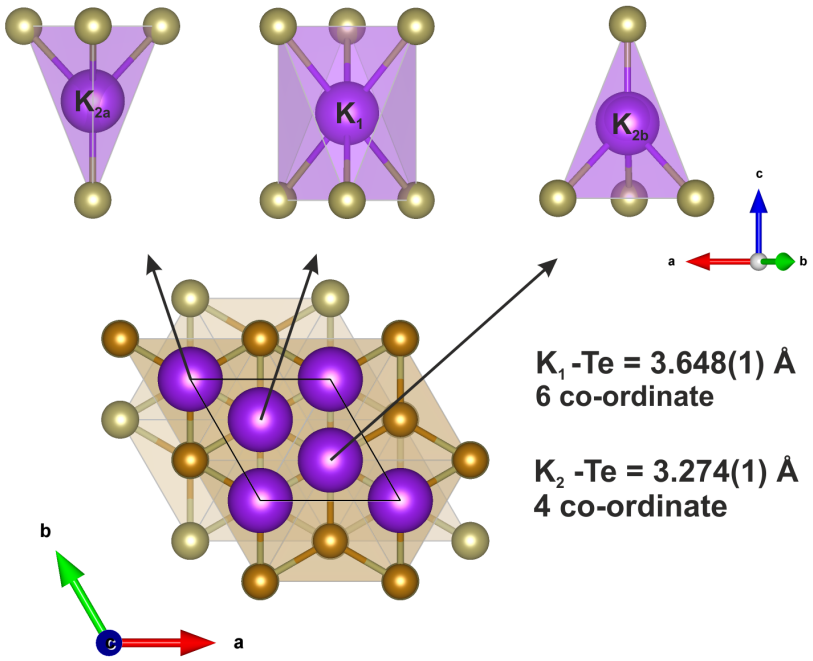

Figure 5.20: The possible co-ordination environments of potassium at each symmetry allowed interlayer site.

Closer inspection shows the site located at (0, 0, $\frac{1}{2}$) lies in a 6 co-ordinate trigonal antiprism with a K–Te bond length of 3.648(1) Å, whereas the other two sites are distorted tetrahedra with a smaller average bond length of 3.274(1) Å. Comparison to reported K–Te bond lengths, such as 3.58 Å in K_2PdTe_2 in which K occupies a 6 co-ordinate trigonal prism,[16] demonstrates the larger site is a better size match for potassium.

5.4.2 Powder Neutron Diffraction

Neutron diffraction was performed primarily to examine the magnetic structure of KFe_5GeTe_2. Although there are no light atoms to be located, these experiments were also useful to confirm the position of K, which is the weakest X-ray scatterer in the structure. Measurements were performed on the D2B instrument at the ILL, France. A 2 g sample was measured in a vanadium can sealed with an indium wire gasket, as described in Chapter 2, and measured at 10 K and 300 K. The Rietveld refinement against ambient temperature data is consistent with the model obtained from PXRD data, shown in Figure 5.21.

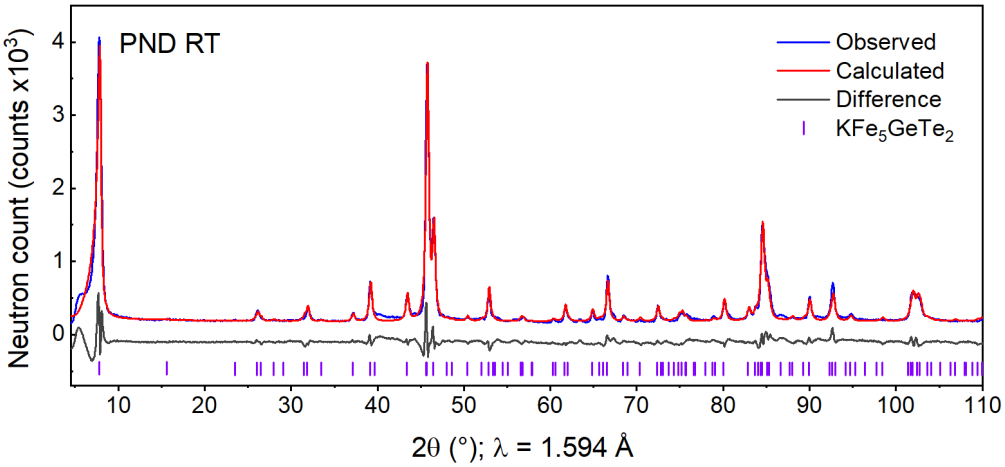

Figure 5.21: Rietveld refinement against the PND pattern of KFe_5GeTe_2 ($R\bar{3}m$) collected at 300 K using the D2B instrument at the ILL. R_{wp} = 11.7 %.

The contrast between the patterns of KFe_5GeTe_2 measured at 10 K and 300 K is shown in Figure 5.22. Unlike $Li(NH_2)Fe_5GeTe_2$, two reflections at 2θ = 26.2 ° and 27.6 ° (hkl = 101 and 104) are observed to have temperature dependent intensities, which is consistent with the PND experiments performed by May et al.[1] on Fe_5GeTe_2. An immediate observation is the lack of magnetic intensity on $00l$ reflections, which indicates the magnetic moments lie parallel to the c-axis and one can speculate that either ferromagnetic or ferrimagnetic order is present. Refinement of the magnetic structure was attempted by generating the possible magnetic modes using the ISODISTORT software. Magnetic reflections were found to be commensurate with the nuclear structure and so can be accounted for by the k = (0 0 0) propagation vector.

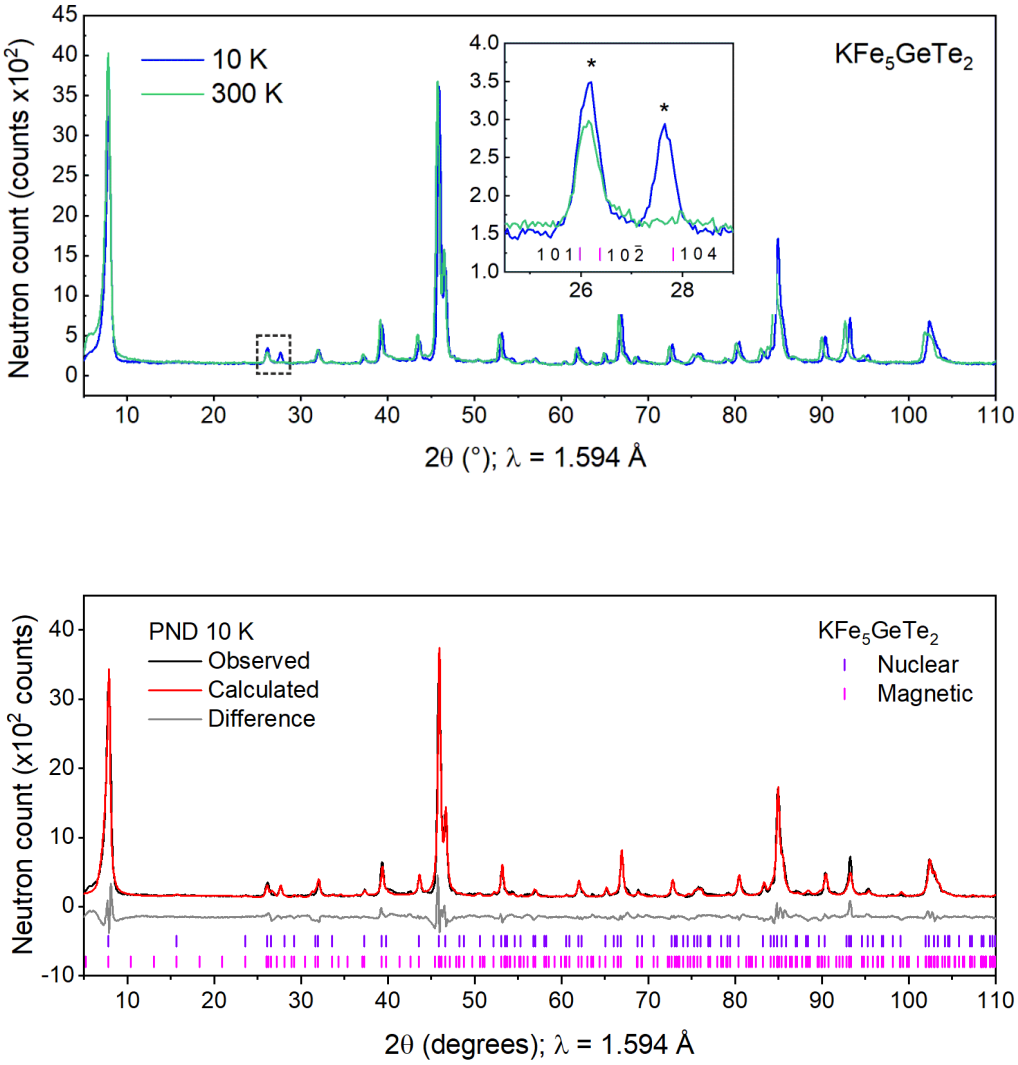

Figure 5.22: Top. PND patterns of KFe_5GeTe_2 collected at 300 K and 10 K using the D2B instrument at the ILL. Reflections with magnetic intensity (hkl = 101, 104) have been marked with an asterisk (*). **Bottom**. Rietveld refinement against the PND pattern of KFe_5GeTe_2 ($R\bar{3}m$) collected at 10 K using the D2B instrument at the ILL. R_{wp} = 12.1 %.

At 10 K, a ferromagnetic model with refined moments along the c-axis of 2.6(3) μ_B per Fe on the Fe2 and Fe3 site was obtained. This gives an average of 2.1 μ_B per Fe over the unit cell, which is consistent with the saturation moment obtained from SQUID magnetometry at 2 K. In this model, the size of the moment on the Fe2 and Fe3 sites were set to be equal to produce a good fit to the data, and produce sensible

moments on each site. Attempts were made to refine a magnetic moment on the Fe1 site, however no significant moment could be refined and this was not required to fit the data. This is consistent with the Mössbauer spectroscopy data collected for this compound discussed in the Mössbauer spectroscopy section. However, due to the limited numbers of observed magnetic reflections more complex magnetic models cannot be excluded.

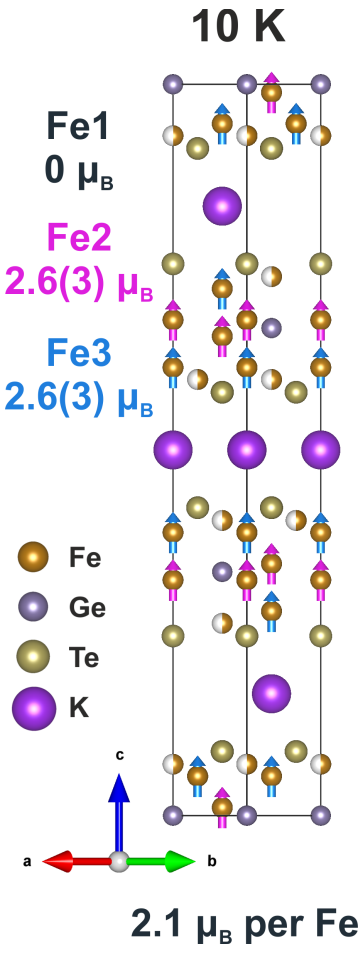

Figure 5.23: The magnetic model of KFe_5GeTe_2 from refinement of the PND pattern collected at 10 K using the D2B instrument at the ILL.

Table 5.5: Refined lattice parameters and bond lengths from Rietveld fits of the PXRD pattern of Fe_5GeTe_2 and the PXRD and PND patterns of KFe_5GeTe_2.

	Fe_5GeTe_2	KFe_5GeTe_2		
Radiation	PXRD	PXRD	PND	
T (K)	300	300	300	10
a (Å)	4.0408(1)	4.0858(3)	4.1066(3)	4.0936(3)
c (Å)	29.2024(3)	35.196(4)	35.284(5)	35.103(4)
V (Å^3)	412.95(1)	510.7(2)	515.3(1)	504.3(2)
$(Fe\text{-}Ge)_{ave}$	2.704	2.665	2.694	2.691
$(Fe\text{-}Te)_{ave}$	2.568	2.610	2.660	2.642

Inspection of the lattice parameters in Table 5.5 shows that the a lattice parameter remains unchanged, whilst the c lattice parameter increases by approximately 6 Å, which is consistent across all samples. The weighted average bond distances show an increase in the Fe–Te bond distance in all intercalated samples, which is consistent with reduction of Fe upon insertion of electrons. The average Fe–Ge bond distance in the intercalated phases shows a subtle decrease in the model obtained using PXRD data, but relatively unchanged in models extracted using PND data. This is perhaps unsurprising considering that only 0.2 electrons per Fe atom are being injected into the structure.

5.4.3 Magnetometry

Figure 5.24 shows the magnetisation vs temperature curves, cooled in zero field and a field of 100 Oe, of both Fe_5GeTe_2 and KFe_5GeTe_2. A small increase in Curie temperature, of approximately 5 K, is induced upon intercalation and can be observed in the region from 280 – 330 K.

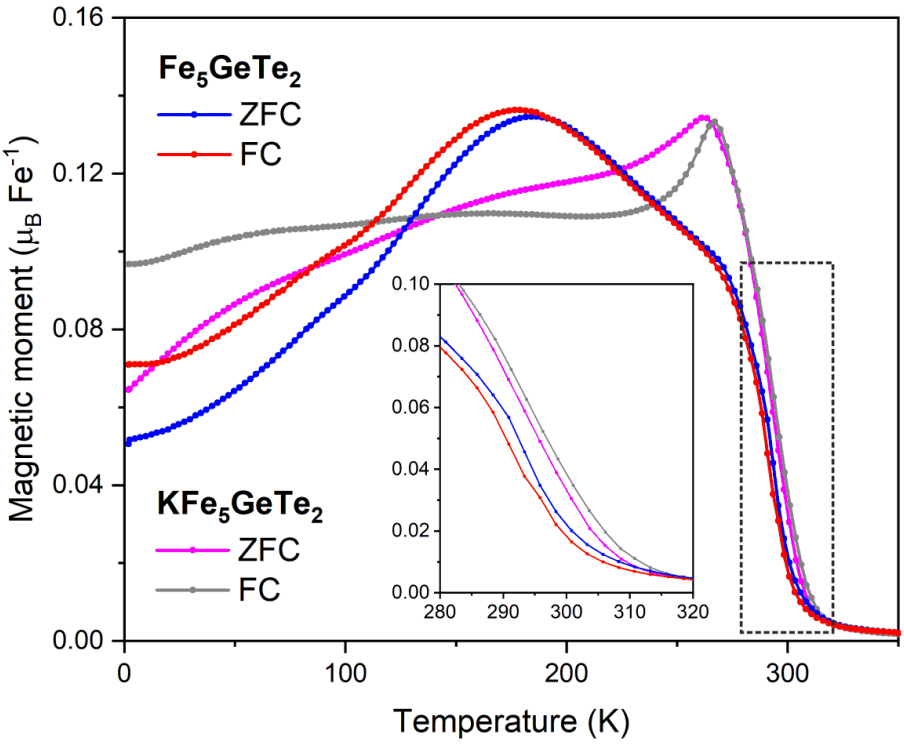

Figure 5.24: Magnetic moment vs temperature of Fe_5GeTe_2 and its potassium intercalate, cooled in a field of 100 Oe.

The behaviour of the magnetisation curves of KFe_5GeTe_2 just below the transition temperature is unusual and different from Fe_5GeTe_2. This could indicate more complex magnetism as described in the literature.[1,6]

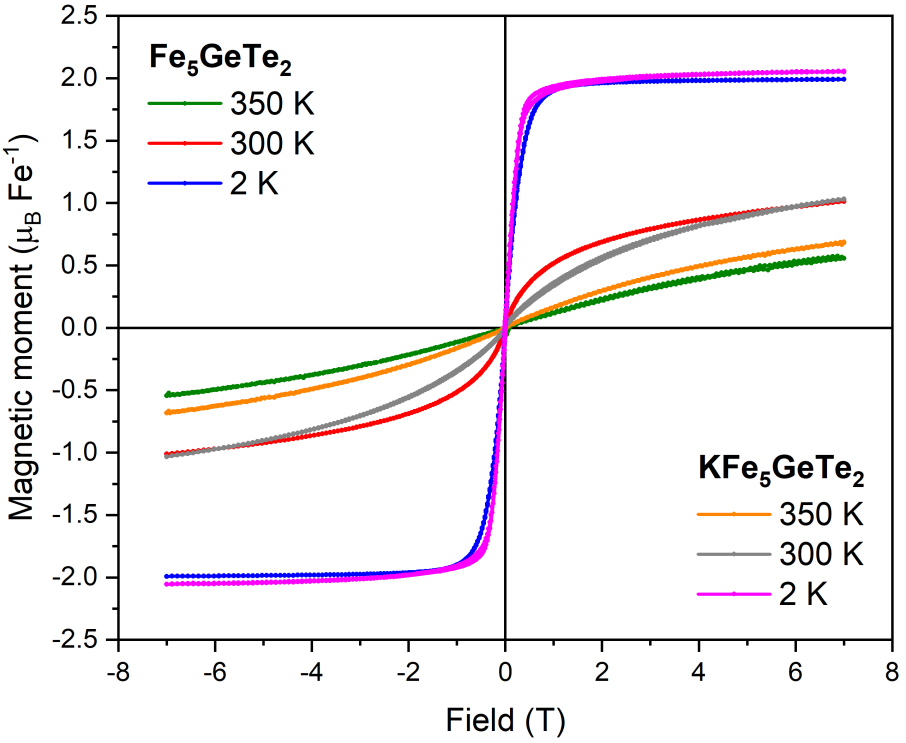

Figure 5.25: Magnetisation isotherms of Fe_5GeTe_2 and KFe_5GeTe_2 measured at 350 K, 300 K and 2 K over the range ±7 T.

Magnetisation isotherms were measured at 2 K, 300 K and 350 K using SQUID magnetometry over a magnetic field range of ± 7 T, shown in Figure 5.25. The curves measured at all temperatures for both Fe_5GeTe_2 and KFe_5GeTe_2 are comparable. The saturation moment remains at approximately 2.0 μ_B per Fe at 2 K, which is averaged over all the Fe atoms in the unit cell. This matches our value obtained from the refinement of PND data. The shape of the isotherms are indicative of a soft ferromagnet which exhibit low retentivity and coercivity. As discussed for the $Li(NH_2)Fe_5GeTe_2$ intercalate, the curvature of the isotherms measured at 350 K indicate superparamagnetic behaviour above the Curie temperature.

5.4.4 Mössbauer Spectroscopy

In order to further probe the magnetic ordering in KFe_5GeTe_2, Mössbauer spectroscopy measurements were performed at 300 K, 150 K, 50 K and 10 K. The fitted data can be found in Figure 5.26 with extracted parameters given in Table 5.6.

At 300 K there is no evidence of any Fe ordering, and the data can be fit as two doublets which encompasses all of the Fe sites in the structure. From the SQUID magnetometry data, some magnetic ordering is expected at 300 K as the Curie temperature is approximately 305 K. However, the magnetic susceptibility at 300 K is relatively small. Although there are three different crystallographic Fe sites, data can be fit using only two doublets. This may be due to significant overlap of doublets, and the constrained linewidths which were required to produce sensible fits.

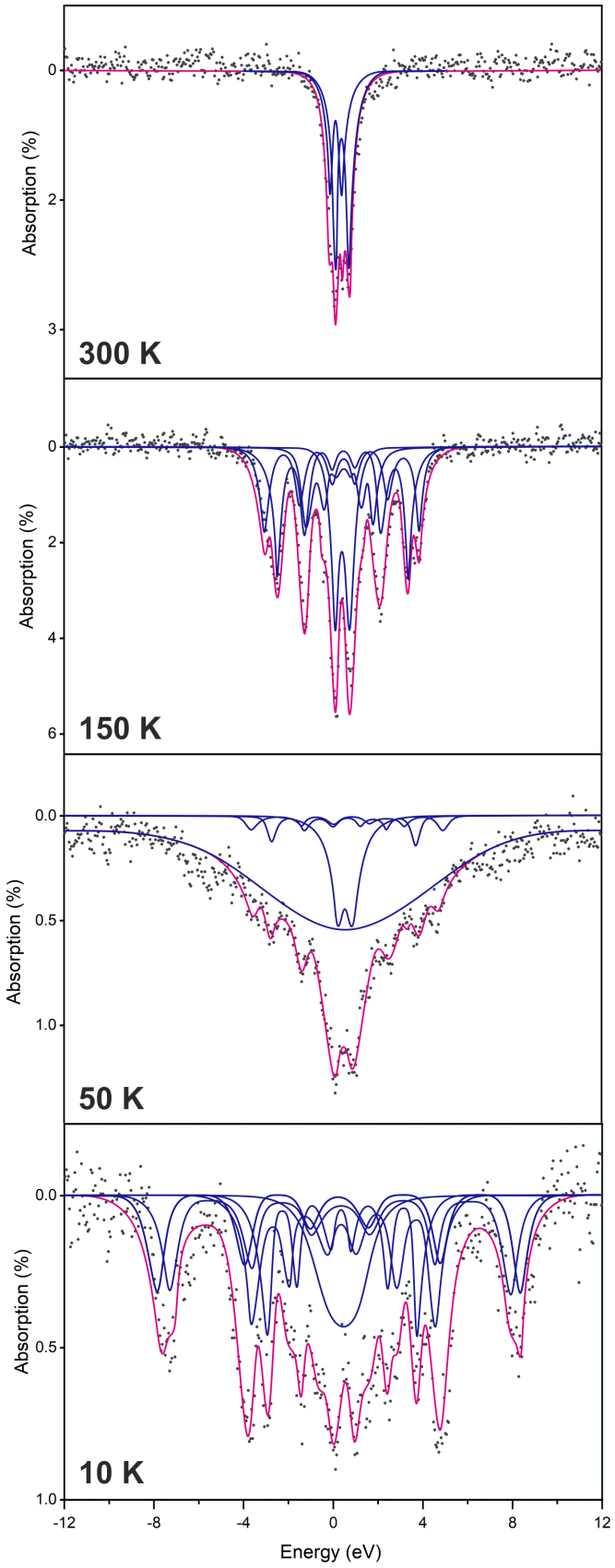

Figure 5.26: Fitted Mössbauer spectra of KFe_5GeTe_2 collected at 300 K, 150 K, 50 K and 10 K.

Table 5.6: Parameters from fitting Mössbauer data collected at 300, 150, 50 and 10 K.

Site	Label	CS (mm/s)	Δ (δ) (mm/s)	Population (%)
		300 K		
Fe	Doublet 1	0.140(13)	0.621(21)	41.4(27)
	Doublet 2	0.447(9)	0.660(15)	58.6(27)
		150 K		
Fe	Doublet 1	0.435(9)	0.614(15)	21.8(7)
	Sextet 1	0.476(14)	0.007(13)	24.3(14)
	Sextet 2	0.446(10)	-0.012(10)	34.2(15)
	Sextet 3	0.421(19)	-0.017(17)	19.7(12)
		50 K		
Fe	Doublet 1	0.475(44)	0.856(74)	11.7(36)
	Sextet 1	0.51(14)	0*	81(34)
	Sextet 2	0.548(78)	-0.003(77)	4.2(16)
	Sextet 3	0.75(12)	-0.20(12)	2.9(13)
		10 K		
Fe	Doublet 1	0.48(13)	1.00(47)	20.4(56)
	Sextet 1	0.428(67)	-0.013(67)	16(17)
	Sextet 2	0.489(57)	-0.013(58)	24.5(60)
	Sextet 3	0.463(31)	-0.047(30)	15.1(48)
	Sextet 4	0.47(11)	-0.06(10)	24(19)

As predicted, the data collected at 150 K show magnetic ordering, of approximately 80 % of the iron sites. Based on its population and lack of long-range ordering in the magnetic model, the Fe1 site has been attributed to the doublet with a population of 21.8(7) %. Although the structural model of Fe_5GeTe_2 and its intercalates in space group $R\bar{3}m$ has three crystallographic Fe sites, when considering the Fe1 vacancy caused by the fractional site occupancy, 5 different Fe environments exist. This is shown in Figure 5.27. With this in mind, we would expect to observe four sextets with a population of 20 % each, or two sextets with populations of 40 % each. It is not unfeasible that a fourth sextet is present but not well resolved, especially given

the similarity in CS and IS parameters. This could also be a consequence of the fixed linewidths required to produce a sensible fit to the data. Consequently, the three sextets could not be assigned based on their populations but collectively can be assigned to the remaining Fe2 and Fe3 sites.

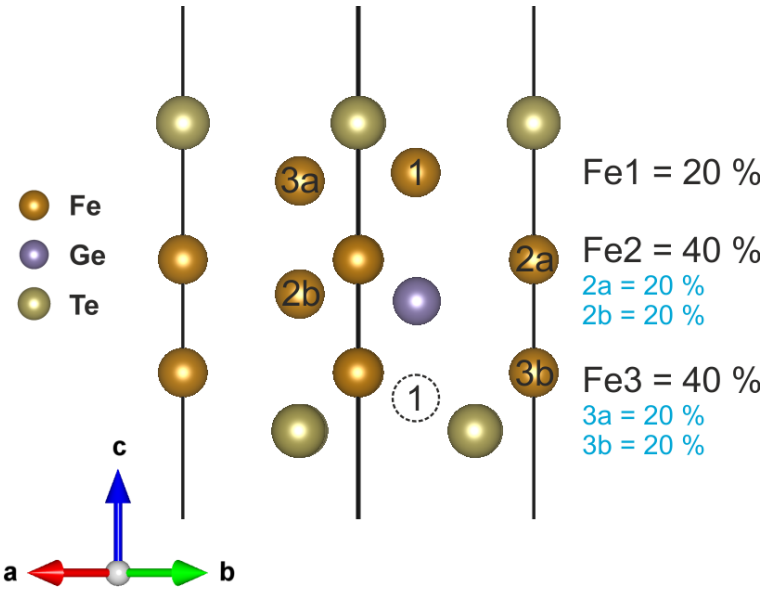

Figure 5.27: Structural model of a single layer of Fe_5GeTe_2 accounting for the Fe1 vacancy. The dashed circle represents the alternative Fe1 site. Models fitted against PXRD and PND data show this site as having 50 % occupancy on each Fe1 position due to the intrinsic long range average picture of the structure given by diffraction methods. Site percentages are given on the right.

The large broad background observed in the data collected at 50 K indicates the presence of on-going ordering and a range of local magnetic environments are present. Although parameters have been extracted, the conclusions we can draw from data are limited. This is indicative of a second magnetic transition not identified through SQUID magnetometry.

Interestingly, the proportion of unordered Fe sites remains the same at 10 K as at 150 K. This could indicate that the transition observed at 50 K is not due to additional Fe centres ordering but a change in magnetic state, such as a spin re-orientation, although this is not observed in the SQUID magnetometry data. This could be probed further by variable temperature PND experiments.

At 10 K, approximately 80 % of the Fe sites are ordered. Again, the doublet with a population of 20.4(56) % has been assigned to the Fe1 site in agreement with the magnetic model obtained from PND data. Given that the populations of the four sextets are within one standard deviation of 20 %, the four sextets have been assigned to the split Fe2 and Fe3 sites. Further assignment could not be made due to the similarity of the centre shift and isomer shift parameters. Like the spectrum measured at 50 K, a broad singlet is required to model part of the background of the data collected at 10 K. This suggests some on-going ordering may still be present at 10 K.

5.5 Discussion

Structurally, both intercalates presented here have clear similarities. Both potassium and the larger NH_2^- anion occupy the same position in the interlayer spacing, forming a 6 co-ordinate trigonal antiprism site with the surrounding Te atoms of the neighbouring layers. No Fe–Ge–Te layer rearrangement is found for either intercalate, and the intercalation process is topochemical for both. One clear difference is the co-insertion of amide in the Li case, even though both phases were synthesised using the same method. This can be rationalised by the higher charge density of Li^+ compared to K^+ having a greater electrostatic attraction to the NH_3 molecules during the intercalation step. In the case of $Li(NH_2)Fe_5GeTe_2$, the additional intercalated moiety means that an additional interlayer site is occupied. Since Li is the smaller of the two species, it is found to occupy a smaller distorted tetrahedral site. Since there are double the number of these sites than are required to satisfy the Li stoichiometry of the reaction, our model describes these sites as half filled. We propose that Li is ordered within each layer, but disordered between layers, based on the distance between the nearest-neighbour and next-nearest-neighbour Li sites. However further experiments would be needed to confirm this.

Another marked difference between these two intercalates is the stability of each. Whilst both are air and moisture sensitive, the lithiated phase has a limited lifetime under inert conditions at ambient temperatures, whereas the potassium intercalate has not been found to degrade under these same conditions. This could be due to a number of reasons. Firstly the interlayer spacing of the $Li(NH_2)$ intercalate un-

dergoes a larger expansion relative to Fe_5GeTe_2 than the potassium intercalate, and this larger deviation may cause higher instability. The host structure may not be able to support even larger intercalated species, although kinetic factors cannot be discounted. Interactions between guest species and the host layers is dominated by H-bonding between NH_2^- and Te in $Li(NH_2)Fe_5GeTe_2$, whereas electrostatic interactions between the K^+ ion and Te dominate in KFe_5GeTe_2. This could also be due to the relative metastability of the intercalated phases against their decomposition products. Other intercalates containing ammonia/amide have also been found to be unstable.[9,10]

PND data collected from both intercalates suggest that long range magnetic ordering is present in the potassium intercalate, which can be fitted to give a ferromagnetic model. However the $Li(NH_2)$ intercalate does not show any magnetic Bragg reflections which can be attributed to the intercalated phase. This could be due to the differences in electronic structure between the two intercalates, or as a result of reduced magnetic domain size since diffraction relies on the presence of large domains. This effect has been reported in the literature[17]. The refined models from PND data, combustion analysis and ICP-MS results all suggest that in the Li case, the guest species exists as $Li^+NH_2^-$, (i.e. ammonia is reduced in the reaction) which would not result in any reduction of Fe_5GeTe_2.

SQUID magnetometry data shows that both intercalates have similar Curie temperatures to Fe_5GeTe_2. However, the magnetic isotherms measured at 2 K show that the saturation moment of KFe_5GeTe_2 is similar to Fe_5GeTe_2, whereas the saturation

moment decreases by approximately 50 % upon intercalation of $Li(NH_2)$. It is difficult to say whether the magnitude of the ordered moment has decreased or whether the size of the moment has remained the same but fewer Fe ions are magnetically ordered. However, the Mössbauer results suggest the vast majority of Fe sites are still participating in magnetic ordering at low temperatures. This could be another consequence of the differences in electronic states of the intercalates.

Mössbauer spectroscopy measurements of both intercalates appear fairly similar, with the exception of the broad spectrum of KFe_5GeTe_2 measured at 50 K. This suggests a magnetic ordering transition occurs at this temperature, although this is not seen in the SQUID magnetometry data. As for $Li(NH_2)Fe_5GeTe_2$, no similar transitions are seen at the measurement temperatures, however a similar transition could be occurring at an intermediate temperature. The spectra collected at 10 K suggest that only the Fe2 and Fe3 sites are magnetically ordered in KFe_5GeTe_2, consistent with the PND analysis, whereas all three Fe sites exhibit magnetic ordering in $Li(NH_2)Fe_5GeTe_2$. This could be another consequence of reductive intercalation of K compared to the neutral intercalation of $LiNH_2$. It is clear from this discussion that the magnetism and coupling mechanisms in these compounds is not trivial and further investigation should be carried out to further characterise their magnetic properties.

5.6 Summary and Conclusions

The phases KFe_5GeTe_2 and $Li(NH_2)Fe_5GeTe_2$ have successfully been synthesised by the intercalation of Fe_5GeTe_2 using potassium or lithium metal and condensed ammonia. The host structure experiences significant layer separation driven by the co-ordination requirements of the intercalated ions, but the intralayer structure and the relative arrangement of the Fe–Ge–Te layers remains unchanged. K is found to occupy 6 co-ordinate trigonal antiprisms with a K–Te bond length of 3.65(1) Å. In $Li(NH_2)Fe_5GeTe_2$, the amide anion occupies the trigonal antiprism site whilst Li partially occupies a distorted tetrahedral site. PND shows the presence of long-range ferromagnetic ordering below the Curie temperature in KFe_5GeTe_2, but not in $Li(NH_2)Fe_5GeTe_2$ possibly due to a small domain size. SQUID magnetometry shows both intercalates retain the high Curie temperature of Fe_5GeTe_2, however the saturation moment measured at 2 K decreases by approximately 50 % upon the intercalation of $Li(NH_2)$. No reduction in saturated moment measured by magnetometry is observed when intercalated with K. Mössbauer spectroscopy suggests all Fe sites participate in magnetic ordering by 10 K in $Li(NH_2)Fe_5GeTe_2$, contrary to KFe_5GeTe_2 in which the Fe1 site does not order down to 10 K. This is supported by the magnetic model extracted from the PND pattern at 10 K.

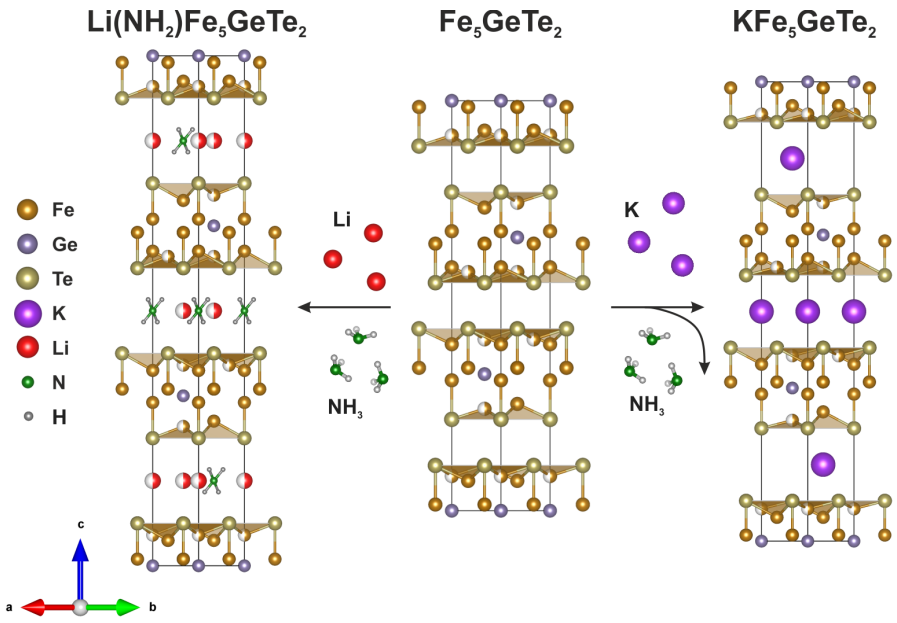

Figure 5.28: A schematic showing the intercalation reactions of Fe_5GeTe_2.

Further work should be done to further understand the magnetism in these compounds, particularly $Li(NH_2)Fe_5GeTe_2$, since no magnetic Bragg peaks which could be attributed to the sample were observed. Additional experiments could include PND measured in an external field which may elicit long-range ordering. Computational experiments using suitable structurally ordered models could also be performed to predict the changes in band structure as a consequence of reductive intercalation of potassium compared to the neutral charge intercalation of $Li(NH_2)$.

References

[1] A. F. May, D. Ovchinnikov, Q. Zheng, R. Hermann, S. Calder, B. Huang, Z. Fei, Y. Liu, X. Xu, M. A. McGuire, *ACS Nano* **2019**, *13*, 4436–42.

[2] J. Stahl, E. Shlaen, D. Johrendt, *Zeitschrift für Anorganische und Allgemeine Chemie* **2018**, *644*, 1923–29.

[3] A. F. May, C. A. Bridges, M. A. McGuire, *Physical Review Materials* **2019**, *3*, 104401.

[4] A. F. May, M.-H. Du, V. R. Cooper, M. A. McGuire, *Physical Review Materials* **2020**, *4*, 074008.

[5] C. Tian, F. Pan, S. Xu, K. Ai, T. Xia, P. Cheng, *Applied Physics Letters* **2020**, *116*, 202402.

[6] S. Ershadrad, S. Ghosh, D. Wang, Y. Kvashnin, B. Sanyal, *The Journal of Physical Chemistry Letters* **2022**, *13*, 4877–4883.

[7] L. Alahmed, B. Nepal, J. Macy, W. Zheng, B. Casas, A. Sapkota, N. Jones, A. Mazza, M. Brahlek, W. Jin, M. Mahjouri-Samani, S. Zhang, C. Mewes, L. Balicas, T. Mewes, L. Peng, *2D Materials* **2021**, *8*, 45030.

[8] R. D. Shannon, *Acta Crystallographica* **1976**, *32*, 751.

[9] M. E. Kamminga, S. J. Cassidy, P. P. Jana, M. Elgaml, N. D. Kelly, S. J. Clarke, *Dalton Transactions* **2021**, *50*, 11376.

[10] M. Burrard-Lucas, D. G. Free, S. J. Sedlmaier, J. D. Wright, S. J. Cassidy, Y. Hara, A. J. Corkett, T. Lancaster, P. J. Baker, S. J. Blundell, S. J. Clarke, *Nature Materials* **2013**, *12*, 15–19.

[11] R. Juza, K. Opp, *Zeitschrift für anorganische und allgemeine Chemie* **1951**, *266*, 313–24.

[12] H. T. Stokes, D. M. Hatch, B. J. Campbell, *ISODISTORT, ISOTROPY Software Suite*, version 6.11.1, **2022**.

[13] B. J. Campbell, H. T. Stokes, D. E. Tanner, D. M. Hatch, *Journal of Applied Crystallography* **2006**, *39*, 607–14.

[14] A. Menshikov, Y. Dorofeev, G. Budrina, V. Syromyatnikov, *Journal of Magnetism and Magnetic Materials* **1988**, *73*, 211–214.

[15] Q. Liu, J. Xing, Z. Jiang, Y. Guo, X. Jiang, Y. Qi, J. Zhao, *Communications Physics* **2022**, *5*, 140.

[16] W. Bronger, S. Jäger, R. Rennau, D. Schmitz, *Journal of the Less Common Metals* **1989**, *154*, 261–270.

[17] P. D. Battle, S. I. Evers, E. C. Hunter, M. Westwood, *Inorganic Chemistry* **2013**, *52*, 6648–53.

'Skyrmions, they're like hedgehogs,

spikes pointing all over the place'

- Shunsuke Sasaki

6

Intercalation Chemistry of Fe_3GeTe_2

Contents

6.1 Introduction

$Fe_{3-\delta}GeTe_2$ (δ = 0.03 – 0.31)[1] is a 2D ferromagnet with a variable Curie temperature, T_C, of between 220 – 230 K, which decreases with lower Fe stoichiometry. This compound has gained increased attention due to its magnetic properties and possible manipulations of T_C by changing the Fe content. The first report on the ferromagnetic $Fe_{3-\delta}GeTe_2$ and the paramagnetic Ni_3GeTe_2 date back to 2006.[2] Since then, various studies investigating their structures and properties have been reported. These studies include the partial doping of Ni[3,4] and Co,[5] in which T_C was found to decrease with increased dopant content. For $(Fe_{1-x}Co_x)_3GeTe_2$, it was found that the Co-substitution gives rise to domain wall pinning, resulting in a hard magnetic phase.[5] The explanation for the decreased T_C in the Ni-substituted phases was ascribed to dilution effects from the Ni substitution.[3] Further literature includes the study of antiferromagnetic (AFM) (ground) states in $Fe_{3-\delta}GeTe_2$,[6–9] patterning of the magnetic domains in $Fe_{3-\delta}GeTe_2$,[10] the magnetic structure of $Fe_{3-\delta}GeTe_2$,[1,11] and the magnetocaloric effect in $Fe_{3-\delta}GeTe_2$.[1] The ability to tune the magnetic properties in $Fe_{3-\delta}GeTe_2$ could give rise to more potential spintronic applications.

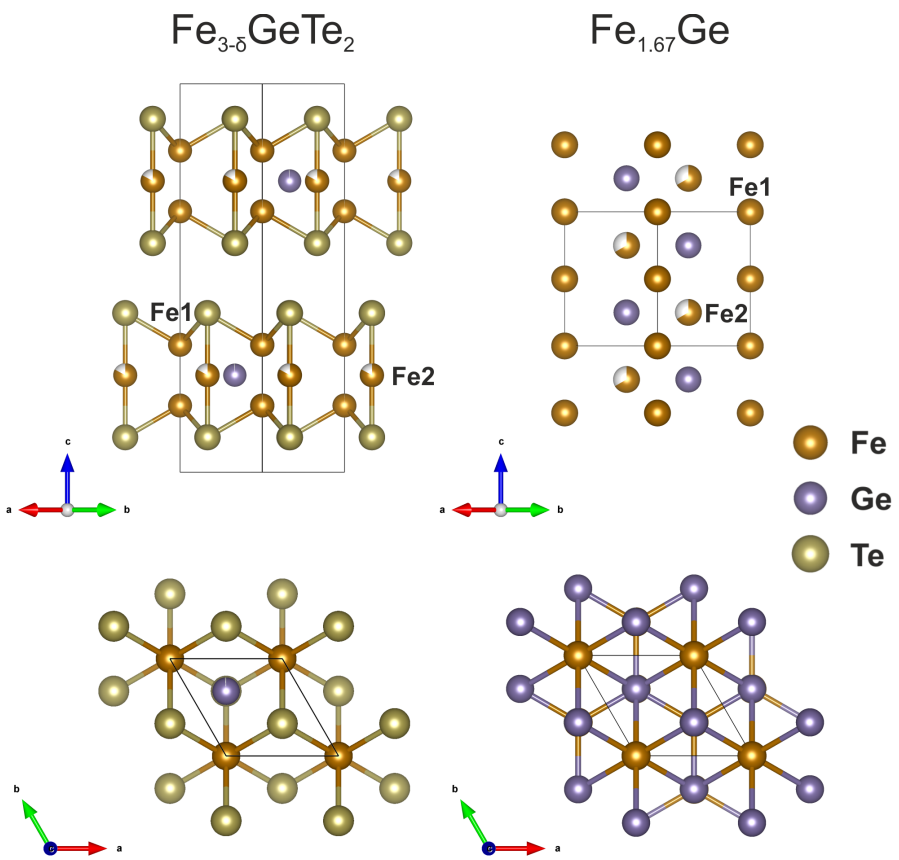

Figure 6.1: Top. Structural model of $Fe_{3-\delta}GeTe_2$ showing the distinct Fe sites. **Bottom**. Structural model of $Fe_{1.67}Ge$.

$Fe_{3-\delta}GeTe_2$ crystallises in space group $P6_3/mmc$ with lattice parameters $a = 3.991(1)$ Å and $c = 16.33(3)$ Å found using single crystal X-ray Diffraction (XRD).[2] These studies also confirm the Fe deficiency lies on the Fe2 site. The close structural relationship to the iron germanium intermetallic $Fe_{1.67}Ge$[12] is shown in Figure 6.1. This suggests the formally mixed-valence formulation $(Fe^{2+})(Fe^{3+})_2(Ge^{4-})(Te^{2-})_2$ is more likely, when compared to the alternative formal oxidation state formulation $(Fe^0)_3(Ge^{4+})(Te^{2-})_2$. However clearly distinguishable oxidation states in this compound is unlikely,[2] and due to the strong hybridization of Fe1, Fe2 and Ge at the Fermi level[1] the assigned oxidation states are merely a formalism. Calculations suggest that the intralayer ferromagnetism is contributed to by only itinerant electrons,

but there is competition between the interlayer ferromagnetic coupling, comprised of both itinerant electrons and localised exchange pathways, and interlayer antiferromagnetic coupling mediated by exclusively localised exchange pathways.[13]

In 2019, intercalation of sodium into the van der Waals gap of $Fe_{3-\delta}GeTe_2$ using $Na^+[Ph_2CO]^{\bullet-}$ in dry THF was reported.[14] No change in T_C upon intercalation was observed, but room temperature magnetism emerged in the samples due to the decomposition of $NaFe_{2.78}GeTe_2$, producing elemental Fe. Here we report the reduced phase $KFe_{2.84}GeTe_2$ synthesised using chemical intercalation and characterised using high resolution PXRD, neutron diffraction, Mössbauer spectroscopy and SQUID magnetometry. Intercalation results in significant structural and magnetic changes compared to the host.

6.2 Synthesis of Fe_3GeTe_2

All syntheses were carried out in a Glovebox Technology argon-filled dry glove box with an O_2 content below 1 ppm or on a Schlenk line. Poly-crystalline samples of $Fe_{3-\delta}GeTe_2$ were synthesised by grinding together iron powder (Alfa Aesar; 99.998 %), germanium powder (Alfa Aesar; 99.99 %) tellurium powder (Alfa Aesar; 99.999 %) in stoichiometric amounts (to produce the target phase with $\delta = 0$) using an agate pestle and mortar until homogeneous. The mixture was then sealed inside an evacuated silica tube and heated at 750 °C for 10 days (ramp rate of 5 °C min^{-1}). Powders were then quenched into an ice/water bath. The Rietveld refinement of $Fe_{3-\delta}GeTe_2$ can be found in Figure 6.2. The stoichiometry of the sample used for subsequent soft chemical manipulation was found to be $Fe_{2.96(1)}GeTe_2$ from the Rietveld refinement.

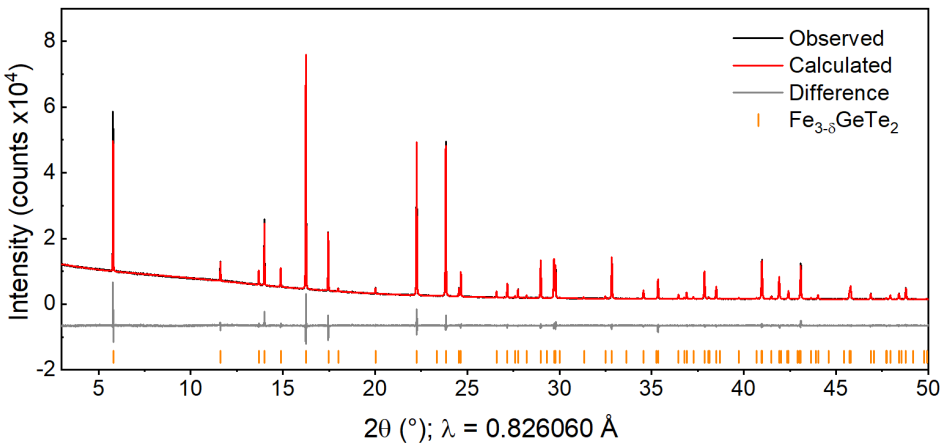

Figure 6.2: Rietveld refinement against PXRD data of Fe_3GeTe_2 ($P6_3/mmc$) collected using the PSD on the I11 beamline, Diamond Light Source. R_{wp} = 3.08 %

6.3 Potassium intercalated Fe_3GeTe_2

Potassium intercalates were synthesised by adding $Fe_{2.96}GeTe_2$ powder, a magnetic stirrer bar, and an amount of K metal (Sigma Aldrich; 99 %) to give the stoichiometry $KFe_{2.96}GeTe_2$ to a Schlenk tube. This was then attached to a Schlenk line along with a cylinder of ammonia (BOC; 99.98 %). The Schlenk tube was then placed in a bath of isopropanol and dry ice and cooled to approximately −78 °C, before a small volume (approximately 10 cm^3) of NH_3 was condensed over the reagents, as described in Chapter 2. The characteristic blue solution of dissolved electrons was observed. Decolourisation usually occured within two minutes of the condensation of ammonia. The mixture was then left to stir until the ammonia had evaporated via the manometers of the Schlenk line, typically 3 hours, leaving a powder of the intercalated product. The resulting solid was then dried under dynamic vacuum for 20 minutes.

6.3.1 Powder X-ray Diffraction

The PXRD pattern of the intercalate appeared visually different to the parent phase $Fe_{2.96}GeTe_2$, as shown in Figure 6.3. The pattern could be well indexed on a hexagonal unit cell, a = 4.059 Å and c = 20.558 Å, similar to that of the parent with an increase in c of 4.226 Å (26.8 %). Assuming the Fe–Ge–Te layers remain intact, this is equivalent to an increase of 2.113 Å in the van der Waals gap, which is approximately 75 % of the of diameter of K^+ (2.8 Å),[15] and suggests that no co-intercalation of NH_3 had occurred. This is consistent with reports of co-intercalation of ammonia with Li increasing the interlayer spacing of FeSe[16] and Bi_2Se_3[17] by 2.7 Å and 3.3 Å respectively, in which the ammonia/amide species dictates the layer separation. This is also consistent with the intercalates in Chapters 3 and 5.

The structural solution utilised a rigid body approach, which takes advantage of the layered structure and assumes the layers remain intact during the low temperature intercalation step of the synthesis. A model that closely resembled the parent phase in terms of atomic positions was built in $P1$ symmetry within the expanded unit cell of the intercalate obtained from the indexing described above. Constraints were then applied to the atoms within a particular layer so that they maintained their relative positions. The positions of the atoms in the first layer were then fixed whilst the position of the other layer was refined freely in the x and y directions relative to the first layer. The displacement in z was set to zero so the two layers were related by $\frac{1}{2}c$ along the c axis, the stacking direction, which assumes the layers remain equally spaced. In the initial stage of the refinement, K atoms were excluded as

the host layers dominate the diffraction pattern. The resulting displacement refined to (0.631(2), 0.473(3), 0). From visual inspection, the resulting structure could be assigned to a hexagonal space group if the layer displacement was corrected to (2/3, 1/3, 0), although this was outside the error of both displacements in x and y. This may be a consequence of the rigid body refinement technique as it does not allow for the refinement of individual atomic positions. The program FINDSYM[18,19] was then used to identify an appropriate space group; $P6_3/mmc$ was assigned to the model. The structural model of the rearranged Fe–Ge–Te layers can be found in Figure 6.4.

Chemically sensible potassium positions were identified through visual inspection and added to the structural model at the $4f$ position at (1/3, 2/3, z) with $z \approx 0.5$, which refined to $z = 0.501(1)$. $z = \frac{1}{2}$ at this position is not special in $P6_3/mmc$, Figure 6.5 shows the asymmetry of this site. Subsequent refinement of the potassium z co-ordinate against PND data was within error of 0.5. Potassium occupies a triangular prism surrounded by 6 Te atoms. The arrangement of the layers is such that one triangular face of this triangular prism coordinates to an Fe atom, while the other does not, hence the K ion is in a very slightly asymmetric environment. Four potassium atoms are generated in the unit cell and the refined occupancy was 0.49(1), giving an overall refined stoichiometry of $K_{0.98(2)}Fe_{2.84}GeTe_2$, which will be denoted as $KFe_{2.84}GeTe_2$, consistent with the maximum theoretical value from the reaction stoichiometry. Refinement of the Fe occupancies indicates some extrusion of Fe occurs during the intercalation process, as the Fe stoichiometry decreases from

2.96(1) to 2.84(1) in the parent materials and intercalated phase respectively. This is also reflected by the presence of Fe as an impurity phase identified through PXRD, shown in Figure 6.3. The K-Te bond length is 3.46(1) Å, and is comparable to the K-Te bond length in K_2PdTe_2,[20] in which K occupies a 6 co-ordinate trigonal prism with an average bond length of 3.58 Å. The Rietveld refinement against the PXRD data is shown in Figure 6.3.

Three small reflections at 2θ = 5.8 °, 10.0 ° and 22.2 ° could not be indexed in hexagonal symmetry or fit using the rigid body model in $P1$ symmetry and were later assigned to the impurity phases: unreacted $Fe_{3-\delta}GeTe_2$ (0.72 %), K_2Te (0.84 %) and Fe (1.24 %) respectively. These side phases have been attributed to a small amount of decomposition during the intercalation process. The final structural model is shown in Figure 6.5 with refinement parameters given in Table 6.1.

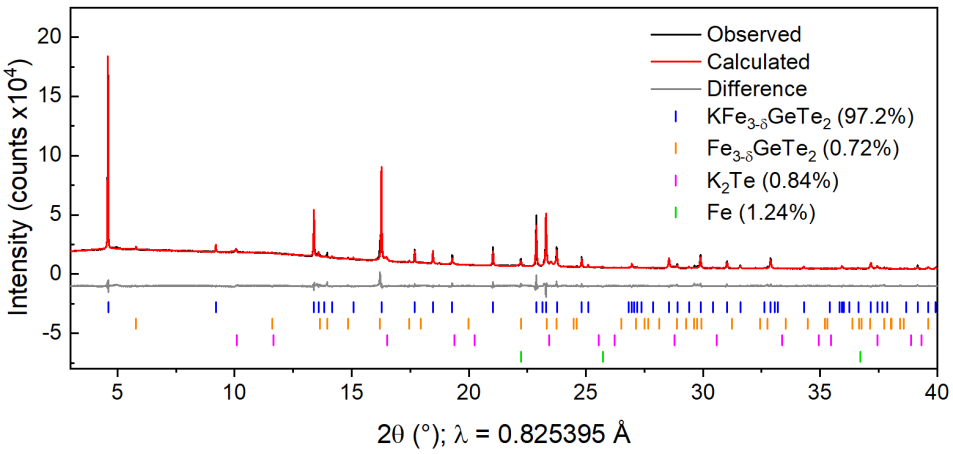

Figure 6.3: Rietveld fit against the PXRD pattern of $KFe_{2.84}GeTe_2$ ($P6_3/mmc$) collected using the PSD on the I11 beamline, Diamond Light Source. R_{wp} = 4.87 %.

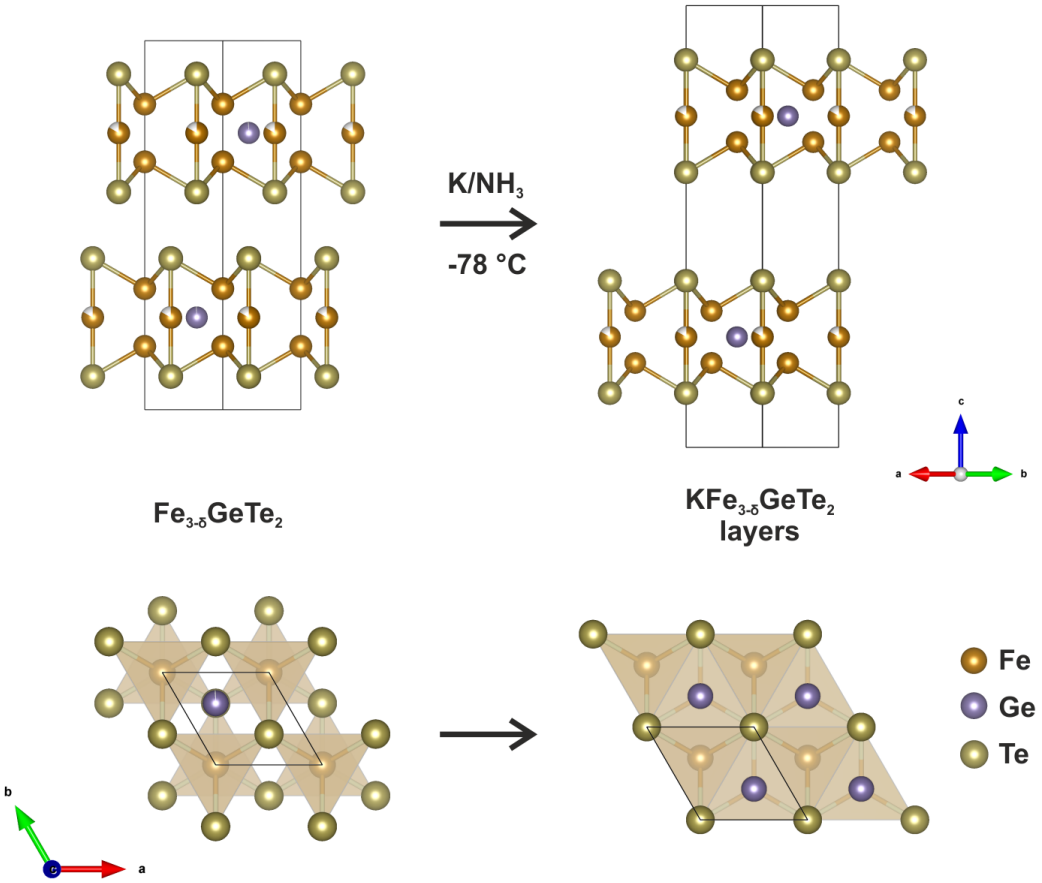

Figure 6.4: Left. The crystal structure of $Fe_{3-\delta}GeTe_2$ exhibiting AB stacking. **Right.** The crystal structure of the Fe–Ge–Te layers of $KFe_{2.84}GeTe_2$ in $P6_3/mmc$. Alternate layers are displaced by (2/3, 1/3, 0) upon intercalation.

In $Fe_{3-\delta}GeTe_2$, the layers are stacked in an ABAB fashion in hexagonal symmetry. Upon intercalation the integrity of the layers is maintained, however they are rearranged relative to one another, with alternate layers being displaced by (2/3, 1/3, 0). The hexagonal symmetry persists but the relative arrangement of layers has changed, with the linear Te–Fe–Te units now eclipsed when viewed along the c direction. This is presumably driven by co-ordination requirements of the intercalated potassium species. If no layer rearrangement were to occur, the potassium would lie in a heavily distorted octahedral site, as is seen in KFe_5GeTe_2 as discussed in Chapter 5.

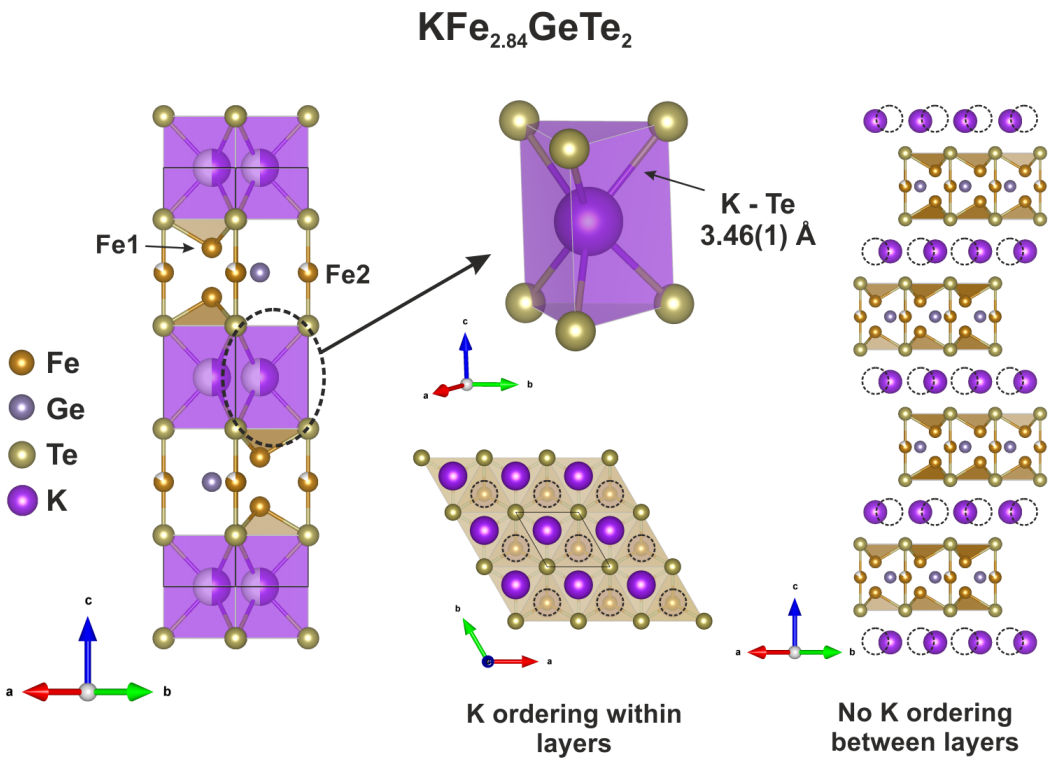

Figure 6.5: Left. The crystal structure of $KFe_{2.84}GeTe_2$ viewed along the [1 1 0] direction. **Centre**. A single slab of potassium in the Van der Waals' gap projected along the *c* axis, vacancies are shown by dotted circles. **Right**. The layer-to-layer disorder of K.

From the refined structural model, the potassium atoms occupy 50 % of all the available triangular prismatic sites in the unit cell. The distance between neighbouring triangular prismatic sites is only 2.365 Å, less than the sum of two K^+ ionic radii, whereas the next-nearest-neighbour distance between such sites is 4.095 Å. Based on this we propose that the sites occupied by potassium ions are ordered within each layer such that the three nearest-neighbour sites surrounding an occupied site are vacant, and the six next-nearest-neighbour sites are all occupied, see Figure 6.5. Random ordering of potassium positions layer-to-layer results in the overall occupancy of 0.5 refined for the K sites using the long-range probe of diffraction, and no cell expansion in the plane is evident. This type of ordering has been reported for the sodium and potassium intercalates of layered chalcogenide, Ta_2PdS_6.[21]

Table 6.1: Refined lattice parameters and bond lengths from Rietveld fits of PXRD patterns collected at 300 K using the PSD on the I11 beamline, and PND patterns collected on D2B at the ILL at 300, 200 and 10 K.

$KFe_{2.84}GeTe_2$ RMM = 525.49 g mol^{-1}, Z = 2						
Diffractometer				I11(PSD) (D2B (ILL))		
Wavelength (Å)				0.825395 (1.594)		
Temperature (K)				300 (300)		
Space group				$P6_3/mmc$ (194)		
a (Å)				4.0875(1) (4.0968(2))		
c (Å)				20.5696(2) (20.579(1))		
V (Å^3)				297.662(5) (298.73(4))		
Atom	Site	x	y	z	Occ	U_{iso} (Å^2)
Fe1	4f	2/3	1/3	0.1911(2) (0.1902(3))	1	0.0050(16) (0.0178(8))
Fe2	2b	0	0	0.25	0.835(9) (0.91(1))	0.0206(9) (0.0178(8))
Ge	2d	1/3	2/3	0.25	1	0.0270(19) (0.0247(16))
Te	4e	0	0	0.3771(1) (0.3768(5))	1	0.0237(21) (0.0131(11))
K	4f	2/3	1/3	0.501(1) (0.498(3))	0.50(1) (0.42(3))	0.0150(19) (0.056(9))

The refined bond distances for $Fe_{2.96}GeTe_2$ and $KFe_{2.84}GeTe_2$ are listed in Table 6.2. The values obtained for $Fe_{2.96}GeTe_2$ from PXRD data are within 1 × σ of those reported by Deiseroth et al. from single crystal XRD data.[2] Analysis of the bond lengths shows lengthening of the Fe–Te bonds in $KFe_{2.84}GeTe_2$ relative to $Fe_{2.96}GeTe_2$, indicative of Fe reduction. There is some discrepancy between the Fe2–Te bond length in $KFe_{2.84}GeTe_2$ extracted from PXRD data and PND data.

Table 6.2: Lattice parameters and interatomic distances of $Fe_{2.96}GeTe_2$ and $KFe_{2.84}GeTe_2$ from the refinement of PXRD data collected using the PSD on the I11 beamline and PND data collected at 300 K, 200 K and 10 K using the D2B instrument at ILL, France.

	$Fe_{2.96}GeTe_2$	$KFe_{2.84}GeTe_2$			
Radiation	PXRD	PXRD		PND	
Temp (K)	300	300	300	200	10
Space group		$P6_3/mmc$ (194)			
a (Å)	4.0034(1)	4.0875(1)	4.0957(2)	4.0955(3)	4.0946(3)
c (Å)	16.3384(1)	20.5696(2)	20.563(2)	20.479(3)	20.386(2)
V (Å^3)	226.775(1)	297.662(5)	298.73(4)	297.47(6)	296.00(6)
Bond distances (Å)					
Fe1-Te	2.662(1)	2.744(3)	2.748(1)	2.744(1)	2.744(1)
Fe2-Te	2.611(1)	2.614(3)	2.667(1)	2.653(1)	2.646(1)
Ge-Fe1	2.634(1)	2.654(2)	2.683(1)	2.683(1)	2.679(1)
Ge-Fe2	2.304(1)	2.360(1)	2.365(1)	2.367(1)	2.366(1)
Ge-Te	3.482(1)	3.521(2)	3.565(1)	3.510(1)	3.549(1)
K-Te	-	3.46(1)	3.327(1)	3.429(1)	3.509(1)

We hypothesise this is because Fe makes a relatively weak contribution to the X-ray scattering compared with the PND data. Trends across the PND data shows thermal contraction of lattice parameters and bond lengths with decreasing temperature, except for the K–Te bonds which appear to elongate. This may be an artefact of the shortened Fe2–Te bond length as Fe2 lies on a special position, in addition to the small estimated standard deviations given by the Rietveld refinement, which are most likely an underestimate.

6.3.2 Variable Temperature PXRD

Temperature-resolved PXRD measurements were performed over a range of 303 – 1173 K. $KFe_{2.84}GeTe_2$ was found to thermally decompose at approximately 650 K. As Figure 6.6 shows the 002 reflection of the intercalate rapidly loses intensity and the 002 reflection of the parent phase grows at the expense of the intercalate. The resulting $Fe_{3-\delta}GeTe_2$ phase (δ is unknown for this phase as the extrusion of Fe from the unreacted parent phase cannot be ruled out) contributes to 25 % of the crystalline decomposed phases, in addition to binary phases $Fe_{3.3}Ge_2$ and K_2Te_3.

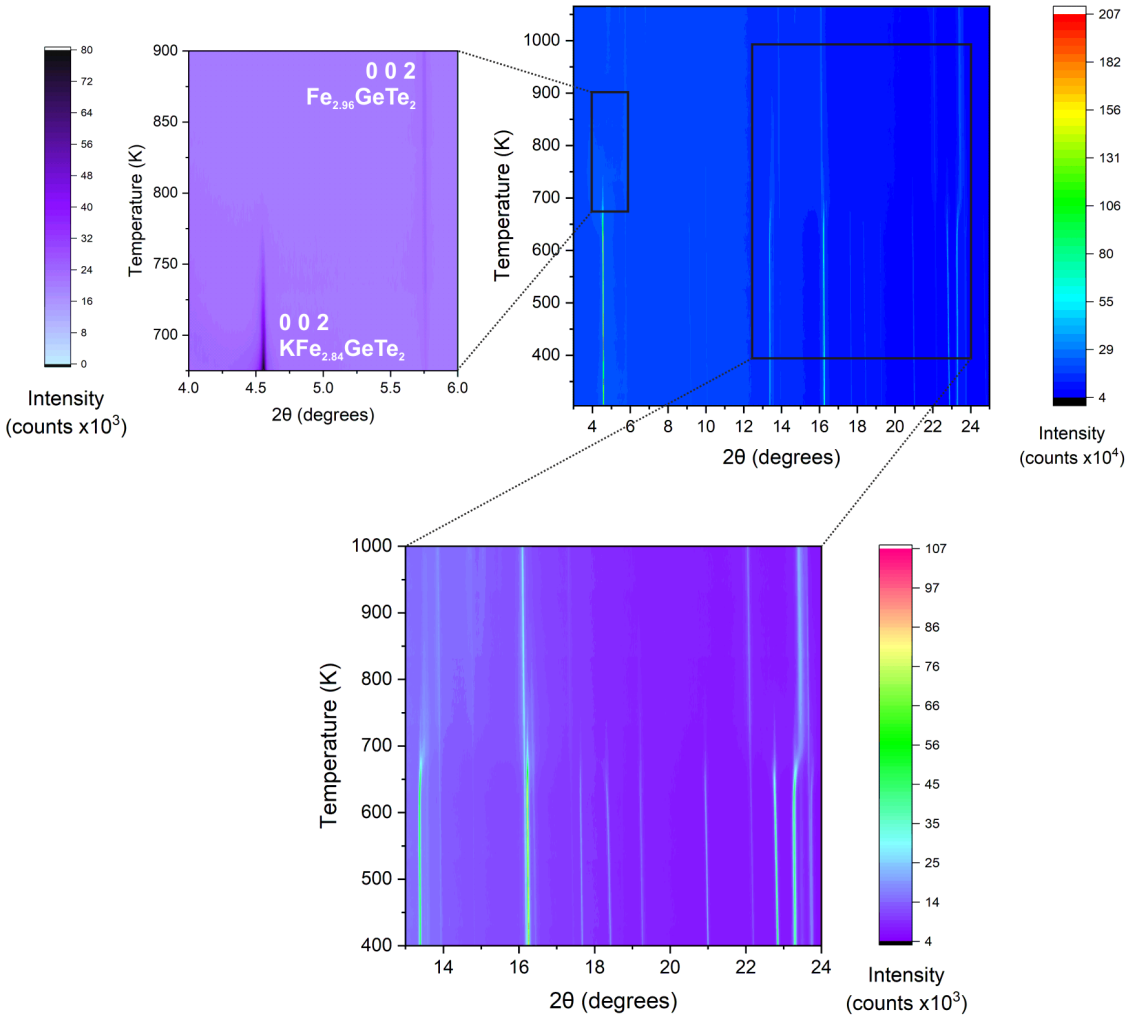

Figure 6.6: A film plot of temperature resolved PXRD data of $KFe_{2.84}GeTe_2$ collected using the PSD on the I11 beamline between 303 – 1173 K. The plot of the range 4.0 ° < 2θ < 6.0 ° shows the 200 reflection the intercalated phase diminish.

Two reflections could not be matched to any phase but only contribute very low intensity. However, there is a significant decrease in overall intensity of the decomposed phases relative to the intercalate, suggesting that some amorphous products are formed.

The Rietveld fit of the thermally decomposed sample collected at 1073 K, shown in Figure 6.7, shows that Fe_3GeTe_2 was found to be regenerated as the majority phase, contributing to 63% of the PXRD pattern, however the overall intensity of this pattern is severely reduced compared to the intercalate measured at 300 K. Because of this it is likely that a significant amount of amorphous side phases are also formed.

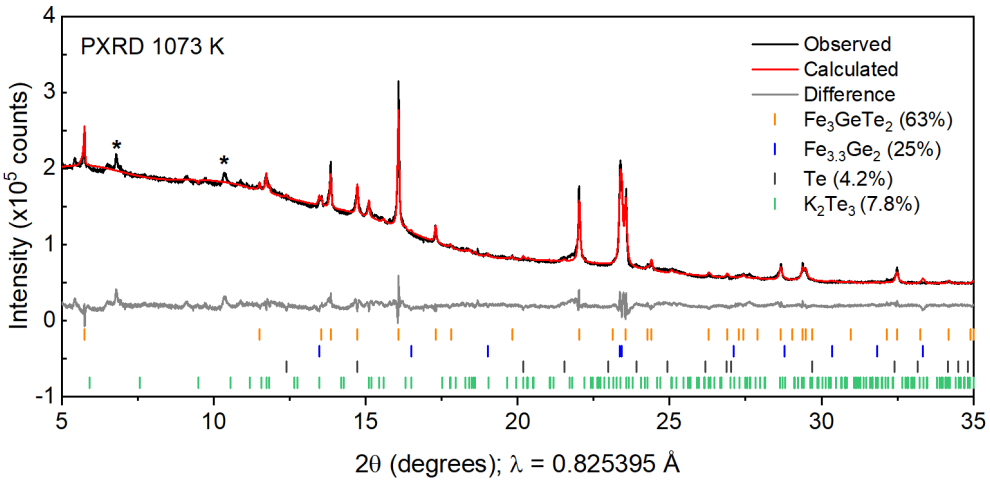

Figure 6.7: Rietveld refinement of thermal decomposition products of $KFe_{2.84}GeTe_2$, collected using the PSD on the I11 beamline. The majority phase is Fe_3GeTe_2 ($P6_3/mmc$). Reflections marked with an asterisk (*) could not be assigned. R_{wp} = 2.52 %.

6.3.3 Magnetometry

Figure 6.8 shows the magnetic susceptibility of $Fe_{2.96}GeTe_2$ and its potassium intercalate $KFe_{2.84}GeTe_2$ as a function of temperature. It is apparent that ferromagnetic ordering is maintained upon intercalation, accompanied by an increase in the Curie temperature of $\approx$ 15 K to T_C = 240 K. Computational studies by Jang et al. have shown that heavy electron-doping (0.5 – 1 electrons) induces ferromagnetic order in $Fe_{3-\delta}GeTe_2$ bi-layers,[6] which is consistent with our experimental results.

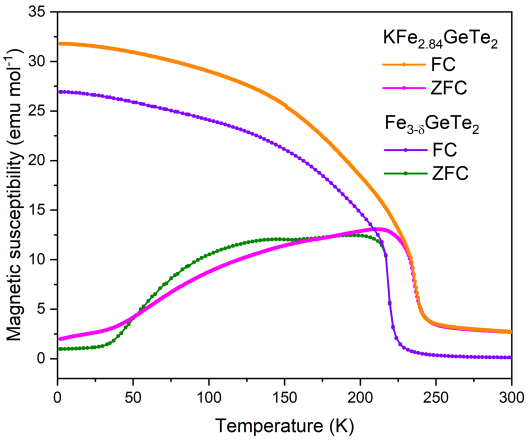

(a) Magnetic susceptibility vs temperature using an applied field of 100 Oe

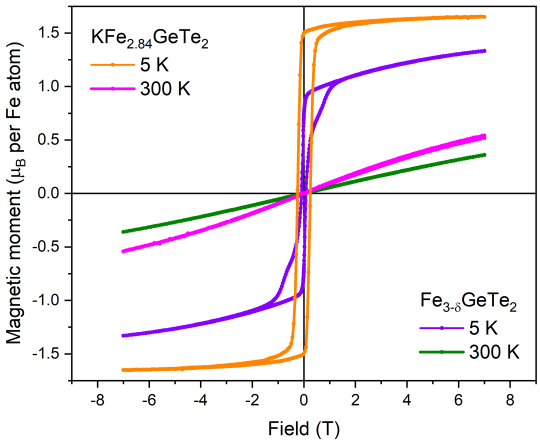

(b) Magnetisation isotherms measured at 5 K and 300 K over the range ± 7 T

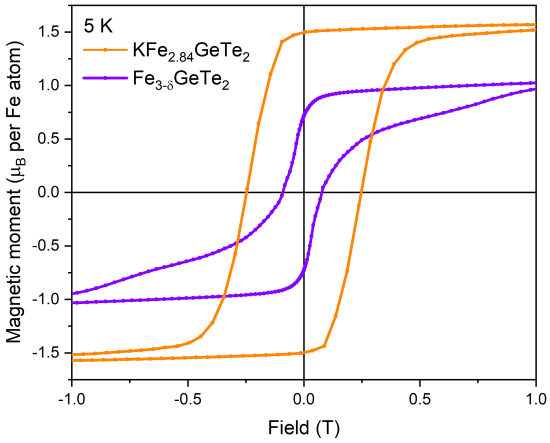

(c) Magnetisation isotherms measured at 5 K shown over the range ± 1 T

Figure 6.8: SQUID magnetometry data for $Fe_{2.96}GeTe_2$ and its potassium intercalate.

The coercive field required to re-orientate the spins also increases relative to $Fe_{2.96}GeTe_2$, from approximately 0.08 T to 0.25 T, shown by the magnetisation isotherms measured at 5 K and 300 K in Figure 6.8. The calculated saturated moment also increases from 1.02 to 1.57 μ_B per Fe atom at 1 T upon intercalation of potassium. Computational studies by Liu et al. report that the AFM coupling between Fe–Ge–Te layers in $Fe_{3-\delta}GeTe_2$ is exclusively mediated by localised exchange pathways.[13] By increasing the physical separation of the Fe–Ge–Te layers, one might expect the AFM contribution to the magnetic ordering to be reduced, which may explain the increased Curie temperature. From an electronic point of view, the addition of electrons to the structure may cause the size of the magnetic moment to increase.

6.3.4 Powder Neutron Diffraction

Powder neutron diffraction (PND) experiments were performed at room temperature (RT), 200 K and 10 K in order to obtain information about magnetic ordering, as shown in Figure 6.9, as well as confirming the crystal structure. The Rietveld refinement against PND data collected at room temperature is shown in Figure 8. The resulting model is in good agreement with the model obtained using PXRD data, and identifies small amounts of unreacted $Fe_{3-\delta}GeTe_2$ and presumably extruded elemental Fe as side phases.

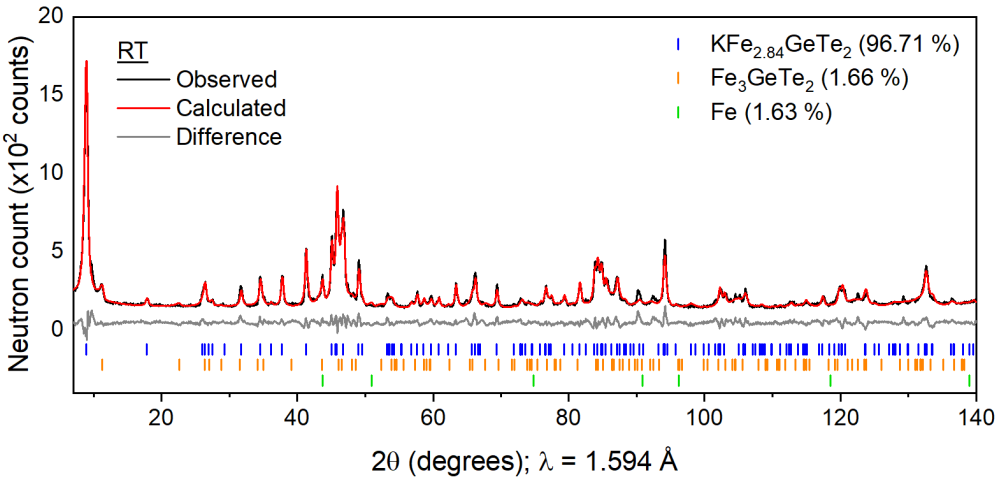

Figure 6.9: Rietveld refinement against the PND pattern of $KFe_{2.84}GeTe_2$ ($P6_3/mmc$) collected at room temperature using the D2B instrument at the ILL. R_{wp} = 5.77 %.

As discussed, the Curie temperature was found to be approximately 240 K. The data collected at 10 K and 200 K show no additional magnetic reflections, only intensity increases of the 010, 101 and 102 reflections were observed. This shows that the magnetic structure is commensurate with the nuclear structure and can be accounted for by the k = (0 0 0) propagation vector.

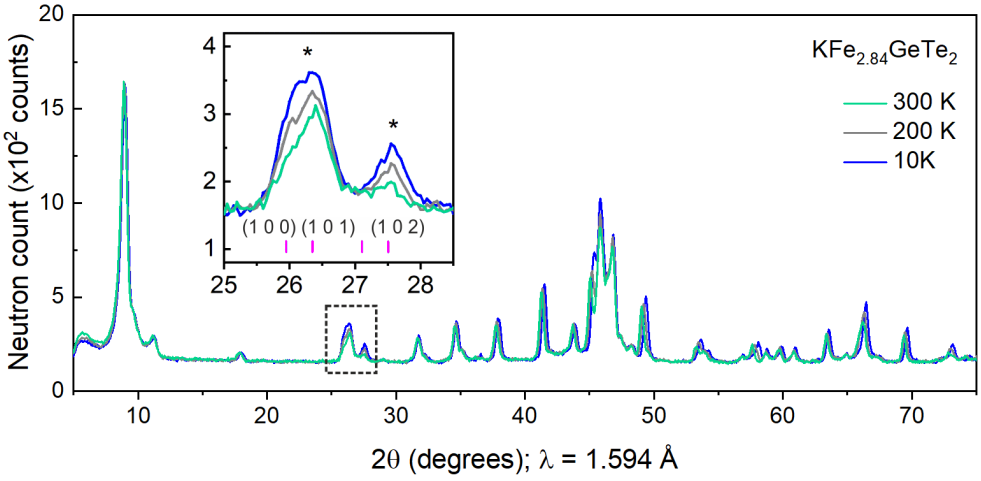

Figure 6.10: PND patterns of $KFe_{2.84}GeTe_2$ collected at 300 K, 200 K and 10 K using the D2B instrument at the ILL. Reflections marked with an asterisk (*) indicate the reflections with magnetic intensity. Miller indices are given above their corresponding tickmarks shown in pink.

The ISODISTORT[22,23] package was used to deduce the magnetic modes, and Rietveld refinements were performed to assess the suitability of the generated modes to fit the PND data. Each mode is a symmetry-adapted linear combination of Fe magnetic moments, allowing for the symmetry-imposed refinement of the magnetic structure. Due to the limited amount of magnetic information, and the superimposition of the magnetic intensity on reflections with nuclear intensity, an absolute solution was not possible. Several models were produced: the local moment model, the low moment model, and the all-mode model.

The local moment model was found by allowing individual magnetic modes on the two Fe sites to freely refine, and accepting the magnetic modes which resulted in the best visual fit to the data, whilst also produced magnetic moments with sensible errors. This model assigns the neighbouring Fe1 atoms as coupled antiferromag-

netically to each other and all Fe2 atoms couple ferromagnetically, with moments of 3.6(3) μ_B and 3.9(5) μ_B respectively. Whilst the average magnetic moment of each Fe over the unit cell is 1.2 μ_B, and agrees with the saturation moment found in the SQUID data, the size of the individual moments are indicative of a localised Fe system. This is contrary to previous single crystal PND experiments at low temperatures of $Fe_{3-\delta}GeTe_2$,[1] which reports a simple ferromagnetic model across all Fe sites with moments of approximately 1 μ_B. A 200 K, the model is similar, however the size of the moment on the Fe1 site decreases faster than on the Fe2 site. The final models are shown in Figure 6.11.

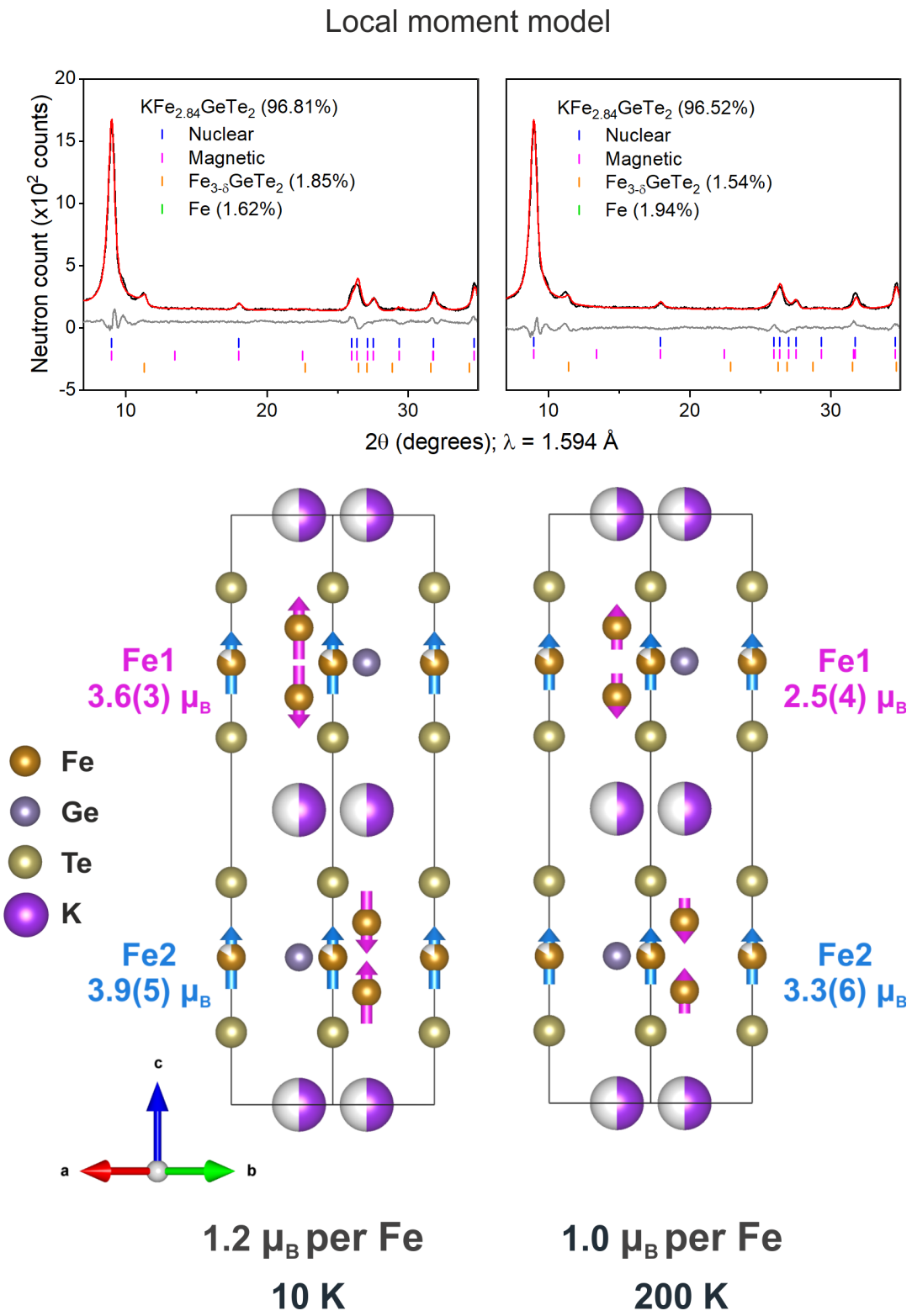

Figure 6.11: Top. The Rietveld fit of PND data collected at ***left*** 10 K and ***right*** 200 K using the local moment model. **Bottom**. The refined magnetic models at ***left*** 10 K and ***right*** 200 K.

An alternative model, the low moment model, was fit to the data for comparison to the magnetic structure reported for $Fe_{3-\delta}GeTe_2$. This was done by only allowing the ferromagnetic modes with moments aligned along c to refine, whilst adding a constraint which would not allow the magnetic moment to refine above 2 μ_B on each Fe. At 10 K, the fit was improved by fixing the Fe1 and Fe2 moments to refine to the same value, which was also done during the refinement process for $Fe_{3-\delta}GeTe_2$.[1] At 200 K, it was found that no substantial magnetic moment could be refined on the Fe1 site, and the Fe2 site gave a refined moment of 1.7(6) μ_B. The models result in average moments of 1.4 μ_B and 0.5 μ_B at 10 K and 200 K respectively, and although this also fits the SQUID data, neither fits the magnetic intensity on the 102 reflection. After further investigation, the reflection is co-incident with elemental Ge, but this assignment was discarded due to the temperature-dependent intensity of this reflection. The two additional reflections from Ge in this range are coincident with reflections from the intercalate, so cannot be identified elsewhere in the pattern. The resulting model is shown in Figure 6.12.

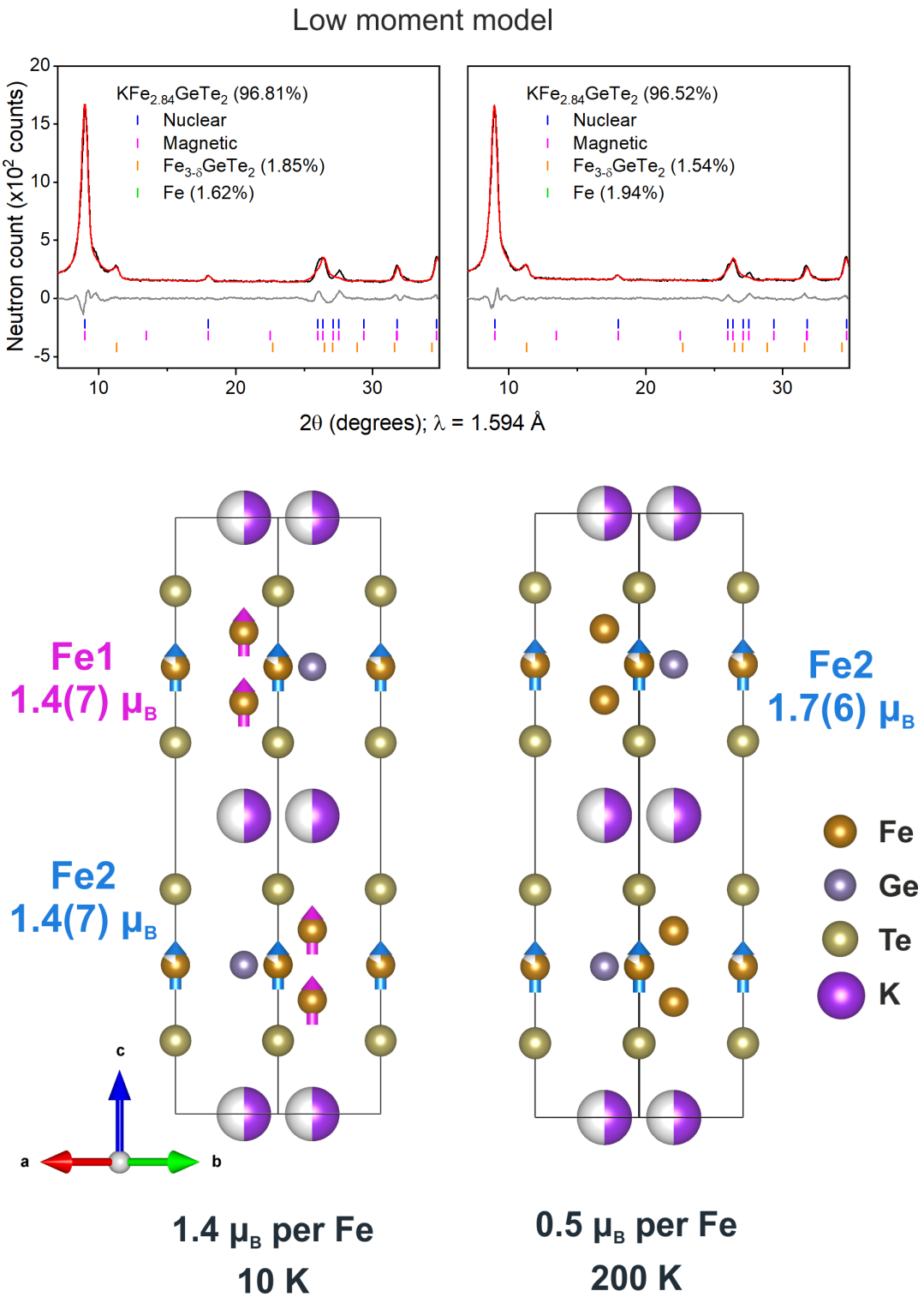

Figure 6.12: Top. The Rietveld fit of PND data collected at ***left*** 10 K and ***right*** 200 K using the low moment model. **Bottom**. The refined magnetic models at ***left*** 10 K and ***right*** 200 K.

As discussed in the introduction of this chapter, complex magnetic structures have been reported for the parent phase, including the observation of skyrmion bubbles,[24] a stripy magnetic domain structure[25] and bubble domains[26] below the Curie temperature, as well as competing ferro- and antiferromagnetism.[13,26] As such, complex structures cannot be excluded for the potassium intercalate. This consideration, in addition to the difficulty fitting the magnetic intensity, led to a model produced by allowing all possible magnetic modes to refine simultaneously. The modes contributing an small amount to the overall moment were discarded, and the active modes were allowed to refine once again. This is the 'all-mode' model, shown in Figure 6.13. The significant difference to the previous models is the presence of canting of the magnetic moments away from the c axis. This could indicate a disordered magnetic structure, since the PND pattern presents a superimposition of all the magnetic domains in the sample. The averaged magnetic moment is still directed along the c axis however, which is consistent with the lack of magnetic intensity on the $00l$ reflections. Like the low moment model, no magnetic moment was refined on the Fe1 site at 200 K, but again the magnetic intensity on the 102 reflection was fitted poorly. Since this model uses several magnetic modes and the amount of magnetic data in the PND pattern is limited, fairly large errors on the refined magnetic moments in the ab plane are obtained. Because of this, the size of the moments on the individual Fe atoms are not given, but the overall moments along the c axis are given as 0.8 μ_B and 0.6 μ_B per Fe atom at 10 K and 200 K respectively. These values however are not in good agreement with the SQUID data.

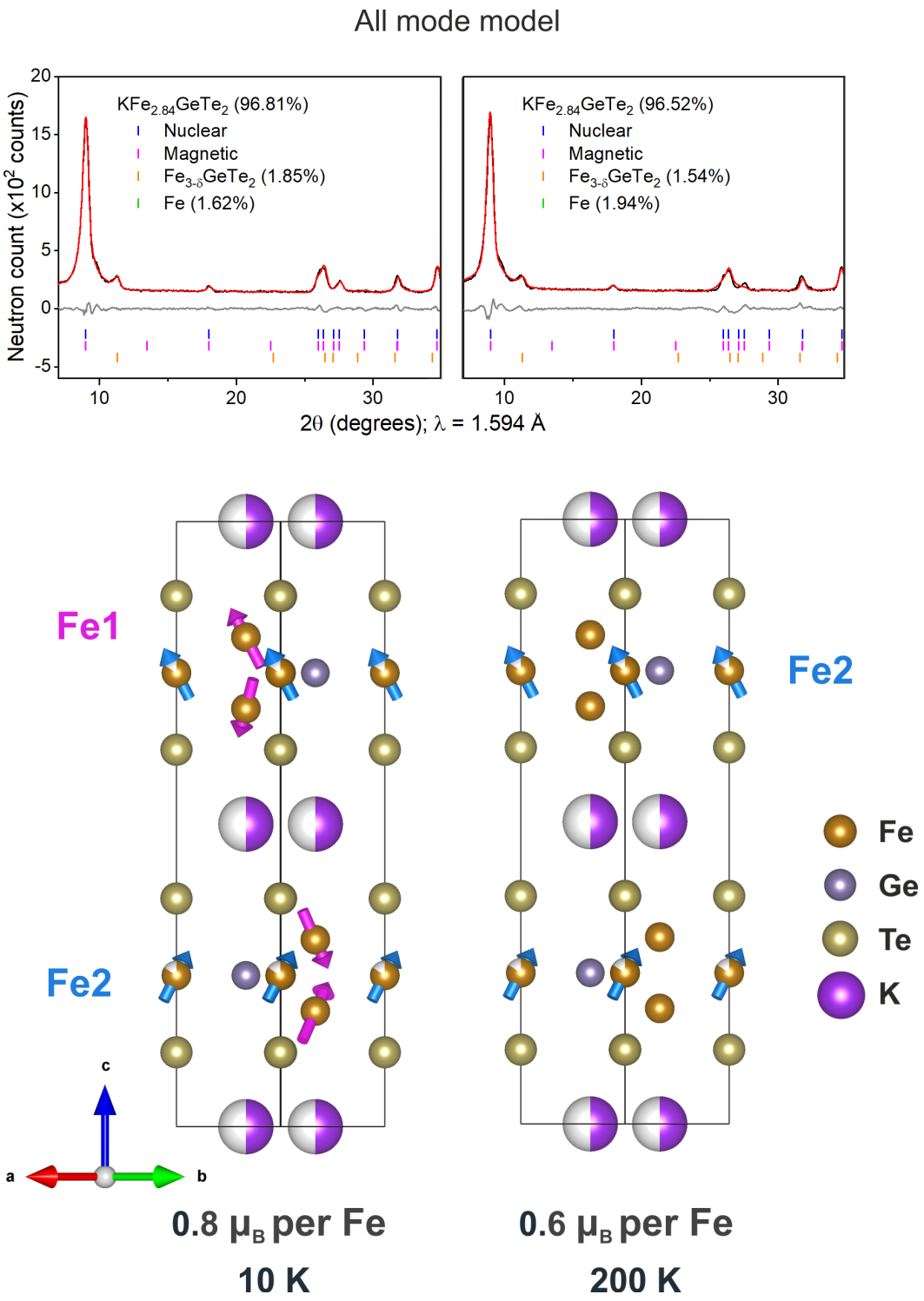

Figure 6.13: Top. The Rietveld fit of PND data collected at ***left*** 10 K and ***right*** 200 K using the all-mode model. **Bottom**. The refined magnetic models at ***left*** 10 K and ***right*** 200 K.

Due to the limited amount of magnetic information and potential complex magnetic structures, it is concluded that there is ambiguity in the magnetic structure and single crystal neutron diffraction would likely be required to address this.

6.3.5 Mössbauer Spectroscopy

Figure 6.14 shows the fitted Mössbauer spectra measured at 300K, 200K and 10K, similar temperatures to those used for the PND measurements. The fit parameters are given in Table 6.3. The spectrum collected at 300 K in the paramagnetic regime can be fit as two doublets, one corresponding to each crystallographic site, which reflect the theoretical populations of Fe1 and Fe2 (70.4 % and 29.6 % respectively), within the uncertainty and the approximation that the ratios of the integrated intensities in the fits faithfully reflect the relative populations. This indicated no magnetic ordering is present at ambient temperature which is consistent with SQUID magnetometry and PND data.

Table 6.3: Parameters from fitting Mössbauer data collected at 300 K, 200 K and 10 K. Paramaeters marked with an asterisk (*) were fixed

Site	Label	CS (mm/s)	Δ (δ) (mm/s)	Population (%)
		300 K		
Fe1	Doublet 1	0.3742(49)	0.586(22)	77.8(76)
Fe2	Doublet 2	0.321(15)	1.073(53)	22.2(76)
		200 K		
Fe1	Doublet 1	0.410877*	0.905115*	73.6(13)
Fe2	Sextet 1	0.778(19)	-0.695(16)	15.1(12)
	Sextet 2	0.334(13)	0.433(11)	11.3(12)
		10 K		
Fe1	Doublet 1	0.423(33)	0.617(63)	12.2(20)
	Sextet 1	0.64(13)	-0.24(12)	7.7(65)
	Sextet 2	0.527(53)	-0.130(52)	25.1(70)
	Sextet 3	0.694(35)	-0.239(30)	12.3(49)
	Sextet 4	0.364(36)	-0.318(24)	24.4(54)
Fe2	Sextet 5	0.133(28)	0.045(24)	18.3(22)

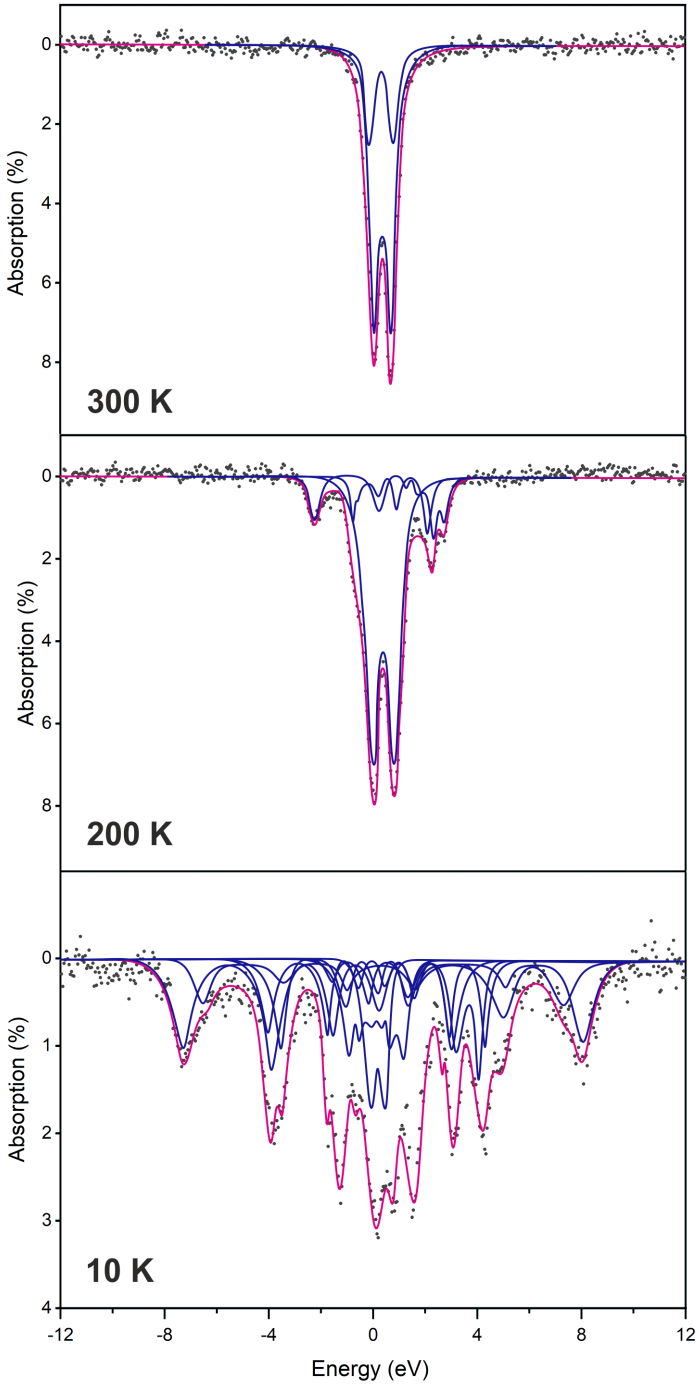

Figure 6.14: Fitted curves of Mössbauer data collected measured at 300 K, 200 K and 10 K.

The data collected at 200 K shows magnetic ordering of some iron sites. Due to the asymmetry of the spectra some parameters were fixed (marked with an asterisk in Table 6.3) in order to produce a sensible fit. The majority site was attributed to the ions in the Fe1 site due to the larger population. Sextets 1 and 2 were assigned to the Fe2 site respectively based on the total population.

At 10 K, the majority of the Fe sites are ordered. Collectively, doublet 1 and sextets 1-4 have been assigned to the Fe1 site with a cumulative population of 81.7(22) %. Sextet 5 has been assigned to Fe2 with a population of 18.3(22) %.

The splitting of the magnetically ordered Fe1 site has been attributed to differences in the immediate environment caused by vacancies on the Fe2 site. The surrounding K distribution and Fe vacancies outside of the immediate co-ordination sphere may also have an effect, but for simplicity only the nearest Fe neighbours have been considered here. The Fe sublattice of one layer of $KFe_{2.84}GeTe_2$ is shown in Figure 6.15, and some possible configurations of Fe2 vacancies immediately surrounding the Fe1 sites using a geometric model is demonstrated. There are four possible configurations: 0, 1, 2 and 3 vacancies on the neighbouring Fe2 site, which explains the four-fold splitting of the magnetically ordered portion of the Fe1 site. Since approximately 1/6 of the Fe2 positions are vacant, the existence of three vacancies surrounding an Fe1 atom is the least likely, both statistically and chemically. Consequently, sextet 1 was assigned to this scenario as it has the smallest population and relatively large error.

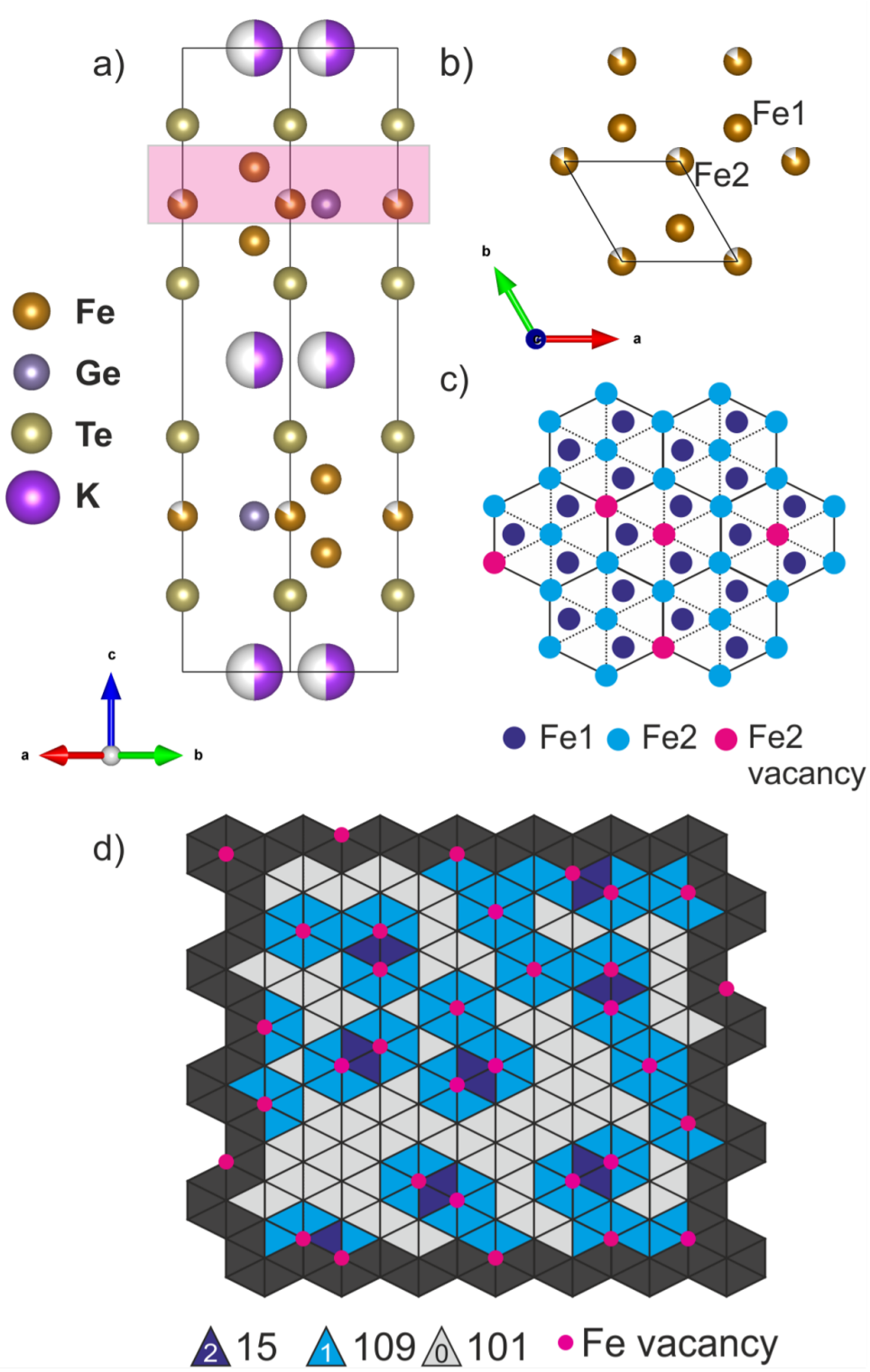

Figure 6.15: a) The unit cell of $KFe_{2.84}GeTe_2$. The shaded area represents the isolated Fe sublattice, which is viewed along the c axis in **b)**. **c)** Some example Fe2 vacancy configurations on the Fe sublattice. The triple vacancy configuration has not been shown here as it is both statistically and chemically unlikely. **d)** an extended Fe sublattice determining the statistical likelihood of 0, 1 and 2 vacancy sites occurring.

Further statistical analysis was carried out using triangular motifs to represent the immediate co-ordination of the Fe1 site (the centre of the triangle), on an extended Fe sublattice. Fe2 vacancies were placed by numbering the vertices sequentially and adding vacancies to random vertices using a random number generator, until 1/6 of the total number of vertices had a vacancy. It should be noted that this model does not account for any chemical interactions and is purely statistical. This analysis suggests that sextets 2 and 4 can each be attributed to the scenarios where there are one or no Fe2 vacancies in the immediate co-ordination, due to their large populations. This would suggest that the scenario where two Fe2 vacancies surround the Fe1 site can be assigned to sextet 3. However, the size of the population errors and other chemical factors such as electrostatics makes absolute assignment difficult using statistics alone.

The analysis suggests that Fe ordering occurs gradually, at 200 K only the Fe2 site is ordered, although this is approximately 40 K below T_C, and by 10 K, 87.8 % of the Fe sites exhibit ordering.

6.4 Discussion

Perhaps the most dramatic change induced by intercalation of potassium into $Fe_{3-\delta}GeTe_2$ is the structural rearrangement. Although the structure can be described using the same space group as the precursor, $P6_3/mmc$, significant rearrangement of the layers takes place. The alternate layers are displaced by (2/3, 1/3, 0) which results in a change in the co-ordination of the interlayer sites. Potassium is found to occupy a triangular prism in $KFe_{2.84}GeTe_2$, whereas the same position in $Fe_{3-\delta}GeTe_2$ would result in a heavily distorted octahedral site. The rearrangement of the layers is presumably driven the co-ordination requirements of the intercalated potassium.

SQUID magnetometry shows an increase of approximately 15 K to the Curie temperature of the potassium intercalate with respect to $Fe_{3-\delta}GeTe_2$. This is hypothesised to be due to the increased physical separation of the Fe-Ge-Te layers, as the layer-to-layer magnetic coupling in $Fe_{3-\delta}GeTe_2$ has been reported to have a significant antiferromagnetic component.[13] It cannot be discounted that the layer rearrangement also has an effect on the magnetic coupling between them. Increased retentivity and coercivity of the intercalated phase compared to the parent is also observed, perhaps due to the same reasons, or the addition of one electron per 3 Fe ions upon intercalation.

Refinement of the nuclear model against the PND pattern collected at room temperature confirms the model produced using PXRD data. Although magnetic intensity was identified, indicating the presence of long-range magnetic ordering, an absolute

model could not be obtained. The local moment model would suggest that the intercalated phase behaves like a localised ferromagnet, contrary to the reports of the itinerant nature of $Fe_{3-\delta}GeTe_2$. Both the alteration of the J couplings through the structural transformation, and filling of the conduction band through injection of electrons may account for these differences. However, this scenario seems unlikely. Although the resulting overall moments are in good agreement with the SQUID magnetometry data, the Mössbauer data would suggest that the Fe1 site is not ordered at 200 K, which does not agree with this model.

The low moment model however shows good agreement with the literature, the SQUID magnetometry and the Mossbauer data, as the Fe1 site is not ordered at 200 K in this model. The caveat of this model is the poor fit to the 102 reflection which has been identified as having magnetic intensity. As discussed, this is coincident with elemental Ge, but this would not result in magnetic intensity at this position and evidence of Ge cannot be found elsewhere in the pattern. Since the parent phase is an impurity, it was considered if this could be attributed to the magnetic intensity of $Fe_{3-\delta}GeTe_2$. However, the weight percentage of this phase is approximately 1.66 % so this is unlikely.

The final model, the all-mode model, might provide additional insight. Although the averaged moment does not agree with our SQUID data, the appearance of canting of moments on both Fe sites could indicate complex magnetic features are present in this system.

The Mössbauer spectroscopy results are complex and challenging to assign unambiguously. They suggest that at 300 K, no magnetic ordering is present as expected. At 200 K however, magnetic ordering is present but only on the Fe2 site. This is consistent with two of the magnetic models discussed above, however it is difficult to fit all of the magnetic intensity in the neutron data using these models. By 10 K the majority of the Fe atoms are ordered, including both Fe2 and Fe1 sites, with a small amount of unordered Fe atoms evident from a doublet and these are assumed to be on the Fe1 site.

6.5 Summary and Conclusions

The successful synthesis and characterisation of the phase $KFe_{2.84}GeTe_2$, synthesised by the intercalation of $Fe_{2.96}GeTe_2$ using potassium metal and condensed ammonia, has been shown. The host structure experiences significant structural rearrangement, driven by the co-ordination requirements of the intercalated K ions, but the intra-layer structure of the Fe-Ge-Te layers remains unchanged. K is found to occupy 6 co-ordinate trigonal prisms with a K-Te bond length of 3.46(1) Å. SQUID magnetometry shows $KFe_{2.84}GeTe_2$ has a Curie temperature of 240 K, an increase of 15 K compared to its precursor $Fe_{2.96}GeTe_2$. Refinement of the nuclear model against PND data collected at room temperature agrees with the structural rearrangement identified using PXRD. Comparison to PND patterns collected at 200 K and 10 K shows the presence of long-range magnetic ordering below T_C, and indicates commensurate ferromagnetic or ferrimagnetic ordering. However, although multiple models have been employed in an attempt to fit the data, no conclusive fit has been found, and single crystal neutron diffraction measurements would be much more informative. The Mössbauer spectra are complex, but show that magnetic ordering on the Fe2 site occurs at 200 K and almost complete ordering of both Fe sites by 10 K.

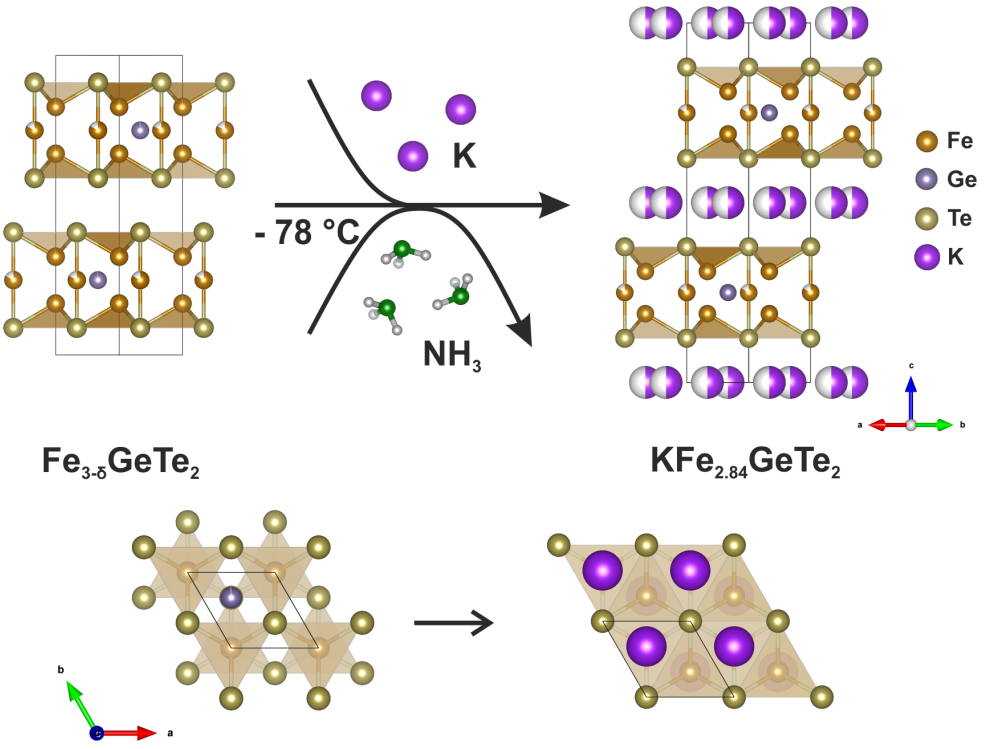

Figure 6.16: Reaction scheme showing the synthesis of $KFe_{2.84}GeTe_2$.

Further work should be performed in order to understand the magnetism in this compound. Single crystal PND would be a useful experiments, however synthesis of these intercalates as a single crystal is often problematic and causes significant reduction in the grain size, as discussed for the intercalates of Ta_2NiSe_5 in Chapter 3. Variable temperature PND could be performed to look for any intermediate magnetic transitions not observed by PND data collected at the three temperatures analysed here.

References

[1] V. Verchenko, A. Tsirlin, A. Sobolev, I. Presniakov, A. Shevelkov, *Inorganic Chemistry* **2105**, *54*, 8598–8607.

[2] H. Deiseroth, K. Aleksandrov, C. Reiner, L. Kienle, R. K. Kremer, *European Journal of Inorganic Chemistry* **2006**, *2006*, 1561.

[3] G. Drachuck, Z. Salman, M. W. Masters, V. Taufour, T. N. Lamichhane, Q. Lin, W. E. Straszheim, S. L. Bud'Ko, P. C. Canfield, *Physical Review B* **2018**, *98*, 144434.

[4] J. Stahl, E. Shlaen, D. Johrendt, *Zeitschrift für Anorganische und Allgemeine Chemie* **2018**, *644*, 1923–29.

[5] C. K. Tian, C. Wang, W. Ji, J. C. Wang, T. L. Xia, L. Wang, J. J. Liu, H. X. Zhang, P. Cheng, *Physical Review B* **2019**, *99*, 1–6.

[6] S. W. Jang, H. Yoon, M. Y. Jeong, S. Ryee, H. S. Kim, M. J. Han, *Nanoscale* **2020**, *12*, 13501–06.

[7] D. Kim, S. Park, J. Lee, J. Yoon, S. Joo, T. Kim, K. J. Min, S. Y. Park, C. Kim, K. W. Moon, C. Lee, J. Hong, C. Hwang, *Nanotechnology* **2019**, *30*, 245701.

[8] J. Yi, H. Zhuang, Q. Zou, Z. Wu, G. Cao, S. Tang, S. A. Calder, P. R. Kent, D. Mandrus, Z. Gai, *2D Materials* **2017**, *4*.

[9] J. Seo, E. S. An, T. Park, S.-Y. Hwang, G.-Y. Kim, K. Song, E. Oh, M. Choi, K. Watanabe, T. Taniguchi, Y. J. Jo, H. W. Yeom, S.-Y. Choi, J. H. Shim, J. S. Kim, *Materials Science* **2020**, *12*, 2844.

[10] Q. Li, M. Yang, C. Gong, R. V. Chopdekar, A. T. N'Diaye, J. Turner, G. Chen, A. Scholl, P. Shafer, E. Arenholz, A. K. Schmid, S. Wang, K. Liu, N. Gao, A. S. Admasu, S. W. Cheong, C. Hwang, J. Li, F. Wang, X. Zhang, Z. Qiu, *Nano Letters* **2018**, *18*, 5974–5980.

[11] A. F. May, S. Calder, C. Cantoni, H. Cao, M. A. McGuire, *Physical Review B* **2016**, *93*, 014411.

[12] A. K. Yasukochi, K. Kanematsu, T. T. Ohoyama, *Journal of the Physical Society of Japan* **1961**, *16*, 429–433.

[13] Q. Liu, J. Xing, Z. Jiang, Y. Guo, X. Jiang, Y. Qi, J. Zhao, *Communications Physics* **2022**, *5*, 140.

[14] D. Weber, A. H. Trout, D. W. McComb, J. E. Goldberger, *Nano Letters* **2019**, *19*, 5031–5035.

[15] R. D. Shannon, *Acta Crystallographica* **1976**, *32*, 751.

[16] M. Burrard-Lucas, D. G. Free, S. J. Sedlmaier, J. D. Wright, S. J. Cassidy, Y. Hara, A. J. Corkett, T. Lancaster, P. J. Baker, S. J. Blundell, S. J. Clarke, *Nature Materials* **2013**, *12*, 15–19.

[17] M. E. Kamminga, S. J. Cassidy, P. P. Jana, M. Elgaml, N. D. Kelly, S. J. Clarke, *Dalton Transactions* **2021**, *50*, 11376.

[18] H. T. Stokes, D. M. Hatch, B. J. Campbell, *FINDSYM, ISOTROPY Software Suite*, version 7.1.4, **2022**.

[19] H. T. Stokes, D. M. Hatch, *Journal of Applied Crystallography* **2005**, *38*, 237–238.

[20] W. Bronger, S. Jäger, R. Rennau, D. Schmitz, *Journal of the Less Common Metals* **1989**, *154*, 261–270.

[21] P. A. Hyde, S. J. Clarke, *Journal of Solid State Chemistry* **2023**, *323*, 124012.

[22] H. T. Stokes, D. M. Hatch, B. J. Campbell, *ISODISTORT, ISOTROPY Software Suite*, version 6.11.1, **2022**.

[23] B. J. Campbell, H. T. Stokes, D. E. Tanner, D. M. Hatch, *Journal of Applied Crystallography* **2006**, *39*, 607–14.

[24] B. Ding, Z. Li, G. Xu, H. Li, Z. Hou, E. Liu, X. Xi, F. Xu, Y. Yao, W. Wang, *Nano Letters* **2020**, *20*, 868–73.

[25] G. D. Nguyen, J. Lee, T. Berlijn, Q. Zou, S. M. Hus, J. Park, Z. Gai, C. Lee, A. P. Li, *Physical Review B* **2018**, *97*, 1–7.

[26] H. Yang, Y. Zhou, L. Li, Z. Chen, Z. Zhang, S. Wang, J. Wang, X. Chen, C. An, Y. Zhou, M. Zhang, R. Zhang, X. Zhu, L. Zhang, X. Yang, Z. Yang, *Physical Review Materials* **2022**, *6*, 084803.

'Hopefully things will start to crystallise...'

- Simon Clarke

7

Summary

Summary

This thesis explores the synthesis and characterisation of the intercalates of two groups of layered compounds, through the use of soft chemical methods. Firstly, the tantalum nickel selenides Ta_2NiSe_x (x = 5, 7) produce intercalates $LiTa_2NiSe_5$, KTa_2NiSe_5, $Li(NH_3)Ta_2NiSe_5$ and $Li_xTa_2NiSe_7$ ($0.4 \leq x \leq 1.5$). Secondly, the same chemistry is applied to a group of layered ferromagnetic compounds, the iron germanium tellurides Fe_xGeTe_2 (x = 3, 5), to give $Li(NH_2)Fe_5GeTe_2$, KFe_5GeTe_2 and $KFe_{2.84}GeTe_2$.

Chapter 3 furthers the work started by Hyde[1] in 2019, which reported the synthesis and preliminary characterisation of $LiTa_2NiSe_5$, synthesised by intercalating the excitonic insulator candidate Ta_2NiSe_5 with Li using n-Butyllithium. Previous work reveals significant rearrangement of the alternate Ta-Ni-Se slabs occurs upon intercalation, which results in the loss of *C*-centring present in Ta_2NiSe_5. This was found using a novel refinement technique which takes advantage of both the layered nature of the precursor and the assumption that the intralayer structure does not change significantly. The intercalated phase was found to crystallise in space group *Pmnb*, an orthorhombic space group. This thesis furthers the characterisation through refitting of PND data to allow for the location of Li, which is supported by computational results. Investigation of the local Li environment through ^{6}Li NMR appears to indicate a single Li environment at room temperature, however low temperature measurements show the appearance of a second, broad resonance. This indicates Li is mobile between multiple sites, which is supported by the com-

putational experiments which shows there are three Li sites which are relatively close in energy. Variable temperature PXRD studies show no monoclinic distortion is present down to 100 K, indicating no excitonic insulator phase is present in the intercalate, however a high temperature phase forms from $LiTa_2NiSe_5$ above approximately 850 °C, and persists upon cooling down to ambient temperature. Further work is required to characterise this phase. Electronically, $LiTa_2NiSe_5$ is found to be metallic, a consequence of filling the conduction band of Ta_2NiSe_5 by injecting electrons. The computational studies revealed some significant changes to the band structure upon intercalation, a consequence of the structural changes. SQUID magnetometry data shows that $LiTa_2NiSe_5$ remains a bulk diamagnet, albeit with a less negative susceptibility, caused by an increase in the opposing Pauli paramagnetism, caused by an increased density of states at the Fermi level. This work has since been published in *Inorganic Chemistry*.[2]

This work was then extended to included potassium and lithium-ammonia intercalates of Ta_2NiSe_5 using the metal-ammonia intercalation method. Both intercalates show similar structural rearrangements as reported for $LiTa_2NiSe_5$ and is one of the significant similarities across the series. Both intercalates crystallise in space group *Pmnb* with an expansion of the *b* lattice parameter (parallel to the stacking direction) which correlates with the size of the intercalated species. SQUID magnetometry shows similar electronic changes occur and the magnetic susceptibilities of all three intercalates of Ta_2NiSe_5 are similar. PND and NMR spectroscopy experiments were performed on $Li(NH_3)Ta_2NiSe_5$ to probe the environments of the light

intercalated atoms; H, N and Li. PND shows that the NH_3 and Li^+ moieties occupy different sites in the interlayer spacing and there is no evidence of site sharing. This is due to the different co-ordination requirements of both species. ^{1}H and ^{15}N NMR shows H and N both occupy single environments on the NMR timescale- supporting the site designation from the PND data. Variable temperature ^{6}Li NMR also shows a single Li environment at ambient temperature, and no signs of additional resonances down to 243 K, indicating Li does not have the same mobility as in $LiTa_2NiSe_5$, possibly a consequence of the presence of the large NH_3 moiety.

Chapter 4 explores the lithium intercalation of related tantalum nickel selenide, Ta_2NiSe_7. High resolution PXRD data reveals the presence of two 200 reflections in some of the samples of Li intercalates, suggesting a biphasic mixture of two intercalated phases was present. Further examination reveals that chemical intercalation of Li using n-butyllithium proceeds via two phases, a Li poor phase $Li_{0.4}Ta_2NiSe_7$ and a Li rich phase $Li_{1.5}Ta_2NiSe_7$. Changing the amount of reagent changes the relative ratios of these two phases, both of which closely resemble the host structure. PND experiments show that the Li poor phase has one almost filled Li site, whilst the Li rich phase has two completely filled Li sites, and supports the step-wise filling of Li sites. SQUID magnetometry shows that the Li poor phase is a bulk diamagnet, as is the host phase Ta_2NiSe_7, whilst the Li rich phase is a Pauli paramagnet, reflecting the reduction of of either the Ta(V) ion or some of the $[Se\text{-}Se]^{2-}$ dimers, (or possibly both). Both aerial and chemical deintercalation using I_2 produces Ta_2NiSe_7, showing the intercalation process is highly reversible. Electrochemical intercalation of Li was

also performed, however intercalation was found to process in a continuous fashion and no phase separation was observed. Despite the reversible chemical intercalation, it was found that Ta_2NiSe_7 cannot be cycled as the full discharge voltage profile extends far beyond what is required to produce $Li_{1.5}Ta_2NiSe_7$, and it is speculated that decomposition occurs at high specific capacities.

Chapter 5 discusses the intercalation of potassium and lithium-amide into Fe_5GeTe_2, a layered ferromagnetic with a Curie temperature of approximately 300 K. Structurally, both intercalates resemble the parent phase with an increased c lattice parameter (parallel to the stacking direction) to accommodate the guest species. PND experiments show that Li^+ and NH_2^- moieties occupy different sites, much like in $Li(NH_3)Ta_2NiSe_5$. Again, this is due to the difference in co-ordination requirements of both species. These experiments also reveal the presence of long-range magnetic ordering in KFe_5GeTe_2, which can be fit using a simple ferromagnetic model, but not in $Li(NH_2)Fe_5GeTe_2$. SQUID magnetometry data also reveals that whilst KFe_5GeTe_2 has a similar Curie temperature and saturation moment to Fe_5GeTe_2, the saturation moment of $Li(NH_2)Fe_5GeTe_2$ is almost halved, whilst the Curie temperature is retained. This could be a consequence of the different electronic features of the two intercalates; whilst intercalation of K^+ results in the reduction of Fe_5GeTe_2, intercalation of $Li^+NH_2^-$ does not. Mössbauer spectroscopy measurements shows magnetic ordering of Fe sites in both intercalates, but reveals some differences between them. Measurements of KFe_5GeTe_2 suggests only 80 % of the Fe sites order down to 10 K, which supports the magnetic model obtained from PND data in which no magnetic

moment is refined on the Fe1 site. In $Li(NH_2)Fe_5GeTe_2$ however, the Mössbauer measurements show all Fe sites participate in magnetic ordering.

Chapter 6 details the potassium intercalation into $Fe_{3-\delta}GeTe_2$ (δ = 0.03 – 0.31), a structurally related iron germanium telluride phase with a Curie temperature of approximately 225 K, depending on Fe stoichiometry. Unlike the intercalates of Fe_5GeTe_2, the intercalated phase undergoes a significant rearrangement of alternate layers but retains the space group of the parent phase, $P6_3/mmc$. This rearrangement changes the geometry of the interlayer sites from highly distorted octahedra to trigonal prisms. Potassium is modelled as half occupying all of these sites to account for the stoichiometry, however is it more likely that potassium is ordered within each layer, but disordered layer-to-layer. The refined total Fe occupancy was found to decrease slightly from 2.96 to 2.84 upon intercalation, which is reflected by the presence of some elemental Fe in the diffraction patterns of $KFe_{2.84}GeTe_2$. SQUID magnetometry reveals an increase in Curie temperature of approximately 15 K and an increased saturation moment of approximately 0.5 μ_B per Fe upon the intercalation of potassium. These are possibly consequences of the increased layer separation and injection of electrons respectively. PND experiments do reveal the presence of long range magnetic order, however no conclusive fit has been achieved. This is due to a combination of a limited amount of magnetic information and the possibility of complex magnetic structures being present in $KFe_{2.84}GeTe_2$. Mössbauer spectroscopy shows magnetic ordering occurs on the Fe2 site first, then at 10 K the ordering of the Fe1 site is split into multiple signals due to the different local

environments caused by the Fe2 vacancies in the immediate co-ordination sphere.

Overall, this work explores low temperature routes to alternative new phases inaccessible via other means. These findings not only focus on the structure-property relationship in these phases, but demonstrates significant control over them. The results presented here provide a holistic examination of the synthesis, structure and properties of soft chemically manipulated layered materials, and shows that intercalation chemistry is a powerful tool for the discovery of new functional materials.

References

[1] P. Hyde, MChem thesis, University of Oxford, **2019**.

[2] P. A. Hyde, J. Cen, S. J. Cassidy, N. H. Rees, P. Holdship, R. I. Smith, B. Zhu, D. O. Scanlon, S. J. Clarke, *Inorganic Chemistry* **2023**, *62*, 12027–37.

'What a magnificent performance, we all can't speake'

- Mick Morgan

A

Appendices

A.1 Appendix I

Structural solution of $LiTa_2NiSe_5$[1]

The PXRD pattern of the intercalate could be well indexed to an orthorhombic unit cell, a = 13.405 Å, b = 3.502 Å, c = 15.739 Å, with a comparable volume to the parent but slightly expanded. Observation of the systematic absences in the pattern indicated the extinction symbol Pn^*a. This could have corresponded to space groups $Pn2_1a$ or $Pnma$, neither of which resembles to the high temperature phase of the host. Attempts were made to take the parent structure and generate an appropriate model for the intercalated structure in either of these two space groups, but the relationship between them was non-trivial. The uncertainty in the space group was added to by the presence of a monoclinic distortion in the parent material, which although not identifiable in the PXRD pattern of the intercalated compound, could still have been present if hidden by the peak broadening. In order to circumvent these uncertainties in the symmetry, a different approach was taken to solve the structure. Firstly, the orthorhombic unit cell that was indexed was placed in $P1$ symmetry and a model that closely resembled the parent structure (minus the monoclinic distortion and in the slightly expanded unit cell) was built inside it. Then a rigid body approach was adopted by dividing the atoms into two groups according to which layer they occupied in the unit cell and constraining them so the there was no refinement of atomic positions within each layer. One layer was kept fixed in the cell and the other was allowed to refine its collective x, y and z position relative to the other. The resulting displacement was refined to

(0.499(136), -0.0156(4), -0.1372(3)). The displacement in x is within error of 0.5 and was assumed to be so for the purpose of this model. The program FINDSYM[2,3] was then used to identify an appropriate space group; $P2_1/m$ was assigned to the model and provided a good fit to the data, although it was not consistent with the extinction symbol suggested by the indexing. Atomic positions were allowed to refine further by lifting the 'rigid body' constraint, this however gave unrealistic bond distances and heavily distorted polyhedra, principally on the Ni sites. It was noticed that if the displacement in y had refined to zero (though this is outside the error) then the relationship between the two layers in the y axis would have been $\frac{1}{2}b$ and the cell could then be assigned as *Pnma*, which is one of the space groups suggested by the systematic absences. Using this new model also gives realistic bond distances and since no clear monoclinic distortion was observed in the data and no significant improvement to the fit could be achieved in $P2_1/m$ (R_{wp} = 2.672 %) versus *Pnma* (R_{wp} = 2.922 %), the *Pnma* model was accepted on this basis. The *Pmnb* setting was then selected for consistency with respect to the axes for the Ta_2NiSe_5 model.

A.2 Appendix II

Table A.1: Full bond lengths of Ta_2NiSe_7 and Lithium intercalates/deintercalates from models refined against PXRD data collected using the PSD on the I11 beamline at Diamond. Values in parentheses () were obtained from PND data collected on Echidna at ACNS.

	Ta_2NiSe_7	$Li_{0.4}Ta_2NiSe_7$	$Li_{1.5}Ta_2NiSe_7$	Deintercalated $Li_{1.5}Ta_2NiSe_7$
Ta1-Ni	4.128(9)	4.144(9)	4.165(9)	4.119(4)
		(4.092(9))	(4.182(9))	
Ta2-Ni	3.016(8)	3.028(8)	3.032(8)	3.028(4)
		(3.051(9))	(3.010(9))	
Ta1-Se2	2.608(5)	2.649(6)	2.628(6)	2.616(3)
		(2.607(7))	(2.678(7))	
Ta1-Se5	2.630(7)	2.658(8)	2.630(6)	2.637(3)
		(2.619(8))	(2.664(8))	
Ta1-Se6	2.642(6)	2.646(5)	2.653(5)	2.612(3)
		(2.636(7))	(2.614(7))	
Ta1-Se6	2.774(8)	2.739(7)	2.770(7)	2.729(4)
		(2.729(9))	(2.702(9))	
Ta1-Se7	2.723(9)	2.681(9)	2.687(9)	2.733(5)
		(2.740(9))	(2.723(9))	
Ta2-Se1	2.732(9)	2.739(9)	2.781(9)	2.719(4)
		(2.677(9))	(2.731(9))	
Ta2-Se1	2.605(6)	2.632(7)	2.602(7)	2.602(3)
		(2.667(7))	(2.634(7))	
Ta2-Se3	2.465(9)	2.510(9)	2.467(9)	2.491(4)
		(2.527(9))	(2.452(9))	
Ta2-Se4	2.541(6)	2.524(5)	2.557(6)	2.406(3)
		(2.500(7))	(2.527(6))	
Ni-Se2	2.761(9)	2.792(9)	2.760(9)	2.749(6)
		(2.757(9))	(2.779(9))	
Ni-Se3	2.415(6)	2.477(7)	2.473(7)	2.406(3)
		(2.423(5))	(2.466(6))	
Ni-Se4	2.440(9)	2.422(9)	2.447(9)	2.482(6)
		(2.483(9))	(2.391(9))	
Ni-Se7	2.396(7)	2.392(7)	2.447(8)	2.405(4)
		(2.352(5))	(2.424(6))	
Se2-Se5	2.534(9)	2.571(9)	2.591(9)	2.523(5)
		(2.532(9))	(2.637(9))	

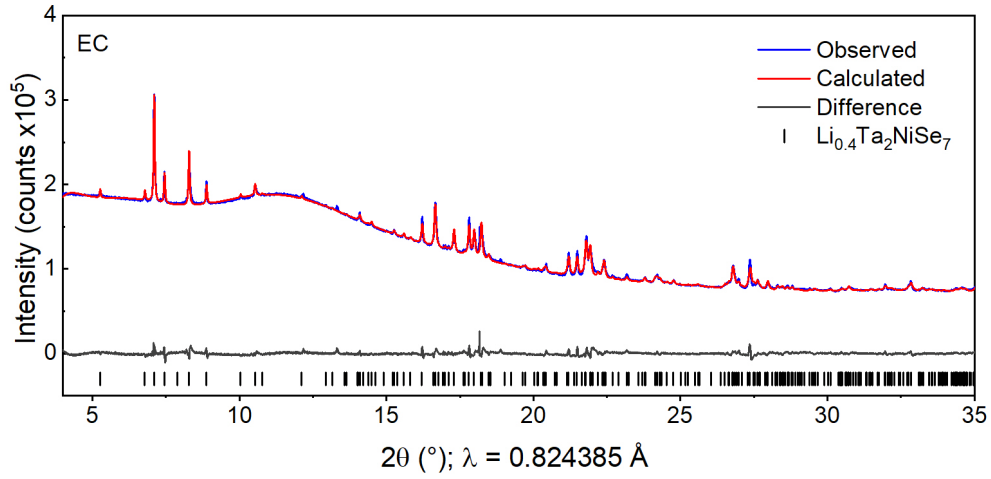

(a) x = 0.4, R_{wp} = 1.24 %.

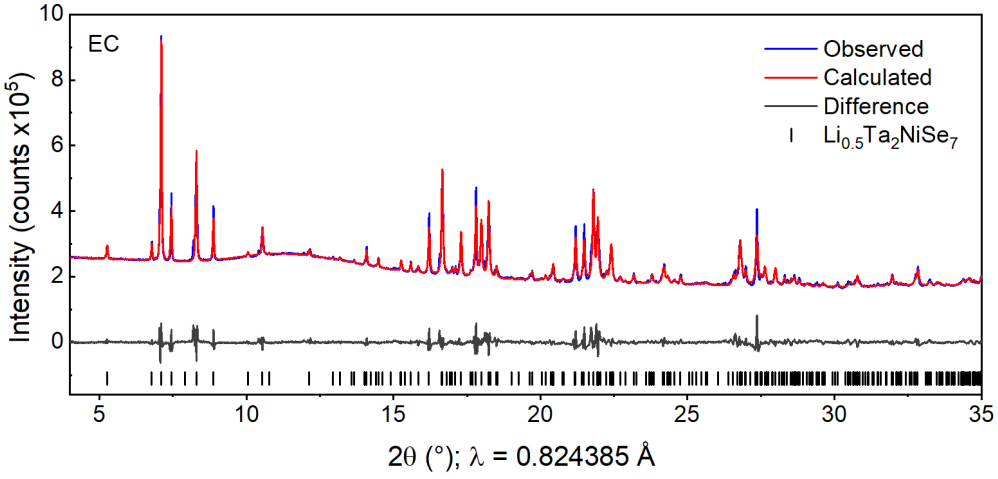

(b) x = 0.5, R_{wp} = 2.58 %.

Figure A.1: Rietveld fits against PXRD data of $Li_xTa_2NiSe_7$ ($C2/m$) synthesised electrochemically, collected using the PSD on the I11 beamline at Diamond.

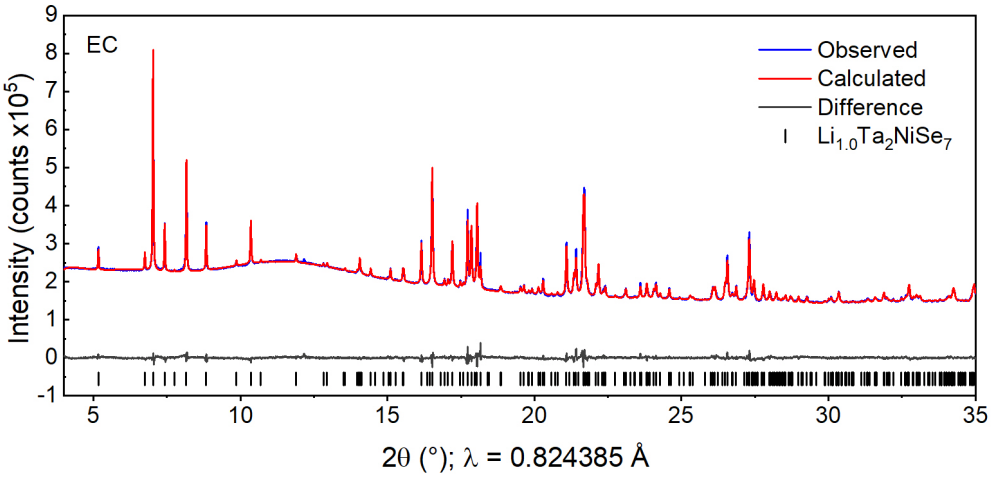

(c) x = 1.0, R_{wp} = 1.21 %.

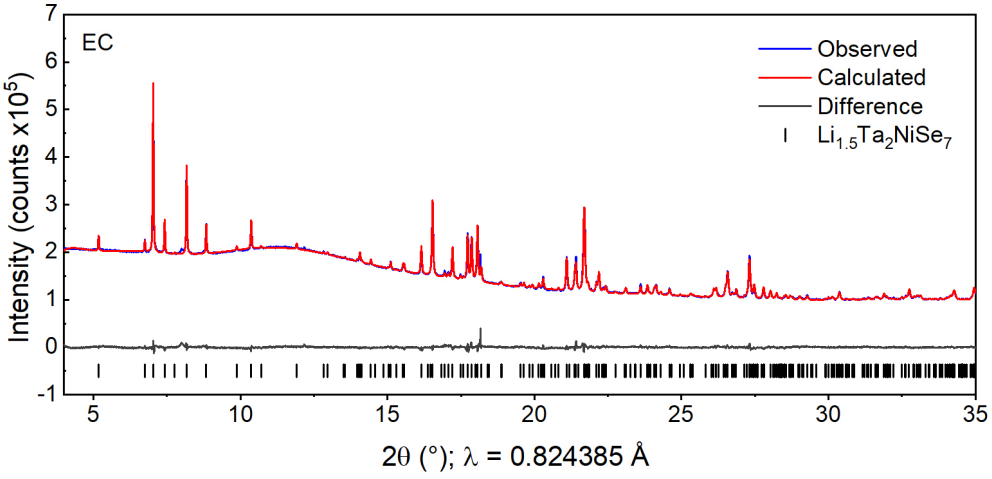

(d) x = 1.5, R_{wp} = 1.02 %.

Figure A.1: Rietveld fits against PXRD data of $Li_xTa_2NiSe_7$ ($C2/m$) synthesised electrochemically, collected using the PSD on the I11 beamline at Diamond.

References

[1] P. Hyde, MChem thesis, University of Oxford, **2019**.

[2] H. T. Stokes, D. M. Hatch, B. J. Campbell, *FINDSYM, ISOTROPY Software Suite*, version 7.1.4, **2022**.

[3] H. T. Stokes, D. M. Hatch, *Journal of Applied Crystallography* **2005**, *38*, 237–238.